KU Leuven
Biomedical Sciences Group
Faculty of Pharmaceutical Sciences
Department of Pharmaceutical
and Pharmacological Sciences

INFLUENCE OF FORMULATION AND PROCESS PARAMETERS ON THE KINETIC STABILIZATION OF AMORPHOUS SOLID DISPERSIONS WITH HIGH DRUG LOADING

Sien DEDROOG

Jury:

Promotor:	Prof. dr. Guy Van den Mooter
Chair:	Prof. dr. Ann Van Schepdael
Jury members:	Prof. dr. Patrick Augustijns
	Prof. dr. Mathy Froeyen
	Prof. dr. Thomas De Beer
	Prof. dr. Amrit Paudel

Dissertation presented in partial fulfillment of the requirements for the degree of Doctor in Pharmaceutical Sciences

March 2022

Acknowledgements

After (a little bit more) than four years of research, I finally got to write my first (and probably only) book. As you can imagine, and as I am sure that every researcher knows very well, I experienced a lot of ups and downs while gathering the results for this PhD thesis. Luckily, there were a lot of people who cheered me up during the lows and celebrated the highs with me as well. I would like to thank all of these people for their profound support; I could not have realized this PhD thesis without you.

First, I would like to express how grateful I am to my promotor, Prof. Guy Van den Mooter, for giving me the opportunity to be part of his research group and for supporting me on every step of the way to a PhD. I remember coming to your office for the first time and asking you for a PhD position, and although you did not really know me at the time, you were very enthusiastic when discussing possible PhD projects. I really admire your enthusiasm, your passion for research. I would like to thank you for sharing that passion with me, for always being available for whatever question I had (your door was literally always open), for showing me that time management was really important (still working on it) and for all the scientific knowledge you have taught me. I am looking forward to continue working with you as a postdoctoral researcher!

I would also like to thank all jury members, Prof. Ann Van Schepdael, Prof. Mathy Froeyen, Prof. Patrick Augustijns, Prof. Thomas De Beer and Prof. Amrit Paudel for their assessment of my thesis manuscript and their constructive feedback. Also the constructive feedback of Christophe Huygens was highly appreciated. I would also like to thank Prof. Peter Adriaensens for the collaboration on the NMR measurements. Next to that, I would like to acknowledge het Fonds Wetenschappelijk Onderzoek Vlaanderen (FWO) and Laboratoires SMB for their financial support.

There is not a day that I have felt alone doing this PhD project, which was not only because of my promotor, but also very much because of all my wonderful colleagues. Already on the very first day of my PhD, Annelies showed me around and made me feel very welcome. Annelies, Melissa, Elene, Tu, Fan, David, Timothy, Eline, Maarten, Lennert, Hannah, Zeynep, Jessy, Savitha and Bernard, I cannot express how grateful I am to all of you for making the lab feel like a second home, for all your help during experiments and your friendship. A special thank you to Timothy, Eline and Robin for being such an amazing writers, I really enjoyed writing manuscripts together with you! Also teaching of practical courses (Receptuurkunde) became a lot more fun because of Petra, Pieter, Tom, Marlies, Timothy, Kristof, Melissa and Marie-Lynn. Thank you all for that! Of course I am also very grateful for all the nice memories of our Christmas parties, afterwork events, lunches and coffee break talks, so also a thank

you for that to Matthias, Neel, Tom, Tom, Pieter, Bing, Nina, David, Melissa, Elene, Eline, Annelies, Timothy, Marlies, Kristof, Arno, Glenn, Bart, Philip, Jari, Jens and Maarten.

I would also like to express my gratitude to Cecilia and Célestine, the master students who worked on my PhD project. Cecilia, thank you for showing me where I can get the best Italian pizza in Leuven. And Célestine, I hope you know how much I appreciated you and everything you have done for my PhD project. I hope you find peace up there.

Outside of the lab, I was very lucky to be surrounded by people who were trying to understand what I was doing in my PhD, and supported me on every step of the way. My best friends, Tumba, I am very lucky to have you as my 'support group'. Thank you for always, no matter what, having my back! Also a special thank you to Pieter, for listening to me complain about experiments gone wrong from time to time (and cheering me up after). My mom and dad, I cannot put into words how grateful I am for all the chances you have given me that led me to this PhD. You always made me feel like I could do anything in the world, as long as I really wanted to. Thank you for the numerous phone calls/talks to encourage me and for always being there for me. At last, but definitely not least, I would like to thank two special men in my life. Lens, my brother, who also started a PhD not long after I did. I am very grateful that we can share this passion for research with each other, and for all the times that you listened to my presentations and gave me tips on how to improve them. And my boyfriend, Kurt, thank you for being my number one supporter! There is no one who can make me smile like you can, who can cook for me like you can or who can help me with data-analysis issues like you can. All of these things were essential for me to finish this PhD thesis, so thank you for all of it!

Abbreviations

Ac	Acetone
ACN	Acetonitrile
AFM	Atomic Force Microscopy
ALS	Alternate Least Squares
API	Active pharmaceutical ingredient
ASD	Amorphous solid dispersion
BCS	Biopharmaceutics Classification System
BDDCS	Biopharmaceutics Drug Disposition Classification System
bp	Boiling point
BSA	Bovine Serum Albumin
CPMAS	Cross Polarization Magic Angle Spinning
CRYO/CM	Cryo-milling
DCM	Dichloromethane
DCS	Developability Classification System
DMA	Dynamic Mechanical Analysis
DMA	Dynamic Mechanic Analysis
DMSO	Dimethyl sulfoxide
DoE	Design of Experiments
DRS	Dielectric Relaxation Spectroscopy
DVS	Dynamic Vapor-Sorption
DZP	Diazepam
EMA	European Medicines Agency
EtAc	Ethyl acetate
EtOH	Ethanol
FaSSIF	Fasted State Simulated Intestinal Fluid
FDA	Food and Drug Administration
FNB	Fenofibrate
FRET	Fluorescence Resonance Energy Transfer
FT-IR	Fourier Transform InfraRed spectroscopy
GFA	Glass Forming Ability
GI	Gastro-Intestinal

GRAS	Generally Recognized As Safe
HME	Hot Melt Extrusion
HPMC	Hydroxypropylmethyl cellulose
HPMC-AS	Hydroxypropylmethyl cellulose – acetate succinate
HSM	Hot Stage Microscopy
HSPLM	Hot Stage Polarized Light Microscopy
HTS	High Throughput Screening
IGC	Inverse Gas Chromatography
IMC	Indomethacin
LOD	Limit of detection
LOQ	Limit of quantification
LTA	Localized Thermal Analysis
MAF	Mobile Amorphous Fraction
mDSC	Modulated Differential Scanning Calorimetry
MeOH	Methanol
MRP	Multidrug Resistance-associated Protein
NAP	Naproxen
NCE	New Chemical Entities
PALS	Positron Annihilation Lifetime Spectroscopy
PCRM	Pure Curve Resolution Methods
PC-SAFT	Perturbed Chain - Statistical Associated Fluid Theory
PDFs	Pair Distribution Function Calculations
Pe	Peclet number
PEG	Polyethylene glycol
PEG-*g*-PVA	polyethylene-glycol-polyvinyl alcohol
PEO	Polyethylene Oxide
Pgp	P-glycoprotein
PLGA	Poly(lactic-co-glycolic acid)
PrOH	2-propanol
PVP	Polyvinylpyrrolidone
PVPVA	Poly(vinylpyrrolidone-co-vinyl acetate)
RAF	Rigid Amorphous Fraction
RCS	Refrigerated Cooling System
RH	Relative Humidity

RHF	Reversing Heat Flow
Ro5	Rule of five
RT	Room Temperature
SAXS	Small Angle X-ray Scattering
SD	Spray drying
SEM	Scanning electron microscopy
SLE	Solid-Liquid Equilibrium
SONICC	Second Order Nonlinear Optical Imaging of Chiral Crystals
ssNMR	Solid state Nuclear Magnetic Resonance
T	Temperature
TEM	Transmission Electron Microscopy
Tg	Glass transition temperature
TGA	Thermal Gravimetric Analysis
Tg_w	Tg width
T_{in}	Inlet temperature
ToF-SIMS	Time-of-Flight Secondary Ion Mass Spectrometry
T_{out}	Outlet temperature
WAXS	Wide Angle X-ray Scattering
XRPD	X-Ray Powder Diffraction

Table of contents

Chapter 1
General introduction

A part of this chapter has been published as a review paper: **Boel E., Koekoekx R., Dedroog S.**, Babkin I., Vetrano M.R., Clasen C., Van den Mooter G. Unraveling Particle Formation: From Single Droplet Drying to Spray Drying and Electrospraying. Pharmaceutics, 12(7), 625 (2020).

1.1. THE CHALLENGES OF ORAL ADMINISTRATION OF DRUGS

Oral administration is the most preferred drug administration route as it is non-invasive, allows self-administration, and can be used for a wide variety of dosage forms at relatively low costs[1,2]. Despite this preference of both patients and manufacturers, there are several barriers that a drug needs to overcome to reach its therapeutic target after oral administration. To exemplify, during phase I clinical studies with vemurafenib, which was a drug with potential to prolong the lives of patients with metastatic melanoma, patients did not respond to very high doses of the drug as such[3]. The lack of response was related to a poor absorption of the drug, which could be resolved by using a solubility enhancing formulation strategy. Here, a formulation strategy was the direct answer to enable the drug therapy in cancer patients[3]. In the following sections, the different factors that determine the oral bioavailability will be discussed, together with possible targets for formulation strategies to increase the oral absorption.

1.1.1. What factors determine the oral bioavailability?

There are five important factors that can influence the oral bioavailability of an Active Pharmaceutical Ingredient (API), which is a measure for the rate and extent at which API molecules reach their therapeutic target unchanged[1,4]. First, the drug product needs to be able to disintegrate, after which the API needs to dissolve in the Gastro-Intestinal (GI) fluids, and thus have an adequate aqueous solubility and dissolution rate (1)[5]. In a next step, the dissolved API has to permeate through the intestinal wall (2), where efflux transporters, such as P-glycoprotein (Pgp) or Multidrug Resistance-associated Protein (MRP), can interfere with the permeation process by redirecting the permeated API back to the GI fluids (3). Additionally, presystemic metabolism of the API by CYP3A4 enzymes, pancreatic enzymes and colonic bacteria[6] can decrease the oral bioavailability as well. After permeation, the API will pass through the portal vein to the liver, where first-pass metabolism can take place, again lowering the bioavailability (4). Subsequently, assimilation might also take place in other organs (5). Hence, the fraction of the API that reaches its therapeutic target is determined by the fraction that is absorbed, the fraction that escapes the intestinal metabolism and the one that escapes hepatic elimination[5]. Other features that could influence the oral bioavailability are the GI motility[7,8], pH, food intake[9], GI physiology of the specific patient population[10] and drug-drug interactions[11].

Accordingly, in order to obtain sufficient oral bioavailability, compounds should have adequate solubility and be able to permeate the intestinal wall. These features have been correlated to concrete physicochemical 'drug-like properties' by Lipinski et al.: an API is more likely to have a good oral absorption when it has less than 5 H-bond donors, less than 10 H-bond acceptors, a lower molecular

weight than 500 g/mol and a Log P lower than 5[12,13]. A high Log P is correlated with poor aqueous solubility, while a high molecular weight and a high hydrogen bonding potential are related to poor permeability[12]. These drug-like properties are known as 'the rule of five' (Ro5), which is generally accepted as the golden standard for the prediction of the absorption behavior of New Chemical Entities (NCE). Nowadays, it is also being applied in the search of novel SARS-CoV-2 therapeutics[14]. In spite of this, it should be kept in mind that the Ro5 does not account for the presence of intestinal wall active transporters or metabolic events[12] and that exceptions on the Ro5 have been reported in literature[15–17].

1.1.2. The diametrical relation between screening approaches and drug-like properties

Drug discovery nowadays is dominated by target-based approaches, where the aim is to generate compounds with a high *in vitro* potency for their target[18]. The shift from phenotypic-based approaches towards target-based approaches started with the introduction of combinatorial chemistry and High Throughput Screening (HTS) in the 1980s. Combinatorial chemistry allowed an automated synthesis of a large number of small molecules[19], while HTS was employed to quickly screen this large amount of compounds in a cost-effective manner[20]. A lot of NCE could be simultaneously assessed for their *in vitro* potency for a target. During these screenings, polar aprotic solvents, such as dimethyl sulfoxide (DMSO), were used to dissolve the compounds because they could solubilize very diverse chemicals, were completely miscible with water and compatible with most targets and cells[20]. However, by dissolving the NCE in an organic solvent, their thermodynamic aqueous solubility was not considered[12]. Moreover, it was found that therapeutic targets are generally hydrophobic and thus have a higher affinity for lipophilic NCE, which in turn led to the selection of NCE with poor aqueous solubility[21–23]. It has been estimated that 75% of NCE are poorly water soluble, which could result in an insufficient oral bioavailability[24,25]. Hence, physicochemical properties associated with a high *in vitro* potency are often diametrically opposed to drug-like properties[18]. In conclusion, these drug screening approaches selected very potent hits, but did not account for physicochemical properties required for a good oral bioavailability.

1.1.3. The Biopharmaceutics Classification System (BCS) and its extensions

In order to address the increasing amount of poorly water-soluble compounds in the drug pipelines, a universal classification system that related the *in vitro* solubility and permeability of NCE to their *in vivo* oral bioavailability was required. In 1995, Amidon et al. introduced the Biopharmaceutics Classification System (BCS), which divides APIs in four classes as a function of their aqueous solubility

and permeability[26] (Fig 1.1.). Both the European Medicines Agency (EMA) and the U.S. Food and Drug Administration (FDA) define an API as highly soluble when the highest marketed dose of the API is able to dissolve in 250 mL over the entire pH range of the GI tract, *i.e.*, pH 1.2 to 6.8, at 37 ± 1 °C[27,28]. An API has a high permeability when the absorbed fraction after oral administration is 85% or more based on a mass balance study or compared to a reference dose which is administrated intravenously[27,28]. The permeability is often assessed relative to a high permeability internal standard (*e.g.,* caffein), where the tested API is considered as having a high permeability when its permeability is equal or higher than that of the internal standard[27,28]. Following these definitions, BCS Class I drugs are those with a high solubility and permeability, which makes them ideal candidates for oral administration (Fig 1.1.)[26]. BCS Class II drugs on the other hand, have a low solubility and high permeability, while Class III drugs have a high solubility and low permeability. The oral bioavailability of Class II drugs is determined by their solubility and dissolution rate and that of Class III drugs by the GI membrane permeation. Class IV drugs are very poor drug candidates for oral administration as they have both a poor solubility and permeability[24].

Several modifications of the BCS have been proposed to predict the *in vivo* oral bioavailability of NCE more accurately[29–37]. For instance, the definition of a highly soluble API can be considered too strict in case of weak acids categorized as BCS Class II, as these APIs often have an adequate solubility and permeability in the upper small intestine[37]. Some extensions of the BCS led to new classification systems: the ABГ system[29], the Developability Classification System (DCS)[30] and the Biopharmaceutics Drug Disposition Classification System (BDDCS)[31–34]. In the ABГ system, APIs are categorized based on the fraction of the API that its absorbed rather than their solubility and permeability[29]. In the DCS, Class II drugs are subcategorized in a dissolution rate limited (IIa) and a solubility limited (IIb) oral bioavailability[30]. In addition to that, Butler and Dressman also proposed that the solubility had to be tested in a larger volume, *i.e.,* 500 mL instead of 250 mL, and that a more biorelevant medium had to be used, such as Fasted State Simulated Intestinal Fluid (FaSSIF)[30]. Wu and Benet developed the BDDCS, where they replaced the permeability component of the BCS with the metabolic clearance of the drug, allowing them to predict the effect of elimination routes and transporters on the oral bioavailability[31–34]. In spite of these modifications, the BCS remains the most popular classification system to correlate *in vitro* physicochemical properties to *in vivo* absorption behavior. When a NCE is categorized in BCS Class II, III or IV, its classification can be used to determine an appropriate formulation strategy in order to improve its drug-like properties and hence the oral bioavailability (Fig 1.1.).

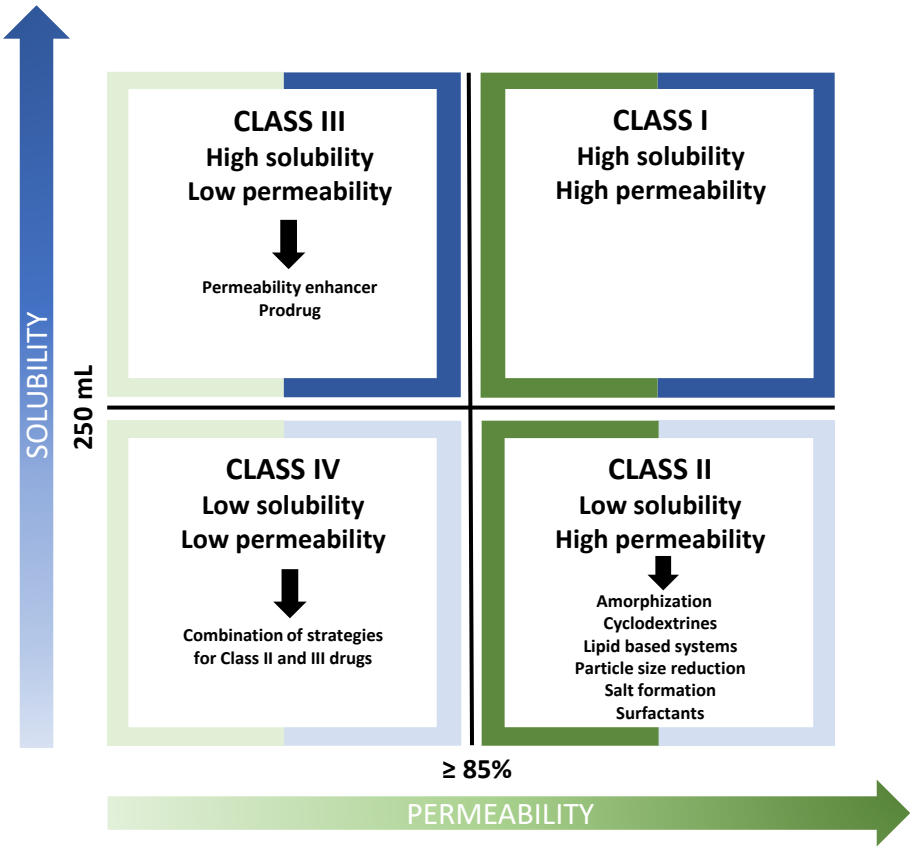

Figure 1.1. *Biopharmaceutics Classification System (BCS) and formulation strategies to increase the oral bioavailability by modifying the solubility and/or permeability. An API is highly soluble when the highest marketed dose of the API is able to dissolve in 250 mL over the entire pH range of the GI tract at 37 ± 1 °C. An API has a high permeability when the absorbed fraction after oral administration is 85% or more*[27,28]*. Modified from Singh and Van den Mooter 2016*[38]*.*

1.1.4. Formulation strategies to increase the solubility and dissolution rate

The oral bioavailability of an API can be both solubility and dissolution rate limited. Before advancing to formulation strategies to tackle these limitations, the difference between these two properties will be clarified. The thermodynamic solubility of a compound is defined as its maximum concentration in solution when it is in equilibrium with an excess amount of solid compound and the solid form does not change over time, *i.e.*, the most stable crystalline state of the solute is present[1,39]. A compound can also have an apparent solubility, which is defined as the solubility of a compound in solution that is in equilibrium with one of its metastable forms[39]. The dissolution rate of a compound is the rate at which it passes into solution, which can be described by the Nernst-Brunner equation (Eq. 1.1.)[24,40]:

$$\frac{dC}{dt} = \frac{DS}{Vh}(C_S - C_t) \qquad \textit{Equation 1.1.}$$

in which dC/dt is the change in API concentration over time, *i.e.,* the dissolution rate, D is the diffusion coefficient, S the specific surface area, V the volume of the dissolution medium, h the thickness of the diffusion layer, C_S the saturation solubility of the API compound and C_t its concentration in solution at time t[40]. For compounds of which the absorption process is dissolution rate limited (Class IIa in the

DCS[30]), particle size reduction can increase the dissolution rate and thus the oral bioavailability. In the Nernst-Brunner equation (Eq. 1.1.), this effect is represented by the surface area S, as smaller particles have a relatively larger surface area, which is directly proportional to the dissolution rate dC/dt[40]. Micronization of particles could for instance be achieved by using a dry-impact milling technique with sufficient shear forces, such as ball milling or air-jet milling[24].

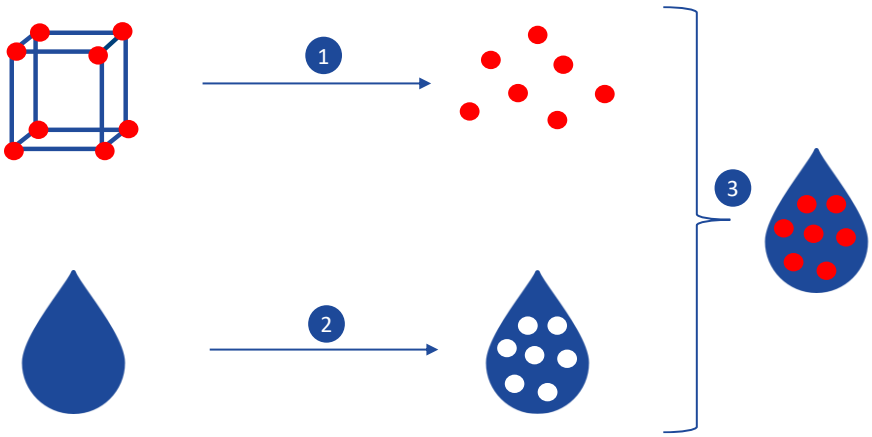

Figure 1.2*. The three steps of the dissolution process of a crystalline solid. The crystal lattice needs to be disrupted (1) and vacancies have to be created in the dissolution medium (2). These vacancies can then be filled with the free drug molecules (3). Modified from Van den Mooter 2012* [41].

On the other side, improving the oral bioavailability of compounds with a poor thermodynamic solubility (Class IIb in the DCS[30]), is not as straightforward. To better understand the possible targets of solubility enhancing formulation strategies, the three subprocesses of a dissolution process will be discussed (Fig 1.2.)[41]. First, the API molecules need to be detached from one another by disrupting the crystal lattice (1), which is an endothermic process represented by the lattice energy. A good indication of the strength of intermolecular forces between API molecules (and hence the energy requirement to break them) is the melting point (T_m) of a crystalline compound[24]. Second, vacancies in the dissolution medium need to be created in order to make room for the solute molecules (2), which is again an endothermic process and represented by the evaporation energy. Last, hydration/solvation of the individual API molecules has to take place (3), which is a spontaneous process of which the energy gain is represented by the solvation energy[41]. The total energy requirement of these three steps determines if the entire dissolution process is an exo- or endothermic process[41].

The solubility of poorly water soluble APIs can be limited by their solid-state characteristics (1) and/or by the hydration/solvation process (3)[24]. For all hydrophobic APIs, the dissolution process is limited by hydration, yet for some of them it is also limited by the presence of strong intermolecular forces in the solid state. When only hydration is the limiting factor, the APIs might dissolve well in a non-aqueous solvent, such as lipids. Therefore, these compounds are both hydrophobic and lipophilic, and are being referred to as 'grease balls'. On the other hand, 'brick dust' compounds are the ones with a poor

solubility in all solvents[42,43]. Several authors have investigated the molecular features of poorly water soluble APIs to classify them as 'grease balls' or 'brick dust' compounds[44,45]. In general, 'grease balls' were large, flexible and lipophilic molecules (high $logP$) while 'brick dust' molecules were smaller, rigid and have relatively lower lipophilicity (low $logP$) and higher T_m[42]. However, these rules cannot be applied to all APIs, as both exceptions and intermediates have been reported, *e.g.,* the solubility of aromatic structures with a high $logP$ can be both solid-state and hydration limited[46]. Yalkowsky et al. translated this correlation between the solid state, the lipophilicity and the aqueous solubility in the General Solubility Equation (GSE)(Eq. 1.2.)[47,48]:

$$log\, S_0 = 0.5 - 0.01\,(T_m - 25) - logP \qquad \textit{Equation 1.2.}$$

where S_0 is the intrinsic solubility, T_m is the Celsius melting point and $logP$ is the octanol-water partition coefficient of the solute[47,48]. The strength of the intermolecular forces is described by the T_m (1) and the ease of hydration by the $logP$ (3)[42].

The distinction between these types of poorly water-soluble APIs is especially important to select an appropriate solubility enhancing formulating strategy. For lipophilic, 'grease ball' compounds, solubilization in co-solvents, liquid surfactants or lipid-based delivery systems might be applied to tackle the solubility issues, while for 'brick dust' compounds more complex modifications of the solid form are required: production of salts, nanocrystals, complexation with cyclodextrins, stabilized polymorphs, co-crystals[49], solvates, amorphous forms or Amorphous Solid Dispersions (ASDs) (Fig 1.1.)[1,24]. In this thesis, the focus is on the application of ASDs to increase the solubility and dissolution rate of poorly water-soluble APIs.

1.2. AMORPHOUS SOLID DISPERSIONS

1.2.1. The amorphous form

As the lattice energy of 'brick dust' compounds is larger than both the evaporation and solvation energy, and thus responsible for their low aqueous solubility, the aim of generating an amorphous form is to minimize this energy requirement by destroying the crystal lattice before oral administration[3]. Hence, the difference between an amorphous material and a crystalline one lies in the lack of any long-range order in case of the amorphous one, which can be ascribed to a random distribution of molecular units. Amorphous materials have the molecular conformation of a frozen liquid with such a high viscosity that molecular motion and relaxation processes are slowed down and they appear as solids[41,50]. Thus, at a molecular level, amorphous forms are similar to liquids, while at a macroscopic level their properties resemble those of solids[45]. Where a crystalline solid is characterized

by a T_m, an amorphous one has a glass transition temperature (T_g), which is the transition from a higher to a lower mobility and viscosity[51]. To clarify this difference, the relative enthalpic/entropic changes in a compound in function of temperature are depicted in Fig 1.3.[38,52]. When a crystalline material is heated, there will be a slight enthalpy/entropy increase, followed by a stepwise increase in enthalpy/entropy at the T_m (1). Subsequent cooling of the liquid will have a different effect depending on the cooling rate. When a low cooling rate is applied, the same path will be followed in the opposite direction, hence, crystal formation will take place (2). Contrarily, application of a very high cooling rate does not leave any time for the material to rearrange in a more ordered state. Instead, a continuous decrease in enthalpy takes place and a supercooled liquid is formed (3). At some point, the temperature decrease will be too fast for the molecules to follow, and the molecules fall out of equilibrium. This point is the T_g, where the supercooled liquid becomes an amorphous solid or glass[52]. Depending on the cooling rate, the T_g will be positioned at a higher or lower temperature, and it is thus no constant but depending on the amorphization process[51].

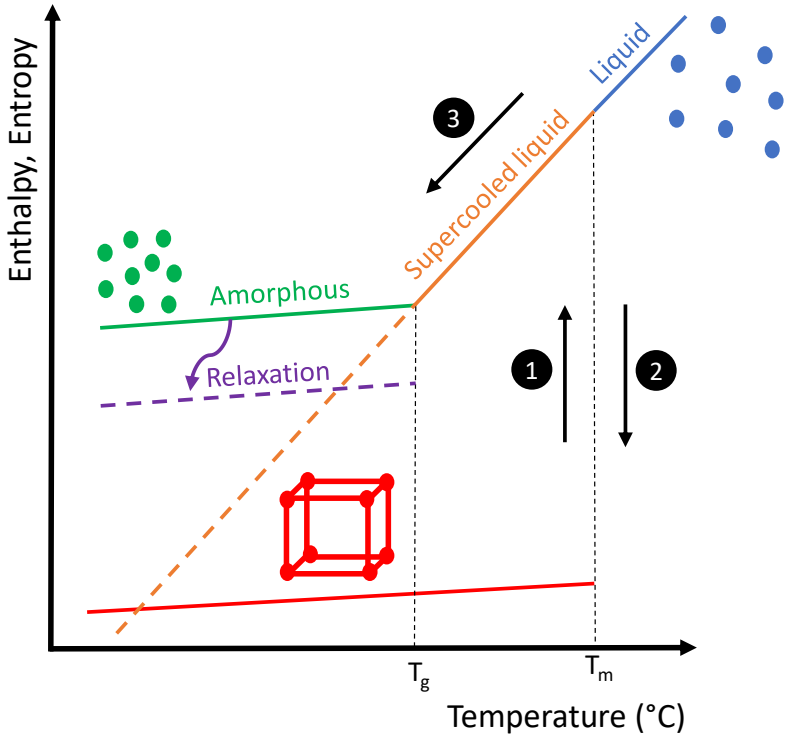

Figure 1.3. *Enthalpy, entropy diagram of the various states of an API in function of temperature. (1) Upon heating of a crystalline material, the enthalpy and entropy will slightly increase (red line) until the melting point (T_m) is reached, where the crystalline material will melt, and a liquid (blue line) is formed. (2) When the liquid is cooled slowly, crystal formation will take place. (3) When it is cooled rapidly, a supercooled liquid will be formed (orange line). Continuing the rapid cooling process will make that the molecules fall out equilibrium. This non-equilibrium point is called the glass transition temperature (T_g), after which an amorphous form is obtained (green line). During storage, the amorphous form might undergo structural relaxation towards its equilibrium state (purple line). Modified from Singh and Van den Mooter 2016[38].*

In Fig 1.3., the enthalpy of the amorphous form is much higher than that of its crystalline counterpart, which is a result of the absence of any long-range symmetry. Because of this, the first step in the dissolution process will require much less energy as there is no lattice energy that needs to be overcome. However, the enhanced thermodynamic properties and molecular mobility of the amorphous form also make it inherently unstable[38]. The first law of thermodynamics states that all systems strive to have the lowest Gibbs energy possible[51], thus, the amorphous form has the tendency to convert back to its lower energetic crystalline form. During storage, this conversion can start with structural relaxation processes, which is depicted in Fig 1.3. by a decrease in enthalpy of the amorphous form, so-called enthalpy relaxation[51]. The molecular mobility of a compound comprises both its intra- and intermolecular relaxations that can be vibrational, translational and rotational[53]. At the T_g, global or α-relaxations, which are cooperative movements of the intact molecule, are the main relaxations taking place. On the other hand, local or sub-T_g relaxations, which happen on a shorter time scale and have a lower activation energy, are most important at a temperature below the T_g[52]. Although it was thought that α-relaxations determined the risk at crystallization, in recent years, it became evident that sub-T_g relaxations also play an important role in the crystallization process[53]. Accordingly, both types of relaxation can be a precedent for crystallization.

The likelihood of these relaxation processes is dependent on the storage conditions, *i.e.,* temperature (*T*) and relative humidity (RH). The higher the storage temperature is relative to the T_g, the higher the molecular mobility and thereby the risk of nucleation and subsequent crystal growth will be[54,55]. This gave rise to the 'T_g – 50 °C rule', that states that the contribution of α-relaxations to the relaxation process can be neglected when the amorphous form is stored under these conditions[39,41,53]. Also, the RH of the storage environment can have implications for the crystallization risk. As the chemical reactivity and hygroscopicity of amorphous forms is increased, water uptake in presence of a high RH is very likely[56]. Water will act as a plasticizer because of its very low T_g (ca. -135 °C[57]), thereby lowering the T_g of the amorphous compound. Thus, for samples stored at the same *T*, the $T - T_g$ will become smaller, the molecular mobility higher and structural relaxation will be facilitated[54,57,58]. Hence, the higher the moisture content, the more likely that crystallization and chemical degradation will occur.

In conclusion, based on thermodynamics, amorphous APIs are expected to have an improved solubility and dissolution rate compared to their crystalline counterpart, yet they have such limited stability that they are rarely used as such as an end product for oral administration[41]. Examples of pure amorphous APIs on the market are zafirlukast (Accolate®) and quinapril hydrochloride (Accupril®)[59,60].

1.2.2. Amorphous solid dispersions

To (partially) overcome these stability issues, an amorphous API can be formulated as an ASD or glass solution, where the amorphous API is molecularly dispersed in an inert carrier, which is most often a polymer, at solid state[61]. The stabilizing effect of the carrier can be based on multiple principles: the presence of API-carrier interactions such as hydrogen bonding or dipolar interactions, the anti-plasticization effect, a reduced molecular mobility and an increased viscosity[62]. Hydrogen bonding between an API and its carrier can be beneficial for both the physical and chemical stability of an ASD[62]. However, the favorable effect of hydrogen bonding on the ASD stability depends on the degradation mechanism of the API, and thus the presence of hydrogen bonding is no assurance for a better stabilized system[63]. Moreover, hydrogen bonds are no necessity for an advantageous effect of the carrier: Van den Mooter et al. showed that the anti-plasticization effect, *i.e.*, elevation of the T_g of the ASD by using a polymeric carrier with a high T_g, was sufficient to prevent crystallization in ASDs of ketoconazole and polyvinylpyrrolidone (PVP), where there was no hydrogen bonding potential between the API and polymer[64]. The higher the T_g of the ASD relative to the surrounding T, the lower the molecular mobility and hence the crystallization risk.

In case of a miscible API-polymer combination, the system typically exhibits a single T_g that is positioned in between the ones of the pure compounds[39,52,65]. The T_g of the system can be predicted using the Gordon-Taylor equation which presumes that the adhesive interactions are of the same order of magnitude as the cohesive ones (Eq. 1.3.)[39,52,65]:

$$T_{gmix} = \frac{w_1 T_{g1} + K w_2 T_{g2}}{w_1 + K w_2} \qquad \textit{Equation 1.3.}$$

in which w is the weight fraction, T_g stands for the glass transition temperature and 1 and 2 are the amorphous compounds with the lowest and highest T_g, respectively. K is a constant that can be estimated using the Simha-Boyer rule (Eq. 1.4.):

$$K \cong \frac{\rho_1 T_{g1}}{\rho_2 T_{g2}} \qquad \textit{Equation 1.4.}$$

where ρ represents the density of the amorphous compounds. However, the Gordon-Taylor equation only holds true for an ideally mixed API-polymer system with the same strength for adhesive and cohesive forces. A deviation from the predicted T_g value can indicate the presence of undetected phase separation, strong specific interactions or a plasticizer such as water[39]. A positive deviation often indicates that the interaction strength between API and polymer is higher than that of interactions in the individual components, which can for instance suggest hydrogen bonding[66,67]. Also a negative deviation, indicating a loss in interaction strength upon mixing, can be observed[39].

Hence, the Gordon-Taylor equation does presume an ideal situation, where the API-polymer mixture is miscible. Miscibility between an API and polymer is indispensable in order to obtain homogenous mixing at a molecular level and preserve the API in its amorphous state[50]. However, the degree of miscibility is dependent on the specific API-polymer combination and therefore an important factor to take into account when selecting a carrier. Moreover, as an ASD remains a high energetic state, thermodynamic and environmental factors could still induce phase separation and subsequent recrystallization of the amorphous form[68]. Thus, as physical stability remains an issue for ASDs, the miscibility between an API and its carrier is a very important requisite for a successful ASD formulation. Accordingly, numerous theoretical and experimental approaches have been proposed to determine the miscibility and facilitate the carrier selection process: the Flory-Huggings theory, API-carrier thermodynamic phase diagrams, solubility parameters, solubility determination in polymer monomers or polymer solutions, a computational docking approach and thermal analysis[62].

Furthermore, a carrier can also have advantageous effects on the dissolution behavior of the amorphous API. When a hydrophilic carrier is used, it will start to dissolve upon contact with the GI fluids and thereby release the molecularly dispersed API as a supersaturated solution, *i.e.,* the concentration of this solution is higher than the thermodynamic solubility of the compound, with enhanced absorption capacity[39]. However, the formation of a supersaturated state also results in an inherent thermodynamic driving force for nucleation, crystal growth and eventually precipitation[62]. In order to benefit from the solubility enhancement of an ASD, the supersaturated state should be maintained long enough to allow for absorption in the GI tract. The carrier plays an important role in maintaining this supersaturated state by increasing the solution viscosity, interacting with API molecules, absorption at the particle surface and slowing down the crystallization kinetics[62]. Moreover, by molecular dispersion of the API in the polymer matrix, its particle size is strongly reduced. From the Nernst-Brunner equation (Eq. 1.1.) follows that a decreased particle size results in an increased dissolution rate. Hence, formulation as an ASD is not only beneficial to increase the solubility of a poorly water-soluble API, but also to increase its dissolution rate.

Accordingly, an ideal carrier must be able to stabilize an amorphous API in its solid state and at the same time, enhance the dissolution rate and maintain the supersaturated state for a long enough period of time for absorption to take place[62]. Favorable properties of a carrier include: a high T_g, the presence of functional groups that enable hydrogen bonding (*i.e.,* hydrogen donors and acceptors), it should be inert and Generally Recognized As Safe (GRAS)[39]. Additional properties are dependent on the applied manufacturing technique and the desired release profile. For immediate release formulations, hydrophilic carriers should be used, while sustained release can be obtained by using water-insoluble carries that swell rather than dissolve when brought in contact with water[39]. In this

work, the focus was on hydrophilic amorphous polymers and other carriers will therefore not be discussed further. Amorphous carriers are either natural product-based polymers or fully synthetic ones. The natural ones are cellulose derivatives, such as hydroxypropylmethyl cellulose (HPMC) and hydroxypropylmethyl cellulose acetate succinate (HPMCAS), while the fully synthetic ones include for instance PVP, polyvinylpyrrolidone-co-vinyl acetate (PVPVA) and polymethacrylates such as Eudragit L and S[62].

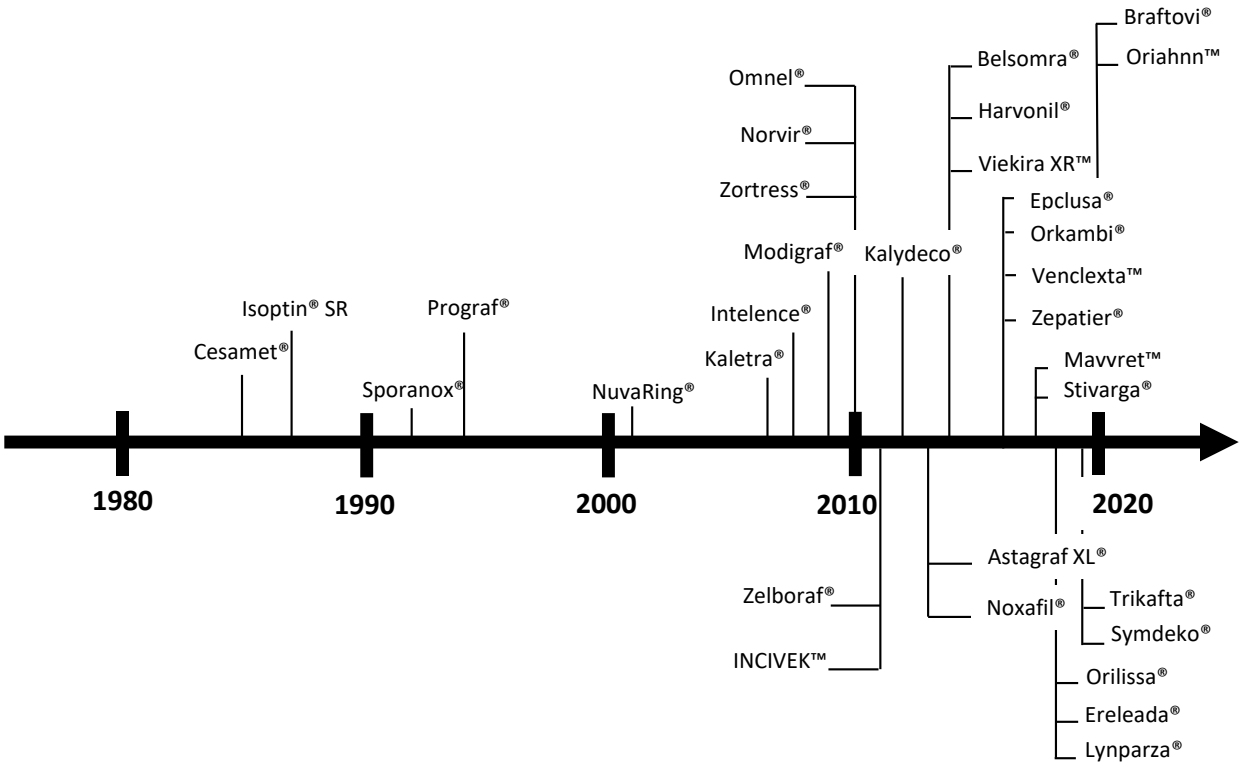

Figure 1.4. *Timeline of marketed ASDs[3,69]. Partially modified from Jermain et al. 2017[3].*

Although physical stability issues remain a challenge for ASD formulation and selection of an ideal carrier can be a time-consuming process, the number of ASDs that has successfully reached the market has increased over the past few years (Fig 1.4.)[69–71]. Currently, there are more than 30 ASD products on the market, inter alia, itraconazole (Sporanox®), etravirine (Intelence ®), lumacaftor and ivacaftor (Orkambi®) and tacrolimus (Prograf®)[3]. Also reformulation of already marketed APIs as ASDs has been proven successful. To exemplify, lopinavir and ritonavir (Kaletra®) for anti-HIV treatment were first marketed together in a soft-gelatin capsule, which had to be stored in a refrigerator and taken six times a day together with food. Reformulation of these APIs as ASD reduced the amount of daily dosage units, eliminated the need for refrigeration and diminished the effect of a meal on the drug plasma concentrations[3]. Accordingly, the amount of ASDs in late-stage development is also increasing. In 2015, it has been reported that 76 ASD products were in the pipeline[70]. Currently, three clinical trials with ASDs are ongoing, from which one is with hot-melt extruded efavirenz[72]. Further, these numbers do

not reflect the amount of research that is being performed in the field of ASDs, as the amount of preclinical ASD products is probably much higher, but the majority of research in this phase is not published[70,73,74]. Additionally, also injectable ASD formulations have been marketed, *e.g.,* paclitaxel (Abraxane®)[70].

1.3. MANUFACTURING TECHNIQUES

Besides the selection of an appropriate carrier, also the ASD manufacturing technique should be selected in function of the API and its desired physicochemical characteristics. The production method could influence the physical state, stability, particle morphology and pharmaceutical performance of an ASD. There are three categories of ASD manufacturing methods available: heat/fusion-based methods, mechanochemical activation/mechanical-based methods and solvent-based methods, from which the latter comprises most techniques[75]. It has been reported that 56% of lab scale methods are solvent-based, 35% heat-based, 7% mechanical-based an another 2% use a combination of techniques (Fig 1.4.)[75]. Combinations that have been described include hot melt extrusion (HME) together with electrospinning and solvent-anti-solvent precipitation with sonication[75]. Moreover, the amount of available manufacturing techniques is still increasing. To exemplify, vacuum drum drying was recently introduced as a new solvent-based method [76]. Also new approaches such as microwave induced *in situ* amorphization of the API in its final product are still being proposed [77]. A non-exhaustive overview of possible manufacturing techniques per category can be found in Table 1.1.

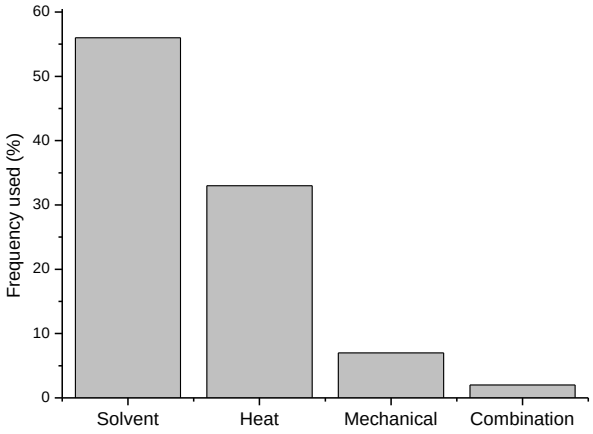

Figure 1.4. *The frequency that manufacturing techniques for amorphous solid dispersions are used per category. Most techniques are solvent based methods. Modified from Edueng et al. 2017*[75]*.*

In pharmaceutical industry, hot melt extrusion and spray drying are most commonly applied[78]. Spray drying has the advantage that it is relatively easy to scale up form lab scale to an industrial scale and moreover, that it is applicable to a wider range of physicochemical characteristics, which is especially important for compounds with thermal and shear stability issues[75]. Hot melt extrusion can be

preferred for processing of highly viscous materials and has the advantage that it is a continuous process and it requires no solvents, thus it is generally considered a more green technology[79,80]. In the following paragraphs, the principles of hot melt extrusion, spray drying, and cryogenic milling will be briefly discussed as these three manufacturing techniques were employed in this work.

Table 1.1. *Non-exhaustive overview of manufacturing techniques for ASDs per category*[3,50,81]*.*

SOLVENT BASED METHODS	HEAT BASED METHODS	MECHANOCHEMICAL ACTIVATION
Spray drying	Hot melt extrusion	Ball milling
Electrospraying	Hot melt granulation	Cryogenic milling
Electrospinning	Melt quenching	
Freeze drying	Spray congealing	
Fluid bed coating	KinetiSol® Dispersing	
Super critical fluids		
Coprecipitation		
Film casting		
Spray freezing		
Thin film freezing		
Vacuum drum drying		

1.3.1. Hot melt extrusion

HME is a continuous manufacturing process in which raw material, *e.g.,* a physical mixture of an API and its carrier, is converted into a product of uniform shape and density by forcing it through a die under defined conditions[82,83]. There are four steps in a HME process: feeding the extruder via a hopper, conveying of the material (and potential mixing and particle size reduction) inside the extruder, flowing through the die and exiting the die followed by downstream processing[83]. A hot melt extruder can thus be considered as a pump that allows both conveying and mixing[84]. It exists out of a heated barrel in which one or more rotating screws transport the material towards a die. Based on the processing steps, an extruder can be dividid in different zones: feeding zone (1), conveying zone (2), melting zone (3) and melt pumping zone (4) (Fig 1.5.)[83].

During this process, there are two important energy inputs that allow amorphization and dispersion of the API in the polymer matrix at a molecular level. First, the barrel is heated above the T_g of the compounds and sometimes even above the above the T_m of the crystalline API[80]. Second, shear forces generated by the continuously rotating screws can accelerate the dissolution of the API in the polymer matrix as well[79]. Moreover, when the mixture exits the die, it is very rapidly cooled to room temperature (RT), resulting in kinetic trapping, which can be considered as 'freezing' the API molecules in the polymer matrix. Kinetic trapping can be beneficial for the prevention of API clustering, nucleation and crystallization[79].

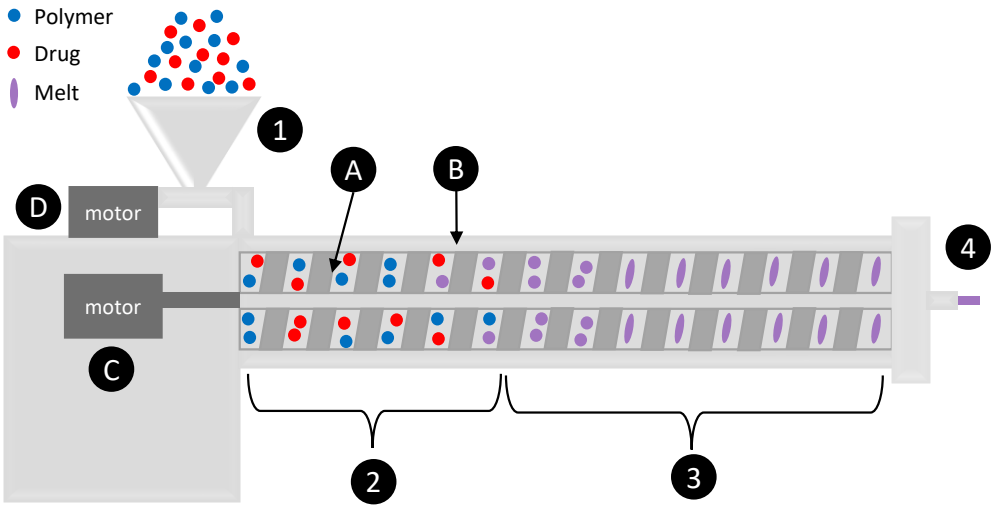

Figure 1.5. *Schematic representation of a typical twin-screw extruder: (1) feeding zone, (2) conveying zone, (3) melting zone and (4) a melt pumping zone. Process parameters that are important for the final ASD product quality are: (A) screw configuration, (B) barrel temperature, (C) screw speed and (D) feed rate. Modified from Patil et al. 2016*[80].

The extent of shear forces that is generated by the screw movements is dependent on the type of extruder and the screw design. There are different types of extruders available: single-screw extruders, twin-screw extruders, which can be co-rotating or counter-rotating and have intermeshing or non-intermeshing screws, and multi-screw extruders, which can have a static or a rotating central shaft[80]. Most extruders in pharmaceutical development are twin-screw extruders. When a twin-screw extruder with a counter-rotating design is used, the material is pushed through the gap in between the screws as they move towards each other, resulting in high shear forces[82]. However, this is also linked with air entrapment, generation of high pressure, a low maximal screw speed and a lower output. When a co-rotating screw is used, lower shear forces are generated, yet the configuration allows for higher screw speeds, while maintaing good mixing and conveying capacity, which makes them more frequently used[82]. Most twin-screw extruders are of the fully intermeshing type, as it allows for self-cleaning and it prevents local overheating by maitaining a continuous material flow. Non-intermeshing extruders have a place in processing of highly viscous materials or removing large amount of volatiles during prodution[82].

Additionally, the configuration of an extruder can be easily modified by changing the screw elements. A first type of screw elements are the typically helical shaped conveying screws, which are excellent at moving the material further downstream in the extruder, but have a rather low mixing capacity[84]. Kneading/mixing screw elements can be implemented to increase the mixing capacity. The paddle-like shape of kneading elements results in accumulation of the material, which facilitates mixing in those zones[84]. All extruders contain conveying elements, which might be accompied by additional kneading/mixing elements, depending on the desired level of mixing.

In addition to the selection of the appropiate equipment design (A), several process parameters can have an impact on the final product quality of the ASD (Fig 1.5.). As mentioned above, the barrel temperature (B) should be installed high enough to allow molecular mixing of the API and polymer, yet not above their degradation temperature[80,85]. A higher temperature also results in a lower viscosity of the liquid mixture and thus a lower torque. Moreover, it should be taken into account that the product temperature is generally higher than the barrel temperature, as mechanical energy is transfered from the screws to the melt. The screw speed (C) has a direct impact on the residence time: the higher it is, the lower the residence time will be. For amorphization, a high screw speed is beneficial in terms of high shear mixing, yet if it is installed too high, there is a risk of incomplete mixing due to a too short residence time. The last process parameter that can be adapted is the feed rate (D), which always has to be balanced with the screw speed to maintain a constant melt flow. Generally, the filling level should be kept at 20 to 50% (in case of twin-screw extrusion), because overfilling might give rise to too high torque and reduced residence time[85].

1.3.2. Cryogenic milling

Although it is well-established that milling is a top-down approach resulting in particle size reduction and that it could thereby reduce crystallinity and induce amorphization, the mechanism behind this solid-state amorphization has not yet been fully elucidated[50,86]. A first hypothesis stated that amorphization occurred via generation of heating effects and subsequent quenching[67]. However, as milling at lower temperatures, *e.g.* cryogenic milling, resulted in a higher degree of amorphization, this approach was discarded[87,88]. Nowadays, it is generally accepted that the amorphization process by milling is a result of an accumulation of crystal defects, which is illustrated in a relative enthalpy/entropy - temperature diagram in Fig 1.6.[86,89].

The degree and kinetics of amorphization depend on the milling process parameters, from which the temperature and milling intensity are the most important ones[88]. The milling temperature is a difficult parameter to control as collisions of the beads (with each other or the milling chamber) can also induce a temperature rise[88]. By applying cryogenic grinding, where the materials are either frozen prior to milling or the equipment is continuously flushed with liquid nitrogen, the effect of temperature-induced changes during milling is minimised[90]. As (re)crystallization is a possible temperature-induced change, the implementation of cryogenic milling enables the production of completely amorphous material wich could not have been produced at RT[90]. The milling intensity can for instance be adapted by altering type and amount of beads inside the milling chamber. Another process parameter that might influence the final product quality is the milling time[91].

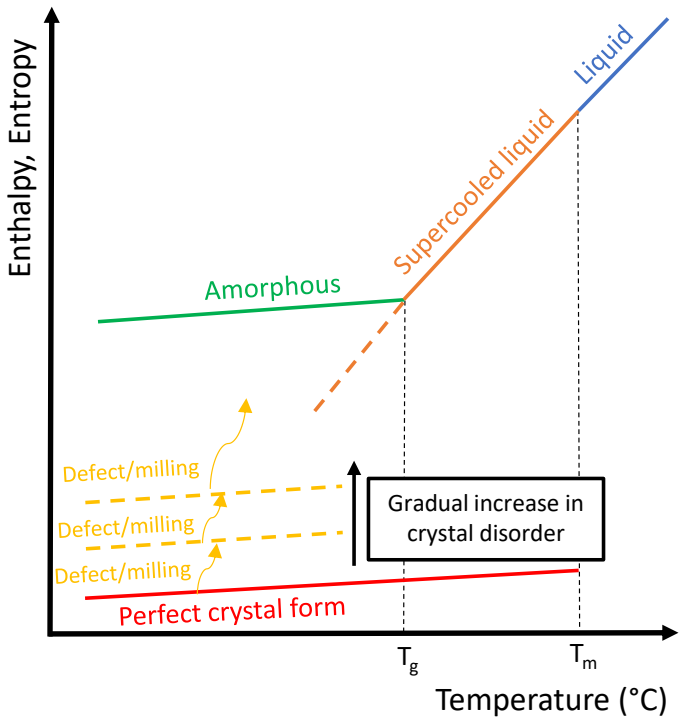

Figure 1.6. *Enthalpy/entropy – temperature diagram. Milling is considered to induce a gradual increase in crystal defects (yellow), eventually leading to formation of the amorphous form (green). Partially modified from Pas et al. 2020*[92]*.*

In spite of the growing interest in cryo-milling of ASDs over the past few years, it has recently been shown that polymer degradation and subsequent polymer-assisted decomposition of the API might take place during production[91,92].

1.3.3. Spray drying

In a spray drying process, a solution of an API and its carrier in an (organic) solvent is atomized through a nozzle (1), thereby generating small droplets which are subsequently dried due to very fast solvent evaporation in the drying chamber (2). The atomization step is highly important in generating a sufficiently large surface area over which heat and mass transfer can take place. Heat is transferred from the hot drying gas in the drying chamber towards the droplet surface while vapor transfer occurs from the droplet surface towards the carrier gas. Finally, the resulting dried particles are separated from the drying gas via a cyclone (3) and collected in a collection vessel (4)[93]. A typical spray drying set-up is depicted in Fig 1.7.

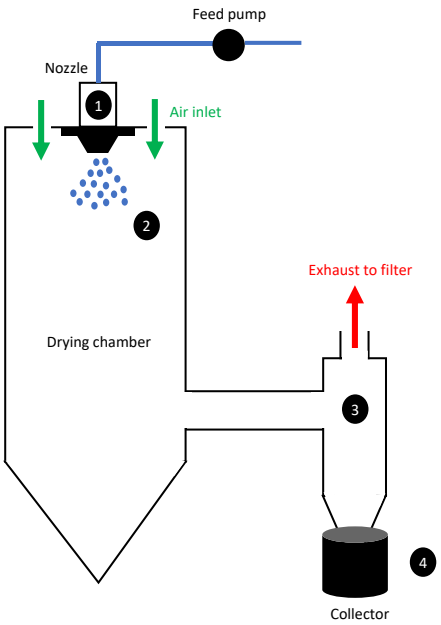

Figure 1.7. *Schematic representation of a spray drying set-up. (1) The solution is pumped towards the nozzle, where it is atomized in very fine droplets, (2) followed by very fast solvent evaporation in the drying chamber resulting in particle formation. (3) The particles are separated from the drying air in the cyclone, (4) after which the particles can be collected in the collection vessel. Modified from Singh and Van den Mooter 2016*[93].

A very pivotal step in this process is the moment at which the very tiny droplets are brought in contact with the heated gas and very fast solvent evaporation takes place. Rapid evaporation results in an increased viscosity and permits kinetic trapping of the API in the carrier matrix. This allows the formation of (supersaturated) molecular dispersions[94]. In the following paragraphs, the drying behavior and the factors that could influence this behavior will be discussed.

1.3.3.1. Theory of droplet drying

Generally, the droplet drying process can be divided in a constant-rate drying stage and a falling-rate drying stage (Fig 1.8.). In a first stage of drying, the droplet drying is mainly characterized by the solvent, similar to evaporation of a pure solvent droplet. The driving force for solvent evaporation is the difference between the vapor pressure of the solvent and its partial pressure in the surrounding environment. However, the drying rate is limited and controlled by the energy required for solvent evaporation and thus by the heat transport towards the surface of the droplet[95]. Before the actual drying process starts, the droplet will be heated until the wet-bulb temperature, which is the equilibrium temperature due to a constant evaporation heat loss of the solvent into the surrounding gas at a given pressure, T and RH, is reached[96,97]. After heating of the droplet to the wet-bulb temperature, drying will start from the surface of the droplet[96]. As drying continues, solvent molecules will keep migrating from the center towards the surface. The migration of the solvent molecules can be mediated through molecular diffusion relative to the solute, convection of fluid within the droplet or capillary solvent flow through a solid porous matrix[93]. The unhindered drying that is analogous to

free solvent evaporation results in droplet shrinkage. If the ambient parameters remain unchanged, the droplet temperature remains equal to the wet-bulb temperature and the drying rate is constant and only controlled by the heat transfer towards the surface of the droplet[98]. For this reason, this stage is named **the constant-rate drying stage** (Fig 1.8.).

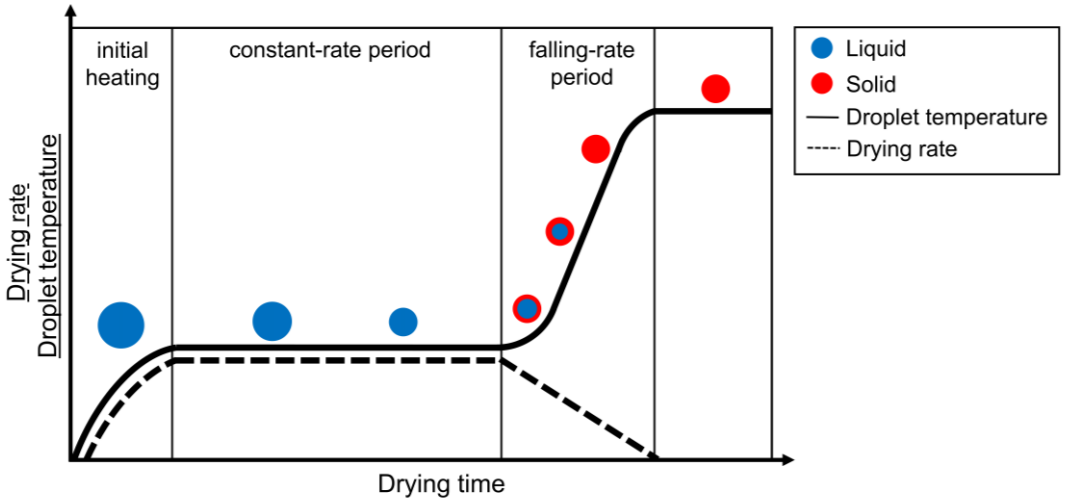

Figure 1.8. *Schematic illustration of the different stages a droplet experiences during the drying process. Temperature evolution is represented by a solid line and drying rate by a dotted line. The liquid fraction is shown in blue and the solid fraction in red*[99].

The second stage of drying is defined by the solutes present in the droplet. As solvent evaporation takes place from the surface of the droplet, the solute concentration at the surface increases, and the growing concentration gradient causes a diffusional solute flux away from the droplet surface towards the center of the droplet. Eventually, the diffusional motion of the solutes towards the center of the droplet becomes lower than the reduction rate of the droplet diameter due to the constant rate solvent loss. At this point, crust formation will occur due to solute enrichment at the droplet surface, leading to decreased drying rate and introducing the second drying stage[100]. This point is referred to as the critical point or locking point. At the start of the second drying stage, a porous solid crust and an internal wet core can be distinguished in the drying droplet. The drying rate is now controlled by the diffusion or capillary flow rate of the solvent from the wet core through (the pores of) the crust. The reduced solvent evaporation rate still results in shrinkage of the wet core and substantial growth of the crust towards the center of the droplet[100,101]. The thickening of the crust will lead to an increasing resistance for mass transfer and thereby a gradual reduction of the drying rate. Hence, this second stage is named the **falling-rate stage of drying** (Fig 1.8.). During this stage, the droplet surface temperature will increase until the dry-bulb temperature, which is the temperature of the surrounding gas, is reached and a non-evaporating solid sphere is developed[96]. This implies that a particle with the lowest possible amount of residual solvent is present, which can either be an equilibrium amount or

residual solvent that cannot be removed by the drying process. Ultimately, the drying rate over time in the falling-rate drying stage can take on different shapes depending on the system and the drying conditions[101,102].

The relation between this two-stage drying process and the final particle morphology can be described by the dimensionless Peclet number (Pe), which indicates the ratio of the evaporation rate to the diffusion rate of the solutes (Eq. 1.5.)[95,103,104]::

$$Pe = \frac{d_d\, J}{D_i} \qquad \textit{Equation 1.5.}$$

where d_d is the droplet diameter, J is volume loss per unit area or the evaporative flux and D_i is the diffusion coefficient of solute i in the solvent system. The Stokes-Einstein equation can be used to determine the diffusion coefficient of a solute (D_i) and shows the different factors that contribute to the molecular mobility of a solute in a solvent system (Eq. 1.6.)[105]:

$$D_i = \frac{k_b T}{6\pi R_{h,i}} \qquad \textit{Equation 1.6.}$$

where k_b is the Boltzmann constant and $R_{h,i}$ is the hydrodynamic radius of a molecule in the solvent system experiencing a dynamic viscosity η at a temperature T.

The value of Pe will indicate whether the evaporation rate is relatively faster compared to the diffusional motion of the solutes or vice versa. At high Pe values ($\mathrm{Pe} > 1$), which is the case for most polymer-solvent combinations, the solvent removal is faster than the diffusional motion of the solutes, and the solutes concentration close to the surface will strongly and non-linearly increase, eventually leading to crust formation. Hollow particles can be formed if the crust is strong but porous enough for the residual solvent in the core to still evaporate without the collapse of the outer solid layer. Buckled or collapsed particles are prominent when the crust cannot withstand the pressure difference caused by the continued internal solvent evaporation. On the other hand, at low Pe values ($\mathrm{Pe} < 1$), the diffusion rate of the solutes is sufficient to avoid a strong enrichment at the receding surface. The concentration gradients are low, and the dissolved solutes remain relatively homogeneously dispersed inside the droplet. In this case, more smooth and spherical particles will be generated due to the lack of early crust formation and uniform drying rates over the whole droplet surface. The generated particles are typically smaller and denser compared to particles dried at high Pe values[95,103,104].

1.3.3.2. Factors that influence the spray drying process

Process parameters

A first process parameter that could impact the spray drying process is the **nozzle design**, which could either be a pressure-nozzle, two/bi-fluid nozzle, rotary atomizer, or an ultrasonic nozzle. Most lab-

scale spray dryers are equipped with a bi-fluid nozzle, which uses pressurized gas to break up the liquid feed into individual droplets, whose size depends on the ratio of the pressurized air flow rate to the liquid feed rate. The acquired droplet size ranges from 5 to 75 µm. Because the velocity of the atomizing air is significantly larger than the concurrently flowing drying air, the Venturi effect occurs, resulting in a risk of backflow and clogging when bi-fluid nozzles are used[106]. However, on an industrial scale, pressure nozzles are widely applied. These nozzles contain swirl inserts or spiral grooved inserts and rely on the application of pressure on the liquid to generate a cone-shaped spray pattern[107]. The droplet size ranges from 20 to 200 µm and is determined by the ratio of the applied pressure to the solution feed rate, resulting in smaller droplets for higher pressures. Hence, bi-fluid nozzles generally create smaller droplets (and thereby smaller particles) compared to pressure nozzles. Also, the energy that is needed for the droplet generation in bi-fluid nozzles is 10 to 30 times higher, however, smaller spray angles are obtained[107]. These differences should be taken into consideration when scaling up from a lab-scale setting to an industrial scale.

When a bi-fluid nozzle is used, the **pressurized air flow rate** is inversely related to the droplet size. Thus, increasing the pressurized air flow in a spray dryer with a bi-fluid nozzle results in smaller droplets, because of the higher relative velocity and larger shear forces[106,108]. The **liquid feed rate** on the other hand, is directly related to the droplet size, with larger droplets when a higher feed rate is applied. However, it has been reported that for very low liquid feed rates of less than 5 mL/min, the droplet size could increase again, which was attributed to a pulsing flow, provided by a peristaltic pump, resulting in non-effective atomization[106,108]. Moreover, when increasing the feed rate, more energy is required for solvent evaporation and hence the outlet temperature in the spray drying process will decrease[93]. Ultimately, the ratio of the pressurized air flow rate and the liquid feed rate will determine the droplet size that is generated. The smaller the droplet size, the shorter the time window for evaporation, which might result in spherical, smooth but hollow particles because of rapid crust formation[106]. Larger droplets on the other hand will dry slower and thus allow for diffusion of solutes to the center of the drying droplet, which results in more shriveled particles or dense particles[106]. Thus, not only different droplet size, but also different particle morphologies could be obtained when varying the pressurized air flow rate and/or liquid feed rate.

The **inlet/drying air temperature** directly affects the heat and mass transfer phenomenon in the droplet[93]. More specifically, the heat transfer rate, is proportional to the temperature difference between the temperature of the gas and the wet-bulb temperature of the droplet, which is lower since the evaporation of the solvent draws heat from the droplet. For a given RH of the gas, the temperature difference increases with the temperature of the gas, so the evaporation rate increases. From Eq. 1.5., it follows that higher Pe values will be obtained with increasing temperature. This increase of Pe results

in a fast crust formation and more irregularly shaped, hollow, or collapsed particles. It is important to note that the actual drying air temperature is not only affected by the installed inlet temperature, but is a product of the liquid feed rate, feed concentration, pressurized air flow rate together with the inlet temperature[38], which can be observed during the spray drying process as the outlet temperature. It is essential that the outlet temperature is not higher than the product T_g, as the crystallization rate also increases when the difference between the particle temperature and its T_g is increased[109]. Contrarily, the temperature should be sufficiently high to kinetically trap the API in the polymer matrix, which requires very rapid solvent evaporation. In addition to this, the temperature will not only directly influence the evaporation rate of the solvent, but also the molecular mobility of the solute, yet the evaporation rate will generally increase more drastically with temperature than the diffusion coefficient of the solutes. Also the relative position of the droplet's drying temperature to the boiling point (bp) of the involved solvent should be considered[110–112]. When the temperature exceeds the boiling point, vapor generated in the core of the droplet can open the solidified skin to be released, with a subsequent healing of these openings. This can occur several times until the crust is strong enough to withstand this cycle. Depending on the mechanical properties of the formed crust, it can not only crack, releasing the internal buildup of vapor, but also inflate, thin, and eventually explode, leaving open shells with large cavities or disintegrating the particle completely into fragments.

Formulation parameters

Next to process parameters, also formulation parameters can have an impact on the drying behavior and thereby the final particle morphology that is obtained: the chemical nature of the solutes, their size and molecular weight, whether they have surface-active properties, their solubility in the respective solvent, the solid concentration and especially the solvent used. In view of this PhD thesis, the contribution of the solvent to the final product quality will be further elaborated.

A solvent for spray drying of ASDs should measure up to the following criteria: having a high volatility, a common solubilizing capacity for the API and its carrier, be non-toxic, have an acceptable viscosity and be non-combustive[93]. The solvent property that affects the evaporation rate and final particle morphology the most is the solvent volatility. The RH of the specific solvent directly affects the wet-bulb temperature. As evaporation is driven by the temperature difference between the gas and the wet-bulb temperature of the droplet, highly volatile solvents will exhibit higher evaporation rates and Pe numbers at a given temperature and partial pressure facilitating the formation of hollow or collapsed particles. Low evaporation rates and volatilities on the other hand assist in the production of dense particles[113,114]. For a system with multiple solvents, the solvents with higher volatility will evaporate faster, causing the Pe numbers to decrease during the droplet drying process[115,116]. Second,

the solubilizing capacity of the solvent influences the onset point of crust formation during drying. For solutes with a high solubility, it takes longer to reach the saturation limit at the surface and to precipitate at the droplet's interface. The formation of a solid layer thus happens only at later stages and allows for the crust to solidify homogeneously because most of the solvent is already evaporated before the locking point. A thicker and more stable crust with minimal deformations is obtained in this case. On the other hand, a thin and brittle shell is expected for solutes with a low solubility in the solvent used, since the saturation limit is reached earlier[117,118]. In principle, when the solutes have a vast difference in solubilities, the first to occupy and dominate the droplet surface are ones with a lower solubility, which are usually also the larger and slower diffusing molecules that initiate crust formation[119]. Additionally, it has also been reported that the solvent power can affect the particle size and surface composition of spray dried particles[120].

1.3.4. Rational selection of a manufacturing technique

The primary criteria for selection of an appropriate ASD manufacturing technique are the physicochemical characteristics of the API that needs to be formulated, for instance its thermal stability and T_m[59]. Generally, solvent-based methods can be used for APIs with more diverse physicochemical characteristics than heat-based ones: APIs can have a broader distribution in molecular weight, T_m and logP[75]. The wide variety of solvents available, with variable dielectric constants, have the capacity to dissolve compounds with very different polarity. For molecules with a high T_m (*i.e.,* 'brick dust' compounds) there is an increased risk of chemical degradation when processed using a heat-based method at the required high temperature[75]. In addition, shear forces could also induce chemical degradation in shear-sensitive materials[60]. Other criteria that should be considered when applying a heat-based method are the T_g of the compounds and the viscosity of the mixture and its extrudability[75]. In conclusion, the rather mild process conditions of spray drying, *i.e.,* relatively lower temperature and shorter exposure time, make it applicable to a wider range of compounds. Secondly, practical considerations such as the equipment availability and the study purpose, *i.e.,* screening or optimization approach, should also be considered. Another practical consideration is the toxicity of the required excipients. For instance, in case of solvent-based methods, the solvent toxicity is especially important. If an ICH Class I solvent is needed to solubilize the API and its carrier, it is only accepted when a relatively higher solubility is reached. Moreover, on an industrial scale, also process yield and batch size are important[59].

As the selection of a manufacturing technique is most of the time still a practical consideration, a lot of research is being performed to assess the performance of ASDs prepared with different techniques. Mostly, hot melt extrusion and spray drying are being compared as they are most widely applied. A

first aspect of interest is the impact of the preparation method on the physical state and physical stability as the nucleation process could be affected[60,121–123]. A second one is the *in vitro* and *in vivo* performance of the ASD. As solvent-based methods generally tend to result in smaller particle sizes, faster API release is observed for these ASDs. Application of heat-based methods on the other hand, usually results in more homogeneous ASDs with a better resistance for crystallization during dissolution testing, which is in turn beneficial for the oral absorption process[60,124].

1.4. SOLID-STATE CHARACTERIZATION

1.4.1. Phase behavior of amorphous solid dispersions

The limited stability of the amorphous form can be partially overcome by incorporation of the API in a carrier matrix. Nevertheless, the presence of a carrier is no assurance for obtaining a single phase system, *i.e.,* an amorphous system that exhibits a single T_g, and even when this would be achieved, there are a lot of factors, such as storage conditions (*i.e.,* temperature and humidity stress), that could still induce crystallization. Therefore, the physical state of ASDs needs to be assessed both immediately after manufacturing and over a longer period (*i.e.,* by performing a physical stability study) by using appropriate solid-state characterization techniques. Before discussing (some) of these techniques in detail, the possible physical states of an ASD will be described.

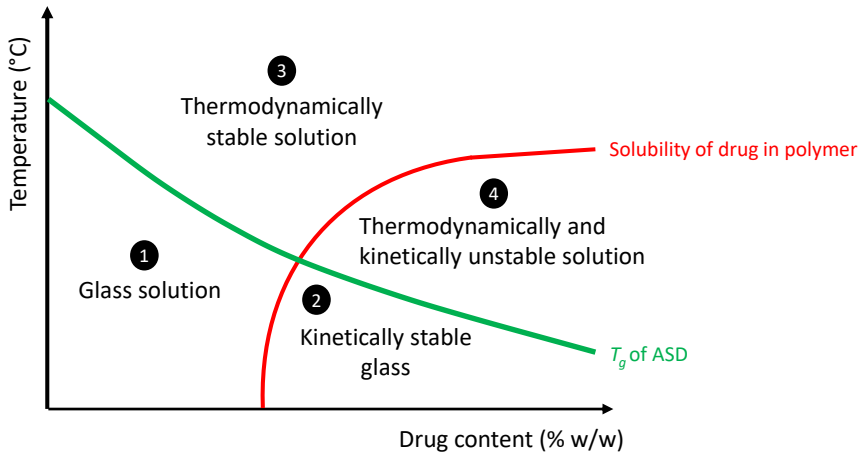

Figure 1.9. *Phase diagram of the API/polymer system in function of temperature (°C) and drug content (% w/w). The thermodynamic solubility of the API in the polymer matrix (red) and the Tg of the ASD (green) divide the phase diagram in four zones: (1) glass solution, (2) kinetically stable glass, (3), thermodynamically stable solution and (4) thermodynamically and kinetically unstable solution. Modified from Lehmkemper et al. 2017*[125].

APIs can be dissolved in a carrier matrix either above or below their thermodynamic solubility limit in the polymer, either resulting in a stable single phase system or a supersaturated one, respectively. This is depicted in Fig 1.9. by means of a state diagram, that describes the phase behavior of ASDs in terms of the thermodynamic solubility of the API in the polymer matrix and the T_g of the ASD[125]. When the

temperature is installed below the T_g and the amount of API is lower than its thermodynamic solubility limit, a glass solution (1) is formed. When the drug loading is higher than this limit, a supersaturated system is formed, which is thermodynamically unstable, yet can be a kinetically stable glass (2)[125]. Increasing the temperature above the T_g will result in liquification of the glass, thereby forming a thermodynamically stable solution (3) or a thermodynamically and kinetically unstable solution (4), again depending on the relative position of the amount of API to its thermodynamic solubility limit in the polymer matrix.

Although kinetically stabilized glasses are metastable, they can be used for pharmaceutical applications if the reduced molecular mobility can prevent crystallization during a pharmaceutically relevant storage period[1]. This is especially important because the solubility of APIs in a polymer matrix is generally relatively low, often even too low to reach therapeutically relevant concentrations[1]. Fortunately, kinetic stabilization of high drug loadings in a polymer matrix is facilitated by kinetic trapping, which can take place both during spray drying and hot melt extrusion[38]. In spite of this, as a supersaturated state is thermodynamically unfavorable, it has the tendency to become more heterogeneous over time. This process can start with amorphous-amorphous phase separation in a drug-rich and a polymer-rich phase[39]. Subsequently, as there is relatively less polymer present in the drug-rich phase and thus less stabilization, nucleation and subsequent crystal growth are likely to take place. Hence, the crystalline fraction will increase until the API is completely crystallized and thereby the solubility advantage will be lost. However, it is not necessary for amorphous-amorphous phase separation to take place before crystallization, as it can also directly start from a homogeneous supersaturated ASD.

In Chapter 4, an overview of solid-state characterization techniques to assess the degree of crystallinity/amorphicity, the miscibility of compounds, their molecular mobility, the presence of interactions and the particle morphology is presented. As modulated Differential Scanning Calorimetry (mDSC) and X-ray Powder Diffraction (XRPD) are the main methods used in this PhD thesis, their principles will be briefly discussed.

1.4.2. Modulated differential scanning calorimetry

DSC is the method of choice for thermal analysis of ASDs, because it can simultaneously provide information about the amorphicity/crystallinity, the miscibility and the molecular mobility of the sample[65]. During a DSC analysis, the sample and reference are subjected to a linear heating (or cooling) rate and the heat flow difference between these two is measured. The results from an analysis can be depicted in a thermogram, where the heat flow is given in function of temperature (or time) and

exothermic signals are usually directed upwards[51]. The presence of an amorphous fraction can be detected as a T_g, which is a step change in the baseline due to a change in heat capacity, while a crystalline fraction can be detected as an endothermic melting peak. DSC allows the detection of a very small amount of crystalline material; it has a limit of detection as low as 1%[126].

However, in case of standard DSC, overlap of signals might lead to misinterpretation[68]. For instance, when there is an overlap of the broad solvent evaporation endotherm with the T_g signal, it might appear as if there is no amorphous fraction present. To overcome this problem, mDSC, where an additional sinusoidal heating rate is applied on top of the linear one, can be applied. This enables a deconvolution of the total heat flow in a reversing heat flow, the heat capacity component, and a non-reversing heat flow, the kinetic component. Events that respond to the temperature modulation can be detected in the reversing heat flow, e.g., T_g, while the ones that cannot because they are kinetically hampered are observed in the non-reversing heat flow, *e.g.,* crystallization, solvent evaporation, enthalpy recovery. This signal separation allows for an unambiguous determination of the T_g via the inflection point or half-height of the heat capacity change in the reversing heat flow. By detection of one (or more) T_g, mDSC plays a pivotal role in the assessment of miscibility of a API and a polymer (or several polymers with one another)[68]. Ideally, an API-polymer mixture is homogeneously mixed and exhibits one T_g, however when the components are immiscible or phase separation in a drug-rich and polymer-rich phase has occurred, two T_g*s* will be detected. Also the molecular mobility of an ASD can be investigated by mDSC, as enthalpy recovery, originating from enthalpy relaxation of the amorphous form towards its more stable equilibrium state, can be detected as an endothermic peak superimposed on the T_g [1,68,127].

1.4.3. X-ray powder diffraction

X-ray powder diffraction has been described as the golden standard for solid-state characterization of pharmaceuticals[68,128]. It can be applied for identification, quantification and even modeling of amorphous systems[1,68]. During a XRPD analysis, monochromatic X-rays are diffracted by the atoms present in the sample[51]. According to Braggs law, positive interference of waves reflected by the crystal planes can only be achieved when the reflected waves are in phase with one another[51]. In case of positive interference, a Bragg peak is detected in the diffractogram. Amorphous materials on the other hand, lack any long range order and thus broad, diffuse scattering signals, *i.e.,* an amorphous halo, are detected in the diffractogram instead of Bragg peaks[1,51,68] For a partially crystalline sample, the crystalline fraction can be calculated from the ratio of the integrated intensity of the Bragg peaks relative to the sum of the integrated intensity of the Bragg peaks and amorphous halo. Depending on the methodology, the limit of detection for crystalline content is in between 1 to 5%[68].

1.4.4. Predicting the solubility of an API in a polymer matrix

As mentioned in section 1.2.2., there are numerous approaches available to predict the miscibility and physical stability of API-carrier systems[52,62,129,130]. In view of this PhD thesis, Perturbed-Chain Statistical Associated Fluid-Theory (PC-SAFT), which is a computational approach that employs a API-carrier thermodynamic phase diagram to make predictions, and one of many DSC-based approaches, *i.e.,* the recrystallization method introduced by Mahieu et al.[131], will be briefly discussed.

PC-SAFT is a thermodynamic model that is employed to estimate the API solubility, which is defined as the maximum API content that can dissolve in the polymer at a certain temperature[125,132]. The thermodynamic solid-liquid equilibrium (SLE), in which the solid is represented by the API and the liquid by the polymer matrix, is employed to calculate the thermodynamic solubility of the API. Assuming a pure solid phase, the following equation can be applied (Eq. 1.7.)[132]:

$$x_{API}^{L} = \frac{1}{\gamma_{API}^{L}} \, exp\left[-\frac{\Delta h_{API}^{SL}}{RT}\left(1 - \frac{T}{T_{API}^{SL}}\right) - \frac{\Delta c_{p,API}^{SL}}{R}\left(\ln\left(\frac{T_{API}^{SL}}{T}\right) - \frac{T_{API}^{SL}}{T} + 1\right)\right] \qquad \textit{Equation 1.7.}$$

In which x_{API}^{L} is the solubility of the API in mole fraction and R the universal gas constant. Δh_{API}^{SL}, T_{API}^{SL} and $\Delta c_{p,API}^{SL}$ are the heat of fusion, the melting temperature and the heat capacities of the API, respectively. All of these can be determined experimentally by for instance DSC analysis. The only parameter that depends on the polymer is γ_{API}^{L}, which is the activity coefficient of the API in the API/polymer phase. The activity coefficient is a measure for the difference in molecular shape and interactions of the API and polymer and is dependent on both temperature and composition of the mixture[132]. Only this activity coefficient must be determined in order to resolve Eq. 1.7. and establish the thermodynamic solubility of the API in the polymer matrix. To enable these calculations, each molecule is considered as a chain of spherical segments that can interact with other molecules in diverse ways: van der Waals interactions, repulsive interactions, hydrogen bonding, dipole-dipole interactions and charges[52,130]. Each molecule is also characterized by its pure component characteristics (*e.g.,* solubility, vapor pressure), which allows calculation of the thermodynamic properties of the mixture in function of temperature, pressure and composition[132]. Advantages of PC-SAFT are that it takes into account almost all types of interactions and that all parameters used have a physical meaning[52]. The result from these PC-SAFT calculations can be presented in a state diagram, as was already demonstrated in Fig 1.9. The solubility line divides the state diagram in a thermodynamically stable part, where the API content is lower than its thermodynamic solubility limit, and an unstable one, where the amount of API is higher than its solubility limit[125]. Thus, the solubility line determines the composition at which thermodynamic stabilization can no longer be achieved, yet kinetic stabilization can still take place.

This computational approach has been successfully applied to predict both the miscibility and physical stability of binary ASDs[125,133–135]. Recently, it has also been used to predict the influence of the solvent used during manufacturing of an ASD on the physical state of ASDs[136,136–138]. Ternary phase diagrams of solvent, API and polymer were established using the equilibrium solubility of the API in the polymer-solvent mixture rather than the polymer alone. Moreover, the process design space for spray drying has also been successfully predicted using this thermodynamic model[139]. Although PC-SAFT is a very valuable approach to make predictions about the phase behavior of ASDs, it does only account for thermodynamic factors and not for kinetic ones, which could also contribute to the physical state of an ASD.

Another promising method to establish the solubility of an API in a polymer matrix is the recrystallization method that was introduced by Mahieu et al.[131]. Using this method, the thermodynamic solubility limit is obtained by demixing of a supersaturated amorphous solution rather than by dissolution of a crystalline API in a polymer matrix. As the molecular mobility in a supersaturated system is relatively high, it slowly decreases during demixing until the thermodynamic solubility limit is reached[131]. In a first step, a supersaturated solid dispersion is generated by co-milling of a physical mixture of an API and its polymer at RT. Subsequently, the glass solution is subjected to a DSC analysis, where it is annealed above its T_g to complete the demixing process, after which the T_g is determined again. After that, the thermodynamic solubility can be derived from a Gordon-Taylor plot, that describes the T_g in function of the API concentration. By applying different annealing temperatures, an API-polymer solubility curve can be generated[131]. Several authors have compared different DSC-based prediction methods with one another[140–142], from which it was found that the melting point depression method and recrystallization method give similar results. An advantage of the recrystallization approach is that there is no well-defined T_m needed, yet on the other hand, the work load is higher[142].

Chapter 2

Objectives

The overall objective of this PhD project is to generate kinetically stabilized supersaturated Amorphous Solid Dispersions (ASDs) and to establish the impact of several formulation and process parameters on the extent of solid state supersaturation that can be obtained. Therefore, the highest drug loading that can be formulated as a single amorphous phase is defined for every condition, which is the maximum drug loading for which an amorphous halo in the XRPD diffractogram and/or a single T_g in the mDSC thermogram is detected. The specific objectives will be discussed per chapter.

Chapter 3: What is the influence of the manufacturing method and the carrier on the solid state supersaturation?

In a first part of the project, the influence of manufacturing methods on the highest drug loadings of ASDs of naproxen (NAP) with one of the following four polymers, polyvinylpyrrolidone (PVP) K25, poly(vinylpyrrolidone-*co*-vinyl acetate) (PVPVA) 64, hydroxypropylmethylcellulose (HPMC) or hydroxypropylmethylcellulose acetate succinate (HPMC-AS) is investigated. This is especially important as today it is not known what the impact of the ASD manufacturing technique on the kinetic stabilization of supersaturated ASDs is. For this purpose, three different manufacturing techniques, *i.e.,* hot melt extrusion, spray drying and cryo-milling, will be applied, thereby covering all categories of manufacturing methods for ASDs. Accordingly, both the influence of another preparation method and a different carrier on the extent of solid state supersaturation can be studied simultaneously.

Chapter 4: What is the impact of the solvent on the solid state supersaturation? And can it be explained by a difference in solubility?

Although the contribution of the solvent to the physicochemical characteristics of ASDs has gained significant interest over the past few years, it is not known to what extent a single organic solvent can influence the kinetic trapping efficiency and thereby the formulation of supersaturated ASDs. Hence, the second objective is to study the influence of the solvent on the highest drug loadings that can be obtained by spray drying and film casting. The latter is included to evaluate the influence of a slower evaporation process. PVPVA 64 was selected as a carrier together with one of four APIs, *i.e.,* NAP, indomethacin (IMC), diazepam (DZP) or fenofibrate (FNB), and one of seven organic solvents, *i.e.,* methanol, ethanol, isopropanol, acetonitrile, dichloromethane, acetone or ethyl acetate. Next to that, the equilibrium solubility of these four APIs in all seven solvents will be determined and subsequently compared to the highest drug loadings that could be obtained using the respective solvent.

Chapter 5: Does the solvent contribute to the physical stability of supersaturated systems?

For a successful ASD formulation, it is indispensable that the supersaturated state can be maintained for a pharmaceutically relevant storage period. Correspondingly, the next objective is to study the

influence of the solvent on the physical stability of ASDs of FNB and PVPVA prepared by spray drying. There were two research questions in this part of the project. First, does the physical stability differ when an ASD of the same API to polymer ratio is prepared using another solvent? And if so, can the onset of crystallization be related to the highest drug loading that was previously obtained using the same solvent?

Chapter 6: How does the solvent contribute to the physical state of supersaturated ASDs?

To gain more insight in the role of the solvent, a combination of Thermal Gravimetric Analysis (TGA) to study the evaporation kinetics and Fourier Transform infrared (FT-IR) spectroscopy to establish interactions in solution can be employed. The aim of these experiments is to explain the solvent dependent highest drug loadings that were determined before. Moreover, these findings can be used to rationally select process parameters that might enable to increase the extent of solid state supersaturation. Accordingly, the potential of process optimization in the workable space will be explored as well.

Chapter 7: What are possible challenges during solid-state characterization by mDSC and XPRD?

Ideally, there neither is a crystalline fraction nor amorphous-amorphous phase separation present in a supersaturated system. To detect this non-ideal phase behavior, the combination of mDSC and XRPD is employed as the standard for solid-state characterization in this work. The last objective is to identify shortcomings of these well-established analytical techniques (in addition to the ones already known) and to demonstrate that their combined use is of utmost importance to avoid erroneous conclusions about the phase behavior of ASDs.

Chapter 3

A comparison of spray drying, hot melt extrusion and cryo-milling for the formulation of highly drug loaded amorphous solid dispersions of naproxen

Results of this chapter are based on: **Dedroog, S.,** Huygens, C., Van den Mooter, G., 2019. Chemically identical but physically different: A comparison of spray drying, hot melt extrusion and cryo-milling for the formulation of high drug loaded amorphous solid dispersions of naproxen. Eur. J. Pharm. Biopharm. 135.

3.1. ABSTRACT

In spite of the large research efforts in the past two decades, it is still difficult, if possible at all, to predict what manufacturing technology will lead to the best amorphous solid dispersions (ASDs) in terms of drug to polymer ratio ("drug loading") and physical stability. In general, ASDs can be prepared by solvent based methods, heat based methods and mechanochemical activation. In the current study, one manufacturing technique per category was selected: spray drying, hot melt extrusion and cryo-milling, respectively. These processes were compared for their capability to formulate high drug loaded ASDs. High drug loadings may allow decreasing the pill burden and/or reducing dosage size, which both increase the therapeutic compliance. A fast crystallizer, naproxen, in combination with PVP K25, PVP-VA64, HPMC or HPMC-AS was used as a model system. Clear differences in the physical structure of the ASDs were observed. Our data indicate that not only the drug loading is dependent on the manufacturing process, but also the carrier that is able to incorporate the highest drug loading. This suggests that a carrier should be selected not only as function of the API, but also as function of the manufacturing process. Overall, hot melt extrusion showed to be most suited to reach high drug loadings for these naproxen-polymer combinations. This was in agreement with our finding that heat is an important energy input for mixing.

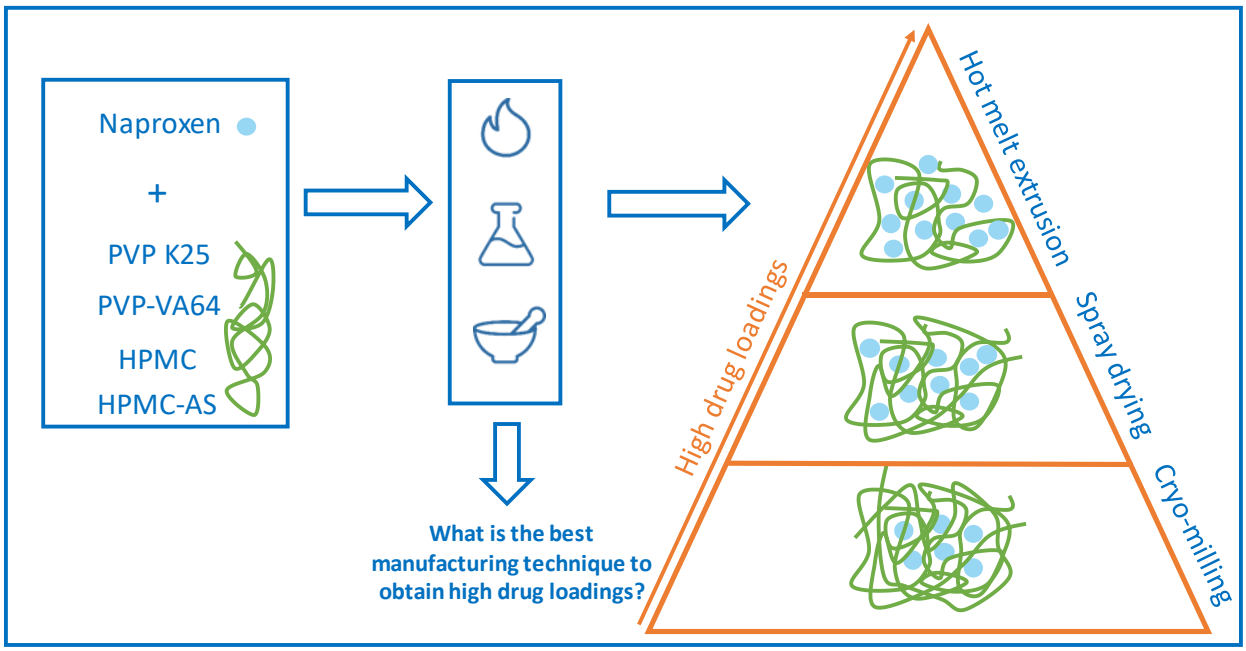

3.2. INTRODUCTION

A drawback of the current drug selection procedures is their high output of drug candidates with unfavorable physicochemical properties[12]. More specifically, ca. 70% of new drug candidates are poorly water soluble[1,24]. Formulation of Amorphous Solid Dispersions (ASDs) of compounds belonging to class II and IV of the Biopharmaceutics Classification System (BCS) is considered as a potential strategy to tackle their solubility and dissolution rate limited bioavailability issues[12,41]. Amorphization of drug compounds results in a higher free energy compared to their crystalline form. The advantage of this higher energetic state is a higher dissolution rate and solubility, but at the same time, it is also responsible for physical stability issues like crystallization of the amorphous form. These physical stability issues can be (partially) overcome by molecularly dispersing the Active Pharmaceutical Ingredient (API) in a polymer matrix, and thus stabilizing the API by the presence of API –polymer interactions and by lowering the molecular mobility[39].

In general, ASDs can be prepared by solvent based methods, heat based methods, mechanochemical activation or a combination of these. Most manufacturing techniques are solvent based, such as Spray Drying (SD), freeze drying, electrospraying, super critical fluids based processing and bead coating. Heat based methods include melt/quench cooling and Hot Melt Extrusion (HME), which uses both heat and shear forces as energy input[50,75]. All kinds of high energy milling are considered as mechanochemical activation. An example of such a milling technique is Cryo-Milling (CM)[143]. In pharmaceutical industry, both SD and HME are most used. The main reason is that they are relatively easy to scale up. An additional advantage of SD is that compounds with thermal and shear instability can be formulated. On the other hand, hot melt extrusion is a solvent-free continuous process and the extrudates do not necessarily require a lot of downstream processing when a calendering step is applied [50,59,75].

Independently of the manufacturing technique used, mainly relatively low drug loadings are utilized for the development of ASDs due to potential physical stability issues. When the drug weight fraction increases, phase separation resulting in amorphous or crystalline drug precipitations may occur[50]. The importance of attaining a higher drug loading is reflected in the present-day push for a lower pill burden. By increasing the drug loading it may become possible to lower the pill burden and/or reduce the dosage size, thereby increasing the therapeutic compliance[144].

The highest drug loading possible can be predicted by calculating the maximum amount of API that can be dissolved in the polymer at a certain temperature. Perturbed-Chain Statistical Associating Fluid Theory (PC-SAFT) is a thermodynamic model using the thermodynamic solid-liquid equilibrium to calculate the solubility of the API in the polymer. The liquid phase is made up of the polymer together

with the dissolved API, while the solid phase is the crystalline API. Combining the calculated solubilities and the experimentally determined glass transition temperatures (T_gs), state diagrams for the solubility of the API in a specific polymer can be established[125,145].

An ASD is thermodynamically stable as long as the drug loading does not exceed the solubility of the API in the polymer, meaning that the API will never crystallize. On the other hand, higher drug loadings than the solubility limit can be reached due to kinetic stabilization. By kinetically trapping the API in the polymer matrix, the molecular mobility of the API is reduced[39,125]. The phenomena by which kinetic trapping is achieved differ between manufacturing techniques. Both rapid solvent evaporation and rapid cooling can kinetically trap the API, using solvent based and heat based methods, respectively[38,50]. Therefore, it should be possible to reach higher drug loadings experimentally than the ones predicted with a thermodynamic model.

Although the research in ASDs already started in the mid-sixties of the previous century[75,146], today it is not clear what manufacturing technology is the most suited for a given API-polymer combination. This is an important observation in the light of high drug loaded ASDs. In this paper, the differences between manufacturing techniques for their capability to obtain high drug loadings are described. Three technologies were selected: spray drying, hot melt extrusion and cryo-milling. With this selection, all categories of manufacturing techniques are covered. The novelty of this paper clearly lies in the comparison of the most relevant technologies from all three categories of manufacturing techniques.

Next to the manufacturing technique, the API-polymer combination is a critical factor for reaching high drug loadings[75]. Naproxen (NAP), which is a fast crystallizer[147], in combination with PVP K25, PVP-VA64, HPMC and HPMC-AS was used as a model system. These polymers belong to the most used carriers for the formulation of ASDs. Their structural formulas are shown in Fig 3.1. As becomes clear from the state diagrams generated with PC-SAFT, the mutual solid miscibility needs to be taken into account. Thus, the state diagrams of naproxen and PVP K25, PVP-VA64 or HPMC-AS served as a starting point for determining the highest drug loading experimentally (Fig 3.2.)[125,145]. The diagram of naproxen and HPMC was not yet described in literature.

Since interactions can also have an influence on the physical stability, the model system was selected based on its interaction potential. Formation of hydrogen bonds between the molecularly dispersed API and the polymer is of great importance for the stabilization of ASDs[39]. Naproxen is well known for its capability to form hydrogen bonds[148,149]. Its carbonyl group and methoxy group are hydrogen acceptors for the hydroxyl groups of HPMC and HPMC-AS. On the other hand, its hydroxyl group can hydrogen bond with both the carbonyl groups of PVP, PVP-VA and HPMC-AS and the hydroxyl groups

of HPMC and HPMC-AS. The hypothesis is that the physical structure resulting from different manufacturing processes, and thus the contribution of hydrogen bonds to solid state miscibility will vary. Therefore, the variations in phase behavior were investigated by preparing the same model system with all three techniques.

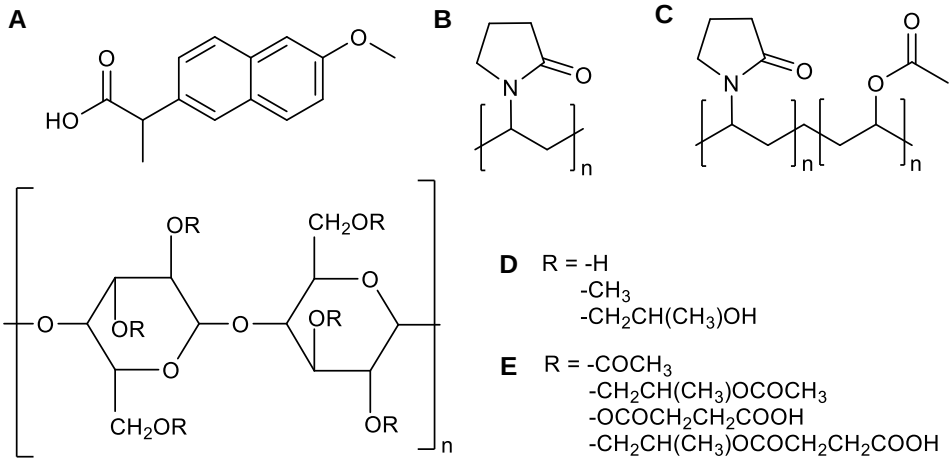

Figure 3.1. *Structural formulas of naproxen (A), PVP (B), PVP-VA (C), HPMC (D) and HPMC-AS (D, E).*

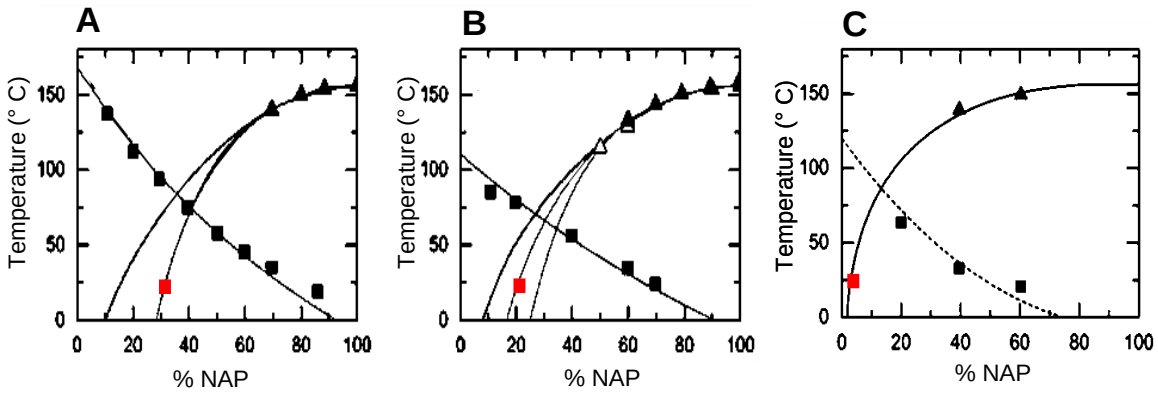

Figure 3.2. *State diagrams of NAP with PVP K25 (A), PVP-VA64 (B) and HPMC-AS (C). The black squares indicate the T_gs and the triangles the solubility of NAP in the polymer. The solubilities were determined experimentally (A, C) or taken from literature (B). The lines with the red squares represent the solubilities calculated with PC-SAFT. These indicate the solubility of NAP in the polymer at RT.*

To the best of our knowledge, a study where the most relevant technologies from solvent based, heat based and mechanochemical activation techniques are compared, has never been carried out before. The objective of this study was to prepare the same API-polymer combinations with spray drying, hot melt extrusion and cryo-milling. Hereby, the differences in capability of reaching high drug loadings were investigated. Since the API-polymer combination is a crucial factor in attaining high drug loadings, it was evaluated for four different polymers.

3.3. MATERIALS AND METHODS

3.3.1. Materials

Naproxen (NAP) was purchased from SA Fagron NV (Waregem, Belgium) and both polyvinylpyrrolidone K25 (PVP K25, Kollidon®) and polyvinylpyrrolidone vinyl acetate 64 (PVP-VA64) were obtained from BASF® ChemTrade GmbH (Ludwigshafen, Germany). Hydroxypropylmethycellulose acetate succinate (HPMC-AS) grade LF is a micronized grade of HPMC-AS, which was purchased from Shin-Etsu (Plaquemine, USA). The fourth polymer, hydroxypropylmethylcellulose (HPMC), was obtained from Colorcon (Dartford, UK). Methanol (MeOH) and dichloromethane (DCM) 99.9% were purchased from ACROS Belgium (Geel, Belgium). All materials were used as received.

3.3.2. Preparation methods

3.3.2.1. Spray drying

Diverse ratios of NAP and polymer were spray dried using a Buchi mini spray dryer B-190 (Buchi, Flawil, Switzerland). In all cases, a 10% w/V solid content was used. For the batches with PVP, PVP-VA and HPMC-AS, MeOH was used as a single solvent. For the ones with HPMC, a binary solvent mixture of MeOH:DCM (1:1; v:v ratio) was needed. The following conditions were applied: drying air temperature of 65 °C, drying air flow rate of 33 m^3/h, feed solution flow rate of 5 mL/min and an atomization air flow rate of 10 L/min. Immediately after spray drying, the ASDs were further dried in a vacuum oven for 4 days at 40 °C. Afterwards, the samples were analyzed and further stored at -28 °C in the presence of phosphorus pentoxide.

3.3.2.2. Hot melt extrusion

Batch extruder

Physical mixtures of the NAP-polymer combinations were prepared using a mortar and pestle and extruded using a Mini extruder (DSM Xplore, Sittard, The Netherlands). This is a fully intermeshing recirculating 5 cm^3 extruder consisting out of two co-rotating screws. The barrel temperature was set at 160 °C, which is above the melting point (T_m) of NAP (ca. 155 °C). For every batch, about 6 g was fed into the extruder and mixed for 5 min with a screw speed of 100 rpm. The extrudates were cooled on aluminum foil and milled using a laboratory cutter mill (Kika, Staufen, Germany). The milled ASDs were analyzed and further stored at -28 °C in the presence of phosphorus pentoxide.

The effect of the barrel temperature on the phase behavior of the ASDs was explored by applying a temperature of 20 °C above the glass transition temperature (T_g) of the polymer involved. The T_gs of

the four polymers were determined using modulated Differential Scanning Calorimetry (mDSC) (see section 3.3.3.1.). To take into account possible water evaporation during extrusion, the T_gs obtained in the second heating cycle were used as a starting point for determining the new processing temperature.

Continuous extruder

To evaluate the influence of additional kneading zones on the phase behavior, a ThermoFisher process 11 twin screw extruder (ThermoFisher Scientific, Karlsruhe, Germany) was used. This is a co-rotating, fully intermeshing twin screw extruder with a functional length of 40 L/D. Two kneading zones were applied. The screw speed was set at 25 rpm and the barrel temperature was kept constant at 160 °C. Herewith, 55 wt% of NAP was extruded in combination with PVP-VA. The same combination was extruded with the Mini extruder, using the same screw speed and temperature. These extrudates were also milled using a laboratory cutter mill (Kika, Staufen, Germany), analyzed and further stored at -28 °C in the presence of phosphorus pentoxide.

3.3.2.3. Cryo-milling

Cryogenic grinding was performed using a CryoMill (Retsch, Düsseldorf, Germany). Physical mixtures of NAP-polymer combinations were prepared using a mortar and pestle before milling. Stainless steel grinding jars of both 5 and 25 mL with two 7 mm beads and one 15 mm bead of the same material were used, respectively. To maintain a constant ball to powder ratio the amount of sample was adapted: 200 mg in case of the 7 mm beads and 1 g in case of the 15 mm one. The samples were pre-cooled for 1 min at 5 Hz, cryo-milled for 30 min at 25 Hz and intermediately cooled for 5 min at 5 Hz to avoid heating of the system. In total, six such cycles were applied. The ASDs were analyzed and further stored at -28 °C in the presence of phosphorus pentoxide.

3.3.3. Analytical methods

3.3.3.1. Modulated differential scanning calorimetry (mDSC)

Modulated Differential Scanning Calorimetry (mDSC) was performed using a Q2000 mDSC (TA Instruments, Leatherhead, UK), equipped with a Refrigerated Cooling System (RCS90) and applying a dry nitrogen purge with a flow rate of 50 mL/min. Calibration for temperature, enthalpy and heat capacity was carried out using indium and sapphire standards. Optimization of the modulation parameters was performed based on the quality of the Lissajous figures and the shape of the modulated heat flow. The final parameters were as follows: a linear heating rate of 2 °C/min combined with a modulation amplitude of 0.5 °C and a period of 30 s. Approximately 1 to 5 mg of the sample

was accurately weighed into aluminum DSC pans (TA Instruments, Zellik, Belgium). For all samples, a heat-cool-heat procedure was performed to explore the influence of additional heating on the mixing efficiency. All heating cycles were executed with the above-described parameters from -15 °C to 180 °C, while the cooling rate was set at 20 °C/min. DSC thermograms were analyzed using the Universal Analysis software (Version 5.5, TA Instruments, Leatherhead, UK).

3.3.3.2. Thermogravimetric analysis (TGA)

For determining the polymer degradation temperature, a thermogravimetric analyzer SDT Q600 (TA-Instruments, Leatherhead, UK) was used. The samples were heated at 5 °C/min to 230 °C in ambient atmosphere, where the recorded weight loss as a function of time was due to degradation. All TGA curves were analyzed using the Universal Analysis software (Version 5.5, TA Instruments, Leatherhead, UK).

3.3.3.3. X-ray powder diffraction (XRPD)

The solid state of the ASDs was characterized using a X'Pert PRO diffractometer (PANalytical, Almelo, the Netherlands) with a Cu tube (Kα λ = 1.5418 Å) and a generator set at 45 kV and 40 mA. In most cases, the XRPD measurements were executed at Room Temperature (RT) and in transmission mode using Kapton® Polyimide Thin films (PANalytical, Almelo, Netherlands). In case of temperature resolved X-ray diffraction, an Anton Paar sample stage (TTK450 Sample Stage) was applied. In that case, diffractograms were recorded every 10 °C between room temperature and 180°C. The following experimental parameters were applied in all cases: continuous scan mode from 4° to 40° 2θ with 0.0167° step size and 400 s counting time. The diffractograms were analyzed using X'Pert Data Viewer (Version 1.7, PANalytical, Almelo, The Netherlands).

3.4. RESULTS AND DISCUSSION

3.4.1. Spray drying

3.4.1.1. Influence of NAP-polymer combination on physical structure

In a first step, the same drug loading of NAP was spray dried in combination with all four polymers. Using a drug loading of 35 wt%, the phase behavior varied for the different NAP-polymer combinations. A single T_g was detected for the ASD with PVP-VA, while the one with PVP resulted in two T_gs (Fig 3.3, A). In case of a one phase amorphous system, the T_g is situated in between the T_g of the pure amorphous drug and the one from the polymer. For example for the ASD of NAP and PVP-VA, the T_g was situated at 57.1 °C, which is in between the 5 °C for amorphous NAP and 110 °C for PVP-VA (Table 3.1.)[150].

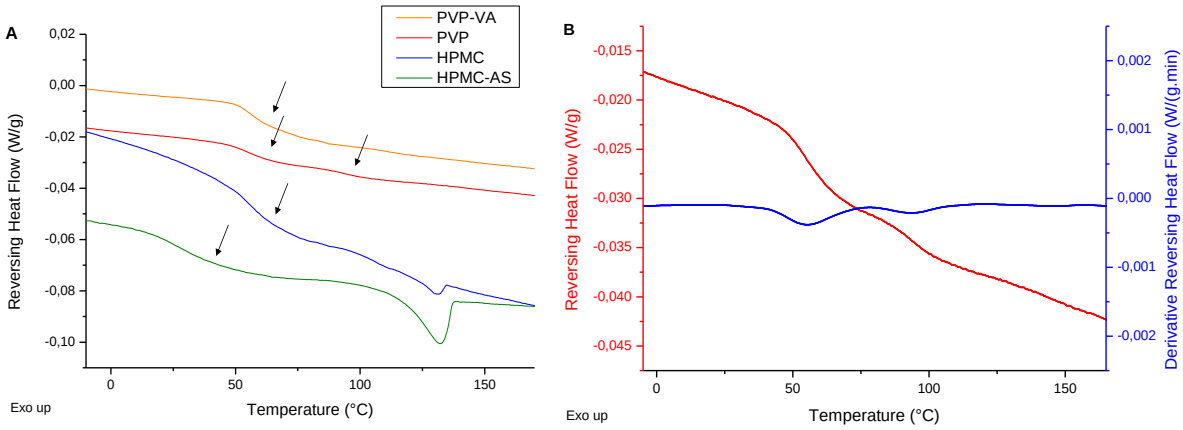

***Figure 3.3**. A: mDSC thermograms of 35 wt% NAP spray dried with PVP-VA (orange), PVP (red), HPMC (blue) or HPMC-AS (green). The arrows indicate the positions of the T_gs. The RHF signals are shown as arbitrary units. B: mDSC thermogram of 35 wt% NAP spray dried with PVP. The derivative (blue) of the reversing heat flow (red) shows peak maximums at the T_gs.*

Since the distinction between two T_gs is not always clear in the Reversing Heat Flow (RHF) signal, we also used the derivative of this signal (Fig 3.3., B). In that case, a peak is generated with a maximum value corresponding to the inflection point in the RHF signal. The presence of two T_gs, reflected in two distinct peaks in the derivative RHF, indicates amorphous-amorphous phase separation in a drug-rich and a polymer-rich phase. Although the NAP-PVP system is amorphous in case of a drug loading of 35 wt%, its immiscibility can be a precursor of crystallization, which will most likely start from the drug-rich amorphous phase. Next to its advantage for distinguishing T_gs, the derivative of the RHF signal was used for determining the T_g width. The broader this T_g width, the more heterogeneous the ASD is. Therefore, it can be stated that the broader this range, the sooner phase separation and thereby crystallization may occur. For both the combinations with HPMC and HPMC-AS, a T_g and a T_m were

observed. Here, the RHF signal is shown, but the T_ms were detected in the total heat flow and non-reversing heat flow signal (data not shown). These T_ms indicated the presence of a crystalline phase of NAP next to the amorphous one (Fig 3.3., A).

These results were in agreement with the ones obtained using XRPD. Both PVP-VA and PVP were X-ray amorphous, while both HPMC and HPMC-AS showed Bragg peaks characteristic for crystalline NAP (Fig 3.4.). The importance of using complementary analytical techniques becomes clear when comparing the DSC and XRPD results. Although the same conclusions about the presence of amorphous/crystalline material can be drawn, XRPD does not give information about the different amorphous phases. Whereas the NAP-PVP system was X-ray amorphous, it was not a single amorphous phase. Since amorphous-amorphous phase separation can lead to crystallization, it should be avoided. Only in a one phase system, the stabilization of NAP by the polymer is maximized, though not guaranteed. To get as much information about the phase behavior as possible, all samples were analyzed using both mDSC and XRPD.

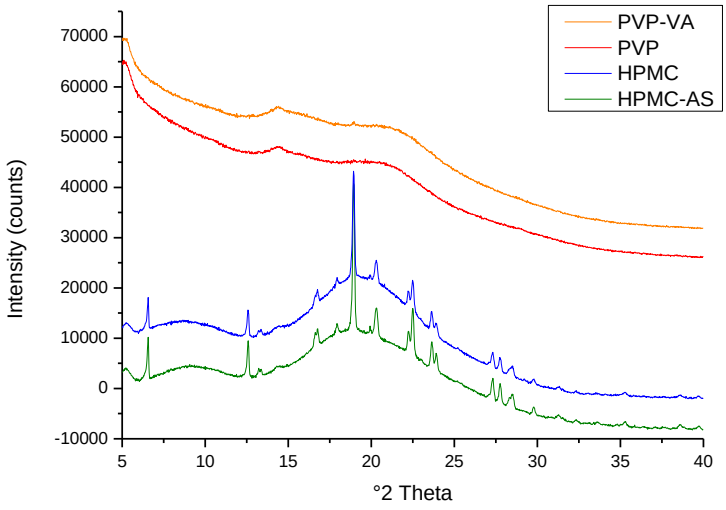

Figure 3.4. *XRPD diffractograms of 35 wt% NAP with spray dried PVP-VA (orange), PVP (red), HPMC (blue) or HPMC-AS (green). The intensities are shown as arbitrary units.*

For all samples, a heat-cool-heat procedure was performed to investigate the influence of additional heating on the mixing efficiency. For all of them, a single T_g was obtained in the second heating run, independently of the phase behavior in the first heating run. In case of 35 wt% NAP spray dried with PVP, two T_gs were detected in the first heating cycle and a single T_g in the second (Fig 3.5.). For the combination of 35 wt% NAP with HPMC-AS, both a T_g and a T_m could be distinguished in the first cycle and a single T_g in the second (Fig 3.5.). Next to this, the T_g width decreased when there already was a single T_g attained in the first heating run, indicating an increase in homogeneity of the system (data

not shown). This clearly points to the importance of heat as energy input for all these NAP-polymer combinations. All further reported drug loadings were derived from the first heating cycle of the DSC experiment.

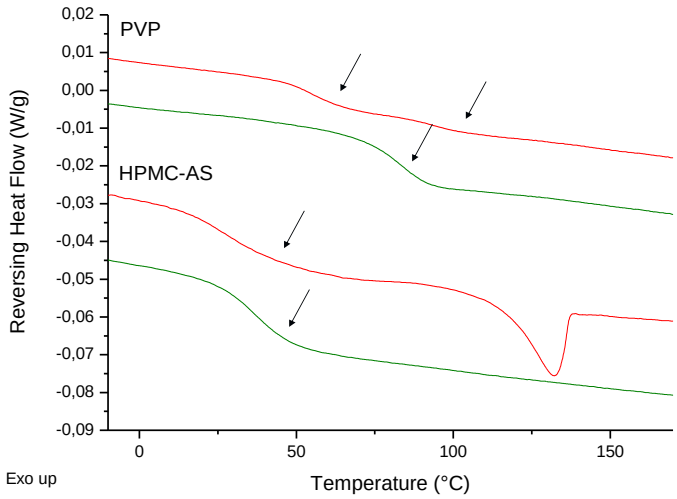

Figure 3.5*. mDSC thermograms of 35 wt% NAP spray dried with either PVP (top) or HPMC-AS (bottom). The first heating cycle (red) and the second (green) are shown. The arrows indicate the positions of the T_gs. The RHF signals are shown as arbitrary units.*

3.4.1.2. Influence of drug loading on physical structure

Ideally, a single amorphous phase should be obtained, in which NAP is molecularly dispersed in the polymer matrix. Since this phase behavior was only detected for the NAP-PVP-VA system, PVP-VA was appointed the most promising polymer for increasing the drug loading further. For the other combinations, the drug loading was lowered until a one phase amorphous system was achieved. The drug loading for which this ideal phase behavior was attained, was defined as 'the highest drug loading possible'. Taking into account the possible process variability, the highest drug loading was not defined as an exact percentage but as a range. Accordingly, the drug loading was lowered with intermediate steps of 5 wt% for the NAP-PVP, NAP-HPMC and NAP-HPMC-AS combinations. The mDSC and XRPD results are only described for the NAP-HPMC-AS system (Fig 3.6.), but the same principle has been applied for the other combinations. In case of the NAP-HPMC-AS system, from 25 wt% on, both a T_g and a T_m could be distinguished (Fig 3.6., A), and at 30 wt%, Bragg peaks were present in the XRPD diffractogram (Fig 3.6., B). Thus, the highest drug loading for this NAP-HPMC-AS system in case of SD is in between 20 wt% and 25 wt%.

The NAP-PVP-VA combination was the only one for which the drug loading could be increased above 35 wt%. It was increased from 35 until 60 wt% with intermediate steps of 5 wt%. Until 40 wt%, a single T_g was detected, but starting from 45 wt% a T_m was detected next to the T_g (Fig 3.7., A). The mDSC

results were in good correlation with the ones from XRPD, showing Bragg peaks starting from 45 wt% drug loading (Fig 3.7., B). Therefore, the highest drug loading for the NAP-PVP-VA system in case of SD was in between 40% and 45%.

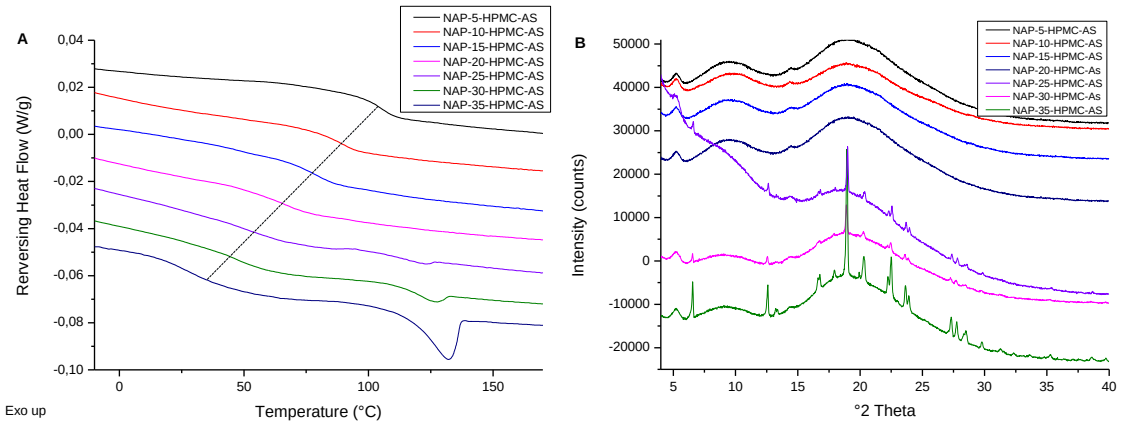

***Figure 3.6**. A: mDSC thermograms of NAP-HPMC-AS system lowering the drug loading from 35 to 5 wt% with intermediate steps of 5 wt%. When increasing the drug loading there was a shift of the T_g towards lower values, which is indicated with the dotted line. B: Corresponding XRPD diffractograms. The RHF signals (A) and intensities (B) are shown as arbitrary units.*

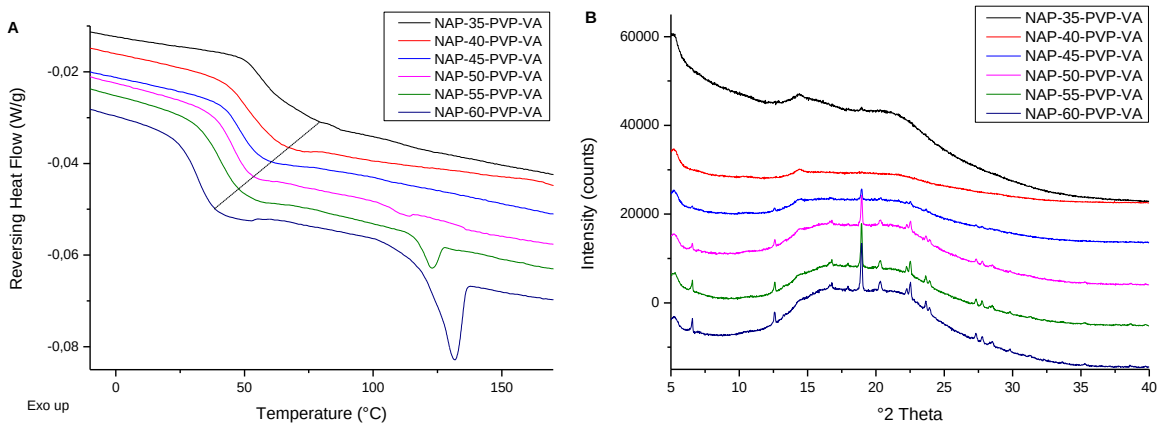

***Figure 3.7**. A: mDSC thermograms of NAP-PVP-VA system increasing the drug loading from 35 to 60 wt% with intermediate steps of 5 wt%. When increasing the drug loading there was a shift of the T_g towards lower values, which is indicated with the dotted line. B: Corresponding XRPD diffractograms. The RHF signals (A) and intensities (B) are shown as arbitrary units*

The four polymers can be ordered for their capability to stabilize high NAP loadings: PVP-VA > PVP > HPMC/HPMC-AS. With a drug loading between 40 and 45 wt%, PVP-VA was the best polymer for obtaining high drug loadings. In case of PVP, the highest drug loading was between 30 and 35 wt%, while for both HPMC and HPMC-AS it was between 20 and 25 wt% (Table 3.4.). It is noteworthy that these drug loadings only apply to spray drying and that variations are possible when applying other manufacturing techniques (see below). It is expected that an API has a higher solid solubility in a polymer where drug-polymer interactions are more pronounced[151]. Therefore, this may be an indication of more favorable interactions between NAP and PVP-VA.

In this study, the main investigated characteristic is the capability to obtain high drug loadings. As described earlier, the API-polymer is a critical factor for reaching these drug loadings. Other important properties to consider when selecting a suitable polymer for SD are the common solvent solubility of API and polymer, solution state chemistry, interaction potential, antiplasticizing efficiency, dissolution rate and ability to maintain supersaturation during dissolution. Although Friesen et al. described HPMC-AS as an ideal polymer for SD based on these characteristics, the drug loadings reached in this study are rather low[152]. This demonstrates that there is no ideal polymer per manufacturing technique, but that a polymer should also be selected according to the API that needs to be formulated. Other than that, it indicates that the capability to reach higher drug loadings is another important characteristic to investigate when selecting a polymer for the formulation of an ASD.

3.4.2. Hot melt extrusion

3.4.2.1. Influence of NAP-polymer combination on physical structure

Physical mixtures of NAP with the different polymers were extruded in a 35:65 (drug:polymer; w:w) ratio. The ASDs with PVP-VA and PVP showed a single T_g, while for HPMC and HPMC-AS both a T_g and a T_m could be distinguished (Fig 3.8., A). Both PVP-VA and PVP are thus promising polymers for increasing the drug loading above 35 wt%. Although the same NAP-polymer combinations and drug loading had been used as for spray drying, two NAP-polymer combinations could be formulated as a single phase amorphous system instead of one, showing that the suitability of NAP-polymer combinations depends upon the applied manufacturing technique.

All four NAP-polymer combinations were X-ray amorphous for a drug loading of 35 wt% (Fig 3.8., B). Despite the fact that a T_m could be detected in the thermograms of the combinations with HPMC and HPMC-AS, there were no Bragg peaks present in the diffractograms, pointing again to the importance of using complementary analytical techniques.

3.4.2.2. Influence of drug loading on physical structure

In case of HME, the drug loading was increased for the NAP-PVP-VA and NAP-PVP systems, but decreased in case of the NAP-HPMC and NAP-HPMC-AS systems to obtain a one phase amorphous system. A full comparison of the highest drug loadings reached per polymer and per manufacturing technique is shown in Table 3.4.

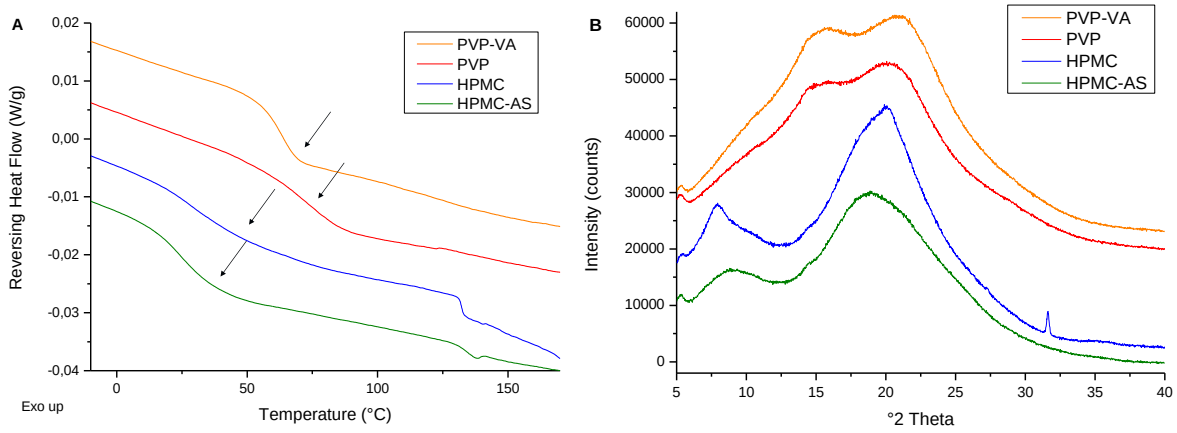

***Figure 3.8**. A: mDSC thermogram of 35 wt% NAP extruded with PVP-VA (orange), PVP (red), HPMC (blue) or HPMC-AS (green). B: XRD diffractograms of 35 wt% NAP extruded with PVP-VA (orange), PVP (red), HPMC (blue) or HPMC-AS (green). The sharp peak in the diffractogram of the ASD with HPMC originates from a crystalline impurity present in the polymer. The RHF signals (A) and intensities (B) are shown as arbitrary units.*

3.4.2.3. Impact of polymer-dependent-barrel temperature on phase behavior

Critical process parameters for HME are the screw speed, screw configuration, feeding rate and barrel temperature. The interested reader is referred to excellent reviews for further information[79,85]. In view of using different NAP-polymer combinations, the barrel temperature is a crucial parameter. Since a polymer needs to be extruded above its T_g but below its degradation temperature, different temperatures should be applied for the different NAP-polymer combinations. The temperature is also of importance for processing of the API, but it can be processed below or above its T_m, resulting in solubilization or miscibility of the API in the polymer, respectively[85,153].

First, the degradation temperatures of the four polymers were determined using TGA (Table 3.1.). Next to this, the T_gs of the polymers and T_m of pure NAP were taken into account. The T_gs of the polymers were determined from the second heating cycle of the mDSC run to take possible water evaporation during HME into account (Table 3.1.). The T_m of NAP was established at 155.2 °C (data not shown). Since the degradation temperature and T_g of PVP are comparable to each other, PVP is known to be a difficult polymer for extruding. When heated to 150 °C, darkening of PVP is described[154]. On the other hand, when increasing the temperature from 160 °C to 230 °C, only 2 wt% degradation of PVP was measured during the TGA experiment. Thus, only a very small amount of PVP was degraded at 160 °C. For the other polymers, the degradation temperatures were well above their T_gs.

All NAP-polymer combinations were processed both at 160 °C and at 20 °C above the T_g of the polymer in question (Table 3.1.). The barrel temperature of 160 °C was installed as a common processing temperature. For PVP-VA and HPMC-AS the T_g-dependent-temperature was below the T_m of NAP,

while for PVP and HPMC it was even higher than 160 °C. By using these barrel temperatures, the influence of processing below or above the T_m of NAP on the final phase behavior was evaluated.

***Table 3.1**. T_gs from second heating cycle, derived processing temperatures and degradation temperatures for PVP, PVP-VA, HPMC and HPMC-AS.*

Polymer	T_g 2nd heating cycle	T_g + 20 °C	T degradation
PVP	161.6 °C	180 °C	159.1 °C
PVP-VA	110.8 °C	130 °C	197 °C
HPMC	147.8 °C	167 °C	176 °C
HPMC-AS	115.8 °C	135 °C	166.8 °C

The results from both processing at 160 °C and at the T_g-dependent-temperature are shown in Table 3.2. For the cases with a barrel temperature of 160 °C, the values for the T_gs and T_m s correlate with the mDSC thermograms shown in Fig 3.5., A. In view of the clear differences in phase behavior for the NAP-PVP-VA combination, these mDSC results are discussed more comprehensively (Fig 3.9.).

***Table 3.2**. Influence of HME processing temperature below/above T_m NAP on the phase behavior of the ASD. The 'X' indicates that there was no second T_g or a T_m present.*

Polymer	Temperature	T_g1	T_g2	T_m
PVP	160 °C	80.4 °C	X	X
	T_g + 20°C	56.2 °C	X	X
PVP-VA	160 °C	63.6 °C	X	X
	T_g + 20°C	45.4 °C	80.4 °C	X
HPMC	160 °C	27.8 °C	X	127.9 °C
	T_g + 20 °C	26.5 °C	X	126.5 °C
HPMC-AS	160 °C	24.3 °C	X	128.1 °C
	T_g + 20°C	25.2 °C	X	126.5 °C

When processing above the T_m of NAP, no clear differences in phase behavior could be detected. Even though there was a shift of the T_g towards a lower temperature, a single T_g remained in case of PVP. With HPMC, a T_g and a T_m were detected for both 160 °C and 167 °C. When processing below the T_m of NAP with HPMC-AS, almost no differences in phase behavior were detected. At both processing temperatures, 160 °C and 135 °C, a T_g and a T_m could be distinguished. On the other hand, in case of PVP-VA, the phase behavior clearly differed. The amorphous-amorphous phase separation indicated that extruding at temperatures lower than the T_m of NAP did not give the system its full capability of both mixing and solubilizing the API in the polymer matrix. This is an important observation in the light

of reaching high drug loadings. It is clear that for some API-polymer combinations it is important that the barrel temperature is installed above the T_m of the API. Therefore, all other batches were processed at 160 °C to give the systems their full potential to mix and thereby reach high drug loadings.

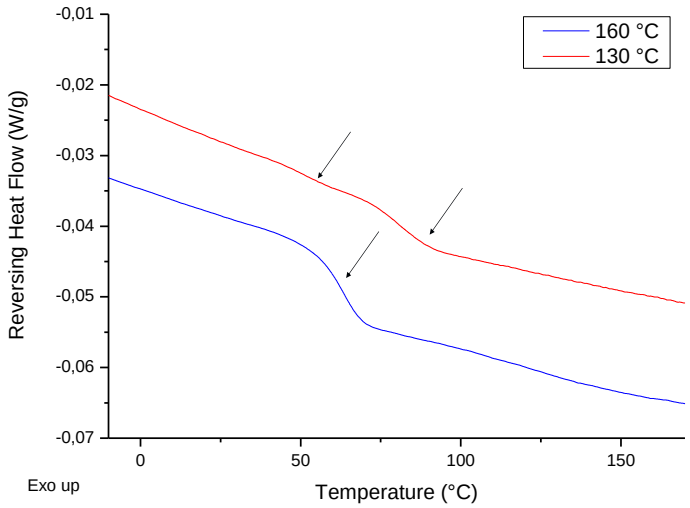

***Figure 3.9**. mDSC thermograms of 35 wt% NAP in combination with PVP-VA at 130 °C (green) and 160 °C (red). T_gs are indicated with arrows. The RHF signals are shown as arbitrary units.*

3.4.2.4. Impact of kneading zones on amorphization

In a HME process, the combination of mixing and melting makes the generation of ASDs possible. For this, two important energy inputs need to be taken into account. First, the heat conduction from the barrel will have an influence on the melting and softening process, which is determined by the installed barrel temperature. Second, the rotation of the screws will result in shear forces that will generate additional heat. This energy input can be altered by changing the screw configuration. Thus, the screw configuration is another critical process parameter. Several studies investigated the need for one or more kneading zones during HME. Nakamichi et al. concluded that at least one mixing zone was needed to make amorphization possible[155]. Saerens et al. showed that addition of a second or third kneading zone did not have an additional advantage for the formulation of ASDs[156]. Hence, one kneading zone at two third of the barrel length is in many cases considered sufficient for mixing at molecular level[85].

In contrast to a continuous extruder, a typical lab-scale batch extruder has no additional kneading zones, but exists out of two conical screws with conveying elements. Therefore, there is no alteration of the screw configuration possible. To evaluate the addition of kneading zones on the final phase behavior of the ASDs, a continuous extruder was used.

The reasoning behind the addition of kneading zones for reaching higher drug loadings becomes clear when comparing the different mDSC heating cycles. Every mDSC experiment existed out of two heating cycles separated by a cooling cycle. As described for spray drying, the second heating cycle resulted in better phase behavior. Despite the fact that there were two T_gs or a T_g and a T_m in the first heating cycle, a single T_g was detected in the second one. A representative example of HME is shown for which 55 wt% NAP was extruded in combination with PVP-VA. Here, two T_gs and a T_m were detected in the first heating cycle and a single T_g was observed in the second (Fig 3.10.). This implies that heat is a very important energy input to obtain ASDs of NAP.

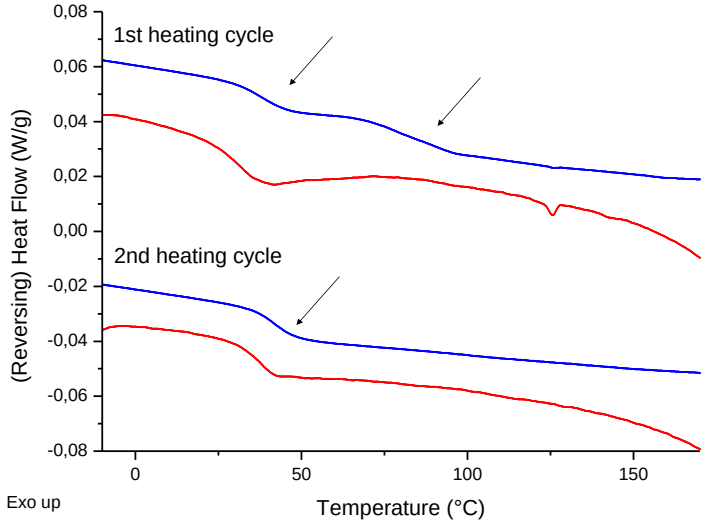

***Figure 3.10**. mDSC thermograms of 55 wt% NAP extruded in combination with PVP-VA. Both the reversing heat flow (blue) and the total heat flow (red) are shown. The arrows indicate the position of the T_gs. The (R)HF signals are shown as arbitrary units.*

Since the energy input can be increased by the addition of kneading zones next to the conveying zones, we evaluated the use of a continuous extruder to prepare ASDs made up of 55 wt% NAP and PVP-VA. The screw speed was set at 25 rpm and the process temperature at 160 °C. An additional batch was prepared with the lab scale extruder, using the same screw speed and process temperature to compare the two processes. In both cases, a T_g and a T_m were detected (Fig 3.11.). The amount of crystallinity was calculated from the heat of fusion, resulting in 0.6% crystallinity in both cases. Thus, it was not possible to reach higher drug loadings using the continuous extruder. This suggested that the addition of kneading zones did not result in enough energy input to increase the amorphization capability.

Lang et al. compared a single screw extruder, a small twin screw extruder and a continuous twin screw extruder with kneading zones for the formulation of ASDs[157]. They observed that only the continuous twin-screw extruder with additional kneading zones resulted in ASDs of itraconazole with HPMC-AS and polyethylene oxide (PEO). In this study, similar results were obtained with the lab-scale extruder and the continuous extruder, pointing to the potential of the former. However, another explanation

for the comparable results could be the remaining differences in processing time, *e.g.,* the mixing time/residence time of 5 min in the batch extruder compared to that in the continuous process. No exact measurements of the residence time in the continuous extruder have been made, but it is clear that the total time inside the extruder is far less than 5 min. Therefore, it can be stated that a full comparison of a batch and a continuous extruder requires optimization of both processes to make the correct conclusions about their capability of reaching high drug loadings.

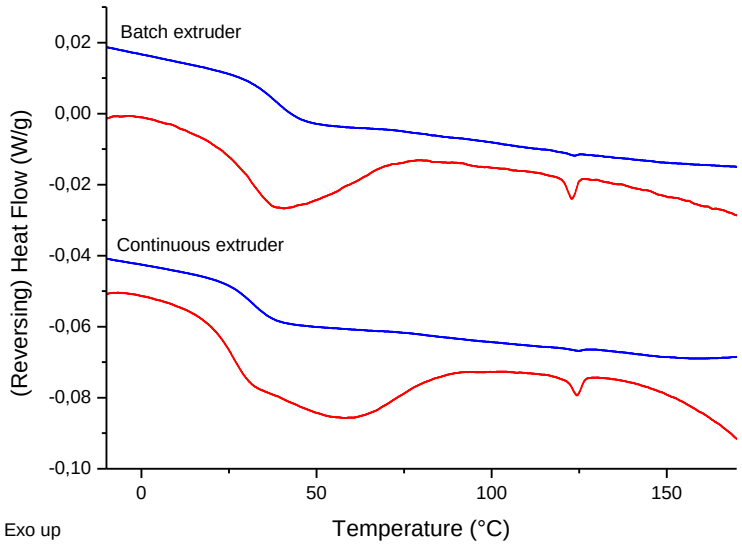

Figure 3.11*. mDSC thermograms of 55 wt% NAP extruded in combination with PVP-VA using a batch extruder or a continuous extruder. The reversing heat flow is shown in blue and the total heat flow in red. The (R)HF signals are shown as arbitrary units.*

3.4.3. Cryo-milling

3.4.3.1. Influence of NAP-polymer combination on physical structure

Physical mixtures of 35 wt% NAP in combination with one of four polymers were cryo-milled. The experiments were performed with small grinding jars of 5 mL, 200 mg powder mass and 2 beads of 7 mm per grinding jar. The mDSC results showed two T_gs for the combination with PVP-VA and one T_g for the one with PVP (Fig 3.12., A). This indicated that in case of CM, PVP was the most promising polymer for increasing the drug loading higher than 35 wt%. For SD this was PVP-VA, while for HME it were both PVP and PVP-VA. This showed again that the success rate of an API-polymer combination clearly depended upon the manufacturing technique used. For both combinations with HPMC and HPMC-AS, a T_g and a T_m were detected (Fig 3.12., A).

Despite the fact that the thermograms of the combinations with PVP-VA and PVP did not show crystallinity (only glass transitions could be observed), the corresponding diffractograms showed diffraction peaks that are characteristic for crystalline NAP (Fig 3.12., B). This is in contradiction with

the higher sensitivity of mDSC compared to XRPD for the detection of crystallinity. For the other two combinations, the mDSC and XRPD results were in good agreement with each other, indicating the presence of crystalline NAP (Fig 3.12., B).

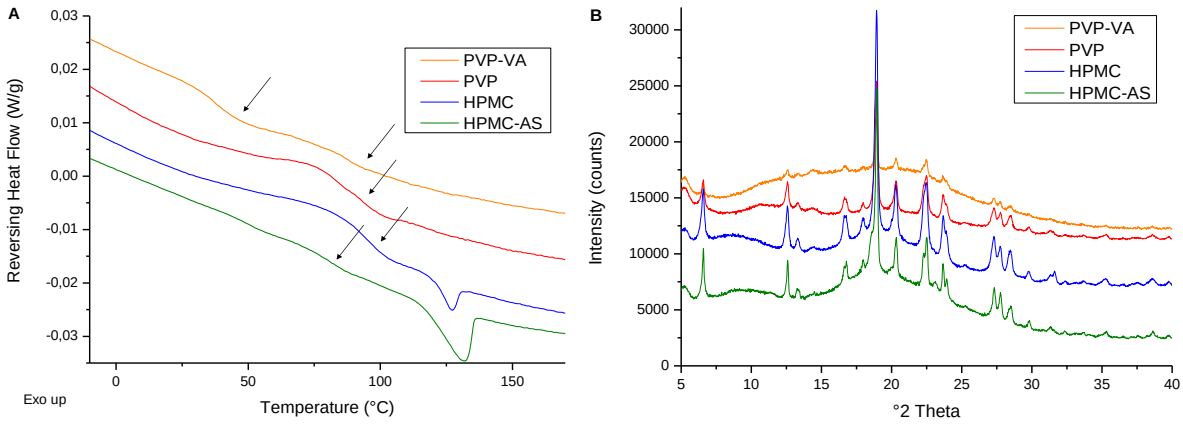

***Figure 3.12**. A: mDSC thermograms of 35 wt% NAP extruded with PVP-VA (orange), PVP (red), HPMC (blue) or HPMC-AS (green). The arrows indicate the position of the T_gs. B: XRPD diffractograms of 35 wt% NAP cryo-milled with PVP-VA (orange), PVP (red), HPMC (blue) or HPMC-AS (green).*

The hypothesis to explain this discrepancy between mDSC and XRPD results was that by cryo-milling the particle size was reduced significantly, leading to improved particle-particle contact. Hence, only a small amount of heat was necessary to dissolve NAP in the polymer. This was further confirmed by performing temperature resolved XRPD for the NAP-PVP combination, where the temperature was increased from RT to 185 °C and a diffractogram was assessed every 10 °C. At RT, Bragg peaks indicating the presence of crystalline NAP were present. The intensity of the peaks was identical at 75 °C, but decreased at 85 °C. From 95 °C, the Bragg peaks completely disappeared, indicating that the sample was X-ray amorphous (Fig 3.13.). This validated the hypothesis that heating up the sample resulted in dissolving of NAP particles in the polymer matrix. The need for complementary analytical techniques became clear when comparing these mDSC and XRPD results. When mDSC would have been used as the only analytical technique, CM might have seemed as promising as SD. A drawback of mDSC is that the sample needs to be heated, which can alter the characteristics of the analyzed sample. Thus, in this case, XRPD was a more trustworthy technique to draw conclusions about the phase behavior of the cryo-milled samples at RT. Bikiaris et al. reported a similar case, where Felodipine dissolved in polyethylene glycol (PEG) during the DSC experiment, while diffraction peaks were present in the diffractograms[158].

A comparison of the obtained drug loadings using mDSC or XPRD is shown in Table 3.3. In case of mDSC, the highest drug loading was defined as the one for which a single T_g had to be observed, while for XRPD the sample had to be X-ray amorphous. Although the obtained drug loadings were clearly lower

using XRPD, PVP was in both cases the most suited polymer for obtaining high drug loadings. For comparison with spray drying and hot melt extrusion, the drug loadings based on XRPD results were used (Table 3.4.).

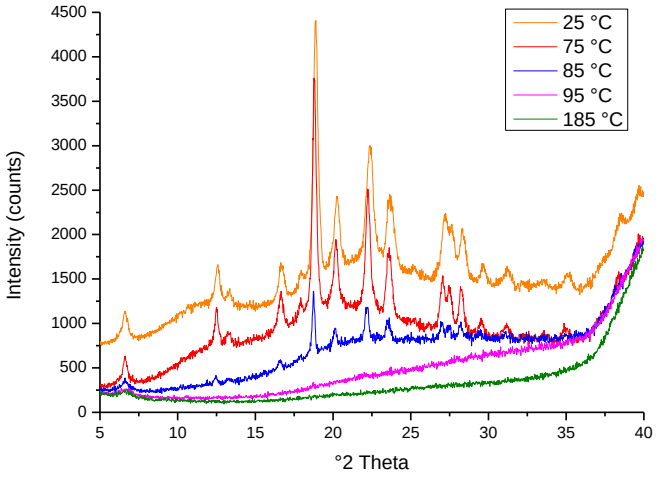

***Figure 3.13**. XRPD diffractograms of 35 wt% NAP cryo-milled in combination with PVP. The temperature was increased from 25 °C (orange) to 185 °C (green). Starting from 85 °C (blue) the intensity of the Bragg peaks decreased and from 95 °C (purple), they completely disappeared. The intensities are shown as arbitrary units.*

***Table 3.3**. Comparison of 'highest drug loadings' based on mDSC or XRPD results in case of cryo-milling.*

Polymer	mDSC	XRPD
PVP	50% - 55%	15% - 20%
PVP-VA	30% - 35%	10% - 15%
HPMC	< 5%	< 5%
HPMC-AS	10% -15%	5% - 10%

On the other hand, these mDSC results showed that heat is a very important energy input for these NAP-polymer combinations. Together with the observations form the second heating cycles, where in all cases a single T_g was detected (Fig 3.5. and 3.10.), the mDSC experiments were a strong prove that these NAP-polymer combinations do not reach their full potential of miscibility yet. This may be reached by performing a full optimization of the process parameters.

3.4.3.2. Influence of drug loading on physical structure

For the NAP-PVP system, the drug loading was increased starting from 35 to 60 wt%. For the other combinations, the drug loading was lowered from 35 to 5 wt%. A full comparison of the highest drug loadings reached per polymer and per manufacturing technique is shown in Table 3.4.

3.4.3.3. A small scale-up experiment: from 5 mL to 25 mL grinding jar

All previously described experiments were performed using a small grinding jar of 5 mL. The volume of these stainless-steel grinding jars can differ: 5, 10, 25, 35 or 50 mL are possible. When scaling up from a 5 mL to a larger grinding jar volume, the change of dimensions can have an influence on the impact of the beads and thereby the final phase behavior of the ASD. Here, 35 wt% NAP in combination with PVP-VA was cryo-milled in both the 5 mL and the 25 mL for 3 hours. The ball to powder ratio was kept constant. At first sight, there is not much difference between the mDSC thermograms of the 5 mL and 25 mL. In both cases, two distinct T_gs indicating amorphous-amorphous phase separation were detected (Fig 3.14., A). However, the glass transition width was broader when using the 5 mL grinding jar than when using the 25 mL one, indicating that the amorphous phase was more heterogeneous in case of using the 5 mL grinding jar.

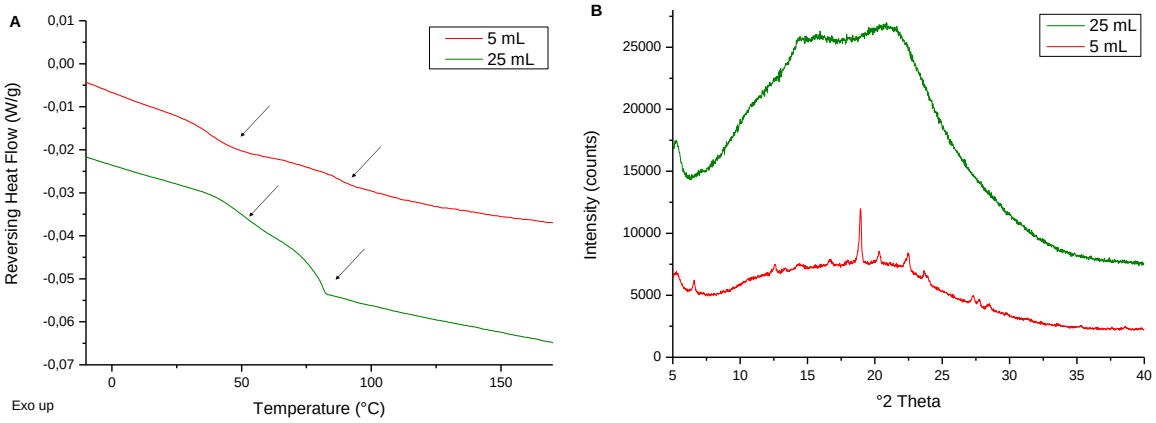

Figure 3.14. *A: mDSC thermograms of 35 wt% NAP cryo-milled in combination with PVP-VA using a 25 mL grinding jar (green) and a 5 mL grinding jar (red). The arrows indicate the position of the T_gs. B: XRPD diffractograms of 35 wt% NAP cryo-milled in combination with PVP-VA using a 25 mL (green) grinding jar and a 5 mL (red) one. The RHF signals (A) and intensities (B) are shown as arbitrary units.*

Even though the DSC thermograms did not show melting transitions, the diffractogram of the batch prepared with the 5 mL grinding jar showed Bragg peaks characteristic for crystalline NAP (Fig 3.14., B). As described above, this can be explained by the dissolution of NAP in PVP-VA during the mDSC experiment. Interesting is that the batch prepared with the 25 mL grinding jar was X-ray amorphous (Fig 3.14., B). This difference was also reflected in the T_g width (Fig 3.15., A). The fact that there was still some crystalline material present in case of the 5 mL grinding jar resulted in a broader T_g width. In case of the 25 mL grinding jar there was no crystalline material left at the start of the mDSC analysis, resulting in a more homogeneous system compared to the 5 mL one.

This small scale up experiment showed the potential of CM as a manufacturing technique for ASDs. When the larger grinding jar was used, it became possible to prepare systems that were already

completely amorphous at RT. Therefore, it can be hypothesized that the optimization of this manufacturing technique could result in higher drug loadings than the ones that were obtained in this study. Next to this, a deeper understanding of the underlying physics of this still non-conventional technique is essential to predict possible changes during scale up.

3.4.4. Comparison of manufacturing techniques

The objective of this study was to prepare the same API-polymer combinations with spray drying, hot melt extrusion and cryo-milling to compare their capability of reaching high drug loadings. The same four NAP-polymer combinations were prepared with all three techniques. For SD and HME, the highest drug loadings were defined as the drug loadings for which a one phase amorphous system was attained, while for CM these were the drug loadings for which an X-ray amorphous ASD was obtained. This distinction was made because of the discrepancy between mDSC and XRPD results for CM, which were not present for SD and HME. Therefore, mDSC can be considered as a reliable technique for the interpretation of the phase behavior in case of SD and HME, but not in case of CM. The drug loadings were determined as described above and reported as a range to consider possible process variation. A full comparison of the highest drug loadings reached per polymer and per manufacturing technique is shown in Table 3.4.

Table 3.4. *Comparison of highest drug loadings of NAP obtained per manufacturing technique and per polymer.*

Technique	Polymer	Drug loading
Spray drying	PVP	30% - 35%
	PVP-VA	40% - 45%
	HPMC	20% - 25%
	HPMC-AS	20% - 25%
Hot melt extrusion	PVP	55% - 60%
	PVP-VA	45% - 50%
	HPMC	20% - 25%
	HPMC-AS	15% - 20%
Cryo-milling	PVP	15% - 20%
	PVP-VA	10% - 15%
	HPMC	< 5%
	HPMC-AS	10% - 15%

From these results, it can be stated that HME was the most promising manufacturing technique for obtaining high drug loadings in case of these NAP-polymer combinations. Since HME is a heat based method, this finding is in line with the fact that heat is a very important energy input for these combinations. The correct order of the techniques is as follows: hot melt extrusion > spray drying > cryo-milling. Based on the mDSC results (Table 3.3.), it might have seemed that cryo-milling was as promising as spray drying, but the heat applied during these experiments led to dissolution of NAP in the polymer, leading to the wrong conclusion. Therefore, the reported drug loadings in Table 3.4. are relatively low drug loadings based on XRPD results. Nevertheless, the scale up from a 5 mL grinding jar to a 25 mL one showed the potential of CM for reaching higher drug loadings than the ones obtained in this study.

An interesting system to compare the three manufacturing techniques was 35 wt% NAP in combination with PVP-VA. Both in case of HME and SD a single T_g was detected, while in case of CM two T_gs could be distinguished (Fig 3.15.). The difference between HME and SD exists in the variation of the T_g width. For HME this T_g width was 54.3 °C, while for SD it was 68.1 °C. This shows that the spray dried ASD was more heterogeneous than the extruded one. Although for all techniques 35% NAP in combination with PVP-VA was formulated, clear differences in phase behavior were detected. The most homogeneous system was prepared using HME. This comparison supports the statement that HME is the best manufacturing technique for obtaining high drug loadings in case of these NAP-polymer combinations.

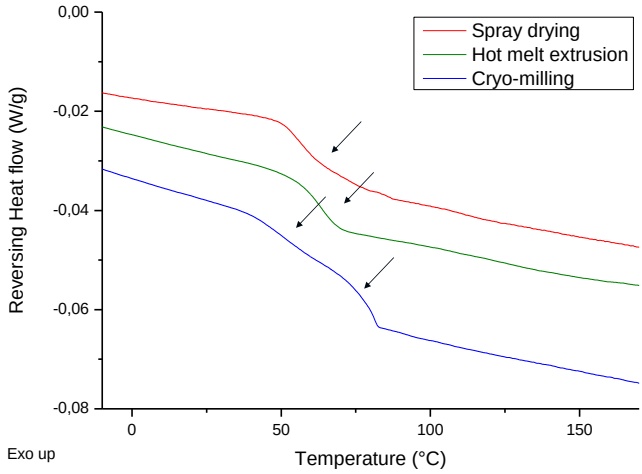

Figure 3.15*. mDSC thermograms of 35 wt% NAP-PVP-VA prepared with all three manufacturing techniques. The arrows indicate the positions of the T_gs. The RHF signals are shown as arbitrary units.*

Although there is a clear difference between the NAP-polymer combinations for the drug loadings that could be obtained, there was no ideal polymer for NAP nor per manufacturing technique. Thus, the selection of a polymer depends upon both the API and the technique used. Considering the results in

Table 3.4., the capability to reach high drug loadings is another important characteristic to evaluate when selecting a polymer for the formulation of ASDs.

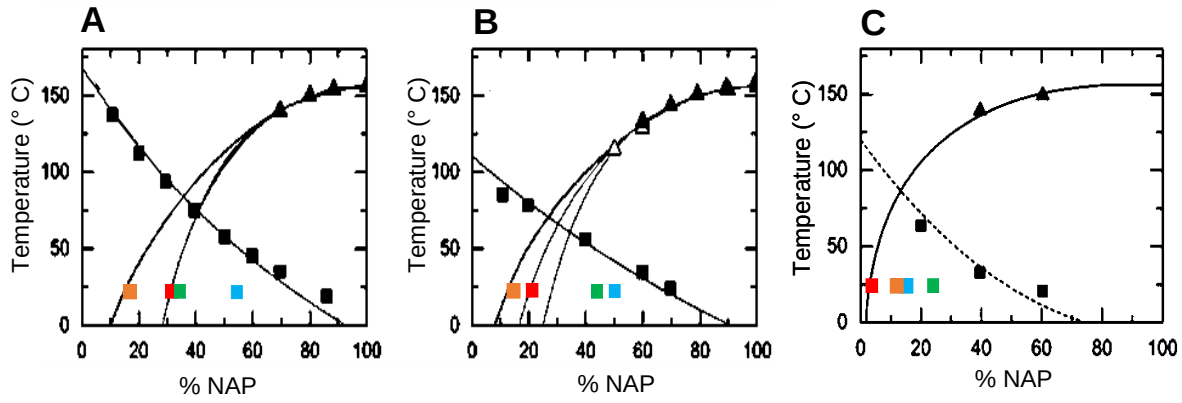

***Figure 3.16**. State diagrams of NAP with PVP K25 (A), PVP-VA64 (B) and HPMC-AS (C). The black squares indicate the T_gs and the triangles the solubility of NAP in the polymer. The solubilities were determined experimentally (A, C) or taken from literature (B). Here, the white triangles were derived from Kyerematenge et al. (2014) and the black ones from Prudic et al. (2014). For PVP and PVP-VA, Flory-Huggings and an empirical model were applied as well. The solubilities calculated with PC-SAFT are indicated with red squares, showing the solubility of NAP in the polymer at RT. The highest drug loadings reached with spray drying (green), hot melt extrusion (blue) and cryo-milling (orange) are indicated.*

The distinction between thermodynamic stabilization and kinetic stabilization becomes clear when comparing these drug loadings with the ones calculated with PC-SAFT. As described earlier, the solubility of the API in the polymer can be calculated using PC-SAFT. Lehmkemper et al. determined the thermodynamic solubility of NAP in PVP-VA, PVP and HPMC-AS. This resulted in the following maximum drug loadings at room temperature: 20.7% for PVP-VA, 31.4% for PVP and 3% for HPMC-AS (Fig 3.2. and 3.16.)[125,145]. Here, higher drug loadings were reached with PVP-VA and HPMC-AS for both HME and spray drying, because of kinetic trapping (Fig 3.16.). In a SD process, the feed solution is atomized in droplets, followed by mixing of the droplets with the drying gas. The drying rate can be a critical factor for amorphization. The solvent evaporation should be rapid enough to kinetically trap the API in the polymer matrix. Thereby the API does not have the time to crystallize during processing. Thus, the drying kinetics should be controlled to make preparation of completely amorphous ASDs feasible[38]. In a HME process, both the installed barrel temperature and applied shear forces heat the sample. When exiting the die, the mixture is rapidly cooled, which should be fast enough to kinetically trap the API in the polymer matrix. These are two different mechanisms that result in kinetic trapping of the API in the polymer matrix. As becomes clear from the results in Table 3.4., these mechanisms make it possible to reach higher drug loadings than thermodynamically predicted. In case of PVP, higher drug loadings could be reached using HME, but in case of SD the calculated drug loading of 31.4% was in between the experimentally determined range of 30% to 35% (Fig 3.16., A). Here, it was not possible to reach higher drug loadings, but at least the calculated drug loading was reached. This shows that the thermodynamic solubility can be considered as the minimum drug loading that should

be achieved at a certain temperature. Since this minimum drug loading was not yet reached for the NAP-PVP and PVP-VA combinations using cryo-milling, an optimization of the process is required.

This study showed clear differences between spray drying, hot melt extrusion and cryo-milling for their capability to reach high drug loadings. In all cases, conventional process parameters were used. Except for the alterations of the barrel temperature in case of HME, no optimization was performed. This implies that the drug loadings reported here may be increased when a full optimization of the process parameters is carried out. For SD, the drying air temperature, drying air flow rate, feed solution flow rate and atomization air flow rate should be optimized. For HME the important process parameters are the screw speed, screw configuration, barrel temperature and the feed rate. In case of CM, the filling level in the milling chamber, the milling frequency, the milling time and the beads combination should be optimized. Even though a full optimization may show even more potential for reaching higher drug loadings for all manufacturing techniques, this study defined the potential differences between the techniques. It can be stated that although the starting material is chemically identical, the final products will be physically different when applying a technology from a different category of manufacturing techniques.

3.5. CONCLUSION

In this study, four NAP-polymer combinations were prepared using spray drying, hot melt extrusion and cryo-milling. By comparing these three technologies, all three categories of manufacturing techniques were covered. The same drug loading of 35 wt% was pursued for all NAP-polymer combinations and every technique. Where PVP-VA was the best polymer for SD, PVP and PVP-VA were both promising for HME and PVP showed the best results in case of CM. This showed that there is no ideal NAP-polymer combination that could be applied for every manufacturing technique. The selection of carrier should be made per API and per technique. More importantly, the highest drug loadings feasible for all combinations were established per technique. Therefrom, it can be concluded that HME was the best manufacturing technique for reaching high drug loadings in case of these NAP-polymer combinations. This is in agreement with the importance of heat as an energy input for these systems. By full optimization of the process parameters even higher drug loadings might be obtained than described here in the article, yet robustness will need to be proven as the manufacturing process is scaled and undergoes the full manufacturing variation. Next to this, it was shown that higher drug loadings could be reached by kinetically trapping NAP in the polymer matrix than was predicted based on thermodynamics. Since this kinetic stabilization can minimize the molecular mobility to an acceptable low level, it is also essential for obtaining an appropriate shelf life. In addition, the biopharmaceutical performance, manufacturability, and chemical stability should be considered.

Acknowledgements

Laboratoires SMB and Het Fonds voor Wetenschappelijk Onderzoek-Vlaanderen (FWO) are acknowledged for financial support. The authors would like to thank Prof. Bart Goderis (Polymer Chemistry and Materials, KU Leuven) and Prof. Peter Van Puyvelde (Chemical Engineering, KU Leuven) for technical assistance.

Chapter 4

The underestimated contribution of the solvent to the phase behavior of highly drug loaded amorphous solid dispersions

This chapter is dedicated to Célestine Kindts who recently sadly passed away.

Results from this chapter are based on: **Dedroog, S.,** Boel, E., Kindts, C., Appeltans, B., Van den Mooter, G., 2021. The underestimated contribution of the solvent to the phase behavior of highly drug loaded amorphous solid dispersions. Int. J. Pharm. 121201.

4.1. ABSTRACT

In spite of the fact that spray drying is widely applied for the formulation of Amorphous Solid Dispersions (ASDs), the influence of the solvent on the physical properties of the ASDs is still not completely understood. Therefore, the impact of organic solvents on the kinetic stabilization of drug components in a polymer matrix prepared by either film casting or spray drying was investigated. One polymer, PVPVA 64, together with one of four poorly water-soluble drugs, naproxen, indomethacin, fenofibrate or diazepam, were film casted and spray dried using either methanol, ethanol, isopropanol, acetonitrile, acetone, dichloromethane or ethyl acetate. For every combination, the highest drug loading that could be formulated as a single amorphous phase was established. The solvent determined the maximum amount of drug that could be kinetically trapped in the polymer matrix and thereby the extent of kinetic stabilization. These maximum drug loadings were compared to the thermodynamic solubilities of the drugs in the seven solvents. Generally, there was no relation between the thermodynamic solubility of a drug and its highest drug loading attained using the same solvent. Hence, the contribution of the solvent to the generation of a supersaturated state should not be underestimated.

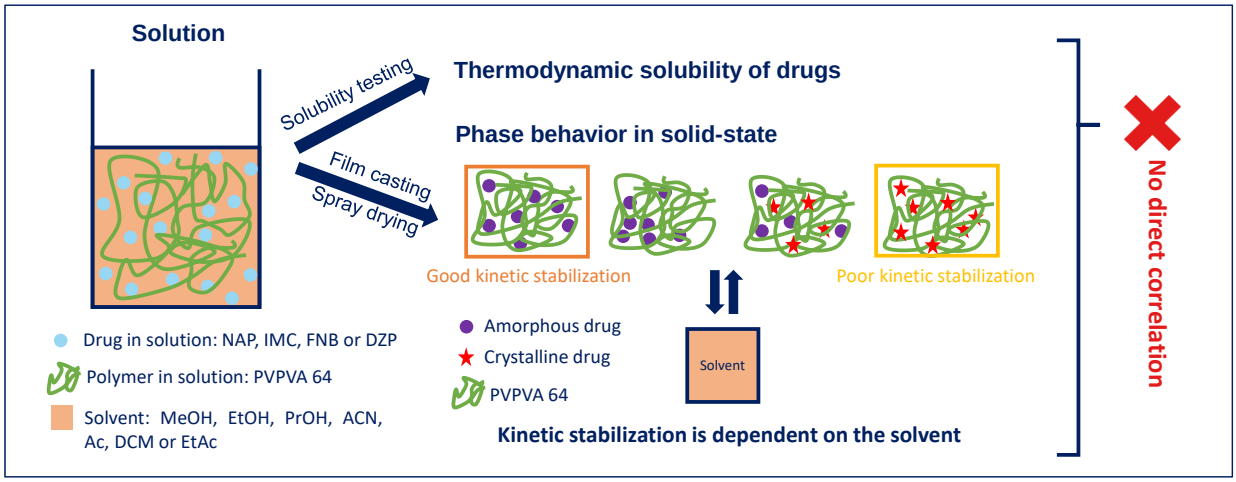

4.2. INTRODUCTION

Drug discovery pipelines consist for 75% out of New Chemical Entities (NCE) that are poorly water soluble, leading to insufficient oral bioavailability[24,25,160]. A successful formulation strategy to overcome these solubility issues is the formulation of Amorphous Solid Dispersions (ASDs)[41], where an Active Pharmaceutical Ingredient (API) is molecularly dispersed in a carrier matrix, which is most often an amorphous polymer, at solid-state[61]. Most manufacturing techniques for ASDs are solvent based methods, from which spray drying is most commonly employed[38,75]. In short, a solution of a drug and a carrier is made up in a common solvent, pumped through an atomizing device and subsequently transformed in a spray of very fine droplets inside of a heated drying chamber. Here, mass- and heat-transfer take place at the droplet surface, resulting in particle formation, after which the particles are separated from the drying gas in the cyclone. In contrast to this very rapid drying process, film casting, also referred to as solvent casting, is conducted by applying a solution of drug and polymer to a predefined area on a surface and letting it evaporate at Room Temperature (RT), resulting in a much slower evaporation process. In spite of the difference in drying rate, film casting has been successfully applied as a predictive screening tool to quickly assess the miscibility of an API and a polymer[161–164].

Both for film casting and spray drying, the solvent should measure up to the following criteria: having an acceptable viscosity and common solubilizing capacity for the API and the polymer, and being highly volatile, non-toxic, and non-combustive[93]. However, this could still comprise numerous solvents and/or solvent mixtures. Over the past years, the impact of the solvent on the phase behavior, particle morphology, dissolution and physical stability of ASDs has gained significant interest[137,165–169]. In all previously mentioned work, the overall aim was to correlate the solution properties, to the drying process and the consequential solid-state characteristics of the spray dried ASDs. To exemplify, Paudel et al. defined the influence of binary solvent mixtures of methanol (MeOH), acetone (Ac) and dichloromethane (DCM) on the miscibility of ASDs of naproxen (NAP) and polyvinylpyrrolidone (PVP)[167]. In another work, Wan et al. described different release rates of celecoxib from a poly(lactic-co-glycolic acid) (PLGA) matrix prepared by spray drying with diverse solvent mixtures of Ac and MeOH[120]. Nevertheless, to the best of our knowledge, it was not yet established to what extent a single solvent can impact the kinetic trapping efficiency and thereby the miscibility of a given API-polymer combination and its possibility to be formulated as a highly drug loaded ASD.

The faster the drying process, the more facilitated kinetic trapping of a drug in its amorphous state will be, thereby promoting the formulation of higher drug loadings by spray drying compared to film casting. When a drug is kinetically trapped in a polymer matrix, it can be dissolved in the polymer above its thermodynamic solid solubility limit, resulting in a kinetically stabilized system, in which phase

separation and subsequent crystallization are (partially and at least temporarily) prevented by the polymer[39]. In contrast to this, when the amount of drug is less than its thermodynamic solubility limit in the polymer, the system is thermodynamically stable, implying that the amorphous drug will never crystallize. The thermodynamic maximum can be calculated using for instance the Perturbed-Chain Statistical Associating Fluid Theory (PC-SAFT), which is a theoretical model that employs the thermodynamic solid (*i.e.,* crystalline drug)-liquid (*i.e.,* polymer with the dissolved drug) equilibrium together with the glass transition temperatures (T_g) of the system to establish two phasic diagrams of the drug and polymer matrix[145]. Additionally, the potential of ternary phase diagrams of drug, polymer and solvent has been described as well[136–139]. Here, the thermodynamic solubility of a drug in the polymer-solvent mixture was employed together with the T_gs to predict the phase behavior of the ASDs.

In the current study, the capability of film casting and spray drying to exceed the thermodynamic solid solubility was investigated by defining the highest drug loading that could be formulated as a homogeneous system, *i.e.,* existed out of a single amorphous phase. The relevance of attaining high drug loadings is supported by the present-day push to lower the pill burden for patients, which might become possible if more drug could be loaded in the same dosage size[144]. More importantly, the relation between the highest drug loadings and the thermodynamic solubilities of the API and its carrier in the solvent was investigated. Ideally, during drying, the thermodynamic solubility limit of the API in the polymer-solvent mixture would never be exceeded to avoid an inhomogeneous distribution of the API in the polymer matrix. Contrarily, when the solubility limit would be surpassed, amorphous phase separation and/or crystallization of the API would be likely to take place[138].

The kinetic stabilization of film casted and spray dried ASDs was investigated using seven single, organic solvents, selected based on their dielectric constant as indication of the polarity and their boiling point as an indication of the non-covalent interactions: MeOH, ethanol (EtOH), isopropanol (PrOH), acetonitrile (ACN), Ac, DCM, and ethyl acetate (EtAc), hereby covering the most commonly used solvents in spray drying processes. Since it could be expected that hydrogen bonds between API and polymer could interfere with the contribution of the solvent to the physical state, the model systems were also selected based on their interaction potential. From previous work, it was found that poly(vinylpyrrolidone-co-vinyl acetate) 64 (PVPVA 64) was a suitable polymer to formulate high drug loaded ASDs by spray drying (Chapter 3). Four model drugs, from which two that are well-known to have hydrogen bonding potential with PVPVA, *i.e.,* NAP and indomethacin (IMC), and two that have none, *i.e.,* fenofibrate (FNB) and diazepam (DZP), were selected (Fig 4.1.)[148,149,170,171]. The carbonyl group from PVPVA could act as a hydrogen acceptor for the hydroxyl groups from both NAP and IMC, while it has no hydrogen donor groups. Next to the presence of interactions, the crystallization

tendency of an API could also influence its potential to be kinetically stabilized in a polymer matrix. Therefore, the dependence of the Glass Forming Ability (GFA) of the drug compounds that could potentially hydrogen bond with PVPVA, namely NAP and IMC, on the solvent was investigated as well.

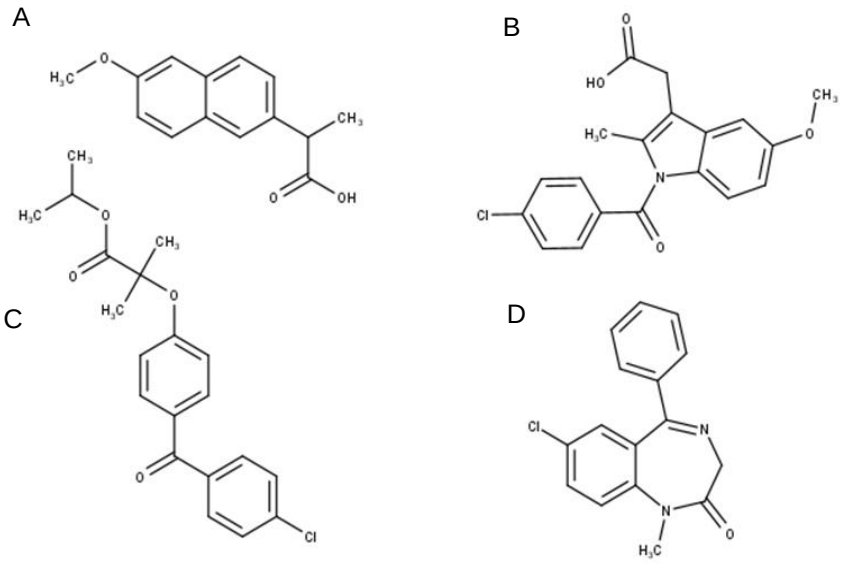

Figure 4.1. *Structural formulas of NAP (A), IMC (B), FNB (C) and DZP (D).*

The objective of this study was to characterize the efficiency of the kinetic trapping for these four API-polymer combinations depending on the solvent employed during either film casting or spray drying. For this, the highest drug loading that could be prepared as a single amorphous phase using a specific solvent was established. Furthermore, the correlation between the maximum drug loadings and the thermodynamic solubilities of the drugs in the various solvents was investigated.

4.3. MATERIALS AND METHODS

4.3.1. Materials

Both naproxen (NAP) (PubChem CID: 156391) and diazepam (DZP) (PubChem CID: 3016) were obtained from SA Fagron NV (Waregem, Belgium), while indomethacin (IMC) (PubChem CID: 3715) was purchased from ABC chemicals (Wauthier-Braine, Belgium) and fenofibrate (FNB) (PubChemCID: 3339) was supplied by Hangzohou Dayangchem Co. (Hangzhou City, China). Poly(vinylpyrrolidone-co-vinyl acetate) 64 (PVPVA 64, Kollidon® VA64) (PubChem CID: 270885), was received from BASF® ChemTrade GmbH (Ludwigshafen, Germany).

Methanol (MeOH) (≥ 99.8%) was purchased from ACROS Belgium (Geel, Belgium). Denaturated ethanol (EtOH) (≥ 97% and 3% V/V diethylether) was received from Chem-Lab Analytical (Zedelgem, Belgium). VWR Chemicals (Leuven, Belgium) supplied acetone (Ac) (≥ 99%) and 2-propanol (PrOH) (≥ 99.9%) was obtained from Carl Roth GmbH (Karlsruhe, Germany). Both dichloromethane (DCM) (≥ 99.5%) and acetonitrile (ACN) (≥ 99.9%) were received from Fisher Scientific (Loughborough, UK). Ethyl acetate (EtAc) (≥ 99.5%) was purchased from Sigma-Aldrich (Brussels, Belgium). The boiling points and dielectric constants of the solvents can be found in Annex 1[172].

Sigma-Aldrich (Gillingham, UK) delivered disodium hydrogen phosphate and Fluka™ (Seelze, Germany) provided monosodium dihydrogen phosphate monohydrate. Both sodium acetate and acetic acid were obtained from VWR Chemicals (Leuven, Belgium). To purify the water, it was de-ionized using a Maxima system (Elga Ltd., High Wycombe Bucks, UK). All materials were used as received.

4.3.2. Crystallization tendency study

The crystallization tendency of the interacting model compounds, *i.e.,* IMC and NAP, was evaluated in MeOH, EtOH, PrOH, ACN, Ac and EtAc by means of a Büchi mini spray dryer B-191 (Büchi, Flawil, Switzerland). Accurate amounts of IMC and NAP were dissolved in 20 mL solvent, resulting in a solid content of 2.0 and 1.3 % w/V respectively, thereby ensuring equal molarity. The following parameters were applied: a drying air temperature installed at the boiling point of the respective solvent, a drying air flow rate of 33 m^3/h, a feed solution flow rate of 5 mL/min and an atomization air flow rate of 15 L/min. All samples were prepared in triplicate and the resulting spray dried samples were analyzed with modulated Differential Scanning Calorimetry (mDSC) right after spray drying (day 0), after one day (day 1) and after one week (day 7) of storage at ambient conditions.

4.3.3. Manufacturing of amorphous solid dispersions

4.3.3.1. Film casting

For all four model drugs, both the drug and PVPVA were dissolved in one of the seven selected solvents (*i.e.,* MeOH, EtOH, PrOH, ACN, Ac, DCM or EtAc). In case of NAP and FNB, the solid content was fixed at 10% w/V, while for IMC and DZP, the solid content was limited to 2% w/V as the solubility of these model APIs was lower. The API to polymer ratio was varied with steps of 5 wt% until the highest drug loading, which was defined as the highest one that was X-ray amorphous, was achieved. The drug loadings that were investigated for every specific API-polymer-solvent combination can be found in Table 4.1. The solutions were casted by pipetting 2 mL of the solution on a predefined area (*i.e.,* 25 cm^2 for NAP and FNB, 16 cm^2 for DZP and IMC) of a glass plate, which was covered with Teflon tape (High-tech-flon, Konstanz, Germany). To slow down the solvent evaporation process, the casted solutions were covered with a funnel and dried for 2 days at ambient temperature. For every condition, the films were prepared in duplicate. Immediately after drying, the entire films were analyzed as such using X-Ray Powder Diffraction (XRPD).

Table 4.1*. Range of drug loadings (wt%) prepared by film casting for every drug-polymer-solvent combination.*

Drug loadings prepared by film casting (wt%)							
	MeOH	**EtOH**	**PrOH**	**ACN**	**Ac**	**DCM**	**EtAc**
NAP	20 – 45	20 – 45	20 – 45	20 – 50	20 – 50	20 – 50	20 – 50
IMC	45-75	65 – 80	65 – 80	70 – 75	45 – 65	55 – 70	60 – 70
FNB	5 – 20	5 – 30	5 – 20	5 – 20	5 – 30	5 – 30	5 – 30
DZP	20 – 35	35 – 45	35 – 45	35 – 45	20 – 35	35 – 60	20 – 35

4.3.3.2. Spray drying

As for film casting, both the drug and polymer were dissolved in one of seven solvents (*i.e.,* MeOH, EtOH, PrOH, ACN, Ac, DCM or EtAc) in order to obtain a solid content of either 10% w/V for FNB and NAP or 2% w/V for IMC and DZP. The ratio of drug and polymer was altered with steps of 5 wt% until the highest drug loading, which was established as the highest one for which a single glass transition could be obtained as an indication for a single amorphous system, for the specific composition was defined. The drug loadings that were prepared for every API-polymer-solvent combination are described in Table 4.2. To investigate the presence of residual solvent after spray drying, 3 batches of 10% w/V PVPVA were spray dried using every solvent as well. The solutions were spray dried using a Büchi mini spray dryer B-190 (Büchi, Flawil, Switzerland) by applying similar process parameters as for the crystallization tendency study, apart from the atomization air flow, which was installed at 10 L/min. Subsequently, the collected ASDs were further dried in a vacuum oven (Mazzali Systems, Monza, Italy)

for 4 days at 25 °C. After secondary drying, the ASDs were analyzed using both XRPD and mDSC, and further stored at -28 °C in the presence of phosphorus pentoxide.

Table 4.2. *Range of drug loadings (wt%) prepared by spray drying for every drug-polymer-solvent combination.*

Drug loadings prepared by spray drying (wt%)							
	MeOH	**EtOH**	**PrOH**	**ACN**	**Ac**	**DCM**	**EtAc**
NAP	40 – 45	40 – 50	40 – 45	40 – 45	40 – 50	40 – 50	40 – 50
IMC	70 – 90	70 – 90	70 – 80	70 – 90	80 – 90	80 – 90	80 – 85
FNB	5 – 20	20 – 30	20 – 30	20 – 30	20 – 35	20 – 30	20 – 30
DZP	35 – 45	35 – 70	35 – 70	35 – 70	25 – 45	25 – 60	35 – 70

4.3.4. Solid-state characterization of the amorphous solid dispersions

4.3.4.1. Modulated differential scanning calorimetry (mDSC)

The thermal behavior of the spray dried samples was investigated by mDSC using either a Q2000 mDSC (TA Instruments, Leatherhead, UK) or a Discovery DSC 2500 (TA Instruments, Leatherhead, UK), which were both equipped with a Refrigerated Cooling System (RCS 90) and a dry nitrogen purge at 50 mL/min. The equipment was calibrated for temperature, enthalpy and heat capacity using sapphire and indium standards. An amount of 1 to 5 mg was accurately weighed into aluminum DSC pans (TA instruments, Zellik, Belgium) and subsequently crimped with the corresponding lids (TA instruments, Zellik, Belgium). For all measurements, a linear heating rate of 2 °C/min was combined with a modulation amplitude of 0.212 °C and a period of 40 s. For NAP and IMC, the samples were heated from -15 °C to 180 °C, while the temperature range was altered to -15 °C to 160 °C or -20 °C to 140 °C for DZP and FNB, respectively. The thermograms were analyzed using the Universal Analysis software (Version 5.5, TA Instruments, Leatherhead, UK) or Trios (Version 5.1, TA Instruments, Leatherhead, UK). The T_g*s* were measured at half height of transition in the reversing heat flow and the T_g width was established by determining the start- and endpoint of the T_g using the derivative of the reversing heat flow. When two Tgs were present, the T_g width was established starting from the beginning of the first T_g to the end of the second T_g.

4.3.4.2. X-ray powder diffraction (XRPD)

To investigate the physical state of both the spray dried and the film casted ASDs, an X'Pert PRO diffractometer (PANalytical, Almelo, the Netherlands) with a Cu tube (Kα λ = 1.5418 Å) was employed. For all measurements, the generator was installed at 45 kV and 40 mA. All film casted samples were analyzed using a continuous scanning mode at RT, for which the samples were placed between two Kapton® Polyimide Thin-films (PANalytical, USA). The samples were scanned from either 4 to 40° 2θ with 400 s counting time for NAP, FNB and DZP, or 10 to 30° 2θ with 800 s counting time for IMC.

Likewise, the spray dried samples were characterized using a 800 s counting time from either 10 to 25° 2θ for FNB and NAP or 10 to 30° 2θ for DZP and IMC, respectively. In all cases, the step size was 0.0167° and spinning was set at 4 s. The diffractograms were analyzed using the X'Pert Data Viewer (Version 1.9a, PANalytical, Almelo, the Netherlands).

4.3.4.3. Scanning electron microscopy (SEM)

For the morphology assessment of the spray dried particles of NAP and PVPVA, Scanning Electron Microscopy (SEM) was employed. The spray dried powders were attached to SEM stubs using double-sided carbon tape (Ted Pella Inc., California, CA, USA) and subsequently platinum coated with a SCD-030 Balzers Union sputter-coater (Oerlikon Balzers, Balzers, Liechtenstein). A Phillips XL30 SEM-FEG (Philips, Eindhoven, The Netherlands) equipped with a Schottky field emission electron gun and a conventional Everhart-Thornley secondary electron detector was used to record the SEM images.

4.3.4.4. Thermogravimetric analysis (TGA)

To investigate the difference in residual solvent of the spray dried ASDs prepared using diverse solvents, for every solvent, 3 spray dried batches of 100 wt% PVPVA were analyzed using thermogravimetric analyzer TGA 550 (TA instruments, Leatherhead, UK). For this, approximately 5 to 10 mg of the sample was weighed in a platinum HT pan (TA instruments, Zellik, Belgium) and heated by applying a linear heating rate of 5 °C/min to 130 °C. The recorded weight loss in function of time was attributed to solvent evaporation, which was deducted using the Universal Analysis software (Version 5.5, TA instruments, Leatherhead, UK).

4.3.5. Solubility testing

The thermodynamic solubility of all drugs in MeOH, EtOH, PrOH, ACN, Ac, DCM and EtAc in absence or presence of 2.5%, 5%, 7.5% and 9% w/V PVPVA was determined by using 10 mL of solvent (either with or without PVPVA) in a volumetric flask of 25 mL, adding an excess amount of drug to it and stir it for 72 h at RT. Afterwards, the samples were transferred to glass test tubes and centrifugated for 5 min at 4500 g at RT. Subsequently, for MeOH, EtOH, PrOH and ACN, the supernatant was diluted using mobile phase before HPLC-UV analysis (see section 4.3.6.). For Ac, DCM and EtAc, a predefined fraction of the supernatant was evaporated, and the resulting solid fraction was dissolved (and if necessary further diluted) in mobile phase before HPLC-UV analysis. For every condition, the thermodynamic solubility was established in triplicate.

In addition, the solubility of PVPVA was determined by accurately weighing an amount of PVPVA and adding it to 10 mL of MeOH, EtOH, PrOH, ACN, Ac, DCM or EtAc in glass test tubes using the shake-

flask method for 72 h at RT. This process was repeated for higher concentrations of PVPVA until a white precipitation was visually observed or the solution was too viscous to add more PVPVA.

4.3.6. High performance liquid chromatography coupled with ultraviolet detection (HPLC-UV)

HPLC-UV analysis was performed using a VWR HITACHI Chromaster System (5160 pump, 5260 autosampler, 5310 column and 5410 UV-detector) with the Chromaster System Manager Software (version 1.1) for data acquisition. To determine the drug concentrations, 10 µL of the sample was injected and pumped over a Nucleodur C_{18} Gravity 5 µm column (150 mm x 4.6 mm) (Macherey-Nagel, Düren, Germany) at a flow rate of 1 mL/min. For all drugs, an isocratic method was employed. In case of IMC, the mobile phase consisted out of a phosphate buffer (20 mM) of pH 6.80 with ACN (65/35 V/V) and the detection wavelength was set at 252 nm, resulting in a retention time of ca. 4 min. Likewise, a phosphate buffer (20 mM) of pH 6.80 in combination with MeOH (20/80 V/V) was utilized in case of DZP. The detection wavelength was set at 250 nm, rendering a retention time of ca. 5 min. Both in case of NAP and FNB, an acetate buffer (25 mM) of pH 3.50, with either MeOH (30/70 V/V) or ACN (15/85 V/V) was applied, respectively. For NAP, at a detection wavelength of 270 nm, this rendered a retention time of about 4 min. At a detection wavelength of 290 nm, this resulted in a retention time of 5 min for FNB. Before usage, all buffers were filtered through a cellulose acetate filter (0.45 µm) (Sartorius Stedim Biotech GmbH, Göttingen, Germany) and sonicated for 30 min. All methods were validated for linearity (R^2 > 0.995) and both the limit of detection (LOD), and the limit of quantification (LOQ) were calculated from the signal to noise ratios. An overview of the HPLC-UV methods including the LOD and LOQ is shown in Annex 2. For all methods, there was no matrix effect observed for the highest concentration of PVPVA investigated, *i.e,* 9% w/V.

4.3.7. Data analysis: Calculation of % saturation of solubility

To facilitate the comparison of the acquired highest drug loadings by film casting/spray drying with the thermodynamic solubility data, the degree of saturation of the solubility of the pure drug compound was calculated for every solvent. More specifically, it was determined for the highest drug loading that was established using XRPD and/or mDSC analysis. In Equation 4.1., both the highest drug loading acquired using a specific solvent and the thermodynamic solubility of the pure drug compound in the same solvent are expressed in mg/mL. This approach allowed to evaluate the differences in saturation level for the maximum amount of drug that could be kinetically stabilized in the PVPVA matrix.

$$\%\ Saturation\ of\ solubility = \left(\frac{Highest\ drug\ loading}{Solubility\ of\ drug}\right) \times 100 \qquad \textit{Equation 4.1.}$$

4.4. RESULTS AND DISCUSSION

4.4.1. Crystallization tendency study of NAP and IMC

As the presence of hydrogen bonds between an API and its carrier can be beneficial for the physical stability of an ASD[39,173], it can be expected that it could also be advantageous to kinetically stabilize more API in the polymer matrix and thereby the formulation of a highly drug loaded ASD. However, next to the interaction potential, the intrinsic crystallization tendency of an API is another important characteristic that should be considered. As two model drugs with interaction potential were included in this study, namely NAP and IMC, the dependence of their GFA on the solvent was investigated.

IMC was found to exhibit a slow crystallization tendency irrespective of the solvent used, and this will be discussed in more detail below for IMC spray dried from EtOH. As reported in Table 4.3., the average crystallinity percentages of IMC spray dried from EtOH were relatively low, and thus IMC could be classified as a GFA Class III compound according to the classification of Van Eerdenbrugh et al.[174]. The mDSC thermograms of IMC spray dried from EtOH were characterized by a single T_g in the reversing heat flow, an exothermal crystallization event and two melting events in the total heat flow, corresponding to the melting of the α- and γ-polymorph of IMC, respectively (Fig 4.2A). In between these two melting events, a second exothermic recrystallization event could be distinguished in the non-reversing heat flow, which could be related to structuring into γ-IMC (data not shown). Accordingly, it was assumed that the γ-polymorph, which is the thermodynamically most stable IMC polymorphic form, was formed upon heating and therefore not present in the initial sample. Consequently, the first exothermal crystallization event was solely attributed to formation of more α -polymorph, and as a result, initial crystallinity percentages were calculated based on the α-IMC melting enthalpy (*i.e.,* 92.15 J/g). In case of Ac, DCM, ACN and PrOH, the determination of the initial percentage of crystallinity was in some cases impeded by the presence of a third polymorphic form, *i.e.,* δ-IMC (data not shown)[175]. Nevertheless, the results were overall in line with those that were obtained for EtOH, demonstrating that IMC could be considered as a GFA class III compound for all solvents investigated.

In contrast to this, NAP showed rapid crystallization behavior irrespective of the solvent applied. The average crystallinity percentages for NAP spray dried using EtOH are reported in Table 4.3. The corresponding mDSC thermograms were characterized by a single melting event (Fig 4.2B). Concerning all solvents investigated, average crystallinity percentages of spray dried NAP ranged from 90 to 98%, implying that this compound could be categorized as GFA Class I compound with respect to the

classification proposed by Van Eerdenbrugh et al.[174]. Hence, for these two model compounds, the crystallization tendency was not influenced by the solvent.

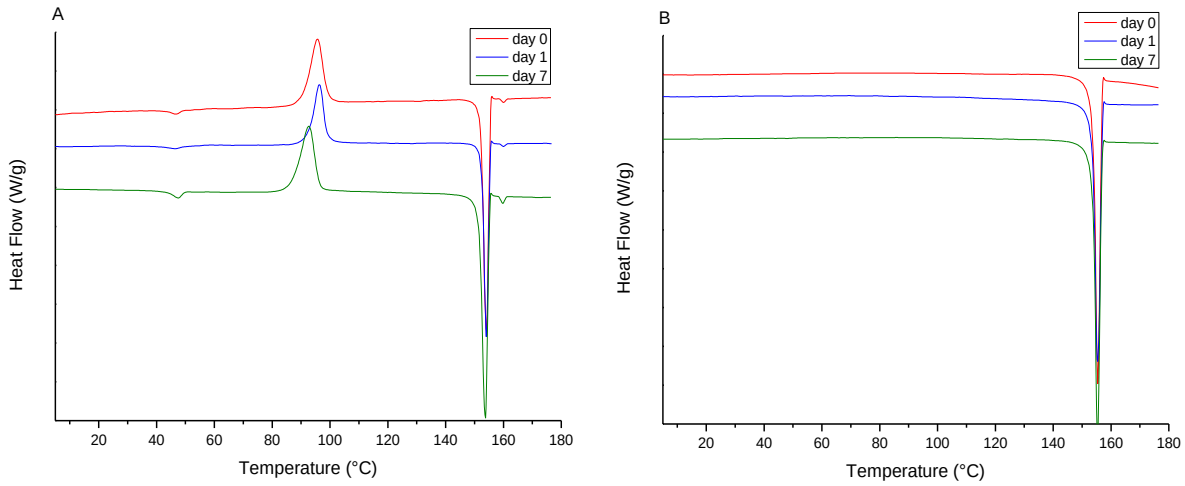

***Figure 4.2**. mDSC thermograms of (A) IMC and (B) NAP spray dried from EtOH, right after spray drying (day 0), after 1 day (day 1) and after one week (day 7) of storage.*

***Table 4.3.** Average crystallinity percentages (%) in IMC and NAP samples spray dried using EtOH ± standard deviation (sd).*

	IMC	NAP
Day 0	24.38 ± 3.91	96.60 ± 1.11
Day 1	27.85 ± 2.58	94.47 ± 1.95
Day 7	26.70 ± 1.36	97.08 ± 1.58

4.4.2. Solubility testing of PVPVA, NAP, IMC, FNB and DZP

The solubility of PVPVA was visually determined using the shake flask method. For 100 mg/mL, the solution of EtAc was slightly opaque, yet no precipitates were observed. For higher concentrations, PVPVA precipitated in EtAc, even so it was still freely soluble in all other solvents. Thus, EtAc was defined as a poor solvent for PVPVA, where the polymer chains were no longer expanded, but started to shrink and subsequently phase separated[113]. Similarly, Dohrn et al. predicted a miscibility gap for PVPVA and EtAc[137]. In case of PrOH, as from concentrations of 750 mg/mL, the solubility was limited by the viscosity of the solution. PVPVA remained freely soluble in all other solvents up to concentrations of 900 mg/mL, meaning that the polymer chains maintained their expanded state.

The thermodynamic solubilities of NAP, IMC, FNB and DZP, both in absence (red) or presence of 2.5% (green), 5% (blue), 7.5% (orange) or 9% w/V (purple) PVPVA are shown in Fig 4.3. For NAP, Ac had the highest solubilizing capacity, *i.e.,* 109.05 ± 3.14 mg/mL, and ACN the lowest, *i.e.*, 24.35 ± 0.57 mg/mL (Fig 4.3A). With increasing PVPVA concentration, the solubility of NAP kept increasing as well, *e.g.,* up to 178.73 ± 16.64 mg/mL in case of Ac. Hence, it might be that the optimal PVPVA concentration for

enhancing the NAP solubility was not yet achieved, however, testing of higher PVPVA concentrations would not be relevant for ASD formulations. Nevertheless, independently of the PVPVA concentration used, Ac remained the best solvent and either PrOH or ACN the worst.

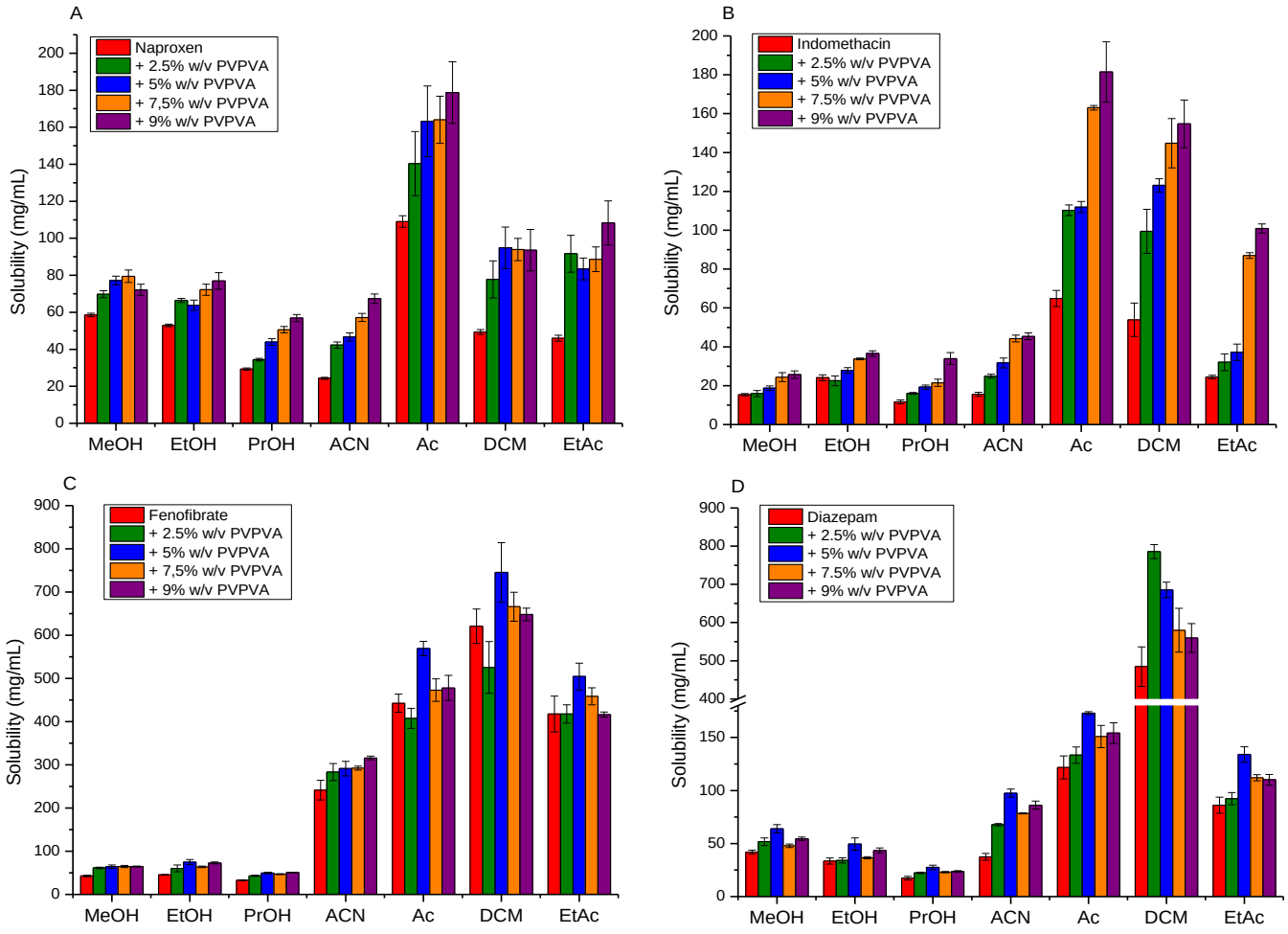

Figure 4.3. *Thermodynamic solubilities of NAP (A), IMC (B), FNB (C) and DZP (D) in MeOH, EtOH, PrOH, ACN, Ac, DCM, EtAc both in absence and presence of PVPVA. Four different concentrations of PVPVA were added: 2.5% w/v (green), 5% w/v (blue), 7.5% w/v (orange) and 9% w/v (purple).*

In Fig 4.3B, it is shown that the thermodynamic solubility of IMC ranged from 11.70 ± 1.00 mg/mL in PrOH to 53.92 ± 8.63 mg/mL in DCM and 64.91 ± 4.15 mg/mL in Ac. When adding PVPVA to the matrix, the IMC solubility was enhanced in all cases, which might indicate that the optimal PVPVA concentration to facilitate IMC solubility was not yet reached. Generally, the addition of PVPVA did not alter the trend observed for the pure solvents.

Similarly, the thermodynamic solubilities of FNB in the seven solvents are depicted in Fig 4.3C. In PrOH, the thermodynamic solubility of FNB was 32.83 ± 0.99 mg/mL, which was increased to 620.70 ± 40.12 mg/mL in DCM. The solubility trend was as follows: DCM > Ac/EtAc > ACN > EtOH/MeOH > PrOH. These results were in good correlation with the findings of Watterson et al., who determined the solubility of FNB in MeOH, EtOH, PrOH, ACN and Ac at different temperatures[176]. Starting from 5% w/V PVPVA,

further increase of the PVPVA concentration did not enhance the equilibrium solubility of FNB, indicating that the optimal amount of PVPVA for solubility facilitation was achieved. For some solvents, addition of more PVPVA even lowered the FNB solubility, *e.g.,* in case of Ac, the solubility was augmented to 569.10 ± 16.67 mg/mL with 5% w/V PVPVA and decreased again to 472.95 ± 26.05 mg/mL and 477.98 ± 29.24 mg/mL for 7.5% w/V and 9% w/V PVPVA, respectively. Moreover, PVPVA did not modify the trend observed for the pure solvents.

The solubilities of DZP ranged from 17.39 ± 1.76 mg/mL in PrOH to 484.64 ± 51.84 mg/mL in DCM, rendering the following trend: DCM > Ac > EtAc > MeOH > EtOH/ACN > PrOH (Fig 4.3D). As for FNB, the optimal PVPVA concentration for solubility enhancement was obtained, which was 5% w/V PVPVA in all solvents, except in DCM, where 2.5% w/v PVPVA was more beneficial. Furthermore, the addition of PVPVA did not alter the solubility trend observed for the pure solvents.

4.4.3. Determination of highest drug loadings by film casting

First, the same drug loading was solvent casted using all seven solvents for all four model compounds. After drying the films for 2 days at RT and subsequent solid-state characterization by XRPD, the drug loading was either lowered or increased, until the highest drug loading that was X-ray amorphous was attained. To exemplify, in Fig 4.4, the XRPD diffractograms of films of NAP and PVPVA prepared with MeOH (Fig 4.4A) and with Ac (Fig 4.4B) are depicted. Bragg peaks could be detected starting from 25 wt% in case of MeOH, while in case of Ac, these were only visible starting from 45 wt%. Hence, the highest drug loading could be formulated using Ac as a solvent (*i.e.,* 40 wt%), while MeOH only gave rise to half of this drug loading in a completely X-ray amorphous state (*i.e.,* 20 wt%). Accordingly, the highest drug loadings ranged from 20 wt% for MeOH to 45 wt% for ACN and EtAc (Fig 4.5A). Following the same approach, the highest drug loadings obtained by film casting of IMC and PVPVA ranged from 45 wt% for Ac to 70 wt% for PrOH (Annex 5, Fig 4.5A). It should be noted that the Bragg peaks present in case of PrOH, indicated the presence of a mixture both the α- and γ-polymorph of IMC, while those observed in case of Ac, could not be assigned to any of the polymorphic modifications reported in literature. However, this did not affect the amount of IMC that could be formulated as an ASD. For FNB, a model API without hydrogen donor groups, the maximum drug loading for MeOH was defined as 5 wt% and was augmented to 20 wt% for Ac, EtOH, DCM and EtAc (Annex 5, Fig 4.5A). For DZP, the highest drug loadings ranged from 25 wt% in case of Ac to 55 wt% in case of DCM (Annex 5, Fig 4.5A).

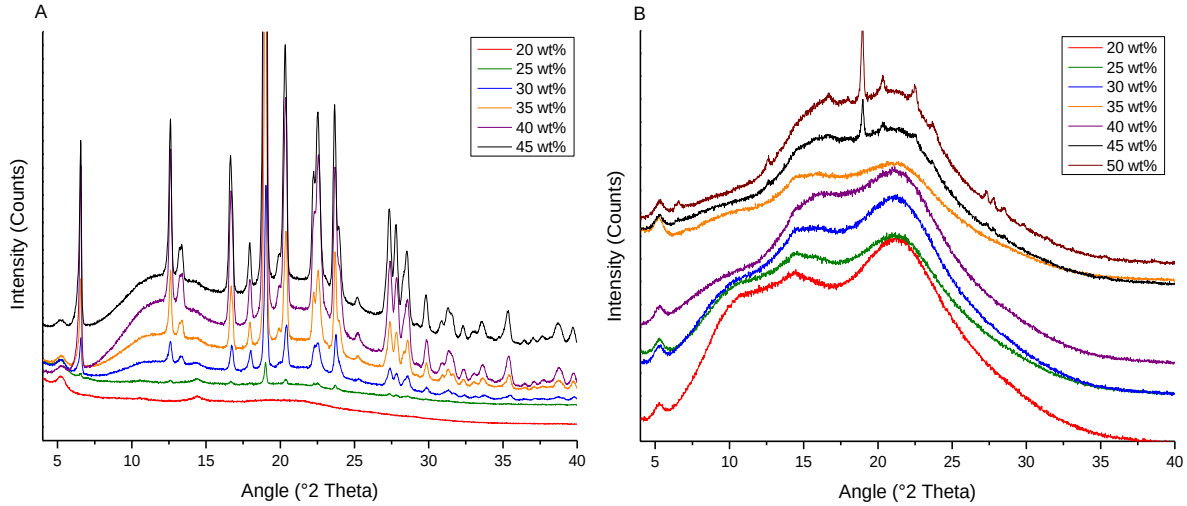

Figure 4.4. *XRPD diffractograms of film casting of NAP and PVPVA with MeOH (A) and Ac (B). For MeOH, the drug loadings ranged from 20 wt% (red) to 45 wt% (black), while for Ac they went from 20 wt% (red) to 50 wt% (brown). The diffraction peaks at 5 and 15 °2ϑ originated from the Kapton film.*

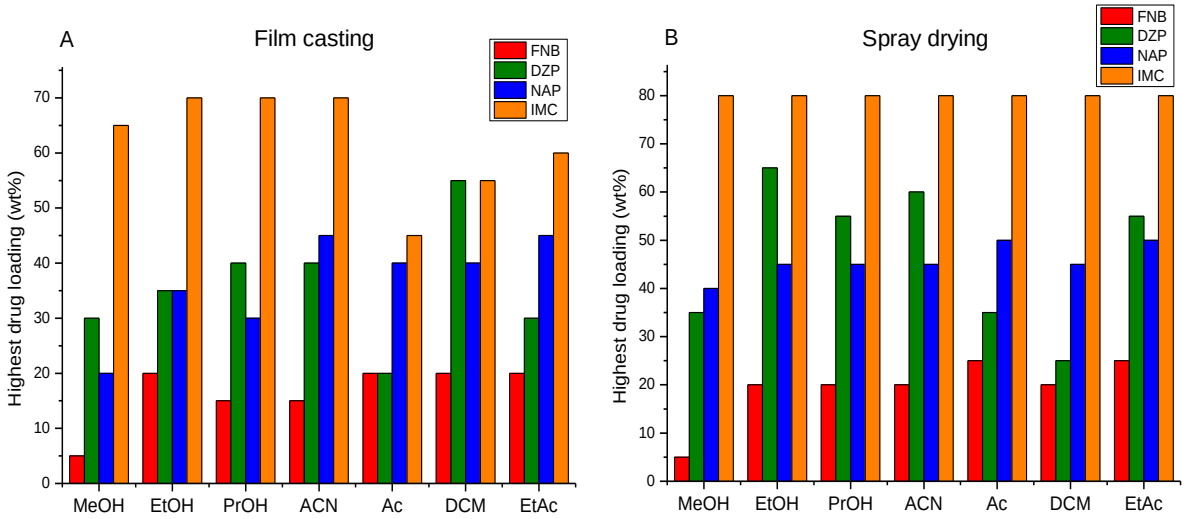

Figure 4.5*. The highest drug loadings per solvent as established by either film casting (A) or spray drying (B). The drug loadings of FNB are depicted in red, those of DZP in green, those of NAP in blue and the ones of IMC in orange.*

From Fig 4.5A, it is evident that the solvent played a decisive role in the amount of API that could be formulated in a completely X-ray amorphous ASD. Hence, independently of the physicochemical characteristics of the APIs, the solvent was the most crucial factor for the degree of structuring in the ASD. However, generally lower drug loadings were attained for the non-interacting model drugs, *i.e.,* FNB and DZP, compared to the interacting ones, *i.e.,* NAP and IMC. Only in case of DCM and PrOH, more DZP could be kinetically trapped in the polymer matrix when compared to NAP. Additionally, the GFA of the interacting model drugs (see section 4.4.1.) could also be related to the range of drug loadings that was obtained, with generally higher drug loadings for a slow crystallizer (*i.e.,* IMC) in contrast to a fast crystallizer (*i.e.,* NAP). It is also worth noting that the XRPD measurements in case of

NAP were conducted at 400 s counting time, while those of IMC were applied at 800 s counting time. Hence, the sensitivity difference between these measurements emphasizes that the formulation of high drug loaded ASDs was facilitated for IMC. Moreover, the thermodynamic solid solubility limit of NAP in PVPVA, *i.e.,* 20.7 wt%, and that of IMC in PVPVA, *i.e.,* 34 wt%, was exceeded in all cases[125,133,134]. These limits are considered as the maximum drug loadings for a thermodynamically stable ASD. The fact that it was possible to achieve higher drug loadings than this thermodynamic maximum, points out that even though the solvent was evaporated at RT, the drying process was still sufficiently fast to enable kinetic trapping of the drug in its amorphous state. Hence, the influence of kinetics next to thermodynamics on the phase behavior of ASDs should not be minimized. The extent to which kinetic trapping was achieved was dependent on the relation between solvent, polymer, and API characteristics. For instance, a possible explanation for the poor performance of MeOH, EtOH and PrOH for solvent casting of NAP based ASDs, could be that NAP preferentially forms dimers in these proton donating solvents, while proton accepting solvents are known to reduce the self-association of NAP, rendering an increased amount of free NAP to hydrogen bond with PVPVA[165].

4.4.4. Determination of highest drug loadings by spray drying

As film casting has been successfully applied as a predictive tool for the phase behavior of spray dried products[161–164], the effect of the solvent on the phase behavior of high drug loaded ASDs could be expected to be similar for both techniques. For the solid-state characterization of the spray dried ASDs, mDSC was employed along with XRPD. Accordingly, the highest drug loading was defined as the maximum drug loading that was both X-ray amorphous and displayed one T_g in mDSC analysis. As mDSC is in general more sensitive for the detection of crystallinity, it should be pointed out the drug loadings reported in this part are generally based on the detection of a smaller amount of crystalline material compared to film casting. Consequently, there was no direct comparison between film casting and spray drying possible, however, the trends regarding the impact of different solvents on the physical state could be compared.

For NAP, it was previously reported that spray drying with MeOH could give rise to drug loadings of 40 wt% (Chapter 3). In Fig 4.6., an example of spray drying with another solvent, EtOH, is depicted. A single phase system was obtained for both the 40 wt% and the 45 wt%, while in case of 50 wt% a melting event, indicating the presence of crystalline NAP, could be distinguished (Fig 4.6A). These results corresponded with the XRPD ones, where Bragg peaks were present for the 50 wt% loaded ASD (Fig 4.6B). Consequently, the maximum drug loading was established at 45 wt%. Similarly, the drug loadings for all other solvents were defined, ranging from 40 wt% for MeOH to 50 wt% for Ac and EtAc (Fig 4.5B). In Table 4.4., the T_gs and their corresponding T_g width are shown for all ASDs of NAP and

PVPVA prepared by spray drying. Similar T_gs and T_g ranges were obtained for the same drug loadings, independently of the solvent employed. Despite the fact that the position of the T_g is an important indicator of the mobility of an ASD, it could not be related to the difference in phase behavior obtained using diverse solvents.

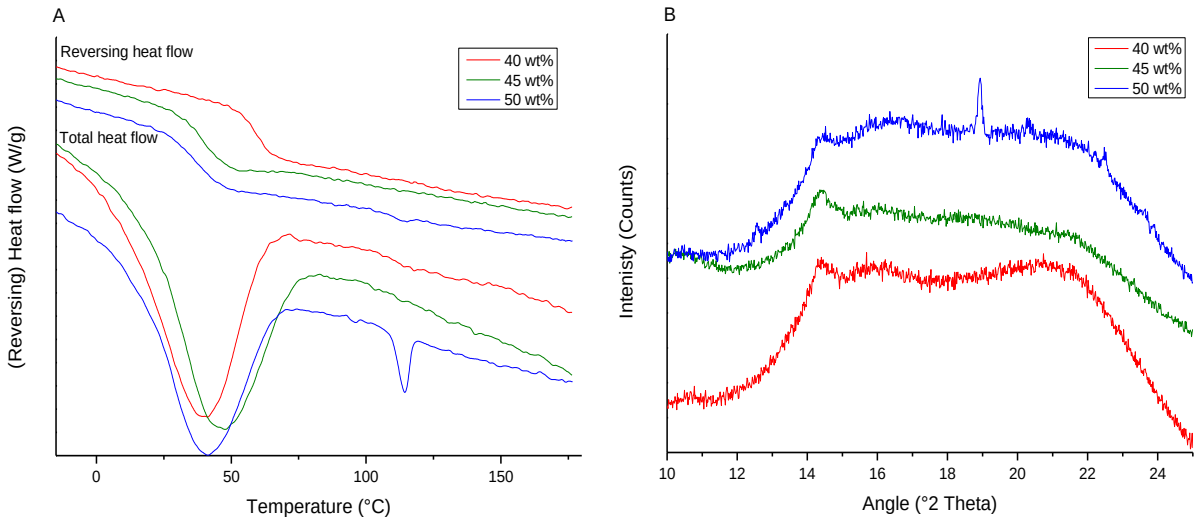

Figure 4.6. *mDSC thermograms (A) and corresponding XRPD diffractograms (B) from spray drying of NAP with PVPVA using EtOH. In Fig A, both the reversing and total heat flow are depicted. Exothermic events are depicted upwards. The color code for both figures was as follows: 40 wt% (red), 45 wt% (green) and 50 wt% (blue). The diffraction peak at 15 °2ϑ originated from the Kapton film.*

Table 4.4. *Position of the* T_g *and* T_g *width of ASDs of NAP and PVPVA prepared by spray drying.*

Solvent	40 wt%		45 wt%		50 wt%	
	Tg (°C)	Tg width (°C)	Tg (°C)	Tg width (°C)	Tg (°C)	Tg width (°C)
MeOH	55.59	41.09	55.59	43.92	-	-
EtOH	55.55	44.76	53.88	45.4	47.94	47.49
PrOH	54.36	44.55	53.54	46.86	-	-
ACN	58.85	42.24	55.37	49.28	-	-
Ac	57.86	42.24	52.39	48.97	48.72	42.66
DCM	56.87	45.58	52.46	43.93	48.54	48.55
EtAc	57.08	49.86	53.50	48.76	49.93	40.35

In addition to the T_gs reported in Table 4.4., the mDSC analysis of some spray dried ASDs of NAP revealed an endothermic event with the characteristics of a second T_g, situated at a higher temperature, *i.e.,* 130 °C, than that of the pure polymer, *i.e*., 110 °C (Fig 4.7A). In case of amorphous-amorphous phase separation in a drug-rich and polymer-rich phase, it would be expected to detect two T_gs, which would typically be situated in between the one of the pure drug and the polymer. However, the positioning of this second T_g contradicted this. For this reason, it was hypothesized that there was amorphous-amorphous phase separation in a Mobile Amorphous Fraction (MAF) and a Rigid Amorphous Fraction (RAF), represented by the first and second T_g, respectively. It was theorized that

the MAF existed out of an amorphous NAP fraction, molecularly dispersed in PVPVA, while the RAF comprised PVPVA that was immobilized by a small crystalline fraction of NAP. The presence of both a MAF and RAF was previously reported for semicrystalline polymers and amorphous polymer matrices in which nanoparticles were dispersed, where the amorphous polymer fraction was immobilized by a crystalline polymer fraction or nanoparticles, respectively[177–183]. Here, the lower molecular mobility of the RAF resulted in a higher energetic state, *i.e.,* a higher T_g than that of the pure polymer. Additionally, Litvinov et al. investigated the influence of miconazole on the heterogeneity of the chain dynamics of the polyethylene-glycol-polyvinyl alcohol (PEG-g-PVA) graft copolymer[184]. Here, the presence of (semi-)rigid amorphous phases could be attributed to the semicrystalline nature of PVA, while the drug was molecularly dispersed in the copolymer matrix, thereby not crystalline and not capable to immobilize the amorphous fractions of the copolymer. In contrast to this, as PVPVA is an amorphous polymer and cannot form its own ordered regions, it was hypothesized that a part of PVPVA was immobilized by the presence of a small crystalline fraction of NAP, thereby forming a RAF. As a result, this rigid phase could only liquefy when the NAP crystals started to melt, which took place at a temperature that was situated above the T_g of the pure polymer.

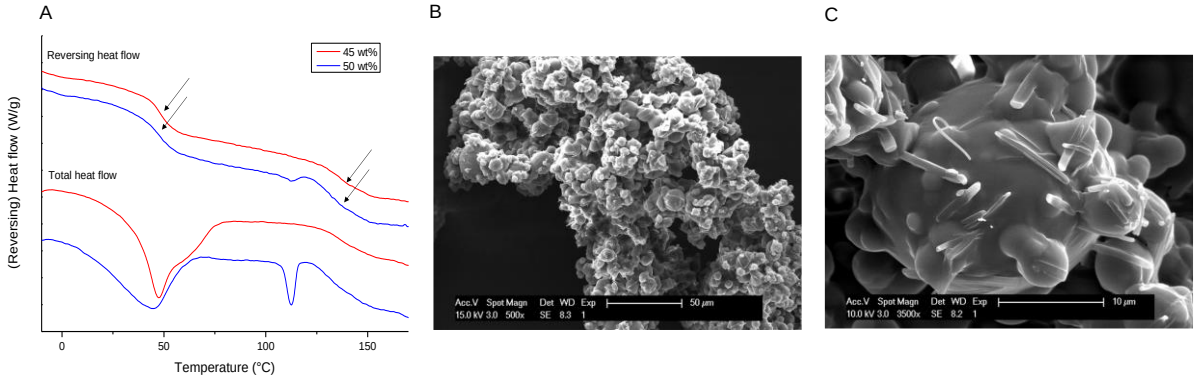

Figure 4.7*. mDSC thermograms (A) and SEM images (B, C) of spray drying of NAP and PVPVA with DCM. Both the reversing and total heat flow are shown for the 45 wt% (red) and 50 wt% (blue). Exothermic events are depicted upwards. The arrows indicate the positions of the* T_g*s. The two SEM images correspond to the 45 wt%.*

In Fig 4.7A, the presence of a RAF is depicted for 45 wt% and 50 wt% of NAP spray dried using DCM. For the 50 wt%, two T_gs and a melting event were revealed, where the melting took place before the second T_g was detected. This demonstrated the importance of melting of the NAP crystals before the RAF could be mobilized and thereby liquefy. This hypothesis was at least partially confirmed by SEM analysis, where needle shaped NAP crystals could be distinguished in case of the 45 wt% loaded NAP spray dried ASD using DCM (Fig 4.7B, C). Hence, it was clear that there was a crystalline NAP fraction that was not detected by mDSC analysis, yet clearly present during the morphology assessment. As reported in previous work, the explanation for this discrepancy might be the dissolution of NAP crystals in the polymer matrix during the mDSC analysis[185]. This second, high temperature T_g was detected

during the mDSC analysis of spray dried ASDs prepared with different solvents, yet it was not repeatable and is therefore subject for further investigation.

In case of IMC, a maximum drug loading of 80 wt% was obtained irrespective of the solvent (Fig 4.5B). For lower drug loadings, a single T_g was observed in the mDSC analysis, while starting from 80 wt% an exothermic crystallization event and two endothermic melting events, indicating the presence of both α - and γ-IMC, could also be distinguished (Annex 6). As described for the crystallization tendency study of IMC, it was assumed that the exothermic crystallization event was solely attributed to the formation of (more) α-IMC upon heating, thereby allowing the calculation of the initial percentage of crystallinity based on the melting enthalpy of the α-polymorphic form. Following this, it could be deducted that there was no crystalline material present in the initial sample for the 80 wt% and that crystallization took place upon heating. As for NAP, similar T_gs and T_g widths were observed for the same drug to polymer ratio, irrespective of the solvent (Annex 3). All XPRD diffractograms consisted out of an amorphous halo up until drug loadings of 90 wt%, which could be explained by the higher sensitivity of mDSC for small traces of crystalline material. Hence, IMC was molecularly dispersed in PVPVA up until 80 wt%, while crystalline fractions were present for higher drug loadings, independently of the solvent.

In a next step, the two non-interacting model compounds, FNB and DZP, were spray dried using all seven solvents as well. The maximum drug loadings of FNB ranged from 5 wt% in case of MeOH to 25 wt% for Ac and EtAc (Annex 6, Fig 4.5B). DCM and Ac gave rise to ASDs with T_gs slightly lower than that of ASDs of the same drug to polymer ratio prepared using other solvents (Annex 3). At the same time, the T_g width was larger, indicating that a more heterogeneous system was obtained. However, for Ac, the spray dried samples did not contain a crystalline fraction up until 25 wt% of FNB, in contrast to most other solvents. A broader T_g is a more preferred phase behavior than the presence of crystalline material. In addition, it should be pointed out that the mDSC analysis of the spray dried FNB samples was not always straightforward. As discussed in Chapter 7, the broad solvent evaporation endotherm could cover up the melting of FNB[185]. Here, the XRPD results showed Bragg peaks, while the sample appeared amorphous based on the mDSC analysis. Therefore, XRPD showed to be more trustworthy for defining the highest drug loadings of FNB.

Likewise, the highest drug loadings for DZP extended from 25 wt% for DCM to 65 wt% for EtOH (Fig 4.5B). For the previous drug compounds, the presence of a crystalline fraction determined the maximum drug loading that could be achieved. In case of DZP, two T_gs, indicating amorphous-amorphous phase separation in a drug-rich and polymer-rich phase, were detected in the mDSC analysis of several samples. As crystallization is very likely to start from a drug-rich phase, this

heterogeneous phase behavior should be avoided. In Annex 6, an example of the mDSC analysis of samples spray dried with DCM, where two T_gs and an enthalpy recovery event were detected, is shown. The T_gs and corresponding T_g widths of these ASDs of DZP are shown in Annex 3. The ASDs spray dried with DCM had the broadest T_gs and thereby the most diversified phase behavior. In addition, lower, broader T_gs were observed for ASDs of DZP prepared with PrOH and EtAc compared to other solvents.

During spray drying, the outlet temperature is of great importance to avoid stickiness of the material and to prevent physical instability. More specifically, the relation between the T_g of the ASD and the outlet temperature (T_{out}) should be considered. The smaller this temperature difference, the more mobile the system will be, and the crystallization rate can be expected to increase. In Annex 4, the outlet temperature ranges observed during spray drying are reported. These temperature differences could however not be related to the observed phase behavior of the ASDs.

After spray drying, the T_gs of the spray dried ASDs might still be influenced by the amount of residual solvent present. The solvent could act as a plasticizer, thereby lowering the T_g, increasing the mobility of the system at RT and decreasing its stability. The presence of residue was investigated for 3 batches of 100 wt% PVPVA per solvent as the polymer is the component that is responsible for most of the solvent retention (Annex 4). TGA analysis revealed that the amount of residual solvent was similar for the different solvents, with a maximum difference of ± 1.6 wt% of solvent. As the presence of an API compound would result in lower residual solvent content, it can be expected that the influence of the residual solvent on the physical state was negligible.

More importantly, independently of the manufacturing technique, the solvent had a decisive impact on the physical state of the ASDs of NAP, FNB and DZP. Film casting and spray drying gave rise to a similar trend with regard to the most ideal solvent for the formulation of high dug loaded ASDs, evidencing that film casting can be of high predictive value for the influence of a solvent on the phase behavior of ASDs. Nevertheless, although the solvent affected the homogeneity of the IMC films, it did not influence the maximum drug loadings of its spray dried ASDs (Fig 4.5). This could be attributed to the combination of enhanced kinetic trapping by spray drying, the interaction potential between IMC and PVPVA and the low crystallization tendency of IMC (see section 4.1.1.). When applying a rapid drying process to a solution of two compounds that can hydrogen bond with one another, it might be that the interaction strength between these compounds is too high and/or the timeframe to separate them is too short, facilitating the formulation of high drug loaded ASDs. Contrarily, as NAP was a GFA class I drug, it was such a fast crystallizer, that even during a faster drying process, *i.e.*, spray drying, the evaporation rate was still not high enough and/or the interaction strength between PVPVA and NAP too low, to avoid crystallization of the drug. It is clear that contribution of the solvent to the phase

behavior was codependent on the evaporation rate, the interactions between the API and polymer and the crystallization tendency of the drug.

4.4.5. Thermodynamic solubilities vs. the highest drug loadings

In the upcoming section, the thermodynamic solubilities (see section 4.4.2.) will be compared with the maximum drug loadings obtained by film casting (see section 4.4.3.) (Fig 4.8.) and spray drying (see section 4.4.4.) (Annex 7). Additionally, these highest drug loadings were expressed as the degree of saturation of the solubility of the pure API in the solvent. When interpreting these results, two important factors should be kept in mind. First, this saturation level only takes into account the initial situation in solution, yet during drying, the degree of saturation constantly increases until a film/particle is formed. Secondly, the degree of saturation considers the solubility of the pure drug compound without the possible solubility increasing effect of PVPVA (Fig 4.3.), hence, in some cases a solubility saturation of more than 100% was observed (Fig 4.8.). Despite this, the saturation level allows to evaluate possible differences in saturation that were obtained when the highest drug loading that could be kinetically stabilized in the polymer matrix was attained.

First of all, as only EtAc was a poor solvent for PVPVA, and all others could be considered as good solvents, the solubility of the polymer could not be correlated with the abovementioned solvent dependent drug loadings.

For NAP, it was clear that the solubility differences could not be related to the solvent dependent drug loadings that were achieved by film casting (Fig 4.8A). For instance, Ac clearly was the best solvent to dissolve NAP under all conditions (Fig 4.3A), however, it did not enable the formulation of higher drug loadings than when applying ACN, the solvent with the worst solubilizing capacity. Because of the poor solubility of NAP in ACN, a high degree of solubility saturation was reached when using ACN as a solvent, however, it still enabled the formulation of higher drug loadings compared to MeOH, in which NAP dissolved better and therefore a lower saturation level was reached for the same amount of NAP. For the highest drug loading prepared with ACN the saturation level was 184.80%, whilst for MeOH this was only 34.15% (Fig 4.8A). Spray drying with Ac enabled the formulation of higher drug loadings, *i.e.,* 50 wt%, but the same was true for EtAc, yet NAP had a much lower solubility (*i.e.,* 45.98 ± 1.60 mg/mL) and consequently a higher degree of solubility saturation (*i.e.,* 108.74%) in EtAc compared to Ac (*i.e.*, solubility of 109.05 ± 3.14 mg/mL and saturation level of 45.85%) (Annex 7).

From Fig 4.8B, the lack of correlation between the thermodynamic solubilities of IMC and its highest drug loadings achieved by film casting becomes evident. Interestingly, the highest solubility (*i.e.,* 64.91 ± 4.15 mg/mL in Ac) resulted in the lowest drug loading (*i.e*., 45 wt%) and thereby also the lowest

solubility saturation (*i.e.*, 13.86%). Both PrOH and EtOH gave rise to a drug loading of 70 wt%, however, in case of PrOH this corresponded to a degree of saturation of 119.65% compared to 58.13% for the same amount of IMC in EtOH. Moreover, as spray drying produced an identical drug loading of 80 wt% for all solvents, there clearly was no relation with the solubilizing capacity (Annex 7).

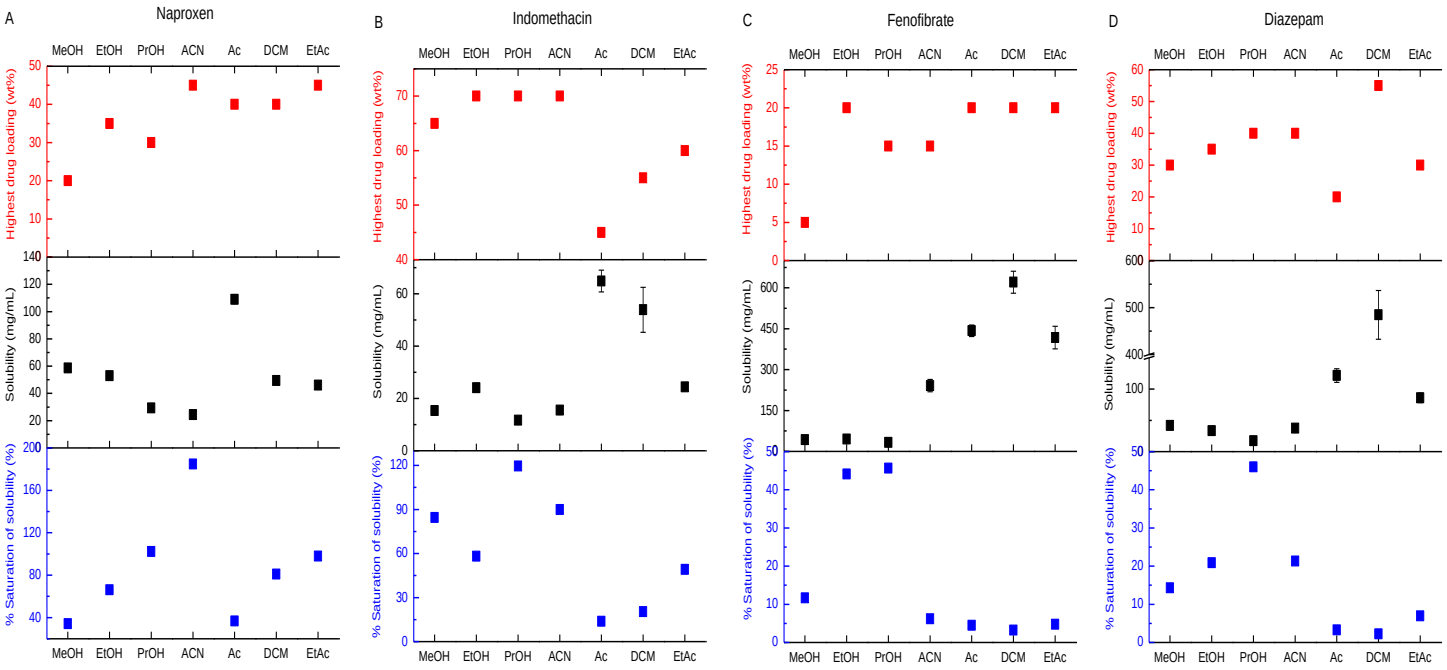

***Figure 4.8**. Correlation between the highest drug loadings acquired by film casting, the thermodynamic solubilities and the % saturation of solubility for the respective highest drug loading of NAP (A), IMC (B), FNB (C) and DZP (D) per solvent. The highest drug loadings are shown in red, the thermodynamic solubility of the pure drug compound in black and the % saturation of solubility in blue. The error bars indicate the standard deviation on the thermodynamic solubility. When not visible, the standard deviation was smaller than the square shown in the scatter plot.*

Although the solubility of FNB in MeOH, EtOH and PrOH was similar, they gave rise to different highest drug loadings when film casting, *i.e.,* 5 wt% for MeOH, 20 wt% for EtOH and 15 wt% for PrOH (Fig 4.8C). These drug loadings corresponded to a degree of solubility saturation of FNB of 11.66% for MeOH, 44.16% for EtOH and 45.70% for PrOH. Thus, despite the lower saturation level in MeOH, no higher drug loadings could be formulated as an ASD using this solvent. Although FNB had a higher solubility in DCM, spray drying enabled the production of even higher drug loadings for EtAc and Ac as opposed to DCM. Counterintuitively, the solvent that had the highest solubilizing capacity and thereby the lowest degree of solubility saturation, DCM, did not foster higher drug loaded ASDs (Annex 7).

For DZP, the highest drug loading by film casting (*i.e.,* 55 wt%) correlated well with the highest solubility in DCM (*i.e.,* 484.64 ± 51.84 mg/mL) and the lowest solubility saturation level (*i.e.,* 2.27%) (Fig 4.8D). In contrast to this, the highest degree of saturation was obtained in case of PrOH for a drug loading of 40 wt% (*i.e.,* 46%), which was higher than the maximum drug loading obtained when using MeOH as a solvent (*i.e.,* 30 wt%), while the degree of solubility saturation was much lower in case of MeOH,

namely 14.31%. Spray drying with DCM yielded a drug loading of 25 wt%, which was not only lower than all other solvents, but also lower than for film casting. This inconsistency could be explained by a sensitivity difference of the selected analytical techniques. A more sensitive approach resulted in the lowest drug loading for DCM, whilst it was the best solvent for DZP and thereby DZP also had the lowest saturation level in this solvent (Annex 7).

Overall, there was no relation between the solubility or the degree of solubility saturation in a specific solvent and the drug loading in an ASD prepared using this solvent. Hence, the impact of the solvent power on the homogeneity of the drug distribution should not be overestimated. At the same time, the contribution of the solvent, although only present at a trace level in the dry ASD, should not be underestimated.

The potential of ternary phase diagrams of drug-polymer-solvent mixtures to predict the phase behavior of ASDs using PC-SAFT has been reported in literature[136–139]. Here, the thermodynamic solubility of the crystalline drug in the polymer-solvent mixture, together with the T_g of the system was employed to define a state diagram. Therefrom, it was found that the solubility in the polymer-solvent mixture was an important factor to predict the homogeneity of the ASDs. Following this, it could be stated that the solvent power was an important solvent characteristic to take into account, however, from this work, it became clear that it is not the only factor that should be considered. Overall, there was no correlation between the solubility in a specific solvent and the highest drug loading achieved using this solvent. Because of kinetic trapping, it was possible to attain much higher drug loadings than would be expected based on the thermodynamic equilibria. Kinetics showed to be more important for the phase behavior compared to thermodynamics.

Nevertheless, the solid-state characterization presented in this work was performed immediately after preparation, thus, the ASDs might crystallize over time until their thermodynamic solid solubility is reached. Lehmkemper et al. demonstrated this for formulations of NAP and PVPVA prepared by hot melt extrusion[125]. Hence, it should be kept in mind that the inclusion of a stability study is indispensable during an ASD manufacturing process. Despite the fact that a supersaturated state might not be maintained for a long period of time, it was clear that the extent of supersaturation was dependent on the solvent used. This is especially important when only one solvent is used to assess the feasibility of ASD production by solvent based manufacturing techniques. By accidently selecting a solvent that results in a poor kinetic trapping efficiency, a very low drug loading might be attained, and one might make erroneous conclusions about the kinetic stabilization potential of the solvent based technique. On the other hand, when a solvent with very good kinetic trapping properties would be selected, it is possible that the prepared drug loading is way above the thermodynamic solid solubility limit, which

might in turn result in a poor physical stability of the ASD. This is a very important finding as current solvent selection procedures do not take this element into account. Hence, to produce an ASD with the most optimal phase behavior, *i.e.,* a homogeneous distribution of the drug in the polymer matrix at a molecular level, the solvent selection procedure should not be limited to finding a common solvent for both API and polymer. To identify additional criteria that should be taken into account, a deeper understanding of factors that could influence the drying process and thereby the kinetic trapping efficiency of the drug in the polymer matrix is indispensable, *e.g.,* the evaporation rate of the solvent and its dependence on the solutes, the GFA of the drug compound and possible interactions between API-polymer, API-solvent and polymer-solvent.

The identification of additional solvent selection criteria is not only important to choose an appropriate solvent for a specific API-polymer combination, but also to optimize the ASD production process. In this work, both for film casting and spray drying, the same process parameters were employed for every drug-polymer-solvent composition. Although this was necessary to compare the highest drug loadings with one another, it is very likely that the selected parameters were not ideal for every combination. Hence, rational solvent selection and rational process optimization are inextricably linked. For instance, when for a specific solvent the evaporation rate is too low, the inlet temperature of the spray drying process might be increased to achieve a faster evaporation process and thereby possibly a higher drug loading could be kinetically stabilized.

Moreover, this might also have implications for the physical stability of ASDs. It is possible that the solvent that enables kinetic stabilization of higher drug loadings, is also capable of maintaining it for a longer period of time. As physical stability issues are inherent to ASDs, this could be an important factor for the ASD production process and will therefore be the subject for further investigations.

4.5. CONCLUSION

From the crystallization tendency study, NAP and IMC were defined as a GFA Class I and Class III drug, respectively. Their crystallization behavior was independent of the solvent. In a next step, the solubilities of PVPVA and the four model compounds in the seven solvents were established. From this, it was found that EtAc was a poor solvent for PVPVA, while all others could be defined as good ones. Generally, the addition of 2.5%, 5%, 7.5% or 9% w/V PVPVA did not alter the solubility trend observed for the pure drugs. For NAP and IMC, the thermodynamic solubility kept increasing with higher PVPVA concentrations, indicating that the maximal solubility enhancement was not yet achieved. The addition of 5% w/V PVPVA let to an optimal solubility increase for FNB and DZP, except for the solubility of DZP in DCM, where 2.5% w/V was more beneficial.

The solvent had a decisive impact on the physical state of all film casted ASDs. More specifically, the solvent determined the highest drug loading that could be formulated in a completely X-ray amorphous state. Moreover, there was no ideal solvent for the formulation of high drug loaded ASDs of PVPVA. It became clear that the role of the solvent was not only dependent on the interaction potential between API and polymer, but also on other physicochemical API characteristics, such as the GFA of the drug compound. Interestingly, although spray drying enabled the production of higher drug loaded ASDs, the same trend as for film casting was observed for NAP, FNB and DZP. Accordingly, the predictive value of film casting for the impact of the solvent on the phase behavior of ASDs was demonstrated. In contrast to this, the effect of the solvent on the homogeneity of the spray dried ASDs of IMC was nullified by the faster evaporation process. This could be related to an interplay between the lower crystallization tendency of IMC, its possibility to form hydrogen bonds with PVPVA and the increased evaporation rate of the spray drying process. Ultimately, it was clear that the contribution of the solvent to the phase behavior was codependent on the evaporation rate, the interactions between the API and polymer and the crystallization tendency of the API.

Furthermore, there was no relation between the thermodynamic solubilities of the API compounds and the phase behavior of the ASDs as obtained by either film casting or spray drying. These results proved that the role of the solvent exceeds its solvent power, and thereby the need for rational solvent selection becomes clear. Currently, solvent criteria are generally limited to finding a good solvent for all constituents, and having an acceptable volatility, toxicity, and viscosity. To identify additional criteria that should be considered, further research to establish the importance of the solvent evaporation rate and the relation between the characteristics of the feed solution (interactions between solvent-polymer-API) and the microstructure of the resulting ASD are indispensable. Moreover, the role of kinetics next to thermodynamics for the formulation of high drug loaded ASDs

was highlighted. Here, the efficiency of kinetic trapping was dependent on both the solvent and API compound. It should be noted that all reported drug loadings were defined immediately after preparation and therefore it is possible that the samples crystallize over time until their thermodynamic solid solubility limit is reached. However, the extent to which supersaturation of the drug compound in the polymer matrix was attained, was clearly dependent on the solvent. Ultimately, the contribution of the solvent to phase behavior of ASDs should not be underestimated.

Acknowledgements

Het Fonds voor Wetenschappelijk Onderzoek Vlaanderen (FWO) and Laboratoires SMB are acknowleged for their support.

Chapter 5

The impact of the solvent on the physical stability of spray dried amorphous solid dispersions of fenofibrate

5.1. ABSTRACT

The physical instability of Amorphous Solid Dispersions (ASDs) remains a challenge for their production. In spite of the extensive research that has been performed on factors that could influence the physical state of ASDs over time, limited research describes the potential influence of the solvent used during the manufacturing process on the physical stability. However, the vast majority of manufacturing techniques for ASDs are solvent based methods, from which spray drying is most widely applied. In this work, the influence of seven single organic solvents on the physical stability of spray dried ASDs of fenofibrate (FNB) was established. For this purpose, three batches containing 10 wt% FNB and poly(vinylpyrrolidone-co-vinyl acetate) (PVPVA) were prepared using every solvent and stored at 25 °C and 53% RH for 6 weeks. Every week, all samples were analyzed using both modulated Differential Scanning Calorimetry (mDSC) and X-Ray Powder Diffraction (XRPD). It became evident that the solvent determined the crystallization onset of these ASDs of FNB, with batches prepared with methanol (MeOH) having the poorest physical stability and the ones made with ethyl acetate (EtAc) having the best. Moreover, the time at which the presence of a crystalline FNB fraction was first detected, could be related to the maximum amount of FNB that could be kinetically stabilized in the PVPVA matrix. In conclusion, the solvent did not only determine the amount of API that could be kinetically trapped in the polymer, but it also impacted the stability of these spray dried ASDs of FNB over time.

5.2. INTRODUCTION

Despite the fact that several ASDs have successfully reached the market, the physical instability of the amorphous compounds remains a challenge for their production. Both during processing and storage (temperature and humidity stress) the amorphous drug may undergo crystallization[186]. Several factors could influence the ease of nucleation and subsequent crystal growth in ASDs: glass transition temperatures (T_g) of drug and polymer, drug-polymer miscibility, solid solubility of the drug in the polymer, drug-polymer interaction, Glass Forming Ability (GFA) of the drug, the storage environment and the manufacturing process[52]. Numerous studies have been performed to investigate the significance of these factors. For instance, the success rate of different polymers (with different T_gs) for the crystallization inhibition might differ[187]. The effect of a high humidity (storage conditions) on phase separation was for example explored in spin-coated films of felodipine and polyvinylpyrrolidone (PVP) K29/32 by Qi et al[188]. Moreover, both the influence of the polymer type and a high humidity have been successfully predicted using Perturbed-Chain Statistical Associated Fluid Theory (PC-SAFT)[145]. Also the impact of downstream processing by tableting of ASD powders should not be underestimated: demixing of naproxen and PVP K25 upon compression has been described in literature[189]. Additionally, the importance of hydrogen bonding for the physical stability has been shown by Huang et al. for ASDs of nifedipine and ethylcellulose/Eudragit RL®[190]. However, hydrogen bonds between API and polymer are no requirement for a profitable effect of the polymer on the formation of nuclei. The importance of the anti-plasticizing effect of the polymer, the increased viscosity and thereby the inhibition of the diffusion of drug molecules for the prevention of crystallization has been described by Van den Mooter et al. for ASDs of ketoconazole and PVP K25, where no hydrogen bonding between these components was present[64].

As most manufacturing techniques for ASDs are solvent based methods, such as spray drying and fluid bed bead coating, the selection of an (organic) solvent to dissolve both the drug and its carrier is required. This solvent could be another factor that could potentially influence the phase behavior of ASDs over time and thereby the shelf life of ASDs. To exemplify, Zhang et al. investigated the effect of acetone (Ac) and Ac/water binary solutions on the physical stability of ASDs of enzalutamide and hydroxypropylmethylcellulose acetate succinate (HPMC-AS)[191]. Here, the addition of a small fraction of water reduced the hydrodynamic radius of HPMC-AS, making it more available for interaction with the drug, which was in turn beneficial for the physical stability of the ASDs. Likewise, Chen et al. demonstrated that the combined use of a polar protic solvent like ethanol (EtOH), and a non-polar one like dichloromethane (DCM), resulted in a better physical stability compared to the use of a single solvent for ASDs of felodipine and Soluplus[192]. Although these findings are of utmost importance for

the future of ASD production by solvent based methods, a deeper understanding of the impact of single solvents on the physical stability is needed before advancing to the complexity of using binary solutions.

In this study, the influence of single solvents on the physical stability of ASDs prepared by spray drying was investigated. Seven solvents were selected based on their volatility (*i.e*., boiling point) as a measure of the non-covalent interactions, and polarity (*i.e.,* dielectric constant, ε): methanol (MeOH), EtOH, isopropanol (PrOH), acetonitrile (ACN), Ac, DCM, and ethyl acetate (EtAc). In Chapter 4, it was already shown that the impact of these solvents on the physical structure of ASDs of fenofibrate (FNB), naproxen (NAP), indomethacin (IMC) and diazepam (DZP) was not limited to the solvent power. The solvent determined the extent to which kinetic stabilization was achieved. Following this, the correlation between the highest drug loading that could be kinetically stabilized using a specific solvent and the physical stability of ASDs prepared using the same solvent was investigated. As the impact of the solvent on the physical structure was most pronounced for ASDs of FNB and poly(vinylpyrrolidone-co-vinyl acetate) (PVPVA), where the highest drug loadings ranged from 5 wt% when using MeOH to 25 wt% using Ac or EtAc, this non-interacting model system was selected for the physical stability study. For all solvents, the same drug loading was prepared, *i.e.,* 10 wt%, and stored at mild conditions, namely 25 °C and 53% RH. As will be described in Chapter 7, it was indispensable to employ both X-Ray Powder Diffraction (XRPD) and modulated Differential Scanning Calorimetry (mDSC) for the solid-state characterization of ASDs of FNB.

5.3. MATERIALS AND METHODS

5.3.1. Materials

Fenofibrate (FNB) (PubChemCID: 3339) was obtained from Hangzhou Dayangchem Co. (Hangzhou City, China). Poly(vinylpyrrolidone-co-vinyl acetate) 64 (PVPVA64, Kollidon® VA64) (PubChem CID: 270885) was supplied by BASF® ChemTrade GmbH (Ludwigshafen, Germany).

Acetone (Ac) (≥ 99%) was purchased from VWR Chemicals (Leuven, Belgium) and methanol (MeOH) (≥ 99.8%) from ACROS Belgium (Geel, Belgium). Both dichloromethane (DCM) (≥ 99.5%) and acetonitrile (ACN) (≥ 99.9%) were supplied by Fisher Scientific (Loughborough, UK). Chem-Lab Analytical (Zedelgem, Belgium) provided denaturated ethanol (EtOH) (≥ 99%, from which 3% V/V diethylether). Ethylacetate (≥ 99.5%) and magnesium nitrate hexahydrate were purchased from Sigma-Aldrich (Brussels, Belgium). Carl Roth GmbH supplied the 2-propanol (PrOH) (≥ 99.9%). Both acetic acid and sodium acetate were received from VWR Chemicals (Leuven, Belgium). Water was de-ionized using a Maxima system (Elga Ltd., High Wycombe Bucks, UK). All materials were used as received.

5.3.2. Manufacturing of amorphous solid dispersions by spray drying

FNB and PVPVA were dissolved together in one of seven solvents (*i.e.,* MeOH, EtOH, PrOH, ACN, Ac, DCM or EtAc) at a solid content of 10% w/V. The ratio of drug to polymer was kept constant at 10 wt% FNB. Spray drying of these solutions was performed using a Büchi mini spray dryer B-190 (Büchi, Flawil, Switzerland). The atomization air flow rate was installed at 10 L/min, the feed rate at 5 mL/min (which was adapted to the solvent used), the drying air flow rate at 33 m^3/h and its temperature at the boiling point of the respective solvent. Afterwards, the spray dried powders were further dried in a vacuum oven (Mazzali Systems, Monza, Italy) for 4 days at 25 °C. Subsequently, their solid-state properties were investigated by performing both mDSC and XRPD, after which the physical stability study was started.

5.3.3. Physical stability testing of amorphous solid dispersions

Three batches were manufactured for every condition to explore the inter-batch variability. After secondary drying, the samples were immediately analyzed and further stored at 25 °C and 53% RH, which was installed using a saturated solution of magnesium nitrate hexahydrate. For a time period of 6 weeks, the physical structure was characterized every week using both XRPD and mDSC, from which the latter was performed in duplicate. Only batches prepared using EtAc were further evaluated up until 9 weeks.

5.3.4. Solid-state characterization of amorphous solid dispersions

5.3.4.1. Modulated differential scanning calorimetry (mDSC)

A Q2000 mDSC (TA instruments, Leatherhead, UK) was employed to investigate the thermal behavior of the spray dried ASDs. It was equipped with a dry nitrogen purge at 50 mL/min and a Refrigerated Cooling System (RCS90). The calibration for temperature and enthalpy was performed with indium standards, while calibration for heat capacity was performed using sapphire standards. To analyze the samples, an amount of 1 to 5 mg was accurately weighed into aluminum DSC pans (TA instruments, Zellik, Belgium) and then crimpled with the corresponding lids (TA instruments, Zellik, Belgium). The samples were heated from -20 °C to 140 °C using a combination of a linear heating rate of 2 °C/min with a modulation amplitude of 0.212 °C and a period of 40 s. The resulting thermograms were analyzed using the Universal Analysis software (Version 5.5, TA Instruments, Leatherhead, UK).

5.3.4.2. X-ray powder diffraction (XRPD)

The physical structure at Room Temperature (RT) was investigated using an X'Pert PRO diffractometer (PANalytical, Almelo, the Netherlands) with a Cu tube (Kα λ = 1.5418 Å) and its generator installed at 45 kV and 40 mA. Approximately 10 mg of sample was placed between two Kapton® Polyimide Thin-Films (PANalytical, USA) and subsequently analyzed by continuously scanning from either 10 to 25 °2θ. The counting time was installed at 800 s, step size at 0.0167° and the spinning was set at 4 s. The resulting diffractograms were analyzed using the X'Pert Data Viewer (Version 1.9a, PANalytical, Almelo, the Netherlands).

5.3.4.3. Thermogravimetric analysis (TGA)

The amount of residual solvent in the spray dried samples was determined using a thermogravimetric analyzer TGA 550 (TA instruments, Leatherhead, UK). For this, approximately 5 to 10 mg of the sample was weighed in a platinum HT pan (TA instruments, Zellik, Belgium) and heated by applying a linear heating rate of 5 °C/min to 130 °C. The recorded weight loss in function of time was attributed to solvent evaporation, which was deducted using the Universal Analysis software (Version 5.5, TA instruments, Leatherhead, UK). Univariate one-way ANOVA, Tukey *post hoc* tests (α = 0.05) were applied to evaluate the significant difference in amount of residual solvent depending on the solvent used during the spray drying process.

5.3.5. High performance liquid chromatography coupled with ultraviolet detection (HPLC-UV)

The FNB content of all spray dried batches was determined in triplicate by HPLC-UV analysis using a VWR HITACHI Chromaster System (5160 pump, 5260 autosampler, 5310 column and 5410 UV-detector) equipped with a Nucleodur C_{18} Gravity 5 µm column (150 mm x 4.6 mm) (Macherey-Nagel, Düren, Germany). Data was acquired with the Chromaster System Manager Software (version 1.1). An isocratic method using an acetate buffer (25 mM, pH 3.50) with ACN (15/85 V/V) was used at a flow rate of 1 mL/min. The detection wavelength was installed at 290 nm and the retention time of FNB was 5 min. The acetate buffer was filtered through a cellulose acetate filter (0.45 µm) (Sartorius Stedim Biotech GmbH, Göttingen, Germany) and sonicated for 30 min before use. The linearity of the method was validated ($R^2 > 0.995$) and the limit of detection (LOD) and the limit of quantification (LOQ) were calculated from the signal to noise ratios. The LOD was established at 0.015 µg/mL and the LOQ at 0.049 µg/mL.

5.4. RESULTS AND DISCUSSION

5.4.1. Solid-state characterization at timepoint zero

As mentioned in Chapter 4, the highest amount of FNB that could be kinetically stabilized in PVPVA by spray drying ranged from 5 wt% when MeOH was used to 25 wt% in case of Ac or EtAc. In this study, the same drug loading of 10 wt% FNB was formulated in triplicate for all solvents, which was above the highest drug loading for MeOH and yet below that for all other solvents. This drug loading was selected because a lower drug loading of 5 wt% would make it even harder to detect the onset of crystallization during the physical stability study.

Before the start of the stability study, all samples were characterized using XRPD, mDSC, TGA and their FNB content was established. The assay assured the presence of approximately 10 wt% FNB for all batches (Table 5.1.). Furthermore, TGA was performed to determine the amount of residual solvent, as it could negatively impact the stability of the systems (Table 5.2.). The DCM samples contained significantly more residual solvent than the ACN and EtAc ones ($p < 0.05$). The EtAc batches also included significantly less residue than the Ac and PrOH batches ($p < 0.05$). There was also a significant difference between the ACN and PrOH batches ($p < 0.05$), with the ACN ones containing less residual solvent after secondary drying. Despite the fact that these differences were significant, the amount of residual solvent for all batches was in the same range, with a maximum difference of 1.47 wt% of solvent.

Table 5.1. *Amount of FNB present in the spray dried formulations (wt%) ± standard deviation (sd)*

Batch	MeOH	EtOH	PrOH	ACN	Ac	DCM	EtAc
1	10.41 ± 0.14	10.30 ± 0.17	10.17 ± 0.25	10.25 ± 0.17	10.27 ± 0.11	10.44 ± 0.06	10.42 ± 0.05
2	10.62 ± 0.05	10.63 ± 0.03	10.14 ± 0.16	10.48 ± 0.08	10.35 ± 0.25	10.31 ± 0.07	10.43 ± 0.05
3	10.59 ± 0.12	10.58 ± 0.07	10.36 ± 0.03	10.11 ± 0.12	10.42 ± 0.06	10.41 ± 0.01	10.56 ± 0.04

Table 5.2. *Residual solvent of spray dried formulations of FNB (wt%) as determined by TGA analysis*

Batch	MeOH	EtOH	PrOH	ACN	Ac	DCM	EtAc
1	3.231	3.313	3.659	3.144	3.566	4.180	3.170
2	3.627	3.584	3.70	3.110	3.480	3.610	2.710
3	3.491	3.453	3.794	3.097	3.650	3.690	3.080

In Fig 5.1., the results from the mDSC (Fig 5.1A, B) and XRPD analysis (Fig 5.1C) at timepoint zero, *i.e.,* immediately after secondary drying, are depicted. An isothermal preheating step of 60 min at 60 °C

was included before the start of the mDSC analysis, which was required to evaporate residual solvent to distinguish the presence of a possible melting event of FNB (see Chapter 7). It should be noted that the isothermal preheating step could give rise to thermal alterations, hence, the mDSC analysis was always performed using an identical method. All samples showed a single T_g in mDSC analysis, although it was slightly lower and broader for DCM and Ac, indicating increased heterogeneity (Fig 5.2.). This difference in uniformity could not be related to a difference in residual solvent content (Table 5.2.). In the total heat flow, there were no melting events detectable (Fig 5.1B). Nevertheless, from Fig 5.1C, it is clear that Bragg peaks were present for MeOH, demonstrating that the sample was partially crystalline. Hence, XRPD was more sensitive for detecting the presence of crystalline traces of FNB.

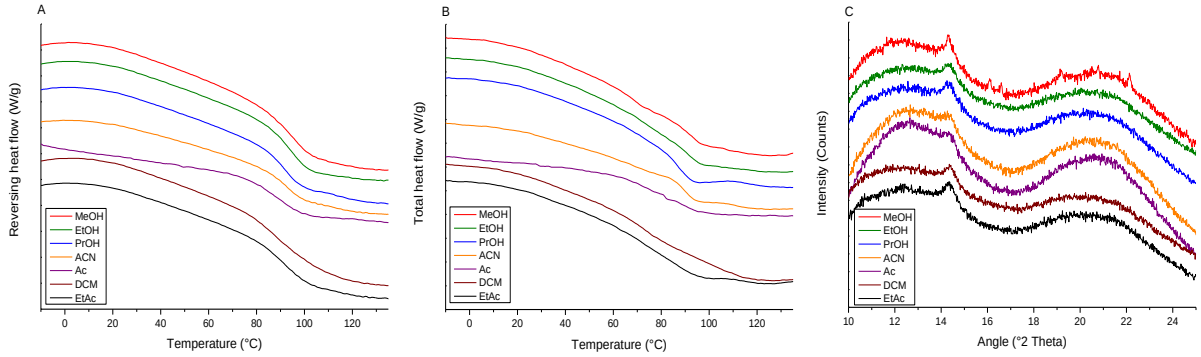

Figure 5.1. *Solid-state characterization of spray dried 10 wt% FNB and PVPVA at timepoint zero of the physical stability study. From the mDSC analysis, both the reversing heat flow (A) and total heat flow (B) are depicted with all exothermic signals directed upwards, together with the corresponding XRPD diffractograms (C). In all cases, one analysis per solvent is shown: MeOH (red), EtOH (green), PrOH (blue), ACN (orange), Ac (purple), DCM (brown) and EtAc (black).*

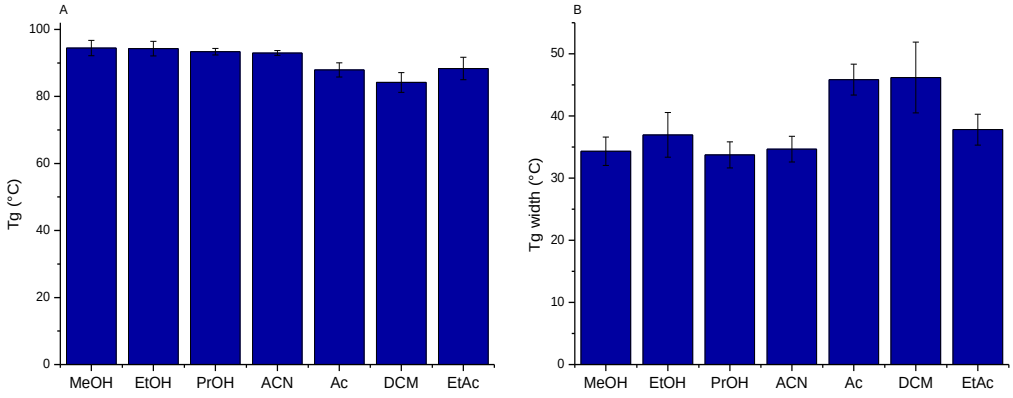

Figure 5.2*. Average Tg (A) and T_g width (B) of 10 wt% FNB batches prepared with different solvents as determined by mDSC analysis. The averages were calculated based on 3 batches and 2 analyses per batch for every condition.*

5.4.2. Physical stability testing

All spray dried ASDs were stored at 25 °C and 53% RH and weekly monitored using both mDSC and XRPD. After 1 week, XRPD reflections were not only present in the diffractograms of the MeOH samples, but could also be detected at 22 °2θ for EtOH, whereas all other ASDs remained X-ray amorphous (Fig 5.3., t1). After one more week, Bragg peaks could be identified for PrOH, ACN and DCM, rendering only Ac and EtAc batches X-ray amorphous (Fig 5.3., t2). In case of Ac, the samples started to crystallize after 3 weeks, while for EtAc, the first Bragg peak could only be observed at 22 °2θ after 6 weeks (Fig 5.3., t5, t6).

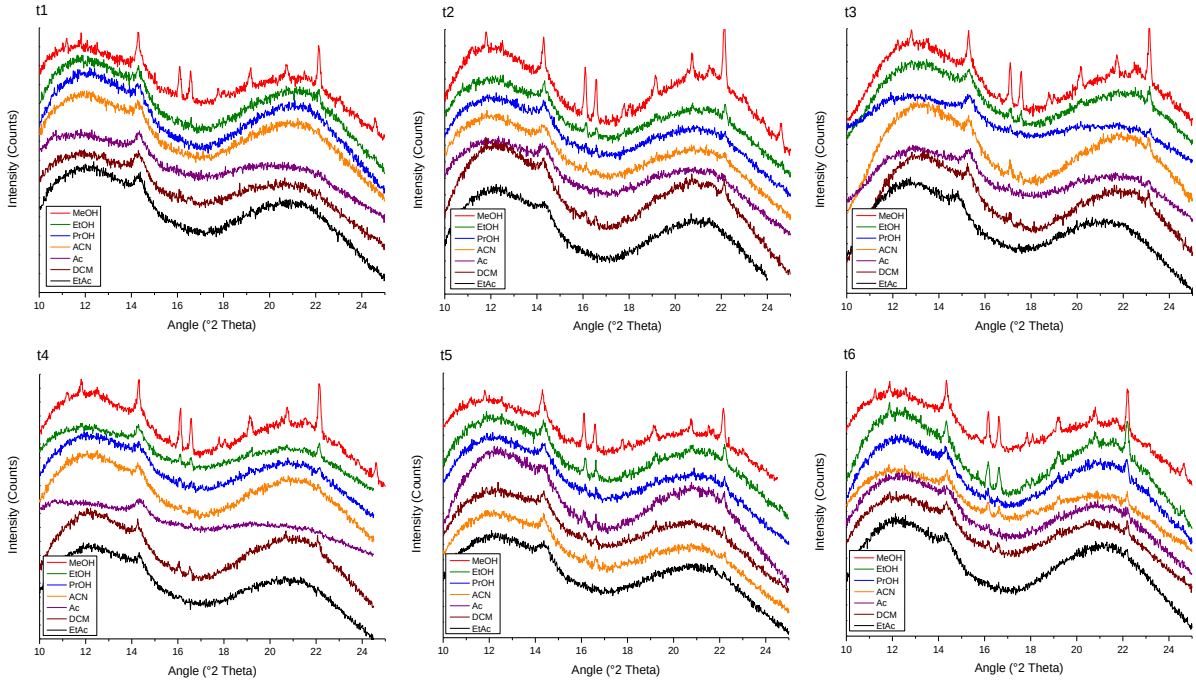

***Figure 5.3**. Weekly XRPD diffractograms from the physical stability study of spray dried 10 wt% FNB with PVPVA. The same color code was applied in all figures: MeOH (red), EtOH (green), PrOH (blue), ACN (orange), Ac (purple), DCM (brown) and EtAc (black).*

These findings were supported by the mDSC analysis, where an endothermic event, corresponding to the melting of FNB (ca. 77.30 °C), could be distinguished in the total heat flow for both MeOH and EtOH after 1 week (Fig 5.4., t1). The amount of crystalline material could not be deduced from this mDSC analysis due to coinciding of the T_g with the melting of FNB. For instance, in case of the ASD prepared using EtOH, a T_g of 93.37 °C with a T_g width of 48.82 °C overlapped with the endothermic melting event of FNB at 77.30 °C. Hence, not only the solvent evaporation endotherm, but also the positioning of the T_g impeded the detection of a possible endothermic melting event of FNB. Although an isothermal preheating step was included in the mDSC analysis, XRPD showed to be more trustworthy for the detection of crystalline material in these ASDs. After storage for three weeks at 25 °C and 53% RH, an

endothermic melting event was also observed for ASDs prepared using ACN and PrOH, yet not for the ones prepared with DCM, Ac and EtAc (Fig 5.4., t3). The same results were obtained after 6 weeks, demonstrating that there was relatively less FNB crystallized in the batches prepared using Ac, DCM and EtAc (Fig 5.4., t6). Nevertheless, the ASDs prepared using DCM already showed Bragg peaks in their XRPD analysis after 2 weeks and the ones formulated with Ac after 3 weeks. Although mDSC is generally more sensitive for small traces of crystalline material, it has been shown several times in this work that XRPD was a more sensitive approach to detect a crystalline fraction of FNB. Moreover, XRPD was applied in a qualitative manner, hence, the amount of crystalline FNB could still be relatively less in batches spray dried using Ac, DCM, EtAc compared to the ones made with MeOH, EtOH, PrOH and ACN.

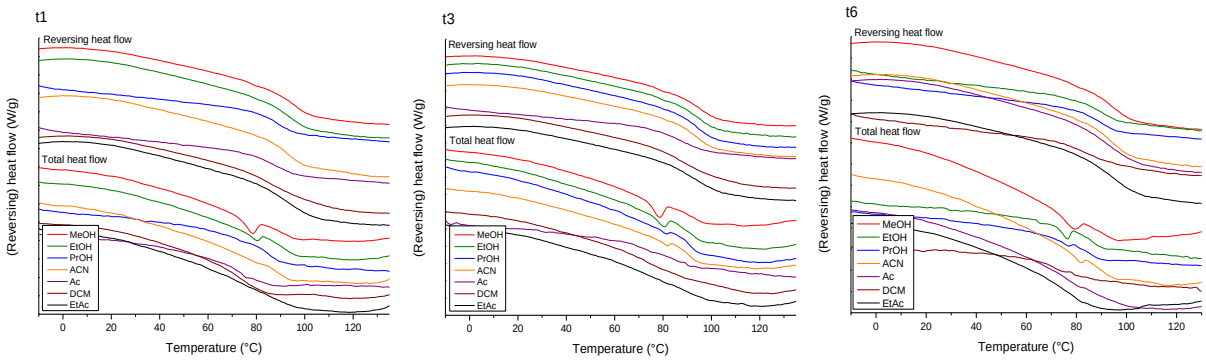

Figure 5.4*. mDSC thermograms from the physical stability study of spray dried ASDs of 10 wt% FNB and PVPVA. Timepoints 1 week, 3 weeks and 6 weeks are shown. Both the reversing and total heat flow are depicted, and the exothermic signals are directed upwards. The color code was as follows: MeOH (red), EtOH (green), PrOH (blue), ACN (orange), Ac (purple), DCM (brown) and EtAc (black).*

As the occurrence of XRPD reflections was not very clear after 6 weeks for the ASDs made using EtAc, these batches were evaluated further up until 9 weeks. Although detected after 6 weeks at 22 °2θ, there were no Bragg peaks detected after 7 weeks, which shows that the amount of crystalline material was close to the detection limit of the XRPD method (Fig 5.5., A). After 8 and 9 weeks, it was clear that there were Bragg peaks present and hence, that the ASDs were partially crystalline (Fig 5.5., A). However, from 6 to 9 weeks, there was no clear increase in the intensity of the XRPD reflections, which might demonstrate that the crystallization rate was relatively low. These results were in good agreement with the ones obtained by mDSC analysis, where there was no melting event detected in the total heat flow after 7 weeks, but after 8 and 9 weeks there was a small endothermic event visible, which originated from the melting of crystalline FNB (Fig 5.5., B).

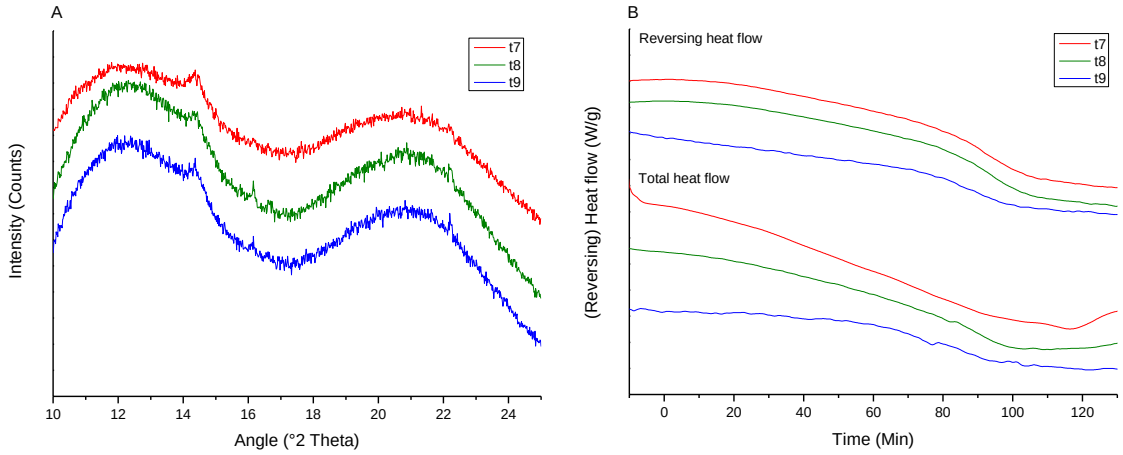

***Figure 5.5**. XRPD diffractograms (A) and mDSC thermograms (B) from the physical stability study of 10 wt% FNB and PVPVA spray dried with EtAc. The EtAc batches were further evaluated after 7 weeks (red), 8 weeks (green) and 9 weeks (blue). For the mDSC analysis, both the reversing and the total heat flow are shown, and exothermic signals are directed upwards.*

The previous XRPD and mDSC results only reported one analysis per solvent, however, there were 3 batches spray dried using every solvent, which were each analyzed by XRPD. Accordingly, the repeatability of the influence of the solvent on the physical stability could be evaluated. For instance, Fig 5.6. shows all diffractograms that were obtained after 3 weeks of storage at 25 °C and 53% RH. Here, all diffractograms contained Bragg peaks, except for the ones spray dried with EtAc, demonstrating the repeatable impact of the solvent on the phase behavior of these ASDs of FNB. Only in case of ACN, one of three diffractograms appeared to be an amorphous halo, which might be related to the different shape of the halo. Generally, batches manufactured using the same solvent showed the same crystallization onset. Ultimately, the contribution of the solvent to the physical stability of these ASDs of FNB was repeatable.

Hence, despite the fact that all batches existed out of a single amorphous phase at timepoint zero (except for MeOH), the solvent used during spray drying determined the crystallization onset of the ASDs during storage, where the highest stability was found for batches spray dried using EtAc. Although the ASDs spray dried with EtAc contained a relatively low amount of residual solvent (Table 5.2.), the amount of residue in these batches was not significantly different from that in all ASDs prepared with other solvents and could therefore not explain the improved physical stability of these ASDs.

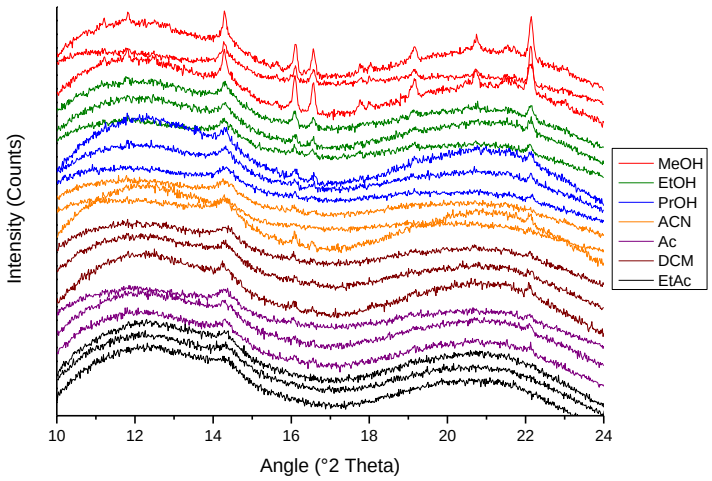

***Figure 5.6**. XRPD diffractograms of spray dried 10 wt% FNB and PVPVA after 3 weeks at 25 °C and 53% RH. Every diffractogram was the result of the XRPD analysis of one batch prepared using MeOH (red), EtOH (green), PrOH (blue), ACN (orange), DCM (brown), Ac (purple) and EtAc (black).*

In spite of the repeatable influence of the solvent on the crystallization behavior, all samples were partially crystalline after 6 weeks at 25 °C and 53% RH, thereby not having a viable shelf life. Hugo et al. reported a longer stability period of 3 months at 25 °C and 60% RH for 25 wt% FNB and PVPVA spray dried with EtOH, however, only mDSC without an isothermal preheating step was employed, which might give rise to a lower sensitivity limit for small traces of crystalline material[166]. If only mDSC would have been employed in this physical stability study, the impact of the solvent on the crystallization onset of the ASDs would have been overlooked. Accordingly, this highlights the importance of using more than one analytical technique for the solid-state characterization of ASDs (see Chapter 7). Moreover, implementation of another manufacturing method than spray drying might also give rise to ASDs of FNB with a better physical stability. For instance, Theil et al. successfully employed hot melt extrusion to formulate ASDs of 15 wt% FNB and PVPVA in which there was no relevant amount of recrystallization detected after a time period of 15 years under ambient conditions[193]. Also, another polymer could be beneficial for the physical stability. To exemplify, the influence of different molecular weight of PVP on the stability of FNB ASDs prepared by hot melt extrusion was investigated, where the lower molecular weight polymer was superior[194]. Also thin film freezing with HPMC and HPMC-AS in a 1:6 w:w FNB:polymer ratio resulted in a better phase behavior over time. After 3 months at 40 °C and 75% RH there was still no crystalline FNB fraction detected [195]. Notwithstanding the potential of other manufacturing techniques and/or other carriers to stabilize FNB for a longer period of time in its amorphous state, the influence of the solvent used during spray drying to the physical stability of ASDs of FNB could be of utmost importance for optimization of an ASD formulation.

5.4.3. Correlation between physical stability and highest drug loadings

It is especially important that the results from this short-term physical stability study could be related to the highest drug loadings as obtained by spray drying (see Chapter 4). When a higher drug loading could be formulated as a single amorphous phase using a specific solvent, the same solvent resulted in a formulation that was stable for a longer period of time. Hence, although a lower drug loading than the maximum one was produced (except MeOH), the solvent was the determinative factor for the physical stability of the formulation. In Fig 5.7., the highest drug loading (green), the timepoint at which the first crystal peaks were detected in XRPD analysis (red) and a saturation level (blue), describing the difference between the selected drug loading of 10 wt% FNB and the maximum amount of FNB that could be kinetically stabilized in PVPVA using the respective solvent, are depicted. This saturation level was calculated as follows:

$$\%\ Saturation\ of\ highest\ drug\ loading\ = \left(\frac{10\ wt\%}{Higest\ drug\ loading\ wt\%}\right) \times 100 \qquad \textit{Equation 5.7.}$$

Here, the highest drug loading is the one that was previously reported in Chapter 4, ranging from 5 wt% for MeOH to 25 wt% for Ac and EtAc. The lower this saturation level was, the earlier a crystalline fraction was detected in the XRPD analysis.

For instance, using PrOH, ACN and DCM, 20 wt% was established as the highest drug loading (*i.e.,* a saturation level of 50% was reached), and the first Bragg peaks were detected after 2 weeks during the stability study of the 10 wt% (Fig 5.7.). Nevertheless, EtOH also allowed the production of drug loadings as high as 20 wt%, but showed to be less stable (*i.e.,* 1 week) than PrOH, ACN and DCM did. As the maximum drug loadings were established using intermediate steps of 5 wt%, it might be that 20 wt% was the upper limit for EtOH, whereas the other three would also allow the production of higher drug loadings in between 20 and 25 wt%. Ac and EtAc enabled the production of higher drug loadings (*i.e.,* 25 wt% and a saturation level of only 40% was reached) and gave rise to ASDs with a better physical stability (*i.e.,* 3 weeks for Ac and 6 weeks for EtAc). The difference in crystallization onset when using Ac or EtAc might again be explained by the screening approach for the highest drug loadings. Possibly, 25 wt% was the upper limit in case of Ac, while drug loadings in between 25 and 30 wt% could also be kinetically stabilized in PVPVA using EtAc as a solvent. As it was only possible to formulate 5 wt% as a single phase using MeOH, all 10 wt% batches were already crystalline at timepoint zero. The relation between the highest drug loadings and the physical stability demonstrated that the solvent had an impact on both the efficiency of kinetic trapping and the kinetic stability of the ASDs. Hence, these results emphasized the important contribution of kinetic factors next to thermodynamic ones to the physical state of ASDs.

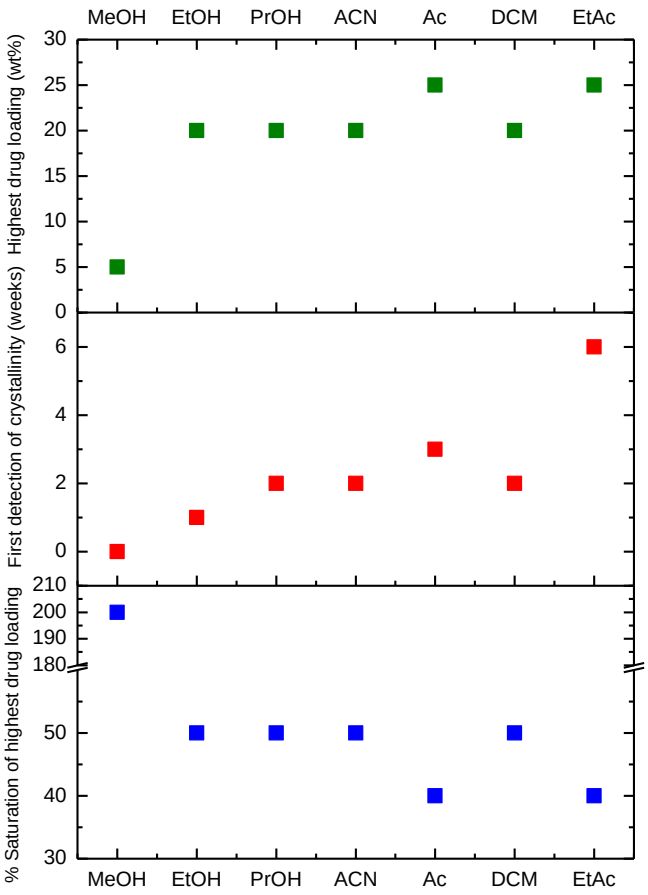

Figure 5.7. *Correlation between the highest drug loading of FNB that could be kinetically stabilized in PVPVA (green), the timepoint at which the first crystal peaks were detected in the XRPD analysis (red) and the degree of saturation of the maximum drug loading that was obtained when preparing ASDs of 10 wt% (blue).*

5.5. CONCLUSION

In this chapter, the decisive impact of the solvent used during spray drying on the physical stability of ASDs of FNB was demonstrated. Three batches containing 10 wt% FNB and PVPVA were spray dried with seven different organic solvents and stored at 25 °C and 53% RH. Immediately after spray drying, the batches prepared with MeOH already contained a crystalline FNB fraction, while the ones made with EtOH crystallized after 1 week, followed by the ones prepared with PrOH and ACN after 2 weeks of storage. After one more week, also the ASDs manufactured with Ac showed Bragg peaks in their XRPD analysis, while the ones prepared with EtAc remained X-ray amorphous up until 6 weeks. This influence of the solvent on the crystallization onset was found to be repeatable. Moreover, the time at which the first crystal peaks were detected in the XRPD analysis during this physical stability study could be related to the highest amount of drug that could be kinetically stabilized in the PVPVA matrix. Thus, the solvent did not only determine the amount of drug that could be kinetically trapped in the polymer, but it also determined the stability over time. Ultimately, a deeper understanding of the contribution of the solvent to the physical state (and thereby physical stability) is required to optimize the kinetic stability of ASDs.

Acknowledgements

The authors would like to thank Danny Winant (Materials engineering, KU Leuven) for his technical assistance. Het Fonds voor Wetenschappelijk Onderzoek Vlaanderen (FWO) and Laboratoires SMB are acknowlegded for their support.

Chapter 6

Gaining insight in the role of the solvent during spray drying of amorphous solid dispersions by studying evaporation kinetics and interactions in solution

The revised version of this Chapter has been submitted to Molecular Pharmaceutics

6.1. ABSTRACT

Spray drying is one of the most commonly used manufacturing techniques for Amorphous Solid Dispersions (ASDs). During spray drying, very fast solvent evaporation is enabled by the generation of small droplets and exposure of these droplets to a heated drying gas. This fast solvent evaporation leads to an increased viscosity that enables kinetic trapping of an Active Pharmaceutical Ingredient (API) in a polymer matrix, which is favorable for the formulation of supersaturated, kinetically stabilized ASDs. In this work, the relation between the solvent evaporation rate and the kinetic stabilization of highly drug loaded ASDs was investigated. Accordingly, Thermal Gravimetric Analysis (TGA) was employed to study the evaporation kinetics of seven organic solvents and the influence of solutes, *i.e.,* poly(vinylpyrrolidone-*co*-vinyl acetate) (PVPVA), fenofibrate (FNB) and naproxen (NAP), on the evaporation behavior. At 10 °C below the boiling point of the respective solvent, methanol (MeOH) had the lowest evaporation rate and dichloromethane (DCM) the highest. PVPVA decreased the evaporation rate for all solvents, yet this effect was more pronounced for the relatively faster evaporating solvents. The APIs had opposite effects on the evaporation process: FNB increased the evaporation rate, while NAP decreased it. The latter might indicate the presence of interactions between NAP and the solvent or NAP and PVPVA, which was further investigated using fourier transform – infrared (FT-IR) spectroscopy. Based on these findings, spray drying process parameters were adapted to alter the evaporation rate. Increasing the evaporation rate of MeOH and DCM enabled the kinetic stabilization of higher drug loadings of FNB, while the opposite trend was observed for ASDs of NAP. Here, the difference between the T_g and the outlet temperature (T_{out}) was determinative for the physical state. Even when higher drug loadings could be kinetically stabilized by adapting the process parameters, the improvement was limited, demonstrating that the phase behavior of these ASDs of FNB and NAP was predominantly determined by the API-polymer-solvent combination rather than the process parameters applied.

6.2. INTRODUCTION

Spray drying is widely applied for the manufacturing of Amorphous Solid Dispersions (ASDs), which are molecular dispersions of an amorphous Active Pharmaceutical Ingredient (API) in a polymer matrix at solid state[61]. The spray drying procedure starts with dissolving the API together with its carrier in a common solvent, which is subsequently atomized into droplets inside the drying chamber, where heat is transferred towards the droplet surface and solvent evaporation occurs. The very fast solvent evaporation gives rise to a fast increase in viscosity, which is a critical factor for kinetic trapping of an API in a polymer matrix and might result in kinetic stabilization of supersaturated molecular dispersions[38]. Generally, the higher the solvent drying rate, the higher the chance at kinetic trapping and thus the formation of supersaturated/highly drug loaded ASDs. Accordingly, it has been reported that the solvent evaporation rate was an even more important factor than the polymer molecular weight and the drug to polymer ratio to decrease the extent of nucleation in ASDs[196].

There are several factors that could influence the drying rate, such as droplet size, physicochemical properties of the solutes, drying gas temperature and especially the type of solvent that is employed[93]. For spray drying, the solvent should measure up to the following criteria: have a common solubilizing capacity for API and polymer (and other additives), an acceptable viscosity, a low toxicity, a high volatility, be non-combustive and the solutes should have an acceptable chemical stability in solution[94]. Although selecting a solvent in which all compounds have a sufficiently high solubility is indispensable, it was found in previous work that the importance of the solubility for the phase behavior of ASDs should not be overestimated[197]. More specifically, the solvent determined the amount of API that could be kinetically stabilized in the poly(vinylpyrrolidone-*co*-vinyl acetate) (PVPVA) matrix, yet there was no relation between this amount and the equilibrium solubility of the API in the respective solvent. Therefore, a molecular level understanding of the interactions between API, polymer and solvent and the resulting physical state of ASDs is of utmost importance to identify additional solvent selection criteria. Accordingly, several authors have been investigating the influence of the solvent on various physicochemical properties of ASDs[120,165–168,198]. In view of the formulation of highly drug loaded ASDs, the impact of the solvent on the evaporation behavior is especially important. The tendency to evaporate*, i.e.,* volatility, is reflected by the boiling point (bp) of a solvent, which is the temperature at which the vapor pressure of the solvent is equal to the atmospheric pressure and thus the temperature at which the liquid will start to vaporize. The higher the bp, the lower the vapor pressure at Room Temperature (RT) and thus the less volatile the solvent will be. Not only the temperature, but also the amount of energy that is required for the liquid to gas transition influences the evaporation behavior, which is represented by the heat of vaporization. Moreover, type and concentration of solutes can also

have an impact on the drying process. The presence of solutes will increase the thermal efficiency of the drying process as there is relatively less solvent present that needs to be evaporated[93]. On the other hand, as the presence of solutes increases the entropy in solution, the vapor pressure will be lower, resulting in an increased bp of the solution compared to the pure solvent. Accordingly, the concentration dependent influence of PVP on the evaporation rate of diverse combinations of methanol (MeOH), acetone (Ac) and dichloromethane (DCM) was demonstrated by Paudel et al[167]. Also Al-Obaidi et al. investigated the evaporation behavior of polymer solutions in Ac/water or Ac/MeOH and related it to the viscosity, polymer conformation and relaxation behavior of ASDs of griseofulvin[198]. Likewise, Mugheirbi et al. studied the impact of the water content on the evaporation behavior of DCM combined with different alcoholic solvents and related it to the physical state of ASDs[199]. Also Na Li et al. demonstrated that the presence of a small fraction of water in the solvent mixture could result in phase separation of ASDs of ritonavir and PVPVA[200]. Moreover, the interplay between the solvent evaporation rate and diffusional motion of the solutes in the specific solvent determines the particle morphology of the spray dried particles[117]. As the relation between solution properties and the particle formation process has been extensively studied[99], this work focused on the influence of the solvent evaporation rate on the kinetic stabilization of highly drug loaded ASDs.

Accordingly, the evaporation kinetics of seven single organic solvents, *i.e.*, MeOH, ethanol (EtOH), isopropanol (PrOH), acetonitrile (ACN), Ac, DCM, and ethyl acetate (EtAc), were investigated by means of Thermal Gravimetric Analysis (TGA). These solvents were selected as it was demonstrated in previous work that their different polarity and volatility could give rise to a diverse phase behavior of ASDs[197]. The influence of solutes on the evaporation behavior was also of interest: PVPVA, fenofibrate (FNB) and naproxen (NAP) and combinations of these APIs with PVPVA were studied. The structural formulas of these compounds can be found in Fig 6.1. NAP was selected as it can hydrogen bond with PVPVA: its carboxylic acid group can act as a hydrogen donor for the carbonyl group of PVPVA[148,149]. In contrast, FNB has no hydrogen bonding potential with PVPVA as it has no hydrogen donor groups[170]. However, it was found that the solvent had a large impact on the physical state of ASDs of FNB, with the maximum amount of drug that could be kinetically stabilized ranging from 5 wt% using MeOH to 25 wt% using Ac/EtAc[197]. Besides the expected effect of the solutes on the vapor pressure, also interactions between API-polymer-solvent could interfere with the evaporation process[167]. From the selected solvents, the alcoholic ones are hydrogen bond donors and acceptors, while Ac and EtAc could only act as hydrogen bond accepting solvents. Hence, the prevalence of API-polymer interactions might depend on the solvent in which they are dissolved, which was investigated using Fourier Transform – InfraRed (FT-IR) spectroscopy. In Fig 6.1., the functional groups for which vibration bands could be detected in the spectral region of 1800 to 1600 cm^{-1} are indicated.

After extensively studying the evaporation kinetics and interactions in solution, the aim of this work was to rationally select new process parameters for spray drying. The potential impact of process parameters on the physical state of ASDs has been extensively described in literature[93,94,99,201–203]. In this study, the parameters were selected in order to adapt the evaporation rate to generate even more supersaturated ASDs. Accordingly, the inlet temperature (T_{in}) was adapted together with the liquid feed rate to modify the droplet size. Ultimately, the kinetic trapping potential was evaluated by demonstrating the potential impact of process optimization on the phase behavior of ASDs of NAP and FNB.

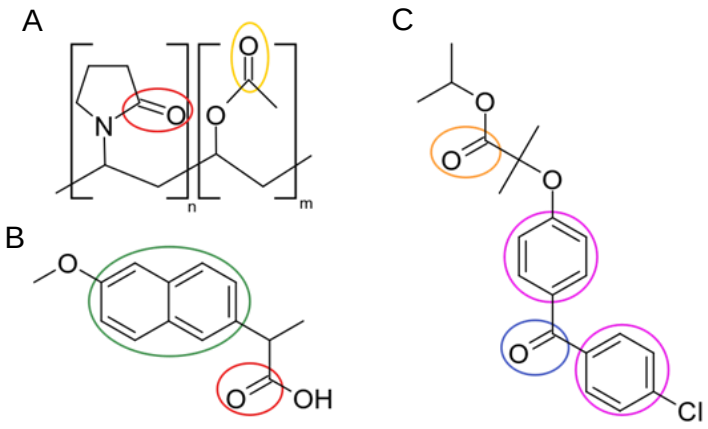

Figure 6.1. *Structural formulas of PVPVA (A), NAP (B) and FNB (C). Both the carbonyl stretching vibration of the vinyl pyrrolidone carbonyl (red) and the vinyl acetate one (yellow) could be detected using FT-IR in the spectral region of 1800 to 1600 cm^{-1} (A). For NAP, the carbonyl stretching vibration (red) and aromatic skeleton stretching (green) could be detected (B). For FNB, two carbonyl stretching vibrations (blue, orange) and aromatic skeleton stretching (purple) could be detected (C).*

6.3. MATERIALS AND METHODS

6.3.1. Materials

Naproxen (NAP) (PubChem CID: 156391) was obtained from SA Fagron NV (Waregem, Belgium) and fenofibrate (FNB) (PubChemCID: 3339) was purchased from Hangzohou Dayangchem Co. (Hangzhou City, China). Poly(vinylpyrrolidone-*co*-vinyl acetate) 64 (PVPVA 64, Kollidon® VA64) (PubChem CID: 270885) was supplied by BASF® ChemTrade GmbH (Ludwigshafen, Germany).

ACROS Belgium (Geel, Belgium) supplied Methanol (MeOH) (≥ 99.8%) and Sigma-Aldrich (Brussels, Belgium) provided ethyl acetate (EtAc) (≥ 99.5%). Acetone (Ac) (≥ 99%) was received from VWR Chemicals (Leuven, Belgium), denaturated ethanol (EtOH) (≥ 97% and 3% V/V diethylether) from Chem-Lab Analytical (Zedelgem, Belgium) and 2-propanol (PrOH) (≥ 99.9%) from Carl Roth GmbH (Karlsruhe, Germany). Both acetonitrile (ACN) (≥ 99.9%) and dichloromethane (DCM) (≥ 99.5%) were purchased from Fisher Scientific (Loughborough, UK). Molecular sieve (type 4 Å, mesh 8 – 12) was obtained from Sigma-Aldrich (Brussels, Belgium).

6.3.2. Thermal gravimetric analysis (TGA)

6.3.2.1. Evaporation kinetics

To study the evaporation kinetics of the seven organic solvents as such (*i.e.,* MeOH, EtOH, PrOH, ACN, Ac, DCM, EtAc), solutions of PVPVA and solutions of PVPVA together with either FNB or NAP a thermogravimetric analyzer TGA 550 (TA instruments, Zellik, Belgium) was used. For the solutions, the solid content was kept constant at 10% w/V, which existed either out of 100 wt% PVPVA or 30 wt% of API and 70 wt% of PVPVA. To investigate the influence of a higher concentration of PVPVA on the evaporation rate of MeOH and DCM, solutions of 30% w/V PVPVA were prepared for these solvents as well. For every analysis, 40 µL of the sample was pipetted directly in a platinum HT pan (TA instruments, Zellik, Belgium) and kept isothermal for 10 min at a temperature 10 °C below the boiling point of the respective solvent. Every sample was analyzed in triplicate.

The recorded weight loss in function of time was attributed to solvent evaporation, from which the evaporation rate could be deducted. In case of the pure solvents, the evaporation followed a linear behavior, or in other words zero order kinetics, hence the following equation (Eq. 6.1.) could be employed:

$$y = a + bx \qquad \textit{Equation 6.1.}$$

Here, y corresponds to the weight (weight%) and x to the time (min). From this, the evaporation rate constant, b (weight%/min), could be established.

For the solutions, the first part of the curve also showed a linear relation, however, it was followed by an exponential decay in weight%, hence, the evaporation followed first order kinetics. The first part of the curve could be described by Eq. 6.1, while for the second part, a biexponential decay function (Eq. 6.2.) was applied:

$$y = y_0 + A_1 e^{-x/t1} + A_2 e^{-x/t2} \qquad \textit{Equation 6.2.}$$

From the time constants (t_1 and t_2, min), the evaporation rate constants (k_1 and k_2) could be deducted. These evaporation rate constants were equal to the reciprocal of the time constants (k_1 and k_2, min^{-1}).

To divide the evaporation behavior into these two parts, the second derivative of the weight change in function of time was used. It allowed to establish the maximal change of the evaporation rate, at which the curve was divided into two. To exemplify, the division of the evaporation curve for MeOH from a solution containing 10% w/V PVPVA is shown in Fig 6.2. The curve was split into two at 4.4 min, which was the peak maximum. Before this point, a linear fit was used to determine the evaporation rate constant, and after this maximum, the biexponential decay fit allowed to establish the two evaporation constants that described the last part of the curve.

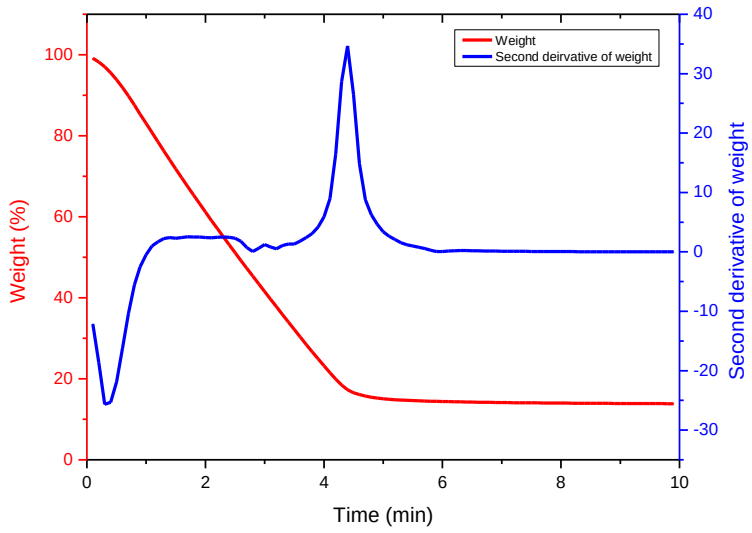

Figure 6.2. *Weight loss in function of time (red) and its second derivative (blue). The peak maximum in the second derivative was used to divide the curve into a linear and an exponential zone.*

6.3.2.2. Residual solvent

To determine the amount of residual solvent in the spray dried ASDs after secondary drying, a thermogravimetric analyzer TGA 550 (TA instruments, Leatherhead, UK) was employed as well. Approximately 5 to 10 mg of sample was accurately weighed in a platinum HT pan (TA instruments,

Zellik, Belgium) and heated at 5 °C/min to 130 °C. Every batch was analyzed in triplicate. The recorded weight change in function of temperature was attributed to solvent evaporation and could be determined using the Universal Analysis software (Version 5.5, TA instruments, Leatherhead, UK).

6.3.3. Fourier transform – infrared spectroscopy (FT-IR)

Prior to FT-IR analysis, all organic solvents were dried overnight using a molecular sieve type 4 Å to remove residual water present in the solvents. Additionally, PVPVA was dried for 4 days at 60 °C to remove the excess of water present. Solutions of PVPVA (10% w/V), FNB (2% w/V), NAP (2% w/V), PVPVA together with FNB (10% w/V) and PVPVA together with NAP (10% w/V) in MeOH, EtOH, PrOH, ACN and DCM were investigated. For the solutions of PVPVA and a drug compound, the following drug loadings were prepared: 10, 20 and 30 wt% of drug. The organic solvents were also analyzed as such. FT-IR spectra were recorded using a Perkin Elmer Spectrum two by accumulating 16 scans with a resolution set at 1 cm^{-1} over a spectral region of 4000 to 1100 cm^{-1}. The region of interest was the carbonyl stretching vibration region (1800 - 1600 cm^{-1}). For the blank, a background spectrum was recorded and subtracted from the sample spectrum. For every sample, 30 µL was pipetted in a semi demountable cell equipped with CaF_2 cell windows. After the FT-IR analysis in solution, the CaF_2 cell windows were opened, and the sample was dried at RT for 1 min. Subsequently, the dried film was analyzed again to compare the interaction behavior of drug and polymer in solution to that in the dried state. All spectra were analyzed using the OriginPro software (Version 8.5, Northampton, United States).

6.3.4. Manufacturing of amorphous solid dispersions by spray drying

The drug and polymer were dissolved together in either MeOH or DCM in order to obtain a solid content of 10% w/V. The drug to polymer ratios were dependent on the highest amount of the APIs that could be kinetically stabilized in the PVPVA matrix, which was reported in previous work[197]. For FNB, 5, 10 and 15 wt% of FNB were investigated when using MeOH as a solvent, while in case of DCM, 20, 25 and 30 wt% of FNB were prepared. For NAP, higher drug loadings of 40 and 45 wt% were studied using MeOH and 45 and 50 wt% of NAP when using DCM. These solutions were spray dried using a Büchi mini spray dryer B-190 (Büchi, Flawil, Switzerland) by applying a drying air flow rate of 33 m^3/h and an atomization air flow rate of 10 L/min. The drying air temperature and feed solution flow rate were adapted, depending on the need for a faster or slower evaporation process. The investigated sets of process parameters are described in Table 6.1. The ADS were further dried in a vacuum oven (Mazzali Systems, Monza, Italy) for 4 days at 25 °C, analyzed using XRPD, mDSC and TGA and stored at -28 °C in the presence of phosphorus pentoxide.

Table 6.1. *Spray drying process parameters per tested condition and per solvent.*

Conditions	Parameters	MeOH	DCM
Higher evaporation rate	Inlet temperature (°C)	85	59
	Flow rate (mL/min)	2.5	2.5
Standard conditions	Inlet temperature (°C)	65	39
	Flow rate (mL/min)	5	5
Lower evaporation rate	Inlet temperature (°C)	-	29
	Flow rate (mL/min)	-	10

6.3.5. Solid-state characterization of amorphous solid dispersions

6.3.5.1. Modulated differential scanning calorimetry (mDSC)

A Q2000 mDSC (TA Instruments, Leatherhead, UK) was used to investigate the thermal properties of the spray dried ASDs of NAP. The system was equipped with a Refrigerated Cooling System (RCS 90) and a dry nitrogen purge at 50 mL/min and calibrated for temperature, enthalpy and heat capacity using indium and sapphire standards. Approximately 1 to 5 mg was accurately weighed into aluminum DSC pans (TA instruments, Zellik, Belgium), which were then closed using the corresponding lids (TA instruments, Zellik, Belgium). The samples were heated from -15 °C to 180 °C using a linear heating rate of 2 °C/min combined with a modulation amplitude of 0.212 °C and a period of 40 s. The Universal Analysis software (Version 5.5, TA Instruments, Leatherhead, UK) was used to analyze the thermograms. The T_gs were measured at half height of transition in the reversing heat flow and the T_g width was established by determining the start- and endpoint of the T_g using the derivative of the reversing heat flow.

6.3.5.2. X-ray powder diffraction (XRPD)

The physical state of the ASDs of both FNB and NAP was investigated using an X'Pert PRO diffractometer (PANalytical, Almelo, the Netherlands) with a Cu tube (Kα λ = 1.5418 Å). The generator was installed at 40 mA and 45 kV. The samples were placed in between two Kapton® Polyimide Thin-films (PANalytical, USA) and continuously scanned from e10 to 25 °2θ. The counting time was installed at 800 s, the step size at 0.0167° and the spinning was set at 4 s. The obtained diffractograms were analyzed using the X'Pert Data Viewer (Version 1.9a, PANalytical, Almelo, the Netherlands).

6.3.5.3. Scanning electron microscopy (SEM)

Scanning Electron Microscopy (SEM) was employed for the morphology assessment of the spray dried PVPVA particles. The spray dried powders were attached to SEM stubs using double-sided carbon tape

(Ted Pella Inc., California, CA, USA) and subsequently gold coated with a SCD-030 Balzers Union sputter-coater (Oerlikon Balzers, Balzers, Liechtenstein). A Phillips XL30 SEM-FEG (Philips, Eindhoven, The Netherlands) equipped with a Schottky field emission electron gun and a conventional Everhart-Thornley secondary electron detector was used to record the SEM images.

6.3.5.4. Solid state NMR (ssNMR)

High-resolution ^{13}C-CPMAS solid-state NMR

Solid-state ^{13}C-CPMAS (Cross Polarization Magic Angle Spinning) NMR spectra were acquired on a Bruker 400MHz spectrometer (9.4 Tesla) equipped with a 4 mm probe. Magic angle spinning was performed at 10 kHz in ceramic zirconia rotors. The aromatic signal of hexamethylbenzene was used to calibrate the carbon chemical shift scale (132.1 ppm). Acquisition parameters used were: a spectral width of 50 kHz, a 90° pulse length of 4.0 μs, an acquisition time of 15 ms, a recycle delay time of 2.5 s, a spin-lock field of 50 kHz, a contact time of 2 ms and between 25000 and 60000 accumulations. High power proton dipolar decoupling during acquisition was set to 70 kHz.

^{13}C liquid-state NMR

The ^{13}C-NMR spectrum of Fenofibrate was measured at room temperature on a 400 MHz Varian Inova NMR spectrometer using a 5 mm OneNMR PFG probe. Hereto a solution of 130 mg/ml crystalline Fenofibrate was prepared $CDCl_3$ supplemented with 15mM $Cr(acac)_3$ as relaxation reagent. The chemical shift scale (δ; in ppm) was calibrated relatively to $CDCl_3$ (77.7 ppm). All spectra were acquired with a 90° pulse of 8.0 μs, a spectral width of 27.8 kHz, an acquisition time of 1 s, a relaxation delay of 6 s and 8000 accumulations. A line-broadening of 3 Hz was applied prior to Fourier transformation to the frequency domain.

6.4. RESULTS AND DISCUSSION

6.4.1. Evaporation kinetics

6.4.1.1. Evaporation kinetics of pure organic solvents

In a first step, the evaporation behavior of the seven organic solvents as such was determined by analyzing the samples at 10 °C below the boiling point of the respective solvent. From Fig 6.3A, it was clear that the slope of the weight loss curve in function of time was steepest for DCM, while it was flattest for MeOH. In Fig 6.4A, the corresponding evaporation rate constants deducted using a linear fit (Eq. 6.1.) are shown. Hence, despite the similar energy input relative to the boiling points of the solvents, a difference in evaporation rate was observed. This difference could not be related to the purity of the solvents. For instance, the effect of residual water was investigated by analyzing purer MeOH (99.9%), which still had a lower evaporation rate compared to EtOH (97%) (data not shown).

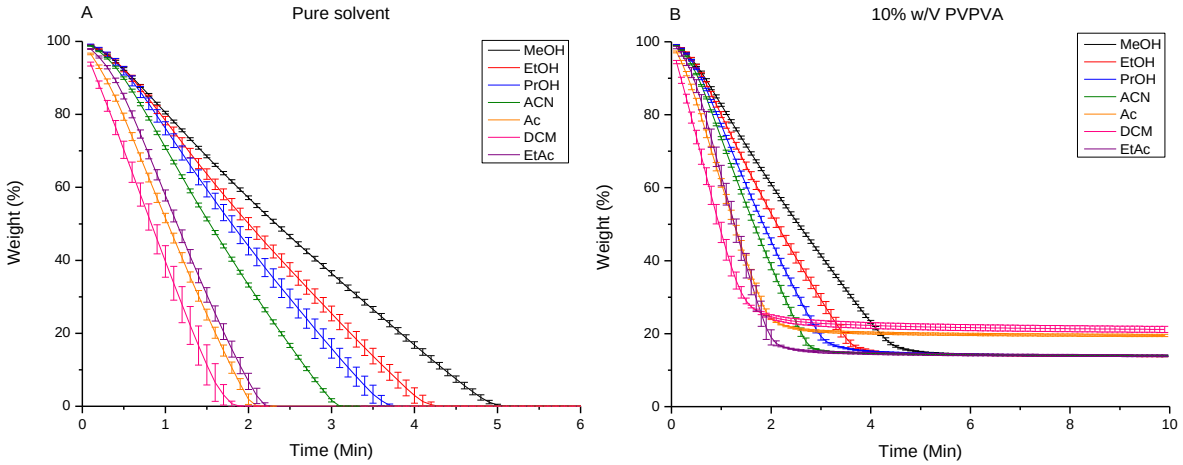

***Figure 6.3**. Weight loss in function of time of pure solvents (A) and solutions containing 10% w/V PVPVA (B) when kept isothermal at 10 °C below the boiling point of the respective solvent. The following color code was applied: MeOH in black, EtOH in red, PrOH in blue, ACN in green, Ac in orange, DCM in pink and EtAc in purple.*

6.4.1.2. The influence of PVPVA on the evaporation kinetics

Solutions containing 10% w/V PVPVA had the same relative evaporation behavior as the pure organic solvents (Fig 6.3B). However, for all solvents (except for PrOH), PVPVA slowed down the evaporation process (Fig 6.4A), which could be explained by the lower vapor pressure of the solutions compared to their pure counterparts, resulting in a lower tendency to evaporate and hence a slower evaporation process. Moreover, the PVPVA concentration gradually increased during evaporation, resulting in an increased viscosity, which in turn further decreased the evaporation rate. The latter was most pronounced for the faster evaporating solvents, *i.e.*, DCM, Ac and EtAc, where a very fast increase in

PVPVA concentration and thereby the viscosity of the solution gave rise to what could be considered as a skin formation through which further solvent evaporation had to take place. The final weight% in case of DCM and Ac was slightly higher compared to the other solvents (Fig 6.3B), which indicated that more DCM and Ac was already evaporated before the start of the TGA analysis.

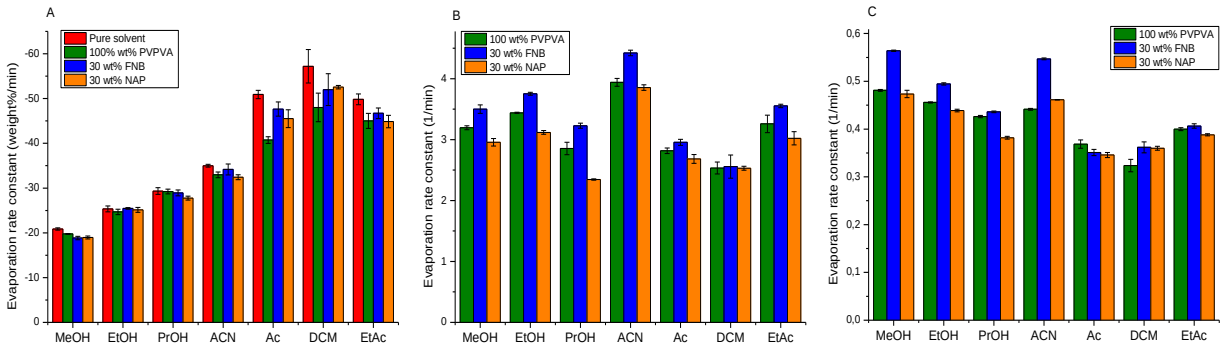

Figure 6.4. *Evaporation rate constants deducted from the weight loss in function of time using a linear fit (A) and a subsequential biexponential fit (B, C). The following color code was applied: pure solvents in red, solutions only containing PVPVA in green, the ones containing both PVPVA and FNB in blue and the ones comprising both PVPVA and NAP in orange.*

To confirm the different impact of PVPVA on the evaporation rate of relatively faster and slower evaporating solvents, the evaporation behavior of solutions of 30% w/V PVPVA in MeOH, *i.e.,* the slowest evaporating solvent, and DCM, *i.e.,* the fastest one, was investigated. In Fig 6.5., the corresponding drying rate constants are reported. It was clear that 30% w/V of PVPVA immediately reduced the rate of volatilization of DCM by ca. 50%, while it initially had no effect on the evaporation of MeOH (Fig 6.5A). Further progress of the evaporation behavior showed similar evaporation rate constants for MeOH and DCM for the second part of the curve (Fig 6.5B, C). This showed that the delaying effect of PVPVA was much more pronounced in case of a faster evaporating solvent, yet, it was also present in case of a slower evaporating solvent at later timepoints, which demonstrated that in both cases skin formation took place, it only took a longer period of time in case of the initially slower evaporating solvent.

The different effect of PVPVA on the drying rate of organic solvents might also have implications for the particle morphology. For instance, it has been described by Boel et al. that the difference in evaporation rate of MeOH and Ac during fluid bed coating was responsible for the morphology of bead coated ASDs of felodipine, where a porous coating was observed for the faster evaporating Ac compared to a homogeneous coating for the slower evaporating MeOH[204]. However, a microscopic evaluation of PVPVA particles spray dried with the seven different solvents revealed that all were collapsed (except for PrOH), hence, the difference in evaporation behavior could not be directly related to the morphology of spray dried PVPVA particles (Fig 6.6.).

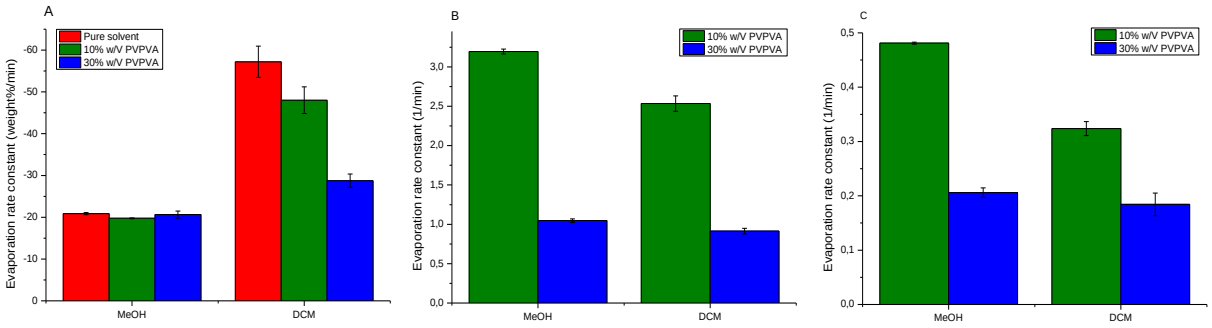

***Figure 6.5**. Evaporation rate constants deducted from the weight loss in function of time using a linear fit (A) and a subsequential biexponential fit (B, C). The constants for pure MeOH and DCM are shown in red, those of solutions containing 10% w/V PVPVA in green and the ones with 30% w/V PVPVA in blue.*

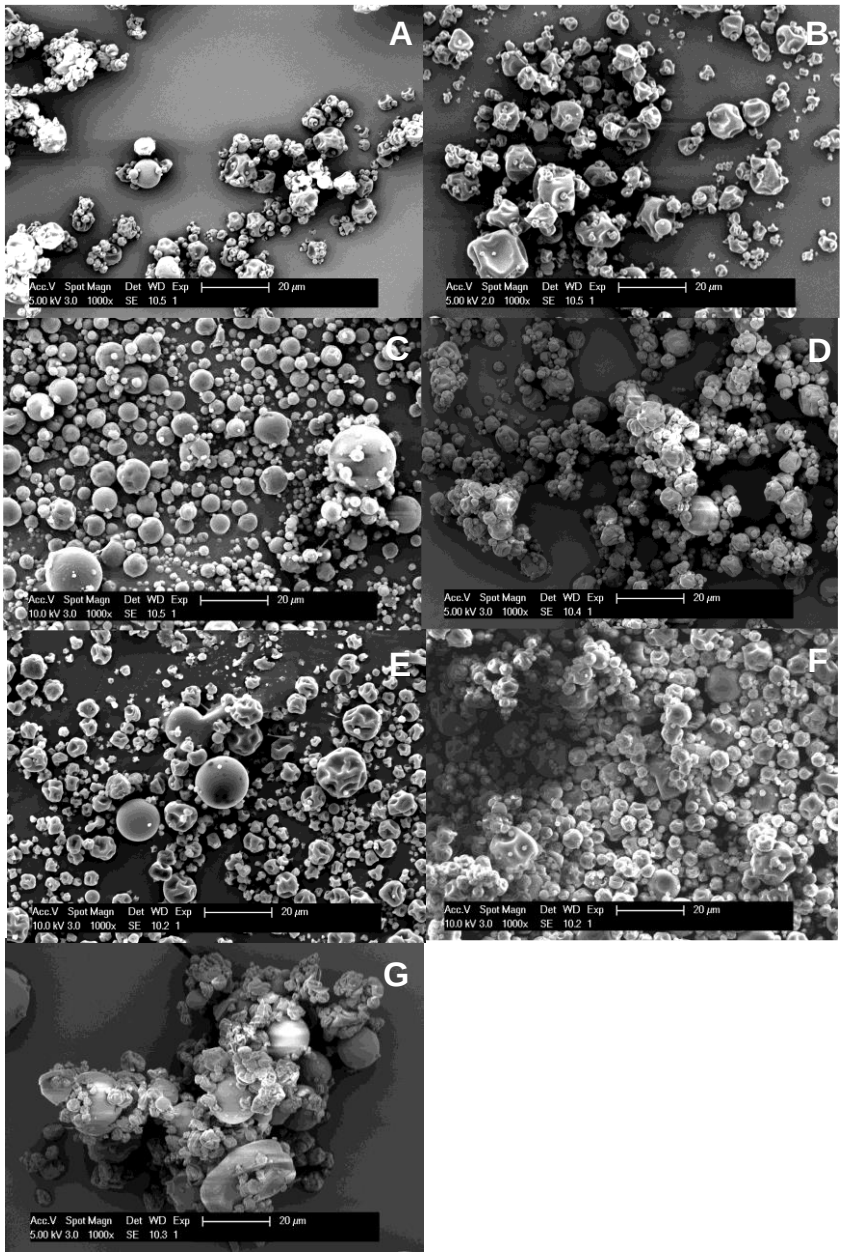

***Figure 6.6**. SEM images of PVPVA particles spray dried using MeOH (A), EtOH (B), PrOH (C), ACN (D), Ac (E), DCM (F) and EtAc (G).*

6.4.1.3. The influence of drug compounds on the evaporation kinetics

In Fig 6.4., the effect of either 30 wt% FNB or 30 wt% NAP on the evaporation behavior is depicted. Initially, the evaporation rate of DCM, Ac and EtAc was increased in case of the 30 wt% drug solutions compared to the ones solely containing PVPVA (Fig 6.4A). This could be explained by a less pronounced viscosity increase during evaporation in presence of the drugs compared to pure PVPVA, which would in turn lead to less rapid skin formation. In Fig 6.4B, it is shown that the evaporation rate constants for 30 wt% FNB solutions were highest, followed by the 100 wt% PVPVA solutions and at last the 30 wt% NAP solutions, independently of the solvent, with as an exception DCM. Further in time, the same trend was still observed in case of MeOH, EtOH, PrOH and EtAc, yet not anymore in case of the other solvents (Fig 6.4C). These results could be an indication of interactions between both NAP and the solvent and NAP and PVPVA, as the latter could result in a viscosity increase and thereby a lower evaporation rate as well. On the other hand, it might indicate the absence of/weaker interactions between both FNB and the solvent and FNB and PVPVA.

6.4.2. FT-IR spectroscopy

6.4.2.1. The behavior of PVPVA, NAP and FNB in solution

In Fig 6.7A, the different behavior of 10% w/V PVPVA in DCM, ACN, MeOH, EtOH and PrOH is depicted. The exact peak positions depending on the solvent are described in Annex 8. For DCM, the first signal, *i.e.*, 1735 cm^{-1}, corresponds to the carbonyl stretching vibration of vinyl acetate (VA) (marked in yellow in Fig 6.1A), while the second one, *i.e.*, 1681 cm^{-1}, originated form the carbonyl stretching vibration of vinyl pyrrolidone (VP) and more specifically to its C=O – C=O dipole interactions (marked in red in Fig 6.1A)[205,206]. PVPVA behaved similarly when dissolved in ACN, while its behavior clearly differed in the alcoholic solvents. Here, the carbonyl stretching signal of VA was split in a non-hydrogen bonded vibration signal, which was situated at higher wavenumbers, and a hydrogen bonded vibration signal, which was positioned at lower wavenumbers. Additionally, the signal corresponding to the VP carbonyl stretching vibration was broadened and shifted towards lower wavenumbers, also indicating the presence of hydrogen bonding with the solvents. Hence, the VP amide carbonyl accepted protons more readily compared to the VA ester carbonyl, which could be attributed to the more polar nature of the VP part of the copolymer and its well-known availability for hydrogen bonding[207]. Interestingly, the peak shift of the VP stretching vibration was dependent on the alcoholic solvent in which PVPVA was dissolved, with the largest shift in case of MeOH (*i.e.,* 1664 cm^{-1}), followed by EtOH (*i.e.,* 1666 cm^{-1}) and the smallest in PrOH (*i.e.,* 1668 cm^{-1}). This evidenced that there were stronger hydrogen bonds between PVPVA and MeOH than between PVPVA and EtOH and those were in turn stronger than the ones between PVPVA and PrOH.

A well-known property of naproxen is that it can self-associate and form both dimers and open-chain oligomers[148,208,209]. From the IR spectra in Fig 6.7B, it became clear that the self-association behavior of NAP was influenced by the solvent (Annex 8). In case of DCM, the first signal corresponded to the carbonyl stretching vibration of the monomer, *i.e*., 1748 cm^{-1}, while the second one correlated to that of the dimer, *i.e.,* 1710 cm^{-1} (marked in red in Fig 6.1B). The other two signals in this spectral region originated from aromatic skeleton stretching vibration, namely, in plane C-H bending at 1636 cm^{-1} and in plane C-C stretching at 1607 cm^{-1} (marked in green in Fig 6.1B)[209]. As previously reported in literature, dimer formation of NAP was diminished in the weakly hydrogen bond accepting solvent ACN[208]. The sole presence of the monomer at 1740 cm^{-1} demonstrated that NAP was more available for interaction with the solvent when compared to the other solvents. In the three alcoholic solvents, NAP manifested itself as both monomer (*i.e.,* 1738 cm^{-1}) and dimer (*i.e*., 1708 cm^{-1}), although there was relatively less dimer present when compared to DCM (Fig 6.7B)[148]. There was however no difference observed between the behavior of NAP in the alcoholic solvents. Accordingly, NAP interacted the strongest with ACN, followed by all three alcoholic solvents and it had the weakest interactions with DCM.

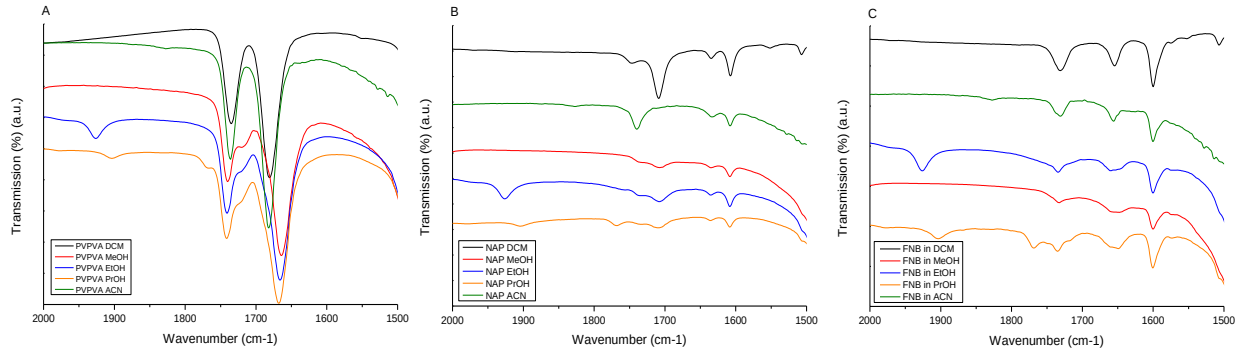

Figure 6.7. *FT-IR spectra of 10% w/V PVPVA (A), 2% w/V NAP (B) and 2% w/V FNB (C) in DCM (black), ACN (green), MeOH (red), EtOH (blue) and PrOH (orange). The transmittance is depicted in arbitrary units.*

The behavior of FNB in the organic solvents is depicted in Fig 6.7C and the corresponding peak positions per solvent in Annex 8. The first peak correlated to the carbonyl stretching vibration of the ester carbonyl, *i.e.,* 1732 cm^{-1} (indicated in orange in Fig 6.1C), the second one to the other carbonyl stretching vibration signal, *i.e.,* 1654 cm^{-1} (marked in blue in Fig 6.1C), and the last signal detected in this spectral region corresponded to the in-plane benzene ring stretch, *i.e.,* 1600 cm^{-1} (indicated in purple in Fig 6.1C)[210]. FNB showed similar behavior in DCM and ACN, but not in the other three solvents. Here, the second carbonyl stretching vibration signal was clearly broadened, indicating hydrogen bonding with these solvents.

6.4.2.2. The presence of interactions between NAP and PVPVA in solution

After characterization of the reference compounds in solution, solutions of different API to polymer ratios were characterized to investigate possible interactions between API and polymer and the impact of the solvent on the prevalence of these interactions.

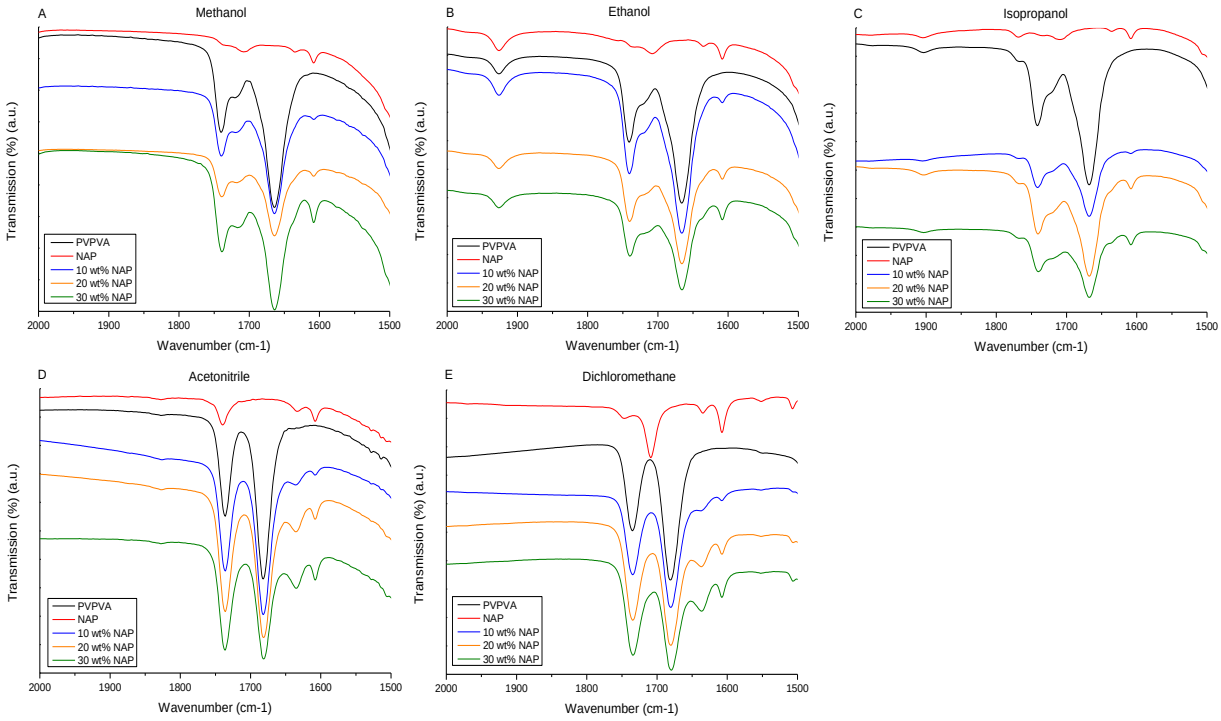

***Figure 6.8**. FT-IR spectra of NAP, PVPVA and 10, 20 and 30 wt% NAP and PVPVA in MeOH (A), EtOH (B), PrOH (C), ACN (D) and DCM (E). The following color code was applied: NAP in red, PVPVA in black, 10 wt% NAP in blue, 20 wt% NAP in orange and 30 wt% NAP in green. The transmittance is delict in arbitrary units.*

In Fig 6.8, the IR spectra of solutions containing 10, 20 and 30 wt% of NAP and PVPVA are shown. The exact peak positions for solutions with 10 wt% NAP are described in Annex 8. For the alcoholic solvents (Fig 6.8A to C), a shoulder in the peak of VP carbonyl stretching vibration signal became visible for the solution containing 20 wt% NAP and became more evident for the one with 30 wt% NAP. This vibration signal originated from the sum of aromatic skeleton stretching of NAP and strong hydrogen bonding between NAP and PVPVA[206,209]. For ACN and DCM, this vibration signal was already clearly detected at 1636 cm^{-1} for 10 wt% of NAP, demonstrating strong hydrogen bonds between NAP and PVPVA for lower drug loadings (Fig 6.8D, E). Moreover, in these solvents, the relative intensity of the VA and VP carbonyl stretching region changed when increasing the NAP drug loading, with a similar intensity of both signals for the highest drug loading of 30 wt%. This could be attributed to part of the VP interacting with NAP combined with an overlap of the VA vibration signal with that of the carbonyl stretching vibration of the NAP monomer. Interestingly, there was no difference observed in API-polymer interactions between ACN and DCM, although the self-association behavior of NAP in these

solvents was clearly different (Fig 6.7B). This demonstrated that the affinity of NAP for PVPVA, a strong hydrogen acceptor, was higher than for ACN, a weak hydrogen acceptor.

More importantly, as the presence of hydrogen bonding was detected for lower drug loadings in case of DCM and ACN, it could be concluded that in these solvents, NAP and PVPVA formed stronger hydrogen bonds compared to in the alcoholic ones. This could be attributed to the multiple interaction possibilities in the alcoholic solvents: hydrogen bonding was not only possible with PVPVA, but also with NAP, resulting in less free PVPVA and NAP to associate with each other. Therefore, the tendency for NAP and PVPVA to hydrogen bond with one another was higher in case of DCM and ACN compared to the other solvents. This is an important finding as these results clearly indicate that the probability of API-polymer interactions is influenced by the solvent, which might have implications for the formulation of highly drug loaded ASDs and/or the physical stability of ASDs.

6.4.2.3. The presence of interactions between FNB and PVPVA in solution

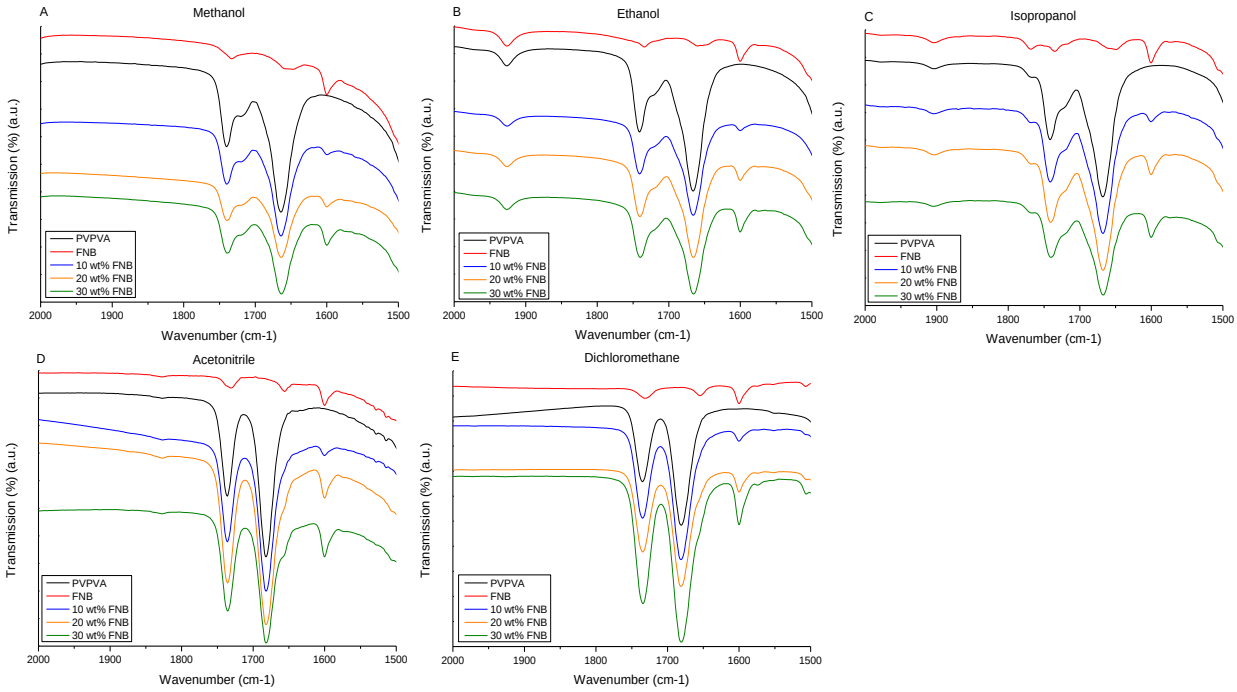

***Figure 6.9**. FT-IR spectra of FNB, PVPVA and 10, 20 and 30 wt% FNB and PVPVA in MeOH (A), EtOH (B), PrOH (C), ACN (D) and DCM (E). The following color code was applied: FNB in red, PVPVA in black, 10 wt% FNB in blue, 20 wt% FNB in orange and 30 wt% FNB in green. The transmittance is depicted in arbitrary units.*

The IR spectra of solutions containing 10, 20 and 30 wt% FNB and PVPVA are depicted in Fig 6.9 and the corresponding peak positions for the 10 wt% FNB solutions are described in Annex 8. For the alcoholic solvents, FNB did not influence the behavior of PVPVA in solution (Fig 6.9A to C). For ACN and DCM, a shoulder peak on the VP carbonyl stretching signal was detected for the solution containing 30 wt% FNB (Fig 6.9D, E). This vibration signal corresponded to the carbonyl stretching vibration signal of

FNB, that overlapped with the VP carbonyl stretching vibration signal. Hence, the IR spectra of FNB together with PVPVA were an overlap of the spectra of the individual components in solution, indicating that there were no interactions between FNB and PVPVA, independently of the solvent.

6.4.2.4. Comparison of interactions in solution and in the dried state

A comparison of the behavior in solution and dried state of pure PVPVA, pure NAP and samples containing 30 wt% NAP and PVPVA is depicted in Fig 6.10A and B. The exact peak positions can be found in Annex 8. In MeOH, the VP carbonyl stretching vibration of PVPVA was broader and positioned at lower wavenumbers and that of its VA group was split in two (Fig 6.10A). After drying for 1 min at RT, the VA vibration signal was no longer split in two, but positioned at 1733 cm^{-1}, which was in between its signals at 1740 cm^{-1} and 1719 cm^{-1} in solution. Additionally, both carbonyl stretching vibrations appeared broader after drying. Drying of the MeOH solution containing 2% w/V NAP resulted in the formation of both monomer (1732 cm-1) and dimer (1687 cm^{-1}) of NAP. When the solution of both NAP and PVPVA was dried, the shoulder peak on the VP carbonyl stretching vibration that was present in solution became more evident, *i.e*., the signal at 1636 cm^{-1} in solution was now clearly detected at 1633 cm^{-1}. The relative intensity of the VP and VA carbonyl stretching vibration also changed upon drying, resulting in a similar intensity of both signals. When drying the solution of PVPVA in DCM, only the VP carbonyl stretching vibration was broader and shifted towards lower wavenumbers, *i.e.,* it shifted from 1681 cm^{-1} in solution to 1670 cm^{-1} in dried state (Fig 6.10B). There was no difference between the IR spectrum of NAP dried from a MeOH solution or from a DCM solution. Moreover, also the IR spectra from NAP and PVPVA together were identical, thus, there was no longer competition with the solvent for hydrogen bonding, resulting in the formation of hydrogen bonds between NAP and PVPVA, independently of the solvent that was present. Although the prevalence of interactions between NAP and PVPVA was much higher in case of DCM compared to MeOH, this did not influence the interactions formed upon drying. Additionally, widening of the carbonyl stretching vibrations of PVPVA, and especially that of the VP, originated from water uptake from the environment when drying at RT for 1 min. This was most pronounced for the VP carbonyl stretching vibration due to the hygroscopic nature of VP[211].

Likewise, Fig 6.10C and D depict the behavior in solution and dried state of pure PVPVA, pure FNB and samples of 30 wt% FNB and PVPVA. The peak positions can be found in Annex 8. Both in case of MeOH and DCM, the ester carbonyl stretching vibration shifted from 1733 cm^{-1} to 1731 cm^{-1} upon drying of the FNB solution, while the other carbonyl stretching signal was positioned at 1657 cm^{-1} in dried state compared to 1654 cm^{-1} in solution (Fig 6.10C, D). When drying the solution of both FNB and PVPVA, the carbonyl stretching vibration corresponding to the VP part shifted towards lower wave,

independently of the solvent. More specifically, in case of MeOH, it was positioned at 1657 cm^{-1} in dried state compared to 1664 cm^{-1} in solution and in case of DCM, it shifted from 1681 cm^{-1} in solution to 1658 cm^{-1} in dried state. Thus, the extent of the peak shift appeared to be dependent on the solvent. To evaluate the repeatability of the peak shift of the VP carbonyl stretching vibration upon drying, three aliquots of the same solution of 10% w/V PVPVA in DCM were characterized (Annex 9). From this, it became clear that the extent of the peak shift upon drying was not repeatable, *i.e.,* vibration signals were detected at 1663 cm^{-1}, 1670 cm^{-1} and 1658 cm^{-1}, which could be explained by a variable water uptake from the environment upon drying, which gave in turn rise to a different level of hydrogen bonding.

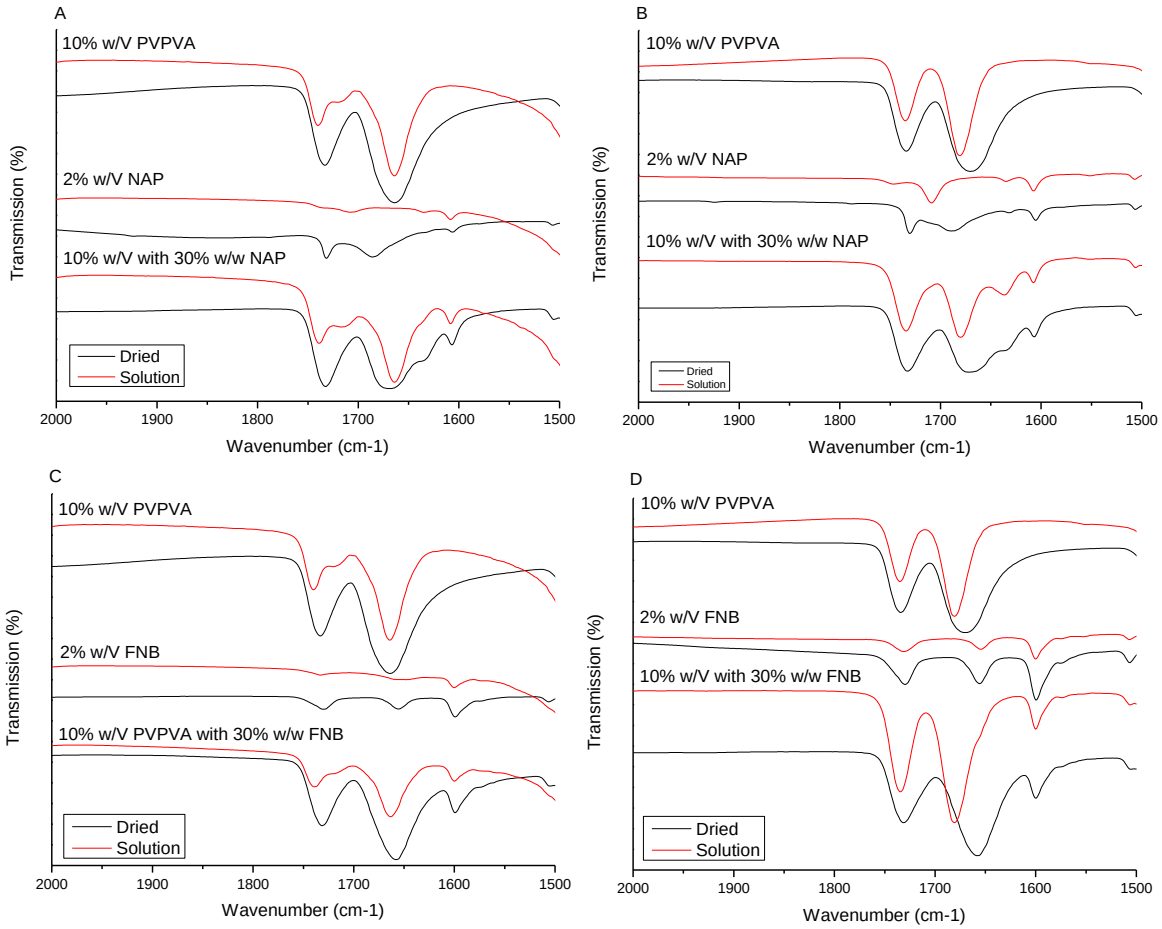

Figure 6.10. *Comparison of FT-IR spectra in solution to those in the dried state for NAP in/dried from MeOH (A) and DCM (B) and for FNB in/dried from MeOH (C) and DCM (D). The spectra from samples in solutions are depicted in red and those from samples in the dried state in black. The transmittance is shown in arbitrary units.*

Moreover, to investigate possible interactions in the dried state between FNB and PVPVA, CPMAS ssNMR and liquid state NMR were applied as well (Annex 9). The NMR spectrum of FNB in deuterated chloroform was employed to evaluate peak shifts that might take place upon amorphization of FNB. Characterization of spray dried FNB and PVPVA in 3 different ratios (10 wt%, 20 wt% and 30 wt% FNB) revealed that the only peak shifts present originated from the different physical state of FNB, *i.e.,* the

amount of crystalline FNB present. Hence, the absence of interactions between FNB and PVPVA in solid state was confirmed by the application of CPMAS ssNMR.

6.4.3. Rational selection of spray drying process parameters

As MeOH had the slowest evaporation rate, formed the strongest hydrogen bonds with PVPVA and it could also interact with both FNB and NAP, it had the poorest properties to be used to formulate highly drug loaded ASDs. In contrast to this, DCM evaporated the fastest and there were no interactions observed between either the drugs and DCM or PVPVA and DCM, which made DCM a promising solvent to be used to prepare highly drug loaded ASDs. Accordingly, the spray drying process parameters were adapted to increase the evaporation rate of MeOH in order to load more API in the PVPVA matrix (Table 6.1.). In case of DCM, both the influence of an increased and a lower evaporation rate on the physical state was evaluated (Table 6.1.).

6.4.3.1. Spray drying of ASDs of NAP

Applying standard process parameters, *i.e*., inlet temperature set at the boiling point of the solvent and a liquid feed rate of 5 mL/min, resulted in a highest drug loading of 40 wt% NAP when using MeOH. However, when preparing 3 batches with the same composition, one of them was partially crystalline in XRPD analysis (Fig 6.11A). Likewise, two out of three batches showed Bragg reflections when a higher evaporation rate was applied. The phase behavior was thus non repeatable, which could be attributed to contingencies, such as environmental conditions (*i.e.,* RH and *T*) that cannot be controlled in a spray drying set-up. Independently of the set of process parameters used, the 45 wt% sample was partially crystalline, although the crystalline fraction was larger in case of the higher evaporation rate, *i.e.,* 2.52 ± 0.17 % compared to 1.76 ± 0.14 % (Fig 6.11.). Accordingly, it was not possible to formulate higher drug loadings of NAP when increasing the drying rate of MeOH. Moreover, increasing the drying rate of MeOH resulted in a poorer phase behavior. In spite of this, a lower residual solvent content was found when a higher evaporation rate was applied (Annex 10).

Using DCM as a solvent and standard process parameters gave rise to a maximum drug loading of 45 wt%, which was determined by the presence of a melting event of NAP in the total heat flow of the mDSC analysis for higher drug loadings (Annex 11). Similarly, the thermogram of 50 wt% NAP prepared using a higher evaporation rate also contained a melting event, although the crystalline content was higher, *i.e.,* 1.58 ± 0.09 % compared to 0.29 ± 0.16 %. Interestingly, when applying a lower evaporation rate, there were neither melting events detected in the mDSC analysis for the 50 wt% nor Bragg peaks in the XRPD analysis (Annex 11). These findings were in contrast with the idea that faster solvent

evaporation would be favorable for kinetic trapping and thus the formulation of kinetically stabilized highly drug loaded ASDs.

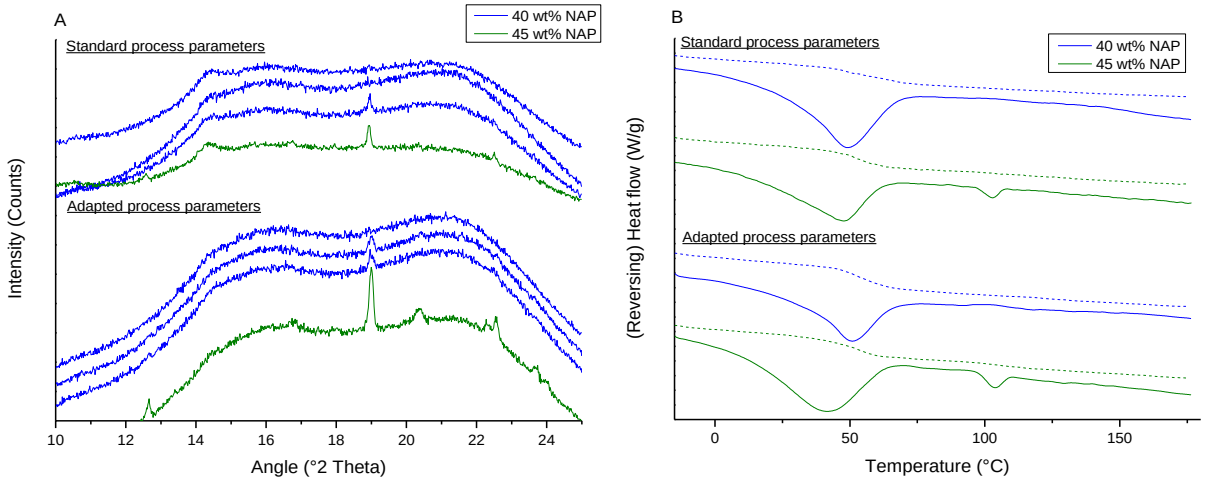

***Figure 6.11**. XRPD diffractograms (A) and mDSC thermorgrams (B) of 40 wt% (blue) and 45 wt% (green) NAP and PVPVA spray dried using MeOH using standard process parameters or parameters that enabled a higher evaporation rate. 40 wt% samples were prepared in triplicate (A). For the mDSC analysis, both the reversing (dashed line) and total heat flow (full line) are depicted, and exothermic signals are directed upwards (B).*

However, not only the evaporation rate, but also the outlet temperature (T_{out}) is a very critical factor for the final phase behavior of a spray dried ASD. In Table 6.2., both the T_{out} in the beginning and the end of the spray drying process are reported. The larger the difference between these values, the more energy consuming the drying process was, *e.g.,* a ΔT of 2 °C in case of process parameters that enabled a higher evaporation rate relative to a ΔT of 5 °C for standard process parameters. Moreover, the solid phase crystallization rate increases when the difference between the T_g of the ASD and the particle temperature (and thus T_{out}) increases[93,212]. To exemplify, as the T_g of 40 wt% NAP and PVPVA ASDs was ca. 55.52 °C, installing an inlet temperature (T_{in}) of 85 °C when spray drying with MeOH gave rise to a T_{out} situated above the T_g (Table 6.2.). This increased crystallization tendency together with the fact that NAP is a very fast crystallizer, classified as a Glass Forming Ability (GFA) Class I compound according to Van Eerdenbrugh et al., resulted in a poorer phase behavior when applying process parameters that enabled a faster evaporation process[147]. On the other hand, installing a lower T_{in} when spray drying with DCM, gave rise to a T_{out} situated further below the T_g of ASDs of NAP than when applying standard parameters, *i.e.,* ASDs of 45 wt% NAP and PVPVA had a T_g of ca. 51.60 °C relative to a T_{out} of 28 °C. Hence, lowering the drying rate indirectly decreased the solid phase crystallization tendency. Likewise, Paudel et al. investigated the effect of the inlet temperature on the phase behavior of ASDs of NAP and PVP K25, where higher inlet temperatures resulted in phase separated systems[202]. Ultimately, the drying air temperature should be sufficiently high to remove the solvent and enable kinetic trapping of the drug in the polymer matrix, yet it should be in balance with the potentially unfavorable impact of a high T_{out} on the crystallization tendency.

Table 6.2. *Outlet temperatures (T_{out}) observed during spray drying of ASDs of 40 wt% NAP and PVPVA using MeOH and ASDs of 45 wt% NAP and PVPVA using DCM.*

Solvent	Condition	T_{in} (°C)	$T_{out, begin}$ (°C)	$T_{out, end}$ (°C)	ΔT_{out} (°C)
MeOH	Standard evaporation rate	65	48	43	5
	Higher evaporation rate	85	60	58	2
DCM	Standard evaporation rate	39	33	28	5
	Higher evaporation rate	59	44	42	2
	Lower evaporation rate	29	28	22	6

The fact that an increased drying air temperature had a disadvantageous effect on the phase behavior of ASDs of NAP, does not exclude the possible beneficial effect of an increased drying rate on the kinetic trapping efficiency. For instance, solely modifying the liquid feed rate to generate smaller droplets could still result in a faster evaporation process without increasing the T_{out}. Therefore, a further process optimization might give rise to the kinetic stabilization of higher drug loadings.

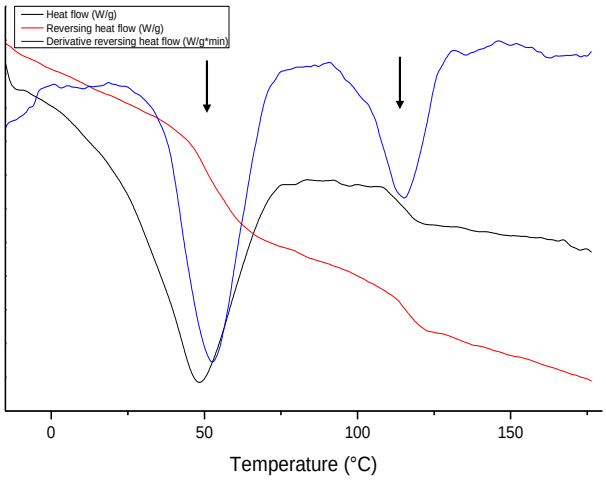

Figure 6.12*. mDSC thermogram of 40 wt% NAP and PVPVA spray dried using MeOH and process parameters that enabled a higher drying rate. The total heat flow (black), reversing heat flow (red) and derivative of the reversing heat flow (blue) are depicted. Exothermic signals are directed upwards, and the arrows indicate the positions of the two T_gs.*

As discussed in Chapter 5, the mDSC analysis of ASDs of NAP and PVPVA sometimes contained a peculiarity that had the characteristics of a T_g. Likewise, a second T_g above the T_g of the polymer was detected for some 40 wt% NAP batches prepared using MeOH and a higher drying rate. In the example depicted in Fig 6.12., the first T_g was positioned at 59.55 °C, which was the Mobile Amorphous Fraction (MAF), and the second one at 115 °C, which was the Rigid Amorphous Fraction (RAF). As all three batches of 40 wt% NAP were analyzed in triplicate by mDSC analysis and only three out of nine analyses indicated the presence of a RAF, it was clear that this phenomenon was not repeatable. Interestingly, for the samples that showed this peculiarity in the mDSC analysis, the diffractogram contained a Bragg

peak (Fig 6.12.), which supported the hypothesis that this step change in heat capacity in the mDSC analysis originated from a RAF that was immobilized by NAP crystals.

6.4.3.2. Spray drying of ASDs of FNB

When using MeOH with standard process parameters, Bragg peaks were present in the XRPD diffractogram starting from 10 wt% FNB (Fig 6.13A). Adapting the parameters to increase the drying rate, resulted in an amorphous halo for 10 wt% FNB, yet for the 15 wt% FNB Bragg reflections could be detected at 16, 17 and 22 °2θ (Fig 6.13B). According to the TGA-analysis, a higher evaporation rate resulted in a lower amount of residual solvent in the 5 wt% FNB batches, *i.e.,* 2.73 ± 0.18 % compared to 4.05 ± 0.25 % (Annex 10).

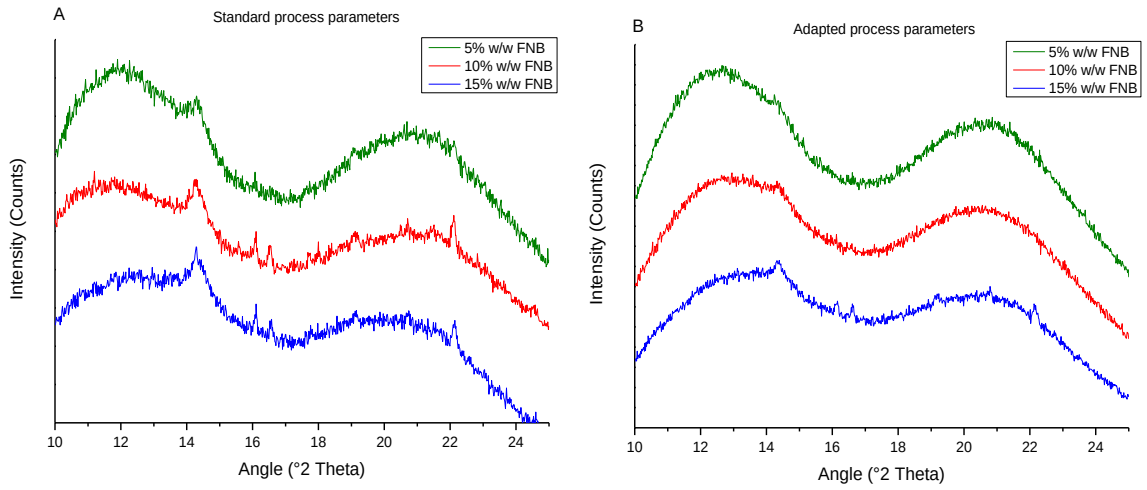

Figure 6.13. *XRPD diffractograms of 5 wt% (green), 10 wt% (red) and 15 wt% (blue) FNB and PVPVA spray dried using MeOH with standard process parameters (A) and parameters that allowed a faster evaporation of MeOH (B).*

When spray drying with DCM, the highest drug loading of FNB that could be kinetically stabilized was previously established at 20 wt% [197]. Applying a lower evaporation rate resulted in a partially crystalline sample for the 20 wt% (Annex 11). Increasing the evaporation rate on the other hand, resulted in an X-ray amorphous 20 and 25 wt% FNB sample, while Bragg peaks were present for the 30 wt% FNB one (Annex 11). These findings were in accordance with the expected favorable effect of an increased evaporation rate on the kinetic trapping efficiency and thereby formulation of highly drug loaded ASDs. The absence of a disadvantageous effect of the higher T_{out} can be explained by the lower drug loadings of FNB that were prepared, namely 5 to 30 wt%, and thus higher product T_g, *i.e.,* ranging from ± 100 °C for 5 wt% FNB to 54.50 °C for 30 wt% FNB [197]. In spite of that, a possible explanation for the partial crystallinity of the 30 wt% FNB sample when increasing the drying rate of DCM, could be the relatively higher T_{out} of 44 °C (Annex 10). However, the physical state of these ASDs of FNB was predominantly determined by the increased drying rate (T_{in}) rather than the T_{out} as was the case for ASDs of NAP.

Evidently, depending on the physicochemical characteristics of the API (*e.g.,* GFA) and the API to polymer ratio, the T_{out} will be a limiting factor for increasing evaporation rate by adaptation of the T_{in}.

In spite of the fact that a higher amount of FNB could be kinetically stabilized by increasing the drying rate, the improvement is limited to 5 wt%, independently of the solvent. Especially for MeOH, this cannot be related to the T_{out}, as an ASD of 10 wt% FNB has a T_g of ± 93.29 °C, which is well above the T_{out} of 60 °C. Accordingly, the physical state was not only determined by the balance of T_{in} and T_{out}, but more importantly, by the drug-polymer-solvent combination. For MeOH, this could be related to the inherently slow evaporation behavior of the solvent relative to the others (even when applying parameters that enable a higher drying rate) together with the fact that MeOH can hydrogen bond with both PVPVA and FNB. Ultimately, the physical state of these ASDs of FNB was determined by the API-polymer-solvent combination rather than the set of spray drying process parameters used.

6.5. CONCLUSION

The combination of TGA and FT-IR spectroscopy was successfully applied to gain insight in the evaporation kinetics and interactions (in solution), respectively. The evaporation rate of the seven organic solvents 10 °C below the bp of the respective solvent clearly differed, with MeOH evaporation the slowest and DCM the fastest. The addition of PVPVA did not alter the relative evaporation rate, yet decreased the evaporation rate for all solvents, which was most pronounced for the relatively faster evaporating solvents, *i.e.,* DCM, Ac and EtAc. FNB and NAP had opposite effects on the evaporation rate: FNB increased the drying rate again, while NAP decreased it. The latter was an indication of interactions between NAP and PVPVA or NAP and the solvent. Accordingly, the FT-IR analyses revealed hydrogen bonding between NAP and MeOH, EtOH, PrOH and ACN, and hydrogen bonding between NAP and PVPVA, which was more pronounced for the solvents that did not interact with PVPVA, *i.e.,* DCM and ACN. However, drying from DCM or MeOH resulted in the same IR spectrum of NAP and PVPVA, demonstrating that the same hydrogen bonding strength could still be obtained. Based on these findings, spray drying process parameters were altered to increase the evaporation rate of MeOH and on the other hand to both lower and increase the drying rate of DCM. For FNB, a higher evaporation rate enabled the formulation of higher drug loadings, which was in line with the idea that an increased drying rate favored kinetic trapping and thereby the formulation of supersaturated ASDs. On the other hand, an increased drying rate did result in poorer phase behavior of ASDs of NAP, while a lower evaporation rate resulted in kinetic stabilization of higher drug loadings. These findings could be related to the relative position of the T_g of the ASD to the T_{out}, where the solid phase crystallization tendency was increased due to the smaller temperature difference. Hence, the drying air temperature should be high enough to enable kinetic trapping, but in balance with the potentially unfavorable impact of a high T_{out} on the crystallization tendency. Moreover, even when higher drug loadings could be kinetically stabilized by altering the process parameters, the improvement was limited. Hence, the phase behavior of these ASDs of FNB and NAP was predominantly determined by the API-polymer-solvent combination rather than the process parameters applied.

Acknowledgements

The authors would like to thank Fonds Wetenschappelijk Onderzoek Vlaanderen (FWO) and Laboratoires SMB for their support. Danny Winant (Materials engineering, KU Leuven), Jasper Beyens (Pharmaceutical analysis, KU Leuven) and Gunther Reekmans (Applied and analytical chemistry, Hasselt university) are acknowledged for technical assistance.

Chapter 7

Solid-state analysis of amorphous solid dispersions: Why DSC and XRPD may not be regarded as stand-alone techniques

Results from this chapter are based on: **Dedroog, S., Pas, T.,** Vergauwen, B., Huygens, C., Van den Mooter, G., 2020. Solid-state analysis of amorphous solid dispersions: Why DSC and XRPD may not be regarded as stand-alone techniques. J. Pharm. Biomed. Anal. 178.

7.1. ABSTRACT

Amorphous solid dispersions (ASDs) are single phase amorphous systems, where drug molecules are molecularly dispersed (dissolved) in a polymer matrix. The molecular dispersion of the drug molecules is responsible for their improved dissolution properties. Unambiguously establishing the phase behavior of the ASDs is of utmost importance. In this paper, we focused on the complementary nature of (modulated) Differential Scanning Calorimetry ((m)DSC) and X-Ray Powder Diffraction (XRPD) to elucidate the phase behavior of ASDs as demonstrated by a critical discussion of practical real-life examples observed in our research group. The ASDs were manufactured by either applying a solvent-based technique (spray drying), a heat-based technique (hot melt extrusion) or mechanochemical activation (cryo-milling). The encountered limiting factors of XRPD were the lack of sensitivity for small traces of crystallinity, the impossibility to differentiate between distinct amorphous phases and its impossibility to detect nanocrystals in a polymer matrix. In addition, the limiting factors of (m)DSC were defined as the well-described heat-induced sample alteration upon heating, the interfering of residual solvent evaporation with other thermal events and the coinciding of enthalpy recovery with melting events. In all of these cases, the application of a single analytical technique would have led to erroneous conclusions, whilst the combination of (m)DSC and XRPD elucidated the true phases of the ASD.

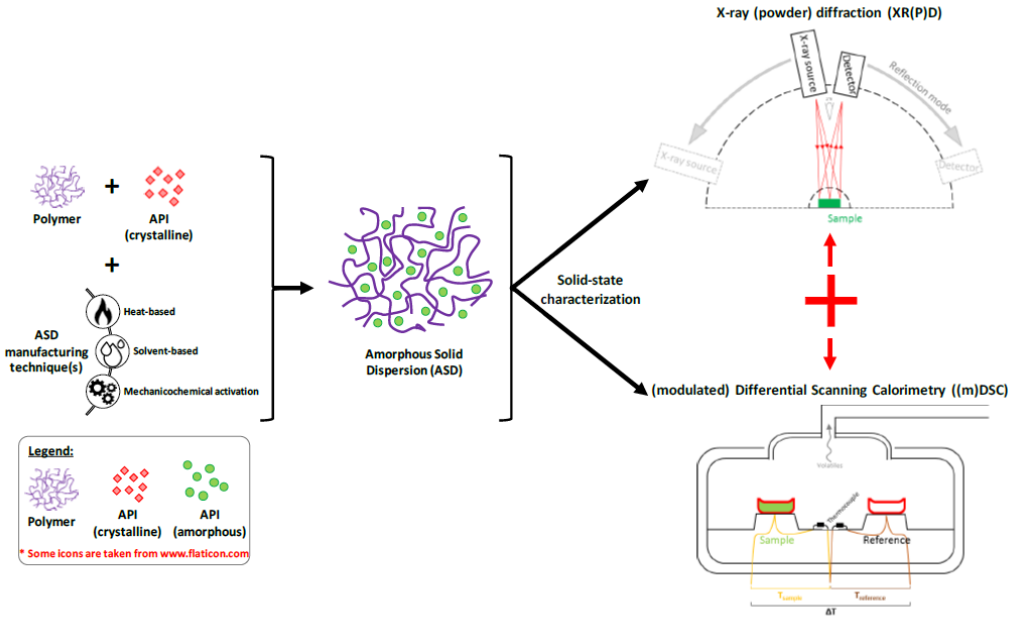

7.2. INTRODUCTION

One of the main issues in pharmaceutical development is that approximately 70% of new drug candidates are poorly water soluble[24,213], leading to low and erratic oral absorption and hence low bioavailability[12]. A promising strategy to increase their dissolution rate and solubility is the formulation of Amorphous Solid Dispersions (ASDs)[41], where an Active Pharmaceutical Ingredient (API) is molecularly dispersed in a polymer matrix, thereby forming a one phase amorphous system (Fig 7.1A, B). The API can be dissolved in the polymer either below or above its thermodynamic solubility in the polymer. The former situation leads to a stable single phase system (Fig 7.1A), while the latter is a supersaturated (metastable) system (Fig 7.1B). As described by Lehmkemper et al., this temperature-dependent solubility of an API in a polymer can be described by a state diagram (Fig 7.2.)[125]. Here, the solubility line (Fig 7.2., red line) makes a distinction between glass solutions (Fig 7.1A) and thermodynamically stable melts on the left, while the right comprises kinetically stable glasses (Fig 7.1B) and thermodynamically, kinetically unstable melts. When the temperature (Fig 7.2., green line) is installed below the glass transition temperature (T_g) of the system, supersaturated systems can form kinetically stable glasses (Fig 7.1B). Nevertheless, above the equilibrium solubility, polymers may not be able to stabilize the API completely and phase separation into a polymer-rich and drug-rich region can occur (Fig 7.1C). This can either already take place during manufacturing or as a result of physical aging, which can be accelerated by increased temperature or humidity. In addition, phase separation caused by mechanical influences or moisture uptake may also occur when an initially stable ASD (Fig 7.1A) was formulated. Since the stabilizing effect of polymers will be diminished in drug-rich regions, formation of phase separation is often a first step towards crystallization. From there, either amorphous drug clusters that are prone to crystallize will develop (Fig 7.1D, 7.1E) or crystallization will start immediately from the drug-rich region (Fig 7.1E). Next to that, crystal formation can also directly take place from a (supersaturated) ASD (Fig 7.1F). Eventually, the API will crystallize completely and the solubility advantage of manufactured ASDs will be lost (Fig 7.1G).

It should be noted that crystallization is much more complex than shown in Fig 7.1. In short, both nucleation and crystal growth are crucial for crystal formation. Both are influenced by thermodynamic factors, for example free energy and entropy, and kinetic factors, such as T_g and molecular mobility[214–217]. For more information, the reader is referred to excellent reviews concerning the crystallization mechanism[215,218]. Moreover, it should be taken into account that the crystallization tendency is clearly dependent on the API that is formulated, more specifically on its Glass Forming Ability (GFA)[65].

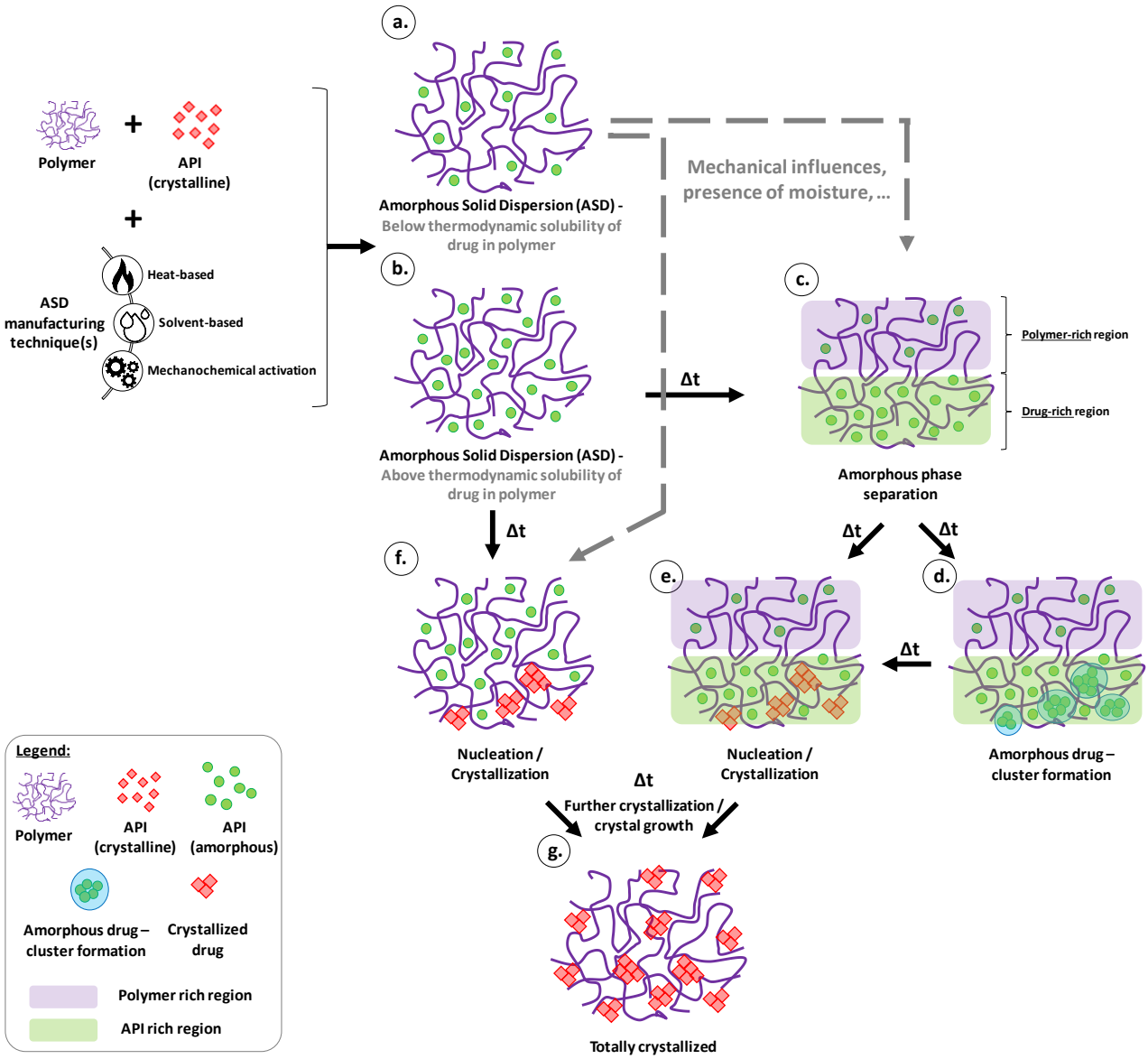

Figure 7.1. *General overview of the phase behavior in amorphous solid dispersions (ASDs). The three main mechanisms of ASD manufacturing are: heat-based (e.g., hot melt extrusion), solvent-based (e.g., spray drying) and mechanochemical activation (e.g., cryo-milling). Legend of different phase behavior encountered: (a) ASD mixed on the molecular level (below the thermodynamic solubility of the drug in the polymer), (b) ASD mixed on the molecular level (above the thermodynamic solubility of the drug in the polymer), (c) phase separation into drug- and polymer-rich phase, (d) amorphous drug-cluster formation over time in the drug-rich phase, (e) crystallization of drug in the drug-rich phase or crystallization from the amorphous drug-clusters that were formed, (f) direct crystallization directly occurring in the supersaturated ASD and lastly (g) total crystallization of the drug due to further crystallization/crystal growth.*

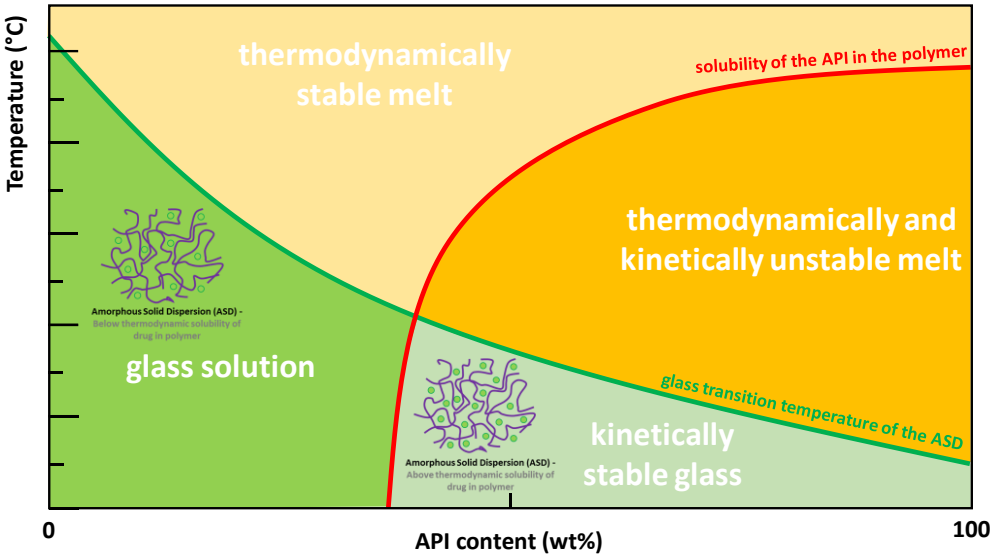

Figure 7.2. *State diagram on the conventional phase behavior of API/polymer systems in which the (temperature dependent) solubility of the API in the polymer and the optimum glass transition temperature of the ASD divide it into four areas, namely: a region that constitutes the thermodynamically stable melt (light orange), one that comprises the glass solution (green), one that contains the kinetically stable glass (light green), and one that is the thermodynamically and kinetically unstable melt (orange). The glass solution can be assigned to the situation in Fig 7.1a and the kinetically stable glass to that in Fig 7.1b.*

It is well known that miscibility of API and polymer(s) is indispensable for the physical stability of ASDs[219]. As a result, detection of (the early onset of) these differences in physical structure of ASDs (as illustrated in Fig 7.1.) is of utmost importance. Hence, a broad range of complementary analytical techniques can be applied (each having its own features). In accordance, Table 7.1. summarizes existing techniques and their classification according to which solid-state characteristics they can disclose. Only the first two characteristics, *i.e.,* crystallinity/amorphicity and phase behavior, can be correlated with Fig 7.1. Here, phase behavior can refer to both amorphous-amorphous and amorphous-crystalline phase separation, meaning that the API can be in its amorphous or crystalline state. Hence, techniques classified under crystallinity/amorphicity can distinguish between amorphous (Fig 7.1A, B, C, D) and (partially) crystalline (Fig 7.1E, F, G) solid dispersions. By determining the phase behavior, a distinction between miscible (Fig 7.1A, B) and phase separated (Fig 7.1C, D, E, F) solid dispersions can be made. Next to these properties, the presence of API-polymer interactions, the molecular mobility, and the particle morphology are important solid-state characteristics to consider during ASD formulation (Table 7.1.).

***Table 7.1**. An overview of the solid-state characterization techniques in ASD formulation. The analytical techniques are classified according to which solid-state characteristics they can disclose crystallinity/amorphicity, miscibility, alpha and beta molecular mobility and particle morphology. Since the focus of this work is the complementary nature of (m)DSC and XRPD, they are depicted in bold. For both the principles and applications of the enumerated analytical techniques, the interested reader is referred to excellent reviews (a = [220], b = [68], c = [221], d = [222], e =[50], f = [65], g = [223] h = [224]). In addition, it should be noted that hyphenated techniques, e.g., DSC-TGA or DSC-Raman, will strengthen the power of the obtained results.*

Structural information	Analytical techniques
Crystallinity/amorphicity	- **X-ray powder diffraction (XRPD)[a,b,e]** - **Modulated differential scanning calorimetry (mDSC)[a,b,e,f]** - Infrared spectroscopy (IR)[a,b,d,e] - Raman spectroscopy[a,b,d,e] - Solid state nuclear magnetic resonance (ssNMR)[a,b,e,f] - Small-angle and wide-angle X-ray scattering (SAXS and WAXS)[a,g] - Dynamic mechanical analysis (DMA)[b,e,f] - Hot-stage microscopy (HSM)[a] - Localized thermal analysis (LTA)[a,e] - Dielectric relaxation spectroscopy (DRS)[a,e,f] - Terahertz pulsed spectroscopy (TPS)[a,c,e] - Second order nonlinear optical imaging of chiral crystals (SONICC)[e]
Miscibility	- **Modulated differential scanning calorimetry (mDSC)[a,b,e,f]** - (Micro)-Raman spectroscopy[a,b,d,e] - Dielectric relaxation spectroscopy (DRS)[a,e,f] - Thermally stimulated current (TSC) - Solid state NMR (ssNMR)[a,b,e,f] - Dynamic mechanical analysis (DMA)[b,e,f] - Atomic force microscopy (AFM)[b] - Localized thermal analysis (LTA)[a,e] - Positron annihilation lifetime spectroscopy (PALS)[e] - Fluorescence resonance energy transfer (FRET)[e]
Molecular mobility	- **Modulated differential scanning calorimetry (mDSC)[a,b,e,f]** - Raman spectroscopy[a,b,d,e] - Dielectric relaxation spectroscopy (DRS)[a,e,f] - Thermally stimulated current (TSC)[e] - Solid state NMR (ssNMR)[a] - Dynamic mechanical analysis (DMA)[b,e,f] - Terahertz pulsed spectroscopy (TPS)[a] - Positron annihilation lifetime spectroscopy (PALS)[e]
Interactions	- Infrared spectroscopy (IR)[a,b] - Solid state NMR (ssNMR)[a,b,e,f] - Raman spectroscopy[a,b,d,e] - Inverse gas chromatography (IGC)[e]
Morphology	- Dynamic vapor-sorption analysis (DVS)[a] - Atomic force microscopy (AFM)[b,e] - Time-of-flight secondary ion mass spectrometry (ToF-SIMS)[e] - X-ray photoelectron spectroscopy (XPS)[e] - Scanning electron microscopy (SEM)[b,e] - Transmission electron microscopy (TEM)[e] - (Hot-stage) Polarized light microscopy ((HS)PLM)[b] - Hot-stage microscopy (HSM)[a]

In this paper, we will highlight the two most commonly applied analytical techniques for solid-state characterization of ASDs, namely (modulated) Differential Scanning Calorimetry ((m)DSC) and X-Ray Powder Diffraction (XRPD). Most importantly, we would like to invigorate the importance of their complementary nature and to stress the remaining uncertainty about the solid-state of ASDs in case only one of both is used. As summarized in Table 7.1., both approaches exhibit information about the presence and the quantity of crystalline and amorphous material, while (m)DSC thermograms can also withhold information about the miscibility and the molecular mobility of the system. For the latter, the interested reader is referred is to comprehensive reviews on structural relaxation measurements[65,225].

To demonstrate the different aspects that (m)DSC and XRPD can uncover, Fig 7.3. illustrates a comparison between (m)DSC thermograms and XRPD diffractograms. The presence of crystalline material reflects itself either in Bragg peaks in case of XRPD or in a melting endotherm in case of (m)DSC (Fig 7.3A). Both the position of the Bragg peaks (° 2θ) and the melting point (°C) are characteristic for a specific polymorph (Fig 7.3B). In addition, (re)crystallization can take place upon heating during DSC analysis, which is detectable as an exothermic peak (Fig 7.3C). When samples are only partially crystalline, Bragg peaks will be smaller and superimposed on amorphous halos in XRPD, whilst melting endotherms will be smaller for (m)DSC (Fig 7.3D). On the other hand, the presence of amorphous material results in amorphous halos in XRPD and T_gs in (m)DSC (Fig 7.3E). Presence of one single T_g indicates that API and polymer are molecularly dispersed, while amorphous-amorphous phase separation will present itself as two distinct T_gs. In (m)DSC, the total heat flow can be deconvoluted into the reversing heat flow (the heat capacity component) and the non-reversing heat flow (the kinetic component). This makes separation of some overlapping events possible. In this particular illustration, the T_g can be determined from the reversing heat flow, while the total heat flow contains all events. In the total heat flow, a T_g can be superposed with an endothermic event, namely enthalpy recovery (Fig 7.3E'). This event can increase with physical aging and can be used to determine molecular mobilities of these systems[225]. In addition, deconvolution of the total heat flow makes it possible to separate solvent evaporation endotherms from T_gs (Fig 7.3F).

This demonstrates that both (m)DSC and XRPD can resolve physical structures of ASDs, with (m)DSC having the possibility to discriminate additional events that occur during heating of the sample. Subsequently, (m)DSC is generally more sensitive to detect crystalline material than XRPD. Nevertheless, the combined use of both techniques is of utmost importance for the solid-state characterization of ASDs[65,219]. It is well known that sample alteration can take place during (m)DSC measurements. For example, Bikiaris et al. described that felodipine dissolved in PEG during DSC analysis, while their Wide-Angle X-ray Scattering (WAXS) analysis showed the presence of crystalline material[158]. Hence, a non-destructive method such as XRPD is valuable to evaluate the physical

structure at Room Temperature (RT). Additionally, the application of a modulated heating rate makes it possible to separate glass transitions from overlapping kinetic signals, but isolation of different kinetic signals is not possible (if they overlap). Consequently, a T_m or a crystallization event cannot be evaluated separately from a solvent evaporation endotherm that might interfere.

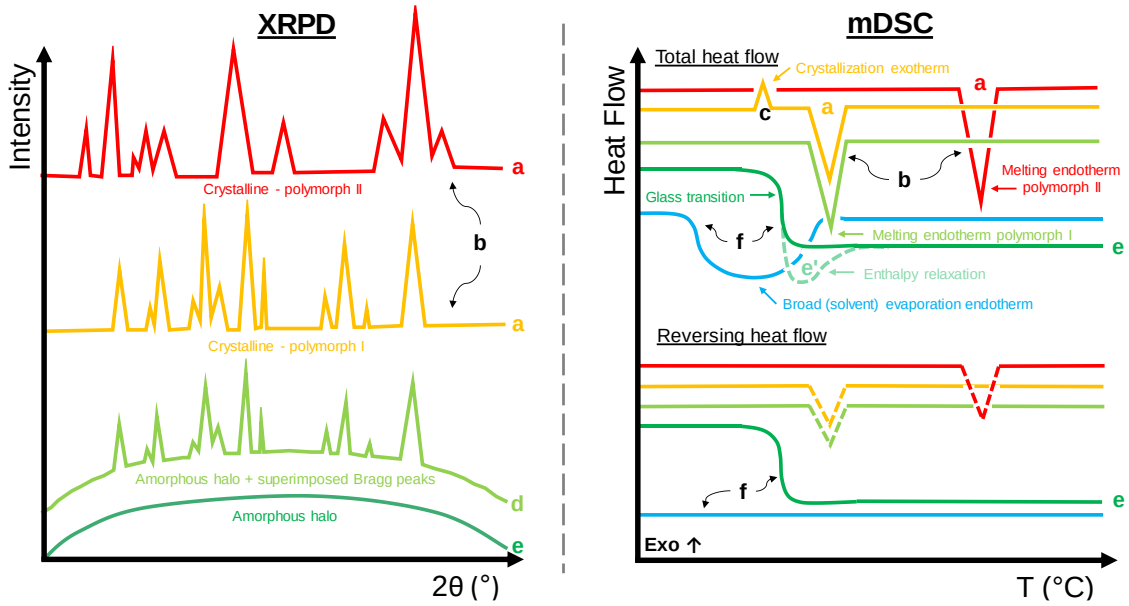

Figure 7.3. *Illustration of the different physical structures that can be elucidated by (m)DSC and XRPD: the XRPD diffractogram(s) illustrates (a) both crystalline materials exhibiting Bragg peaks, (b) distinction between polymorphs as they demonstrate different diffraction patterns, (d) partial amorphous material which presents itself as superimposed Bragg peaks on an amorphous halo and (e) amorphous material (or melted/dissolved) to demonstrate an amorphous halo without reflections. The (m)DSC thermogram(s) illustrates the following thermal events: (a) melting of crystalline material visible in the total heat flow and partially in the reversing heat flow observed as endothermic events, (b) different melting points (T_m) for distinct polymorphs, (c) crystallization of drugs as exothermic events only visible in the total (and non-reversing) heat flow(s), (e) a molecularly mixed system showing one glass transition (T_g) which can be deconvoluted into the reversing heat flow (in case phase separation would be present, two distinct T_gs would be observed), (e') a relaxated molecularly mixed system demonstrating (endothermic) enthalpy recovery superimposed on the glass transition which after deconvolution is only observable in the non-reversing heat flow and is not detectable in the reversing heat flow and (f) residual solvent evaporation appearing as broad endotherms which by deconvolution are only observable in the non-reversing heat flow and are not present in the reversing heat flow.*

In this paper, strengths and limitations of both XRPD and (m)DSC are discussed based on real-life examples. In all cases, using a single analytical technique would have led to erroneous conclusions about the phase behavior of the ASD. Since the combined use of XRPD and (m)DSC is not always evident or straight forward, we would like to emphasize on situations in which the application of these orthogonal analytical techniques was imperative. Notwithstanding, it has to be mentioned upfront that the cases discussed in this work are not exhaustive and that it may be possible to encounter other limitations of using (m)DSC or XRPD as stand-alone technique for the solid-state analysis of ASDs.

7.3. MATERIALS AND METHODS

7.3.1. Materials

Naproxen (PubChem CID: 156391) was obtained from Certa (Braine-l'Alleud, Belgium), whilst fenofibrate (PubChem CID: 3339) was purchased from Hangzhou Dayangchem Co. (Hangzhou City, China), indomethacin (PubChem CID: 3715) and ketoconazole (PubChem CID: 456201) from ABC Chemicals (Wauthier-Braine, Belgium) and itraconazole (PubChem CID: 55283) from Janssen Pharmaceutica NV (Beerse, Belgium). Chemical structures are depicted in Fig 7.4. Methanol (MeOH) 99.9% was obtained from ACROS Organics (Geel, Belgium) and dichloromethane (DCM) from Fisher Scientific (Leicestershire, U.K.). Bovine serum albumin (BSA), heat shock fraction, pH 7, ≥ 98%, was obtained from Sigma-Aldrich Chemie GmbH (Steinheim, Germany). Gelatin 50PS, supplied by Rousselot bvba (Gent, Belgium), was manufactured using an acid-pretreatment (Type A process) and is characterized by having a Bloom value of 56 grams, a viscosity at 6.67% (w:w) of 1.75 mPa.s, and an isoelectric point of 8.5. Hydroxypropylmethyl cellulose (HPMC 5 mPas) was obtained from Colorcon (Idstein, Germany) and Kollidon 25 (= Polyvinylpyrrolidon K25 = PVP K25) and Kollidon VA 64 (= Polyvinylpyrrolidon vinylacetate = PVPVA) were received from BASF (Ludwigshafen, Germany).

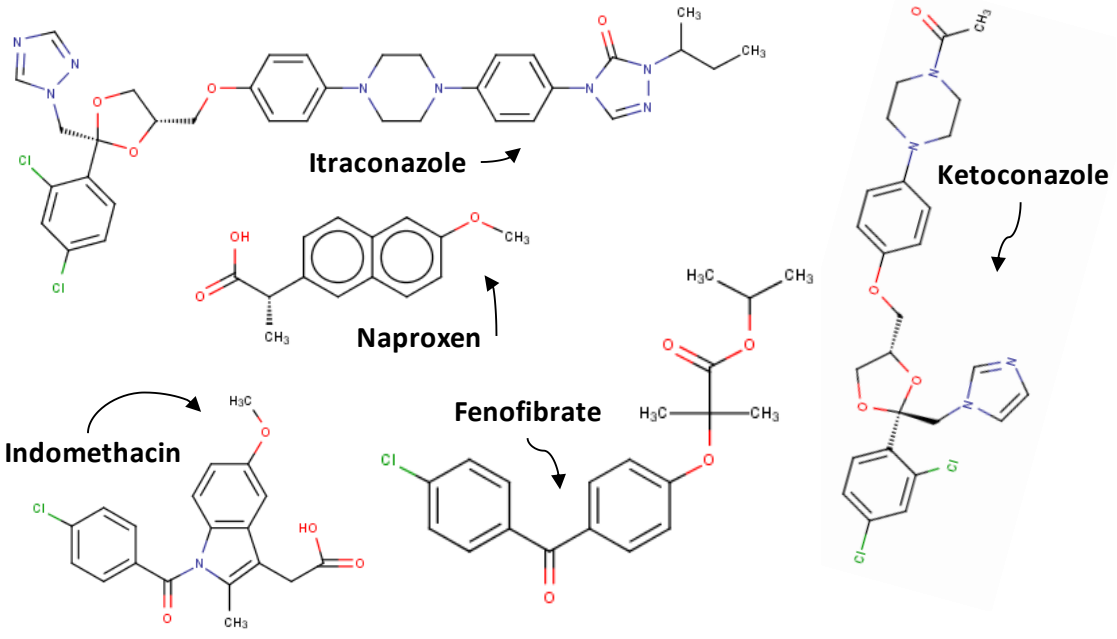

***Figure 7.4**. Chemical structures of fenofibrate, indomethacin, itraconazole, ketoconazole and naproxen. Created with MarvinSuite software (ChemAxon).*

7.3.2. Preparation of amorphous solid dispersions

7.3.2.1. Preparation of amorphous solid dispersions by cryo-milling (CRYO)

ASDs were prepared by concomitantly milling powder mixtures at reduced temperature (liquid nitrogen ≈ -196 °C) in an oscillatory CryoMill (Retsch GmBH, Haan, Germany). In some cases, 1 g of drug-polymer mixtures was cryo-milled for 3 hours at 25 Hz in a 25 mL stainless steel grinding jar containing only one stainless steel bead of 15 mm. In other cases, 200 mg samples were prepared by using 5 mL jars containing a number, not exceeding three of 7 or 10 mm stainless steel beads by using the same equipment. To prevent "overheating/heating" of the jar, the 3 hours interval was spread evenly over six shorter intervals of 30 min at 25 Hz alternated with 5 min of oscillation at 5Hz. All samples were analyzed either immediately by (m)DSC and/or by XRPD or were stored in a freezer at T ≤ -28°C before analysis.

7.3.2.2. Preparation of amorphous solid dispersions by spray drying (SD)

Fenofibrate was spray dried in combination with PVPVA using a Buchi mini spray dryer B-190 (Buchi, Flawil, Switzerland). A binary solvent mixture of MeOH:DCM (1:1, v:v ratio) and a solid content of 10% w/v was used. The following process conditions were applied: drying air temperature of 52 °C, drying air flow rate of 33 m^3/hour, feed solution flow rate of 5 mL/min and an atomization air flow rate of 10 L/min. Immediately after spray drying, the ASDs were further dried in a vacuum oven for 4 days at 25 °C. All samples were analyzed either immediately by (m)DSC and/or XRPD or were stored in a freezer at T ≤ -28°C before analysis.

7.3.2.3. Preparation of amorphous solid dispersions by hot melt extrusion (HME)

Physical mixtures of the API (naproxen or indomethacin) and the polymer (HPMC or PVPVA) were prepared using a mortar and pestle and extruded using a Mini extruder (DSM Xplore, Sittard, The Netherlands). The barrel temperature was set at 160 °C, which is above the melting point (T_m) of both naproxen (155 °C) and indomethacin (159°C). For every sample, approximately 6 g was fed into the extruder and mixed for 5 min at 100 rpm. The extrudates were cooled on aluminum foil and milled using a laboratory cutter mill (Kika, Staufen, Germany). All samples were analyzed either immediately by (m)DSC and/or XRPD or were stored in a freezer at T ≤ -28°C before analysis.

7.3.3. Solid-state characterization of amorphous solid dispersions

7.3.3.1. X-ray powder diffraction (XRPD)

An automated X'pert PRO diffractometer (PANalytical, Almelo, The Netherlands) with a Cu tube (Kα λ = 1.5418 Å), and a generator set at 45 kV and 40 mA was used to carry out XRD experiments (specified in next sections).

Transmission mode measurements at room temperature

Measurements in transmission mode were performed at room temperature, using Kapton® Polyimide Thin-films (PANalytical, USA). The selected experimental settings included a continuous scan mode from 4° to 40° 2θ with 0.0167° step size and 400 s counting time. The diffractograms were analyzed using X'Pert Data Viewer (Version 1.7, PANalytical, Almelo, The Netherlands).

Temperature resolved XRPD-measurements

For temperature resolved XRPD-measurements, an Anton Paar sample stage (TTK450 Sample Stage) was applied. The analyses were carried out by collecting several consecutive diffractograms by increasing the temperature with 10 °C for every subsequent measurement after starting at 25 °C (25 °C → 35 °C → 45 °C → … → X °C, respectively). The selected experimental settings included a continuous scan mode from 4 ° to 40 ° 2θ with 0.0167 ° step size and 400 s counting time. The diffractograms were analyzed using X'Pert Data Viewer (Version 1.7, PANalytical, Almelo, The Netherlands).

7.3.3.2. Modulated differential scanning calorimetry ((m)DSC)

A Q2000 DSC (TA Instruments, Leatherhead, U.K.) was used for assessing the thermal behavior of the ASDs. It was equipped with a refrigerated cooling system (RCS90) accessory under a dry nitrogen purge at a flow rate of 50 mL/min. Before measuring, routine calibration was carried out using indium standard for temperature and enthalpy calibration, while sapphire was used for heat capacity calibration. Samples were prepared by accurately weighing 1 – 5 mg of the sample into standard aluminum pans provided by TA instruments (Zellik, Belgium) followed by crimpling with aluminum standard lids (Zellik, Belgium). All samples were heated at a rate of 2 °C/min within the range of -15 °C to 230 °C depending on the characteristics of the API and the polymer. At the same time, temperature was modulated with an amplitude of either 0.212 °C every 40 s or 0.5 °C every 30 s. DSC thermograms were acquired and analyzed by using the Universal Analysis software (version 5.5, TA Instruments, Leatherhead, UK).

7.3.3.3. Scanning electron microscopy (SEM)

In case morphology and particle size examination was requested, Scanning Electron Microscopy (SEM) images were acquired. By means of double-sided carbon tape, collected powders were adhered to SEM stubs as first sample preparation step. Subsequently, they were all platinum coated with a SCD-030 Balzers Union sputter-coater (Oerlikon Balzers, Balzers, Liechtenstein) for further analysis. SEM images were recorded by a Phillips XL30 SEM-FEG (Philips, Eindhoven, The Netherlands) equipped with a Schottky field emission electron gun and a conventional EverhartThornley secondary electron detector. Spot size 3 was selected and the acceleration voltage was set at 2, 5, 10, 15 or 20 kV respectively, depending on the needs.

7.3.3.4. Thermogravimetric analysis (TGA)

To determine the amount of residual solvent in the spray dried samples, a thermogravimetric analyzer SDT Q600 (TA-Instruments, Leatherhead, UK) was used. The samples were heated at 5 °C/min to 125 °C in ambient atmosphere and their weight loss in function of temperature was recorded. All TGA curves were analyzed using the Universal Analysis software (Version 5.5, TA Instruments, Leatherhead, UK).

7.4. RESULTS AND DISCUSSION

In the upcoming sections a selection of real-life examples are discussed for which neglecting the combined use of complementary techniques like (m)DSC and XRPD would have led to ambiguous results because of "missing" information. Hence, the relevance of using both analytical techniques to resolve the solid-state characteristics of ASDs is demonstrated.

7.4.1. Limiting factors of XRPD for ASD solid-state analysis

7.4.1.1. Lack of sensitivity to detect small traces of crystallinity

With conventional XRPD equipment (and conventional run times) detection limits of approximately 5% (or lower)[226,227], depending on the API, can be reached. This makes XRPD less sensitive to traces of crystallinity than (m)DSC. As a result, remaining crystalline traces, which can act as seeds for further crystal growth, are possibly overlooked in case amorphicity of ASDs is only evaluated by means of XRPD analysis.

An interesting case, illustrating this particular shortcoming of XRPD, is the 25% drug-loaded hot melt extrudate of naproxen and HPMC which solid-state investigation is depicted in Fig 7.5. If decision-making had only taken its diffractogram into account (Fig 7.5b), full amorphicity of the ASD would have been assumed because of lack of Bragg peaks. Contrarily, this was not the case when taking (m)DSC data into consideration (Fig 7.5A). Thermal analysis revealed a small but clearly distinguishable endothermic melting event (T_m) at 118 °C. This corresponded to a residual drug crystallinity of approximately 1.24%, based on the heat of fusion of naproxen's crystalline form (T_m = 115.7 °C), which XRPD was unable to detect. The observed lower melting point of naproxen, 118 °C instead of 155.7 °C (T_m of the starting material), was devoted to melting point depression as to the best of our knowledge no polymorphs have been reported. In addition, formulation of higher drug loadings of naproxen with HPMC (up until 35%) resulted in the same discrepancy between (m)DSC and XRPD analysis (see Chapter 3). Based on thermal analysis, a drug loading of 35% corresponded to a residual crystallinity of approximately 4.83%, which was not detectable using XRPD (data not shown). For higher drug loadings, both (m)DSC and XRPD analysis would have disclosed the higher amount of residual crystallinity.

In this regard, it becomes clear that (m)DSC has a lower detection limit than XRPD for the determination of small amounts of crystalline material. It should be emphasized that the detection of any crystalline content is of utmost importance to maximize the physical stability of the ASDs. Notwithstanding, the detection of a small amount of crystalline content may still be challenging using (m)DSC. Hence, in case of uncertainty, other analytical techniques may be inquired (Table 7.1.). For

example, in recent times, Second Order Non-linear optimal Imaging of Chiral Crystals (SONICC) is applied for the detection of crystallinity in ASDs of chiral APIs that were amorphous using conventional analytical techniques[65,228].

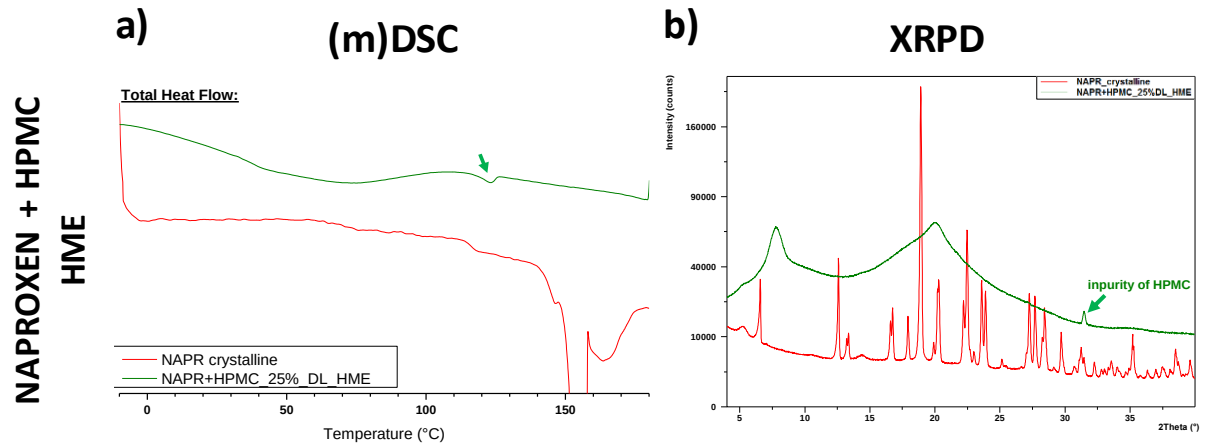

Figure 7.5. *Solid-state characterization by (m)DSC and XRPD demonstrating the lack of sensitivity to detect small traces of crystallinity by XRPD. a) (m)DSC thermograms of hot-melt extruded naproxen and HPMC at a drug loading of 25% (dark green) and crystalline naproxen (red) b) Corresponding XRPD diffractograms (same color coding as for (m)DSC). The sharp peak in the diffractogram of the ASD with HPMC originates from a crystalline impurity present in the polymer. The (reversing) heat flow (a) and intensities (b) are shown as arbitrary units.*

7.4.1.2. Impossibility to differentiate between distinct amorphous phases

A second limiting factor of XRPD analysis is that no discrimination between distinct amorphous phases can be made. This would be desirable to uncover amorphous-amorphous phase separation in a polymer-rich and a drug-rich phase, if present. As mentioned, detection of this particular phenomenon is of utmost importance as phase separation is deemed a strong precursor for nucleation and subsequent crystallization. Fortunately, due to their complementary nature, discrimination between these phases is possible with (m)DSC where distinguishable glass transitions can be exhibited.

More specifically, Fig 7.6. illustrates examples of 45% drug-loaded indomethacin-PVPVA and 35% drug-loaded naproxen-PVPVA extrudates. In both cases, XRPD analysis assigned lack of crystallinity as illustrated by the absence of Bragg peaks in their corresponding diffractograms (Fig 7.6B, D). Without further characterization, one would not have been able to state unambiguously that indomethacin was molecularly dispersed in the PVPVA matrix. Hence, additional (m)DSC data (Fig 7.6A) was necessary for further elucidation. In case of the 45% drug-loaded indomethacin-PVPVA, the (m)DSC thermogram displayed two distinct T_gs at approximately 83 °C (indomethacin-rich phase) and 101 °C (PVPVA-rich phase), indicating the presence of amorphous-amorphous phase separation. This became more clear when plotting the derivative of the reversing heat flow, which is depicted in Fig 7.6A and 7.6C. Since this derivative exhibits peaks at the position of the T_gs, it helps to distinguish the exact position and width of the T_gs. For the 35% drug-loaded naproxen-containing extrudate, on the other hand, no phase

separation had occurred as was clear from the presence of a single T_g at 63.3 °C, showing itself as a single peak in the derivative at the same temperature (Fig 7.6C). Thus, although both ASDs were X-ray amorphous, (m)DSC analysis clarified their structural differences. Hence, this case clearly indicates that the analytical gap in solid-state characterization with XRPD can be filled by performing (m)DSC analysis. As a result, (m)DSC provided additional information about the physical structure of the ASDs, which XRPD analysis lacked.

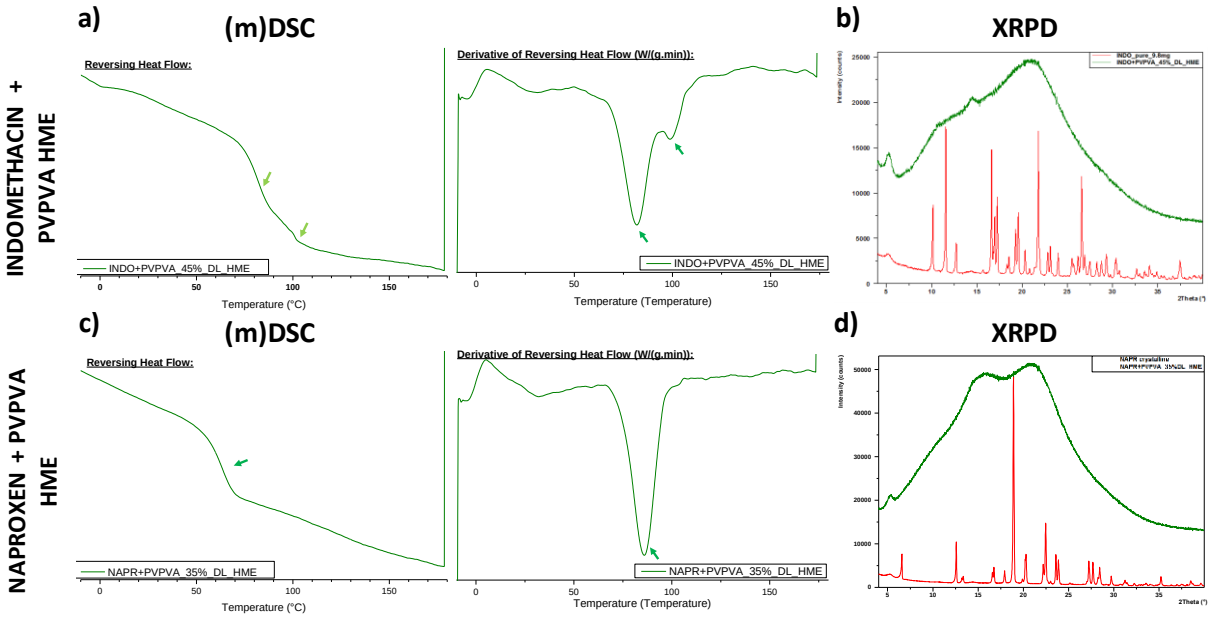

***Figure 7.6**. Solid-state characterization by (m)DSC and XRPD demonstrating the impossibility of XRPD to differentiate between distinct amorphous phases. a) and c) (m)DSC thermograms of hot-melt extruded ASDs of indomethacin (45%) or naproxen (35%) and PVPVA (dark green). The total heat flow, the reversing heat flow and its derivative are shown. b) and d) accompanying XRPD diffractograms of the same samples (crystalline drugs included – red diffractograms). The (reversing) heat flow (a and c) and intensities (b and d) are shown as arbitrary units.*

Although (m)DSC is most commonly used, Table 7.1. gives an overview of other analytical techniques that can be applied to assess the miscibility of the API and the polymer in ASD formulation. For this purpose, XRPD can also be combined with computational methods, namely Pair Distribution Function Calculations (PDFs), Pure Curve Resolution Methods (PCRM) and Alternate Least Squares (ALS)[222,229].

7.4.1.3. Difficulties in detecting nanocrystallinity and/or (nano)crystals suffering from a high degree of crystal defects

Nanocrystallinity and (nano)crystal defects constitute a third difficulty in XRPD analysis as they both contribute to Bragg peak broadening eventually leading to the formation of what seems to be an "amorphous" halo at the position of the most abundant Bragg peaks[229]. These two features, crystallite size and strain ("structural defects"), accordingly have to be kept in mind while interpreting XRPD results[230]. It should be noted that crystallite size does not equal particle size, as polycrystalline aggregates might be present. Decreasing crystallite size will correspond to less crystal planes per

crystal and hence a decreased chance on positive interference of reflected X-rays. The same is observed for crystal defects as planes are interrupted or imperfect. As a result, residual crystallinity greater than those mentioned in section 7.4.1.1. might be unobservable in a recorded XRPD diffractogram and hence catalogued as "XRPD amorphous".

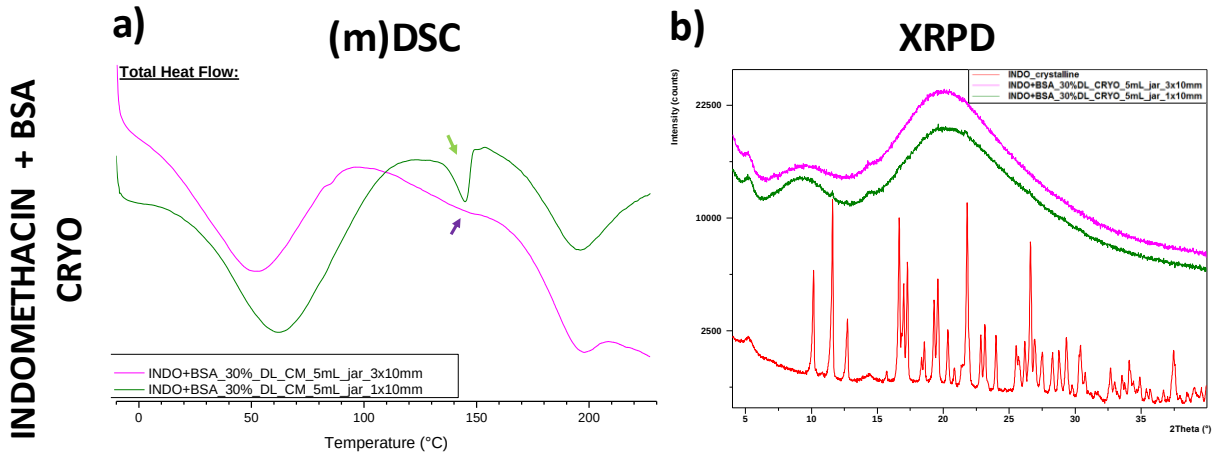

***Figure 7.7**. Solid-state characterization by (m)DSC and XRPD demonstrating XRPD its difficulty in detecting nanocrystallinity and/or (nano)crystals suffering from a high degree of crystal defects. a) ASDs consisting out of 30% indomethacin and BSA cryo-milled under two conditions: 5 mL grinding jar and 1 x 10 mm bead (dark green) and 5 mL grinding jar and 3 x 10 mm beads (purple). b) Corresponding XRPD diffractograms. The arrows indicate the positions of the melting points. The (reversing) heat flow (a) and intensities (b) are shown as arbitrary units.*

An example of this pitfall is amorphization by cryo-milling, because the mechanisms of amorphization during cryo-milling are deemed to be crystallite size reduction and crystallite defect induction, which in turn can transition towards the amorphous state[86]. In Fig 7.7., the solid-state evaluation of two cryo-milled ASDs, containing 30% indomethacin and BSA, is depicted. From the XRPD analysis, lack of crystalline content would have been assumed due to the sole presence of a diffuse "amorphous" halo (Fig 7.7B). On the other hand, thermal analysis of the one cryo-milled in the presence of a single 10 mm bead (Fig 7.7A) revealed a residual drug crystallinity of approximately 19.5%. Contrarily, the solid-state analysis of the ASD cryo-milled using three 10 mm beads resulted in a fully amorphous ASD based on both (m)DSC and XRPD analysis (Fig 7.7a, b).

In order to identify the root cause of XRPD's inability to detect these high amounts of residual crystallinity, SEM was performed (Fig 7.8.). SEM assessment of the starting materials and the cryo-milled samples clearly showed the transformation of nicely shaped crystals in the micrometer range before cryo-milling (Fig 7.8A, B) towards less structurally defined agglomerates in the nanometer range afterwards (Fig 7.8C, D). Hence, this might be an indication of the formation of nanocrystals being present and XRPD's inability to detect them.

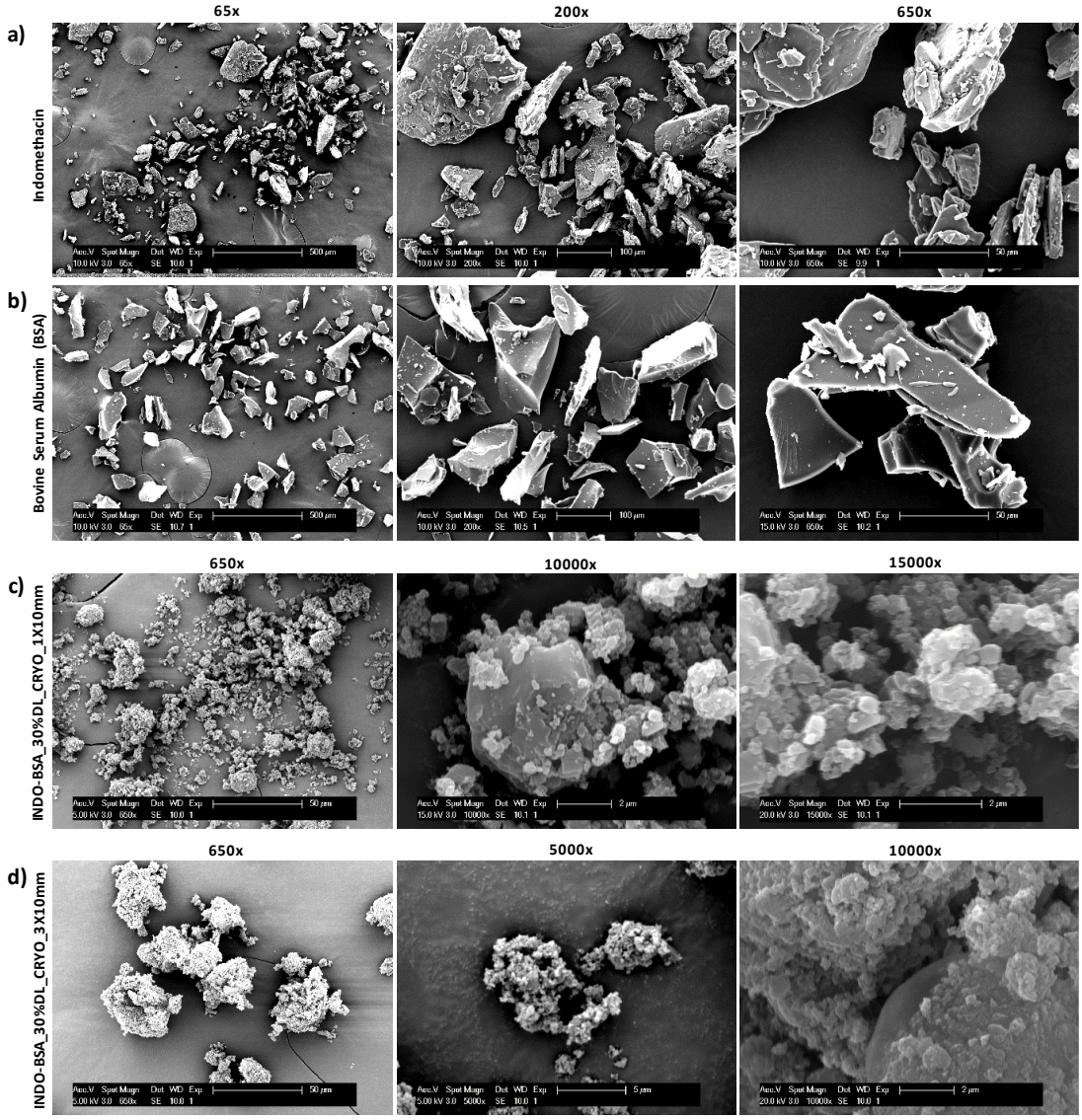

***Figure 7.8**. SEM assessment of the starting materials (indomethacin (a) and BSA (b)) and the cryo-milled ASDs containing 30% indomethacin (c and d) clearly visualizing the transformation of nicely shaped crystals with clearly defined crystal planes in the micrometer range before cryo-milling (a and b) towards less structurally defined agglomerates in the nanometer range afterwards (c and d).*

In addition to the abovementioned analytical technique (section 7.4.1.1.) that can detect nanocrystallinity, Small Angle X-ray Scattering (SAXS) is another promising technique for the detection of nanoheterogeneity[223]. Nevertheless, in this specific case, (m)DSC showed to be a good supplementary analytical technique to XRPD.

7.4.2. Limiting factors of (m)DSC for ASD solid-state analysis

Likewise, thermal characterization of ASDs by (m)DSC may not be regarded as a stand-alone technique for their solid-state characterization. From literature, it is already known that the obtained thermograms can differ depending on the application of different parameters, *e.g.,* heating rates or

isothermal hold time[231,232]. Nevertheless, even when applying the same set of parameters, one should keep the following limitations in mind to avoid misinterpreting.

In the upcoming sections, two pitfalls of (m)DSC analysis that were encountered will be discussed. In these cases, decision-making solely based on the acquired (m)DSC thermograms would have led to erroneous conclusions. The first being the well-known thermal change upon heating which might alter the original state of the sample[65,231,232]. The second being the presence of residual solvent revealing itself by a broad endothermic evaporation endotherm, which can potentially overlap with (exothermic) crystallization or (endothermic) melting events.

7.4.2.1. Sample alteration upon heating

Thermal analysis of two cryo-milled ASDs containing naproxen and either PVP or BSA (Fig 7.9A, D) resulted in what seemed to be a molecular dispersion of naproxen in both carriers (35% drug-loaded naproxen-PVP: T_g = 87.2 °C; 30% drug-loaded naproxen-BSA T_g = 121.65 °C). The lack of crystallinity was in contradiction with the detection of characteristic Bragg peaks for naproxen in the thermally unaltered XRPD samples (Fig 7.9B, E). As mentioned, it is considered that (m)DSC is more sensitive towards detection of crystalline traces and hence should have detected the residual crystallinity of naproxen. In order to further investigate this discrepancy, temperature-resolved XRPD analysis was performed on both samples (Fig 7.9C, F). Therefrom, it became clear that the diffractograms transitioned from being "XRPD crystalline" towards "XRPD amorphous" either within the range 85-95 °C (35% drug-loaded naproxen-PVP) or 135-145 °C (30% drug-loaded naproxen-BSA). Since this event took place at lower temperatures than the melting point of naproxen (T_m = 154.3 °C), it was caused by dissolution of naproxen particles in the PVP/BSA matrix instead of melting of naproxen itself. This discrepancy between XRPD and (m)DSC results was most likely caused by the extensive particle size reduction that took place during cryo-milling. As becomes clear from Fig 7.8. and section 7.4.1.2., nanocrystals were formed, resulting in an increased particle-particle contact. Hence, the combination of a low heating rate (2 °C/min) and the large surface area, and hence large contact area between drug particles and polymer, made dissolution in the polymer matrix possible. It should be noted that these examples include both synthetic and biopolymers, meaning that the dissolution event is not restricted to a certain type of polymer. In addition, dissolution occurred either at or above the T_g of the system, where the increased mobility of the system facilitated the dissolution process. The dissolution event was not clearly visible, what might be due to differences in dissolution of distinct domains at discrete temperatures making this event smeared out over a broad temperature range between T_g and T_m. As a result, both orthogonal techniques as well as a temperature-resolved set-up of XRPD were needed to uncover the physical state of the ASD at RT.

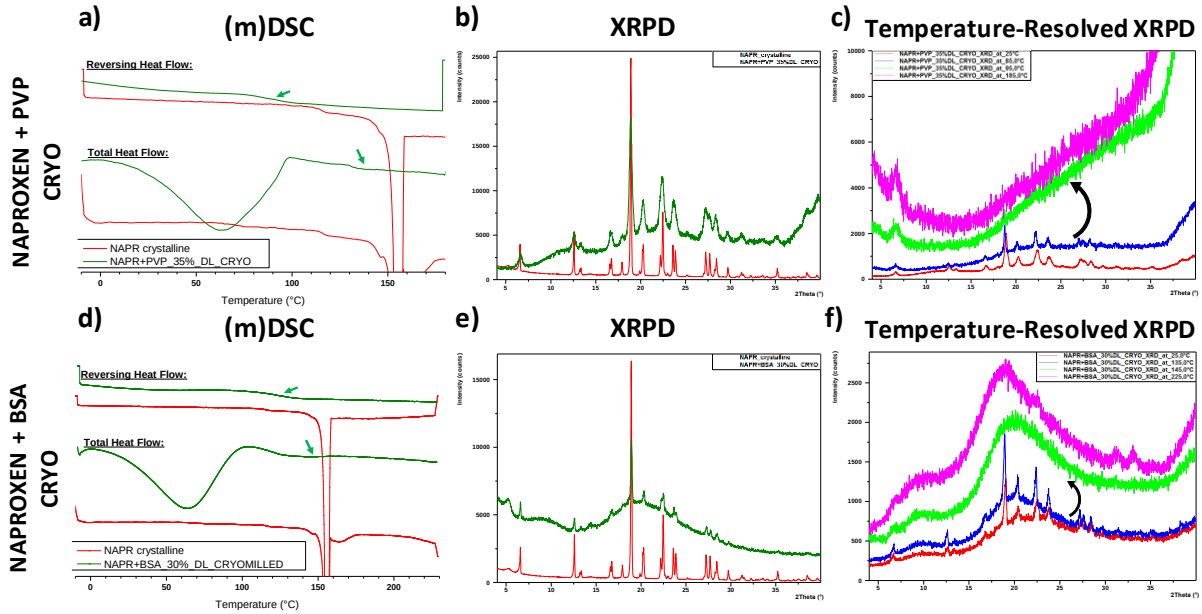

***Figure 7.9**. Solid-state characterization by (m)DSC and XRPD demonstrating sample change upon heating during thermal analysis. The (m)DSC thermograms (a and d), XRPD diffractograms (b and e) and temperature-resolved XRPD diffractograms (c and f) of cryo-milled naproxen with either PVP at a drug loading of 35% (top) or with BSA at a drug loading of 30% (bottom) are depicted. The ASDs are shown in dark green and crystalline naproxen in red. The arrows indicate either a T_g or the absence of a T_m. The (reversing) heat flow and intensities are shown as arbitrary units.*

7.4.2.2. Residual solvent evaporation interfering with other thermal events

Residual solvent evaporation can also constitute erroneous conclusions when only considering (m)DSC analysis, as thermal events occurring during evaporation are not always easily distinguished.

A first example that suffered from such interference is presented in Fig 7.10. Here, 5-35% drug-loaded spray dried ASDs of fenofibrate and PVPVA contained a substantial amount of residual solvent. More specifically, based on TGA-analysis, 4.27%, 3.86%, 3.90%, 2.87%, 2.55%, 1.96% and 2.19% residual solvent, respectively. It is evident from Fig 7.10. that XRPD-reflections were detected starting from 10% drug loading of fenofibrate whilst thermal analysis identified only drug loadings of 30% or higher as being partially crystalline. Hence, sample alteration during thermal analysis needed to be excluded.

Therefore, thermal analysis was performed subsequent to keeping the samples isothermal at 40 °C for 30 min. Here, for the 25% drug-loaded sample, a small melting event could be distinguished on top of the broad solvent evaporation endotherm (Fig 7.10D). Before application of a preheating step, it was not possible to detect a melting event for the 25% drug-loaded ASD (Fig 7.10A), while this additional step made it distinguishable. This was an indication of the coinciding of the solvent evaporation endotherm with this event rather than dissolving of fenofibrate in PVPVA during heating. It should be noted that substantial isothermal hold times (or even at higher temperatures) or always implementing one should be handled with care as it will impact the thermal history[231]. For lower drug loadings, the melting endotherms were still not detectable as shown for the 20% drug-loaded ASD (Fig 7.10D), which

might be explained by the lower amount of crystalline material in these ASDs. Hence, temperature-resolved diffractograms of the 20% drug-loaded ASD were recorded from 25 °C to 125 °C. The most important diffractograms are presented in Fig 7.10c. Here, the existing reflections disappeared in the interval from 65 °C to 75 °C, which was attributed to melting of the residual crystalline fenofibrate. It should have been possible to detect this residual crystallinity during thermal analysis if the broad solvent evaporation endotherm did not coincide with the melting endotherm of fenofibrate. Consequently, one should pay attention to this particular limitation when analyzing APIs with a low melting point.

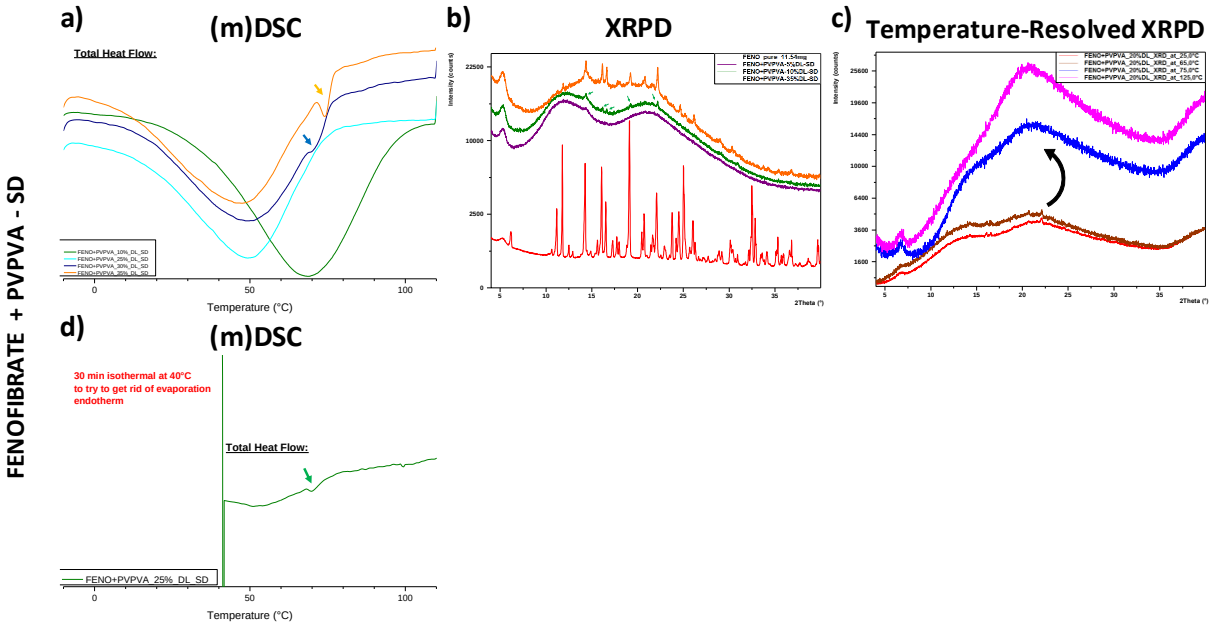

***Figure 7.10**. Solid-state characterization by (m)DSC and XRPD demonstrating the interference of residual solvent evaporation with melting during thermal analysis. a) (m)DSC thermograms of some selected spray-dried ASDs containing fenofibrate and PVPVA at drug loadings between 5% and 35%: 10% (dark green), 25% (light blue), 30% (dark blue) and 35% (orange). b) XRPD diffractograms of a 5%, 10% and 35% drug-loaded ASD of fenofibrate and PVPVA. c) Temperature-resolved XRPD diffractograms of the 20% drug-loaded sample. d) (m)DSC thermogram of the 25% drug-loaded sample after isothermal heating for 30 min at 40 °C took place before thermal analysis. The (reversing) heat flow (a, d) and intensities (b, c) are shown as arbitrary units.*

A second example concerns crystallization events occurring simultaneously with evaporation of water (and possible residual solvents in the starting material) during thermal analysis. Fig 7.11. and 7.12. show the solid-state analysis of four 30% drug-loaded ASDs, namely ketoconazole (Fig 11A and 12A) and itraconazole (Fig 7.11B and 7.12B), containing either BSA or gelatin 50PS as carrier, which all seemed to be (m)DSC crystalline and XRPD amorphous. At first sight, this was not surprisingly, as (m)DSC is more sensitive than XRPD for the detection of crystalline content. Nevertheless, residual drug crystallinities were high, namely 29.6% in case of ketoconazole and 49.1% in case of itraconazole. High residual crystallinities were also observed for the ASDs containing gelatin 50PS (Fig 7.12.). Although the possibility to form nanocrystals during cryo-milling should be kept in mind, it could have

been possible to detect these high percentages of drug crystallinity during XRPD analysis. Accordingly, temperature-resolved XRPD experiments were performed for two BSA-containing systems between 25 °C and 225 °C (Fig 7.11.). The obtained diffractograms revealed that crystallization of the drugs started between 65 °C-75 °C (ketoconazole) or 75 °C-85 °C (itraconazole). Secondly, disappearance of Bragg peaks was observed at 145 °C-155 °C (ketoconazole) and 165 °C-175 °C (itraconazole), which correlated well with the melting points of the pure drugs ($T_{m\ \text{ketoconazole}} \approx 147.95$ °C, $T_{m\ \text{itraconazole}} \approx 165.87$ °C). A closer look at the (m)DSC thermograms could insinuate onset of crystallization at the above-indicated temperature ranges. It should be noted that both evaporation and (re)crystallization can also be evaluated from the non-reversing heat flow; nevertheless, the same overlap was detected here.

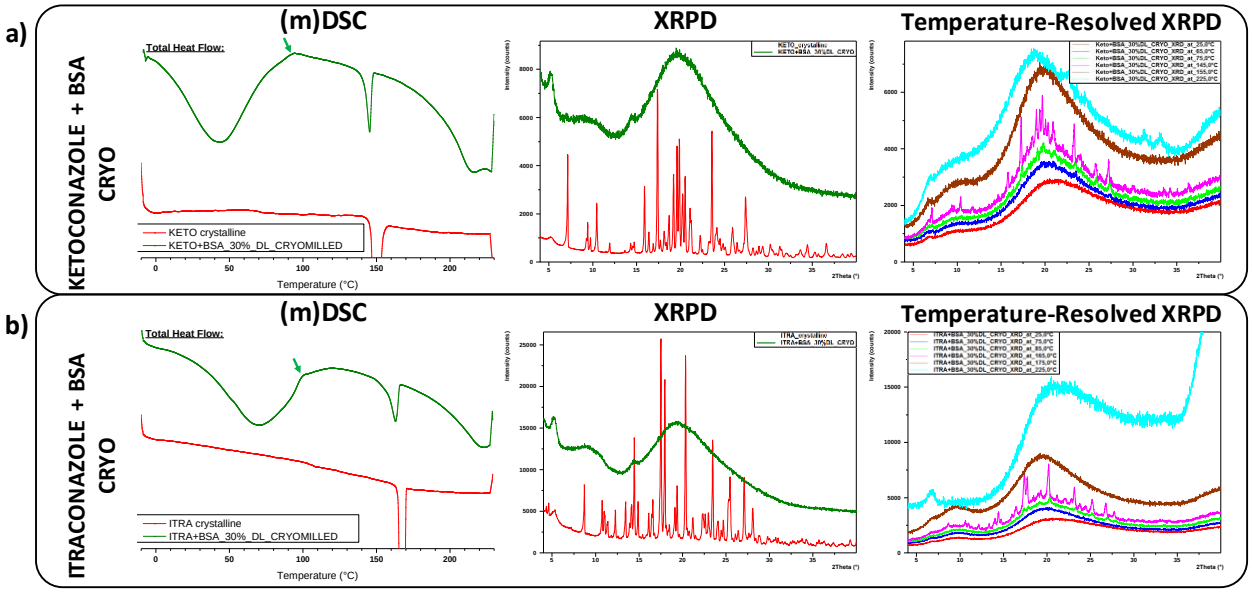

***Figure 7.11**. Solid-state characterization by (m)DSC and XRPD demonstrating the interference of residual solvent (water) evaporation with crystallization during thermal analysis. The (m)DSC thermograms (left), XRPD diffractograms (center) and temperature-resolved XRPD diffractograms (right) for 30% of ketoconazole (a) or itraconazole (b) cryo-milled with BSA as a carrier are shown. The crystalline APIs are shown in red and the cryo-milled ASDs in dark green. The (reversing) heat flow and intensities are shown as arbitrary units.*

When comparing these BSA-containing systems (Fig 7.11.) with those containing gelatin 50PS (Fig 7.12.), the exothermic crystallization events were more pronounced in case gelatin was used as carrier. To conclude, if only thermal analysis would have been applied, the initial crystalline contents of these samples would have been overestimated. Hence, this limitation of (m)DSC shows a combination of sample alteration during heating and the coinciding of a broad solvent evaporation endotherm with the possible detection of this alteration. Consequently, the application of (m)DSC and XRPD was essential in unambiguously determining the solid-state of these ASDs and hence proved their combined strength.

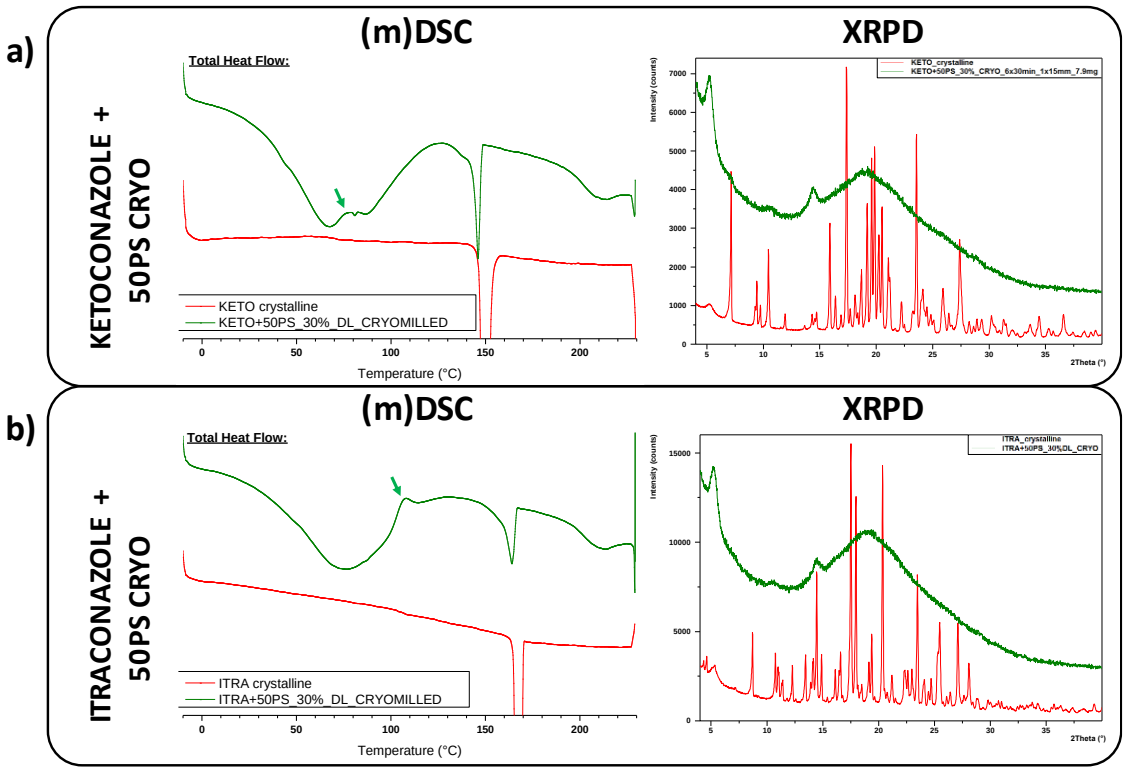

***Figure 7.12**. Solid-state characterization by (m)DSC and XRPD demonstrating the interference of residual solvent (water) evaporation with crystallization during thermal analysis. The (m)DSC thermograms (left) and XRPD diffractograms (right) for 30% of ketoconazole (a) or itraconazole (b) cryo-milled with gelatin 50PS as a carrier are shown. The crystalline APIs are shown in red and the cryo-milled ASDs in dark green. The (reversing) heat flow (a) and intensities (b) are shown as arbitrary units.*

7.4.2.3. Enthalpy recovery coinciding with melting events

The third encountered limitation of (m)DSC analysis is caused by the presence of another thermal event, namely enthalpy recovery. Because this event is the consequence of enthalpy relaxation, it can be used for relaxation measurements and estimation of the physical stability of ASDs. Fig 7.13. depicts the (m)DSC analysis (Fig 7.13A) and the XRPD analysis (Fig 7.13B) of a 30% drug-loaded ASD of indomethacin and HPMC, manufactured by cryo-milling. In this example, (m)DSC analysis revealed two endothermic events (partially overlapping with one another) in the total heat flow and a single T_g in the reversing heat flow (Fig 7.13A). In addition, XRPD diffractograms showed Bragg peaks that were characteristic for γ-indomethacin (Fig 7.13B). Hence, the two endothermic events in the total heat flow were assigned to melting of residual crystalline indomethacin and enthalpy recovery, from which the latter is always detected at the same position as the T_g. The coinciding of enthalpy recovery with a melting event, makes it difficult to detect crystalline traces. Hence, although in some cases there might still be an indication of crystalline traces in (m)DSC analysis, this overlap could give rise to erroneous conclusions about the physical structure of ASDs.

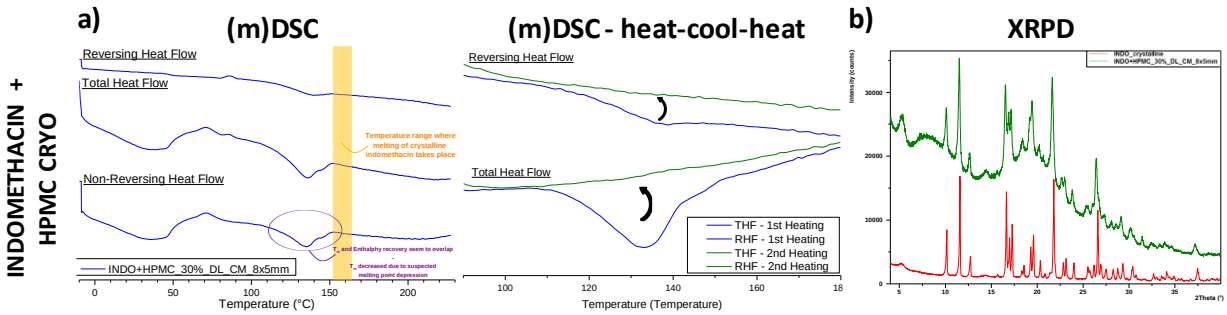

Figure 7.13. *Solid-state characterization by (m)DSC and XRPD demonstrating the coinciding of enthalpy recovery with melting events. The (m)DSC thermograms (a) and XRPD diffractograms (b) of cryo-milled indomethacin and HPMC at a drug loading of 30% are shown which were processed with 8 beads of 5 mm in a 5 mL grinding jar. The (reversing) heat flow (a) and intensities (b) are shown as arbitrary units.*

It should be noted that when applying a heat-cool-heat procedure in (m)DSC analysis, it could have been possible to differentiate between enthalpy recovery and melting. After the first heating cycle, the thermal history would have been erased; making that melting would have been the only endothermic event that could have been detected in the second heating cycle. Nevertheless, because of the miscible nature of indomethacin and HPMC, in the second heating cycle only a single T_g could be distinguished (Fig 7.13A). Therefore, the application of a heat-cool-heat procedure cannot resolve the overlap of enthalpy recovery and melting events for ASDs. This example clearly shows that both (m)DSC and XRPD analysis were indispensable for determining the correct physical structure of the ASDs.

7.5. CONCLUSION

In the present work, the importance of combining orthogonal analytical techniques for the solid-state characterization of ASDs was demonstrated. Six practical examples showed that the combined application of (m)DSC and XRPD made it possible to assign the correct physical state to the ASDs being evaluated. Herewith, limiting factors of (m)DSC and XRPD in solid-state analysis were linked to these practical examples and discussed into more detail to establish that their separate use can often lead to erroneous conclusions. It was demonstrated that lack of sensitivity, impossibility to differentiate between distinct amorphous phases and nanocrystallinity or (nano)crystal defects can be limiting factors in XRPD-analysis whilst thermal changes of samples upon heating and residual solvent evaporation coinciding with other thermal events can complicate solid-state characterization by (m)DSC. In all treated cases, both techniques were indispensable to characterize their initial solid-state unambiguously. Nevertheless, it should be mentioned that other techniques than (m)DSC and XRPD can also have their place in the characterization of ASDs even though (m)DSC and XRPD are established techniques.

Acknowledgements

We would like to acknowledge Rousselot N.V. (Meulestedekaai 81, 9000 Gent, Belgium), Laboratoires SMB (26-28 Rue de la Pastorale, 1080 Brussels) and Het Fonds voor Wetenschappelijk OnderzoekVlaanderen (FWO) for their financial support. The authors would also like to thank Prof. Bart Goderis (Polymer Chemistry and Materials, KU Leuven) and Bernard Appeltans (Drug Delivery and Disposition, KU Leuven) for technical assistance.

Chapter 8

General discussion

8.1. KINETIC STABILIZATION OF AMORPHOUS SOLID DISPERSIONS

The overall aim of this PhD thesis was to manufacture kinetically stabilized supersaturated ASDs and to evaluate factors that might determine the extent of supersaturation that could be achieved. To generate a supersaturated ASD, the API should be dissolved in the polymer matrix above its thermodynamic solubility limit, thereby forming a thermodynamically unstable mixture. In spite of the fact that the inherent instability of supersaturated systems can be a challenge for attaining a viable shelf life, there are two important reasons to prefer them over lower drug loaded systems. First, the present-day push for a lower pill burden requires the formulation of higher drug loadings as it might reduce the amount of daily dosage units required and thereby increase the therapeutic compliance of patients[144]. Second, the thermodynamic solubility of APIs in a polymer matrix is generally low, often even too low to reach therapeutically relevant concentrations[1].

Although supersaturated systems are thermodynamically unstable, they can be kinetically stabilized under the right circumstances. In this project, kinetic stabilization of supersaturated concentrations was achieved by kinetic trapping of an API in the polymer matrix, which was either a result of fast solvent evaporation leading to a fast viscosity increase during spray drying or rapid cooling of the liquid mixture upon exiting the die during hot melt extrusion. Accordingly, the important contribution of kinetic factors next to thermodynamic ones to the phase behavior of ASDs became abundantly clear. In Chapter 3, it was described that both spray drying and hot melt extrusion allowed to produce kinetically stabilized supersaturated ASDs of NAP that contained more API than the thermodynamic solubility limit as predicted by PC-SAFT[125,159]. Also by spray drying with IMC and PVPVA, the highest drug loading exceeded the equilibrium solubility limit (Chapter 4)[133,134]. For FNB and DZP, the equilibrium solubility limit in PVPVA was not yet established and could therefore not be compared to the maximum drug loadings determined in this work (Chapter 4). However, as both these APIs have no hydrogen bond donors and thus no hydrogen bonding potential with PVPVA, it could be expected that their solubility limit in PVPVA is lower compared to that of NAP and IMC[151]. As generally higher drug loadings could be obtained for DZP than for NAP, these DZP ASDs could also be considered as kinetically stabilized supersaturated systems.

On the other hand, in case of spray drying of NAP and PVP, the highest drug loading was found to be slightly lower than predicted by PC-SAFT (Chapter 3). However, the highest drug loadings were determined with intermediate steps of 5 wt%, and the maxim drug loading ranged from 30 to 35 wt%, in between which the solubility limit of 31.4 wt% was situated. Moreover, cryo-milling never enabled the formulation of supersaturated ASDs of NAP, independently of the polymer (Chapter 3). As the

thermodynamic solubility limit of an API in a polymer matrix defines the maximum API to polymer ratio for which physical instability is less likely to be an issue, this limit can be considered as the minimum drug loading that should be achieved during ASD manufacturing. When a lower maximum drug loading is found, process optimization might enable the formulation of this drug loading (or higher) (see section 8.3.2.). Hence, the use of a thermodynamic model, such as PC-SAFT, to predict the equilibrium solubility limit is an important tool during ASD development[132–135,145], yet it should be kept in mind that ASDs are per definition non-equilibrium systems and thus their phase behavior depends on both thermodynamic and kinetic factors.

Throughout the project, it became clear that several factors determined the success rate of kinetic stabilization of supersaturated ASDs. From the factors depicted in Fig 8.1., the influence of all formulation parameters, *i.e.,* the physicochemical characteristics of the API, carrier and solvent, the manufacturing technique and applied process parameters will be discussed in the following sections. Also environmental factors, *i.e.,* temperature and Relative Humidity (RH) of the surroundings, could influence the extent of supersaturation that could be achieved, and that both during development and during storage[125,145,233,234].

Figure 8.1*. Overview of factors that could influence the success rate of kinetic stabilization of supersaturated ASDs.*

8.2. IMPACT OF FORMULATION PARAMETERS ON KINETIC STABILIZATION

8.2.1. Is the extent of supersaturation inherent to the API?

In Chapter 4, two APIs that could hydrogen bond with PVPVA were studied, yet their crystallization tendency differed: according to the classification by Van Eerdenbrugh et al., NAP was a Glass Forming Ability (GFA) class I compound, *i.e.,* a fast crystallizer, while IMC was categorized as GFA class III, *i.e.,* a slow crystallizer[174]. When comparing the thermodynamic solubility limit of these APIs in PVPVA and the maximum amount of drug that could be kinetically stabilized using PVPVA, the extent of supersaturation was relatively higher for IMC. Although this could be related to the slower crystallization tendency of IMC, a relation between the GFA classification system and the extent of solid state supersaturation that can be obtained has not yet been proposed. Moreover, it has recently been described that GFA class III compounds do not necessarily give rise to single phase amorphous systems[235]. In addition to that, some authors describe a clear relation between the GFA and the physical stability of ASDs[236], while others do not[237]. Hence, to answer the title of this section: the potential for kinetic stabilization of supersaturated systems might to some extent be predetermined by the API, yet it also depends on multiple other factors, as described in the following sections. To make unambiguous statements about the relation between the GFA classification and the extent of supersaturation that can be obtained, much more API-polymer combinations should be considered.

8.2.2. Kinetic stabilization as factor for carrier selection

An ideal carrier must be successful at both stabilizing the amorphous API in its solid state and maintaining its supersaturated state upon dissolution long enough for absorption to take place[62]. In Chapter 3, PVP, PVPVA, HPMC and HPMC-AS were compared for this first aspect. Both using hot melt extrusion and cryo-milling, PVP was able to kinetically stabilize a higher amount of NAP, while in case of spray drying, PVPVA showed to be the best polymer to obtain high drug loadings of NAP. However, the thermodynamic solubility of NAP in PVP (*i.e.,* 31.4 wt%) is higher than that in PVPVA (*i.e.,* 20.7 wt%), thus it could have been expected that higher drug loadings were found using PVP, independently of the manufacturing technique. A possible explanation for this discrepancy is the influence of the solvent during spray drying. Both for PVP and PVPVA, MeOH, which can act as a hydrogen bond donor (and acceptor), was used. As PVP is known to hydrogen bond with MeOH[209] and VP is more available for hydrogen bonding with MeOH compared to VA (Chapter 6), there was relatively more of the better hydrogen bond acceptor available when PVP was used. The stronger interactions between MeOH and

PVP could leave less free PVP to hydrogen bond with NAP, which might explain the relatively lower drug loadings for NAP in PVP by spray drying. Another aspect that might explain this difference is the potential disadvantageous effect of the residual solvent on the phase behavior, which also depends on the affinity of the polymer for the solvent in question. Despite the fact that the impact of the solvent might be a plausible explanation for the difference between PVP and PVPVA, PVPVA was selected for all further investigations by spray drying.

Although it was clear that PVP and PVPVA were superior for kinetic stabilization of highly drug loaded ASDs of NAP, this does not neceseraly mean that they are better carriers for NAP. A carrier should also be able to maintain the supersaturated state during dissolution for a long enough time period, which was not taken into account in this work. Several authors have studied the supersaturation potential of carriers[152,238–241], where HPMC and HPMC-AS were generally good candidates. Moreover, it has been shown that HPMC-AS could be more effective in maintaining supersaturation than PVPVA, because of its slower dissolution rate[239]. Hence, to identify an ideal carrier, a balance between the kinetic stabilization potential and potential to stabilize the supersaturated state during dissolution is of utmost importance.

8.2.3. Impact of the solvent on kinetic trapping efficiency

In recent years, the contribution of the solvent to the phase behavior of (supersaturated) ASDs has gained significant interest[120,136,165–168,242]. However, up until now, the impact of a single organic solvent on the kinetic trapping efficiency was not yet established. In Chapter 4, it was described that the solvent determined the extent of solid state supersaturation that could be achieved by film casting and spray drying, yet it could not be related to the equilibrium solubility of the API in the respective solvent. This was an interesting finding as the common solubilizing capacity of the solvent for the API and its carrier is nowadays one of the most important solvent selection criteria[38,94]. In contrast, the potential of ternary state diagrams of API-polymer-solvent mixtures, which are based on the solubility of the API in the polymer-solvent mixture, to predict the phase behavior of ASDs using PC-SAFT has been described as well[136,138,242]. As mentioned above, an explanation for this discrepancy could be that the phase behavior of ASDs is determined by an interplay of kinetic and thermodynamic factors, while PC-SAFT only accounts for thermodynamic ones.

Another critical solvent characteristic is the volatility, which affects the evaporation rate and accordingly also the chance for kinetic trapping of the API in the polymer matrix in a supersaturated state. Correspondingly, as described in Chapter 6, the contribution of the solvent to the physical state was successfully related to the evaporation behavior and the presence of interactions in solution. In general, the higher the solvent evaporation, the higher the kinetic trapping efficiency and thus the

higher the amount of API that could be kinetically stabilized in PVPVA. Similarly, Wu et al. reported that the evaporation rate was even more critical than the polymer molecular weight and the drug to polymer ratio to decrease the extent of nucleation in ASDs[196].

In spite of the clear relation between the solvent, its evaporation rate and the degree of solid state supersaturation that could be obtained, there are a lot of other physicochemical characteristics that could be influenced by the solvent, such as the diffusional motion of solutes, the polymer conformation in solution and the viscosity. Moreover, together with the initial droplet diameter and the diffusional motion of the solutes, the evaporation rate determines the particle morphology (Chapter 1). To exemplify, PVPVA slowed down the evaporation rate of all solvents, yet this effect was more pronounced for the relatively faster evaporating solvents, which was explained by a faster concentration and viscosity increase, resulting in earlier crust formation (Chapter 6). Although this effect did not result in a different particle morphology when spray drying, it did in case of fluid bed coating, where a porous coating was observed for the faster evaporating Ac compared to a homogeneous coating for the slower evaporating MeOH[204]. The evaporation rate during spray drying is generally much higher compared to fluid bed coating, where evaporation has to take place from a surface. Hence, the very fast solvent evaporation during spray drying resulted in hollow, collapsed spray dried particles, independently of the solvent (except for PrOH).

As particle formation is a result of a complex interplay of multiple factors, a lot of research is being performed to gain more insight in this process[99]. Experimentally, single droplet drying techniques could be employed as a more simplified approach to droplet formation[100]. Several experimental set-ups could be applied: using a filament, an acoustic levitator, levitation by air flow, or a free-fall technique, from which the latter can resemble the drying process during spray drying best[100,103,243,244]. In this PhD project, a single droplet drying set-up using the free-fall technique was built in collaboration with Prof. Vetrano (Mechanical Engineering, KU Leuven) in order to record a difference in drying behavior between MeOH and Ac droplets. However, as the optimization of this set-up was a time consuming process, the experimental work will be continued by another PhD researcher in our group. Additionally, a lot of research is being performed about modeling the drying process, and that both during single droplet drying and spray drying[99].

8.3. INFLUENCE OF PROCESSING ON KINETIC STABILIZATION

8.3.1. Kinetic stabilization as factor for selection of a manufacturing technique

Despite the fact that some authors have compared manufacturing techniques one by one (mostly hot melt extrusion and spray drying), today it is not known how the selection of a manufacturing technique could influence the extent of solid state supersaturation that can be obtained. In this work, hot melt extrusion showed to be the most promising manufacturing technique to prepare highly drug loaded ASDs of NAP, which was related to the beneficial effect of heat on the dissolution of NAP in the polymers (Chapter 3). Similar results were obtained by Boel et al. for the manufacturing of ASDs of itraconazole and fenofibrate[245]. Likewise, Haser et al. reported that ASDs of 60 wt% NAP and PVP K25 contained a smaller crystalline fraction when prepared using HME compared to spray drying[123]. Moreover, crystal growth was much less pronounced in case of HME, which was explained by the fewer nucleation sites and the fact that they were better dispersed. Interestingly, the effect of the processing method on the physical stability was only observed for drug loadings above the thermodynamic solubility limit of NAP in PVP K25[123]. Also for felodipine and HPMC-AS, ASDs prepared using HME had a superior physical stability[246]. In general, these findings indicated that HME was not only better to kinetically stabilize higher drug loadings immediately after preparation (as was the case in this thesis), but also to maintain the supersaturated state over time. However, it should be kept in mind that this could also be influenced by the applied process parameters and downstream processing.

Cryo-milling gave rise to lower maximum drug loadings, even lower than the thermodynamic solubility limit of NAP in the polymers (Chapter 3). At first, this was related to insufficient process optimization, as a small scale up experiment from a 5 to a 25 mL grinding jar showed promising results with regard to the formulation of higher drug loadings. However, in the meantime, it was found that cryo-milling with synthetic polymers results in polymer degradation and polymer-assisted API degradation[91,92]. As a result, it is very likely that the actual NAP content in the ASDs was even lower than the theoretical drug loadings. Hence, cryo-milling was an even worse technique for kinetic stabilization of high drug loadings than initially described in Chapter 3. Moreover, these findings suggested that the manufacturing technique could also influence the polymer intrinsically (*e.g.,* stability, dissolution behavior) and thereby potentially also the extent of supersaturation that could be achieved. Nevertheless, this does not exclude cryo-milling as a promising amorphization technique: several authors have been successfully applying cryo-milling for the manufacturing of co-amorphous systems, where no polymer was used and thus no polymer-assisted degradation of the API(s) could take place[247,248].

Film casting was employed as another solvent based method to evaluate if the contribution of the solvent to the phase behavior was dependent on the manufacturing technique (Chapter 4). The maximum drug loadings obtained by film casting were generally lower than for spray drying, and thus this method resulted in poorer kinetic stabilization of supersaturated ASDs. This can be attributed to the lower evaporation rate in case of film casting, and thus less chance of kinetic trapping, resulting in lower drug loadings. In spite of that, the same trend was observed with regard to the contribution of the solvent to the phase behavior, independently of the technique. In addition to the already well-established predictive value of film casting for assessing the miscibility of compounds[163,164], this demonstrated that also the influence of a solvent could be predicted.

In addition to the techniques investigated in this work, it is possible that other manufacturing methods could be as good as HME (or better) for the kinetic stabilization of supersaturated systems. For instance, Ziaee et al. demonstrated that rotary evaporation resulted in more homogenous ASDs of ibuprofen than spray drying and electrospinning did[249]. Also new manufacturing approaches such as microwave *in situ* amorphization could potentially perform better[77].

8.3.2. What is the added value of process optimization for kinetic stabilization?

A lot of researchers have studied the impact of process parameters on the physicochemical characteristics of ASDs, which is frequently done using a Design of Experiments (DoE) [250–255]. Although the phase behavior of ASDs is often included as a response in a DoE, the extent of supersaturation that can be obtained as a result of kinetic stabilization is not. In this project, both for hot melt extrusion and spray drying, some process parameters were altered in order to investigate the potential effect of process optimization on the amount of API that could be kinetically stabilized in the polymer matrix.

In case of HME, both the effect of the barrel temperature and the presence of additional kneading blocks was investigated (Chapter 3). It was found that in case of PVP and PVPVA, the barrel temperature had to be installed above the T_m of NAP (*i.e.,* at 160 °C) in order to obtain a completely amorphous ASD, and that the temperature could not be installed higher, as PVP started to degrade at 150 °C. In spite of the fact that heat was an important energy input, the increase in barrel temperature was limited by the polymer degradation temperature. Also API degradation could be a limiting factor for further increasing the energy input, in which case spray drying might be a better alternative[256]. Moreover, there was no improvement in phase behavior when a continuous extruder with a kneading zone at two third of the barrel length was employed instead of the batch extruder. However, as a high shear configuration is known to give the best results with regard to mixing capacity[85,155], it is possible that the addition of more kneading zones could increase the extent of solid state supersaturation, yet this was not explored in this project.

In view of the decisive impact of the solvent evaporation rate on the kinetic trapping efficiency during spray drying, the evaporation rate was modified by adapting the drying air temperature and liquid feed rate at the same time to evaluate the potential impact of an extreme change in drying rate (Chapter 6). For FNB, increasing the solvent evaporation rate resulted in a slight improvement in phase behavior, which was in line with the idea that a higher solvent evaporation rate was an important factor to decrease the extent of nucleation[196]. Interestingly, the opposite trend was observed for NAP, where a lower drying rate was more beneficial for the phase behavior. This could be related to the relatively higher position of the T_{out} to the product T_g when the T_{in} was increased, thereby increasing the crystallization tendency of NAP. Although the importance of the T_{out} for the phase behavior[93,94,161,257,258], surface composition[259] and particle morphology[260,261] of spray dried particles has been described in literature, these findings demonstrated that the balance between the T_{in} and T_{out} might also be a limiting factor for process optimization with regard to the formulation of higher drug loadings. Moreover, the relative importance of the T_{out} clearly depended on the API and the API to polymer ratio. It should be noted that it might still be possible that generating smaller droplets without increasing the drying air temperature enables the formulation of higher drug loadings of NAP.

In general, the adaptation of process parameters resulted in limited improvement with regard to the extent of supersaturation, demonstrating that the manufacturing technique and the API-polymer-(solvent) combination predominantly determined the phase behavior. Nevertheless, it should be noted that these adaptations were performed in the workable space, and thus that process optimization could still have potential when a completely different set of process parameters would be selected as a starting point.

8.4. CHALLENGES DURING MANUFACTURING OF (KINETICALLY STABILIZED) SUPERSATURATED AMORPHOUS SOLID DISPERSIONS

8.4.1. Challenges of solid-state characterization

A first challenge that was encountered during the manufacturing of supersaturated ASDs, was the detection of heterogeneous phase behavior using appropriate analytical techniques. Even though well-established analytical techniques were employed, it became clear that in some cases, it was indispensable that more than one technique was applied to avoid erroneous conclusion about the physical state. As discussed in Chapter 7, in a lot of cases, mDSC and XRPD complement each other very well for this purpose. However, depending on the characteristics under investigation, the application of other analytical techniques might be required.

For instance, in Chapter 4, the results from the mDSC and XRPD analysis of ASDs of IMC were shown. The presence of several polymorphic forms of IMC together with crystallization during the mDSC analysis complicated the determination of the initial amount of crystalline material (yet it was possible when some assumptions were made). As the XRPD diffractograms showed amorphous halos for all ASDs of IMC and the mDSC analysis was not always straightforward, Raman microscopy, which is a vibrational spectroscopic technique with a higher sensitivity for crystalline traces than XRPD[262–265], was employed to confirm the absence of a crystalline fraction (data not shown).

Also in Chapter 4 and 6, the presence of a peculiar phenomenon in the mDSC analysis of some ASDs of NAP was described: a signal situated above the T_g of the pure polymer with the characteristics of a second T_g. Based on findings in the field of polymer science[177–183], it was hypothesized that this second T_g originated from a polymer fraction that was immobilized by the presence of (nano)crystals of NAP, thereby forming a Rigid Amorphous Fraction (RAF). As neither mDSC nor XRPD revealed the presence of a crystalline fraction (except for the batches described in Chapter 6), several other techniques were employed to study this phenomenon further: Dynamic Mechanic Analysis (DMA), ^{1}H NMR relaxometry and Scanning Electron Microscopy (SEM). Only the latter showed the presence of the typical needle-shaped crystals of NAP, demonstrating the added value of a microscopic evaluation to investigate (surface) crystallization. Moreover, this phenomenon was clearly not repeatable, as it was not even always present when the same sample was analyzed in triplicate by mDSC. However, as the detection of a RAF might indicate the presence of crystalline traces, it could be an interesting subject for further investigations.

In addition to that, it might be argued whether or not a single T_g in the mDSC analysis proves that the ASD is completely homogeneous and exists out of a single amorphous phase. Although mDSC is widely applied to assess the miscibility of compounds, it cannot detect phase separated domains smaller than approximately 30 nm[263]. Accordingly, Qian et al. found that two batches prepared using HME that had similar phase behavior based on mDSC and XRPD analysis, clearly differed in homogeneity by Raman microscopy, which could be related to their difference in physical stability[266]. Also ^{1}H NMR relaxometry is more sensitive than mDSC for the detection of phase separation[267–269]. Despite the availability of more sensitive techniques, mDSC gives a good indication of the homogeneity of an ASD.

In conclusion, the importance of applying more than one analytical technique for the solid-state characterization of ASDs was emphasized in this work. In most cases, mDSC and XRPD are a good starting point for the solid-state analysis, yet the shortcomings of both techniques should be kept in mind and accordingly, another analytical technique should be applied when needed.

8.4.2. The limits of process optimization

Even though there was no DoE performed in this project, the limited impact of process optimization on the extent of supersaturation that could be achieved was described in section 8.3.2. Although it is well-described that a too high barrel temperature could give rise to degradation issues during HME[256] and that a too high outlet temperature during spray drying could result in stickiness and physical instability[93,94,257,258], it was demonstrated that these factors also limited further increase in the amount of API that could be kinetically stabilized. Generally, the adaptation of process parameters resulted in little improvement of the phase behavior, which makes one to question the potential and relevance of process optimization with regard to increasing the extent of supersaturation. If only a small increase in supersaturation can be obtained, is it worth the effort of performing a DoE? And if it is this difficult to increase the extent of supersaturation, will the ASD not start to crystallize immediately?

Nevertheless, this does not mean that process optimization is not of utmost importance to modify other factors that are essential for a successful ASD formulation, such as the desired particle morphologies, particle size (distribution), release profiles during dissolution testing and residual solvent content levels.

It is also worth mentioning that all ASDs in this work were manufactured using a lab-scale set-up, and that scaling up to an industrial scale could propose some challenges with regard to process optimization. For instance, most lab-scale spray dryers are open loop systems, while production-scale spray dryers operate using a closed-loop or a recycle mode, where the drying gas (containing solvent vapor) is condensed, reheated and reused[270]. The presence of solvent vapor in the drying gas could influence the efficiency of the evaporation process and thus adaptation of the process parameters might be required. Also the increased residence time at high outlet temperatures in a production-scale spray dryer could be disadvantageous for the chemical and physical stability of the ASDs. Hence, when scaling-up, additional process optimization might be needed to obtain the desired physical state and residual solvent levels[93]. Nevertheless, the findings in this work can still be considered valuable for ASD manufacturing at an industrial scale, as they indicated which aspects could potentially influence the extent of solid state supersaturation that could be obtained.

8.4.3. It's all about balance: supersaturation in solid state, during dissolution and over time

In the previous sections, different factors that could influence the extent of solid state supersaturation were described. Although it is favorable to attain a supersaturated solid state, it should also be feasible to maintain this supersaturated state, and that both during dissolution and over time. First, as

mentioned above, the supersaturated state should also be maintained during dissolution for a long enough period of time for absorption to take place. In general, the higher the amount of API, the harder it is to maintain the supersaturated state in solution and to prevent crystallization and subsequent precipitation of the API, which also depends on the carrier used. In addition to that, the release mechanism is also dependent on the drug loading, with lower drug loadings generally resulting in a better drug release and *in vivo* oral bioavailability[271–274]. Accordingly, a lot of research is being performed to gain a mechanistic understanding of the release mechanisms of ASDs in order to improve the dissolution performance of highly drug loaded ASDs[271,273]. Moreover, the dissolution performance might also be influenced by the manufacturing technique used. For instance, as spray drying generally results in smaller particle sizes, it has been reported that the dissolution rate of spray dried ASDs is higher than that of extruded ASDs[124,246]. Hence, also the possible impact of the manufacturing method on the dissolution performance should be considered.

Another very important aspect is the physical (and chemical) stability of the supersaturated ASD. Even when a supersaturated system can be kinetically stabilized, there is no guarantee that the kinetic stabilization will be maintained for a pharmaceutically relevant storage period. In this work, the focus was on the physical state of ASDs immediately after preparation (Chapter 3, 4 and 6). Only in Chapter 5, the influence of spray drying with another organic solvent on the physical stability of ASDs of FNB has been discussed. Next to this, the solvent could also potentially influence the chemical stability of ASDs, which has been demonstrated for ASDs of the photosensitive nifedipine[275]. In this work, there were no photosensitive APIs investigated, but the potential (dis)advantageous effect of the solvent on photodegradation could be another important factor for solvent selection.

Lehmkemper et al. have studied the relation between the amount of API that could be kinetically stabilized in a polymer matrix, the thermodynamic solubility and physical stability[125,145]. They found that in most cases, the thermodynamic solubility predicted by PC-SAFT was a good indicator for the amount of API that could be maintained in its amorphous state during a physical stability study, while higher drug loadings led to crystallization. Exceptions on this rule were detected, yet the supersaturated amount was in those cases close to the solubility limit[125,145]. These findings demonstrated the importance of conducting a physical stability study for supersaturated ASDs in addition to the evaluation of the phase behavior immediately after preparation. On the other hand, Zhang et al. reported that ASDs of itraconazole with either PVPVA or HPMC-AS had a good physical stability when stored at RH < 60%, despite the fact that the amount of itraconazole surpassed the thermodynamic solubility limit[233]. In addition, ASDs with PVPVA were more susceptible to an increase in RH and subsequent crystallization of the API than the ones with HPMC-AS[233], which might be another

important factor for carrier selection in addition to ability of the carrier to kinetically stabilize a high amount of API (section 8.2.2.). Hence, predictions by a thermodynamic model can also play a pivotal role in evaluating the phase behavior over time, however, the fact that a system is supersaturated, does not imply that it cannot be kinetically stabilized for a long enough time period to have a viable shelf life.

In general, there are three important elements for a successful formulation of supersaturated ASDs: achieving a supersaturated state immediately after preparation, maintaining it for a pharmaceutically relevant storage period and stabilizing it during dissolution so absorption can take place. This PhD project focused on the first aspect by gaining insight in the factors that influence the extent of supersaturation that can be achieved. In addition to the above-mentioned remaining questions, there is still a lot of room for further research with regard to the relation of solid state supersaturation and the dissolution performance and physical stability of ASDs. For instance, how can the dissolution performance of highly drug loaded ASDs be improved? And how does the applied manufacturing technique influence the kinetic stabilization of a supersaturated system over time?

Chapter 9

Summary/Samenvatting

9.1. SUMMARY

In this thesis, supersaturated solid dispersions were manufactured under different conditions. To generate a supersaturated state, the API has to be dissolved in the polymer matrix above its thermodynamic solubility limit, thereby forming a thermodynamically unstable mixture. The supersaturated state can however be kinetically stabilized under the right circumstances. Accordingly, the overall aim of this project was to investigate the influence of several formulation and process parameters on the kinetic stabilization of supersaturated solid dispersions.

To situate this PhD project in the field of pharmacotechnology, the challenges of oral administration were described with a focus on the importance of aqueous solubility and permeability to achieve a sufficient oral bioavailability. In this regard, the Lipinski's rule of five, the BCS and several modifications to this classification system, *i.e.,* the ABГ system, BDDSC and DCS, were discussed. The need for classification systems that can relate the *in vitro* solubility and permeability of NCE to their *in vivo* oral bioavailability was explained by the increasing amount of poorly water-soluble drugs in the drug pipelines, *i.e.,* 75% of NCE have a poor aqueous solubility. In light of solubility enhancing formulation strategies, the different aspects of a dissolution process were described and related to the difference between 'grease balls' and 'brick dust' compounds. The solubility enhancing strategy of interest, *i.e.,* amorphous solid dispersions, was introduced by first discussing the advantages of the amorphous state of an API over its crystalline counterpart. Subsequently, amorphous solid dispersions were described as a solution to (partially) overcome the physical stability issues of the amorphous form. The increasing success of ASD formulations has been demonstrated by showing the increasing amount of marketed ASDs over the past ten years. To continue, an overview of the different manufacturing techniques for ASDs was given, after which hot melt extrusion, cryo-milling and spray drying were briefly discussed. In the last section of the introduction, the different physical states of a solid dispersion were described, with a focus on the impact of the relative position of the drug loading to the thermodynamic solubility of the API in the polymer matrix, thereby stressing the importance of kinetic stabilization of supersaturated systems. As last, the principles of mDSC and XRPD were explained, together with the potential of two approaches to predict the solubility of the API in the polymer matrix, *i.e.,* PC-SAFT and the recrystallization method.

In Chapter 2, the various formulation and process parameters studied in this project were named. First, it was described how the influence of three manufacturing techniques on the extent of solid state supersaturation was investigated. This was combined with a comparison of four different polymers for the formulation of ASDs of NAP. Second, the focus was on the contribution of the solvent to the phase behavior, where the dependence of the extent of solid state supersaturation on the solvent was

studied, followed by several approaches to explain this dependence. Moreover, the impact of the solvent on the physical stability of ASDs of FNB was studied as well. It was also described that while investigating the influence of these parameters, several challenges with regard to solid-state characterization of ASDs using mDSC and XRPD were encountered.

In a first part of the project, spray drying, hot melt extrusion and cryo-milling were compared for their capability to formulate highly drug loaded ASDs of NAP and one of the following four polymers, *i.e.,* PVP K25, PVPVA 64, HPMC or HPMC-AS. This allowed to simultaneously study the effect of the preparation method and the carrier selection on the extent of solid state supersaturation. It was found that PVPVA was most suited to achieve high drug loadings of NAP by spray drying, that PVP and PVPVA were both promising using HME and that PVP was most suited when cryo-milling was applied. Hence, it was concluded that the optimal NAP-polymer combination was dependent on the technique. Even more importantly, the highest drug loadings could be obtained using HME, independently of the polymer used, which was in agreement with the importance of heat as an energy input for these systems. The highest drug loadings were above the thermodynamic solubility limit of NAP in the different polymers, demonstrating that kinetically stabilized supersaturated ASDs were obtained by spray drying and hot melt extrusion. In case of cryo-milling, only drug loadings below the equilibrium solubility limit were obtained.

In Chapter 4, the influence of different organic solvents on the kinetic stabilization of supersaturated ASDs prepared by either spray drying of film casting was described. PVPVA 64 and one of the following four poorly water-soluble APIs, *i.e.,* NAP, IMC, DZP or FNB, were formulated together as an ASD using one of seven organic solvents, *i.e.,* MeOH, EtOH, PrOH, ACN, Ac, DCM, EtAc. The highest drug loading that could be formulated as a single amorphous phase was determined for every API-polymer-solvent combination. In case of film casting, the solvent determined the extent of solid state supersaturation that could be obtained for all APIs. When spray drying, the effect of the solvent on the physical state of ASDs of IMC was nullified, which was related to the faster evaporation process, the lower crystallization tendency of IMC and its hydrogen bonding potential with PVPVA. For the other three APIs, the solvent still decided the extent of solid state supersaturation that could be achieved. Although spray drying generally enabled the formulation of higher drug loadings, the same trends were observed as for film casting, demonstrating the predictive value of film casting for the impact of the solvent on the phase behavior. Additionally, the importance of kinetics next to thermodynamics for the generation of supersaturated ASDs was highlighted by demonstrating that the highest drug loadings depended on the solvent, the API, and the manufacturing technique. Furthermore, the thermodynamic solubilities of the APIs in the seven solvents were determined, both in absence and presence of PVPVA (*i.e.,* 2.5%, 5%, 7.5% and 9% w/V). It was found that PVPVA did not alter the solubility trend of the pure

APIs. Moreover, there was no relation between the thermodynamic solubility of the API and the highest drug loading attained using the same solvent. The overall conclusion of this chapter was that the contribution of the solvent to the phase behavior of ASDs should not be underestimated and that it was not (solely) related to a difference in solubility.

The next chapter was about the impact of the solvent on the physical stability of spray dried ASDs of FNB. The FNB-PVPVA system was selected as it was the one for which the solvent had the largest influence on the kinetic stabilization of the supersaturated state. For every solvent, three batches of the same drug loading of 10 wt% FNB were prepared, stored at 25 °C and 53% RH for 6 weeks and weekly analyzed using mDSC and XPRD. The solvent determined the crystallization onset of these ASDs of FNB, and thus whether or not the supersaturated state could be kinetically stabilized over time. The influence of the solvent on the crystallization onset was found to be repeatable. Moreover, the timepoint at which the presence of a crystalline fraction was detected, could be related to the highest drug loading that could be kinetically stabilized. Hence, the higher the extent of solid state supersaturation could be, the longer lower (supersaturated) drug loadings were maintained in an amorphous state. These interesting findings asked for a deeper understanding of the impact of the solvent on the physical state (and physical stability) to optimize the kinetic stabilization of supersaturated ASDs prepared by solvent-based methods.

Therefore, Chapter 6 addressed the relation between the solvent evaporation rate and the kinetic stabilization of highly drug loaded ASDs. The evaporation kinetics of the seven organic solvents as such and of solutions containing only PVPVA or PVPVA with either FNB or NAP were investigated by means of TGA. At 10 °C below the boiling point of the respective solvent, MeOH had the lowest evaporation rate and DCM the highest. PVPVA decreased the evaporation rate for all solvents, yet this effect was more pronounced for the relatively faster evaporating solvents, *i.e.,* DCM, EtAc and Ac. FNB and NAP had opposite effects on the evaporation behavior: FNB increased the evaporation rate again, while NAP decreased it. As the latter could be an indication of interactions between NAP and PVPVA and/or NAP and the solvent, the presence of interactions in solution was further investigated using FT-IR. Hydrogen bonding was detected between NAP and MeOH, EtOH, PrOH and ACN, and between NAP and PVPVA, which was more pronounced for the solvents that did not interact with PVPVA, *i.e.,* DCM and ACN. Based on these findings, the effect of a higher drying rate of MeOH and that of both a higher and lower evaporation rate of DCM on the phase behavior of ASDs of NAP and FNB was studied. The evaporation rate was modified by rational selection of spray drying process parameters. Increasing the evaporation rate of MeOH and DCM enabled the kinetic stabilization of higher drug loadings of FNB, while the opposite trend was observed for ASDs of NAP, where the relative position T_g of the ASD to the T_{out} was determinative for the phase behavior. Even when a higher extent of solid state

supersaturation could be achieved by adapting the process parameters, the improvement was limited, demonstrating that the phase behavior of these ASDs of FNB and NAP was predominantly determined by the API-polymer-solvent combination rather than the process parameters applied.

During this PhD project, the solid-state characterization of supersaturated ASDs by mDSC and XRPD was not always straightforward. Accordingly, Chapter 7 describes the importance of applying more than one analytical technique for the solid-state analysis, thereby stressing the complementary nature of mDSC and XRPD. Limiting factors of mDSC and XRPD were related to practical examples encountered during this PhD project that revealed that the application of a single analytical technique would have led to erroneous conclusions about the phase behavior.

In the last chapter, it was explained that the generation of supersaturated ASDs can be preferred over lower drug loaded ones. Subsequently, the different factors that could influence the kinetic stabilization of supersaturated ASDs were discussed: the physicochemical characteristics of the API, carrier and solvent, the manufacturing process, the process parameters, and environmental factors. Finally, the challenges that can be encountered during the formulation of supersaturated ASDs were discussed, from which a very important aspect was finding a balance between the generation of a supersaturated state, having a good physical stability, and obtaining the desired dissolution profile.

9.2. SAMENVATTING

In deze thesis werden oververzadigde vaste dispersies bereid onder verschillende omstandigheden. Om een oververzadigde toestand te bekomen, moet er meer actief farmaceutisch ingrediënt (AFI) aanwezig zijn dan de thermodynamische oplosbaarheidslimiet van het AFI in de polymeer matrix. Ondanks het feit dat er hierdoor een thermodynamisch onstabiele toestand gecreëerd wordt, kan een oververzadigd systeem kinetisch gestabiliseerd zijn onder de juiste omstandigheden. De algemene doelstelling van dit project was de invloed van verschillende formulatie- en procesparameters op de kinetische stabilisatie van oververzadigde amorfe vaste dispersies (AVDs) te onderzoeken.

Om dit project te situeren in het farmacotechnologische domein, werden eerst de uitdagingen die gepaard gaan met de orale toediening van geneesmiddelen besproken, waarbij er gefocust werd op het belang van een hoge oplosbaarheid en permeabiliteit om een voldoende hoge orale biologische beschikbaarheid te bekomen. In dit verband werden de Lipinski's regel van vijf, het BCS en verschillende aanpassingen aan dit classificatiesysteem besproken, namelijk het ABΓ systeem, BDDCS en DCS. Het werd uitgelegd dat deze classificatiesystemen noodzakelijk zijn om de toenemende hoeveelheid slecht wateroplosbare geneesmiddelen (momenteel geschat op 75% van de nieuwe chemische entiteiten (NCE)) correct te kunnen classificeren en hun *in vivo* orale biologische beschikbaarheid te kunnen voorspellen. Vervolgens werden de verschillende stappen van een oplossingsproces besproken en werd het verschil tussen zogenaamde 'grease balls' en 'brick dust' componenten verklaard. Hierna werden AVDs geïntroduceerd door eerst de theorie achter het oplosbaarheidsvoordeel van een amorfe vorm ten opzichte van een kristallijne vorm uit te leggen. AVDs werden besproken als een oplossing om de stabiliteitsproblemen van een amorfe vorm te verminderen. Het toenemende succes van AVD formulaties werd aangetoond door een overzicht te geven van het toenemende aantal AVD formulaties op de markt. Vervolgens werd er een overzicht gegeven van de verschillende productiemethodes voor AVDs, waarna de principes van 'hot melt extrusion', 'spray drying' en 'cryo-milling' werden besproken. In het laatste gedeelte van de introductie werden de verschillende fysische toestanden van een vaste dispersie behandeld, waarbij er gefocust werd op het belang van de relatieve positie van de geneesmiddelbelading ten opzichte van de thermodynamische oplosbaarheidslimiet van het AFI in de polymeer matrix. Als analytische technieken om deze verschillende fysische toestanden te detecteren werden mDSC en XRPD kort besproken. Tenslotte werden twee methodes om de oplosbaarheid van het AFI in de polymeer matrix te voorspellen behandeld, namelijk PC-SAFT en de rekristallisatiemethode.

In het tweede hoofdstuk werden de onderzochte formulatie- en procesparameters benoemd. Een eerste aspect was de invloed van verschillende AVD productiemethodes op de mate van vaste toestand

oververzadiging die bereikt kon worden. Dit werd gecombineerd met het vergelijken van vier polymeren voor de formulatie van AVD van NAP. Als tweede werd er gefocust op de bijdrage van het solvent aan het fasegedrag van AVDs en het vinden van een verklaring voor deze invloed. Daarbij werd het effect van het solvent op de fysische stabiliteit van AVD van FNB ook onderzocht. Tenslotte werden verschillende situaties besproken waarin het gecombineerde gebruik van mDSC en XRPD noodzakelijk was om het correcte fasegedrag van een AVD te achterhalen.

Het derde hoofdstuk van deze thesis behandelde de vergelijking van 'hot melt extrusion', 'spray drying' en 'cryo-milling' voor hun vermogen om AVDs met hoge geneesmiddelbelading te bekomen. Dit werd onderzocht voor AVDs van NAP met een van de volgende polymeren, PVP K25, PVPVA 64, HPMC of HPMC-AS, waardoor zowel het effect van de productiemethode als de carrier op de mate van vaste toestand oververzadiging kon worden onderzocht. Er werd vastgesteld dat PVPVA het beste polymeer was om een hoge geneesmiddelbelading te bekomen met 'spray drying', terwijl PVP en PVPVA beide goede polymeren waren via 'hot melt extrusion' en PVP het meest veelbelovende polymeer was via 'cryo-milling'. Hieruit bleek dat de optimale NAP-polymeer combinatie afhankelijk was van de techniek. In het algemeen konden de hoogste geneesmiddelbeladingen bekomen worden met 'hot melt extrusion', wat overeenkwam met de bevinding dat warmte een belangrijke energie input was voor de mengbaarheid. Daarbovenop waren de hoogste geneesmiddelbeladingen in geval van 'spray drying' en 'hot melt extrusion' hoger dan de thermodynamische oplosbaarheidslimit, wat aantoonde dat kinetisch gestabiliseerde oververzadigde AVD van NAP konden worden bekomen. In geval van 'cryo-milling' daarentegen waren de geneesmiddelbeladingen steeds lager dan de evenwichtslimiet.

In het volgende hoofdstuk werd de invloed van het solvent op de kinetische stabilisatie van oververzadigde AVD besproken. Hiervoor werden AVD van PVPVA 64 met een van de volgende slecht wateroplosbare AFIs bereid, NAP, IMC, DZP of IMC, waarbij een van de volgende zeven organische solventen gebruikt werd, MeOH, EtOH, PrOH, ACN, Ac, DCM of EtAc. Voor iedere AFI-polymeer-solvent combinatie werd de hoogst mogelijke geneesmiddelbelading bepaald waarvoor een eenfasig amorf systeem kon worden bekomen, en dat zowel met behulp van 'spray drying' als 'film casting'. In geval van 'film casting' was het solvent steeds de bepalende factor voor de mate van vaste toestand oververzadiging die bekomen kon worden. Dit was ook het geval voor alle AVDs bereid met 'spray drying', behalve voor de AVDs van IMC, wat gerelateerd werd aan het snellere verdampingsproces gecombineerd met de lagere kristallisatietendens van IMC. Ondanks het feit dat in geval van 'spray drying' over het algemeen hogere geneesmiddelbeladingen bereikt konden worden, werden dezelfde trends geobserveerd voor beide technieken, wat de predictieve waarde van 'film casting' voor de impact van het solvent op het fasegedrag van AVDs aantoonde. Bovendien werd het belang van kinetica naast thermodynamica voor het genereren van oververzadigde AVDs benadrukt. Daarnaast

werden de thermodynamische oplosbaarheden van de vier AFIs in de zeven organische solventen bepaald zonder PVPVA en met PVPVA (2.5%, 5%, 7.5% en 9% m/V), waaruit bleek dat PVPVA geen effect had op de oplosbaarheidstrend van de pure AFIs. Bovendien werd er geen verband gevonden tussen de thermodynamische oplosbaarheid van een AFI en de hoogste geneesmiddelbelading die bereikt kon worden met behulp van hetzelfde solvent. De algemene conclusie van dit hoofdstuk was dat de invloed van het solvent op het fasegedrag van AVDs niet onderschat mag worden en dat het niet (alleen) te wijten is aan een verschil in oplosbaarheid.

De invloed van het solvent op de fysische stabiliteit van AVDs van FNB werd besproken in hoofdstuk vijf. Het FNB-PVPVA systeem werd geselecteerd omdat het solvent hierbij een grote invloed had op de hoogste geneesmiddelbelading die bereikt kon worden. Voor ieder solvent werden drie loten met 10% m/m FNB bereid, die bewaard werden bij 25 °C en 53% relatieve vochtigheid en wekelijks geanalyseerd werden met behulp van mDSC en XRPD. Het tijdspunt waarop er een kristallijne fractie aanwezig was, was afhankelijk van het solvent, wat betekent dat het solvent de beslissende factor was voor hoelang de oververzadigde toestand kinetisch gestabiliseerd kon worden. Bovendien kon dit tijdspunt gerelateerd worden aan de hoogste geneesmiddelbelading die bereikt kon worden, d.w.z. hoe hoger de mate van vaste toestand oververzadiging kon zijn, hoe langer de lagere (oververzadigde) geneesmiddelbelading gestabiliseerd kon worden. Er werd geconcludeerd dat het noodzakelijk is om een dieper inzicht te verwerven in de bijdrage van het solvent aan het fasegedrag van AVDs met als doel de kinetische stabilisatie van oververzadigde AVDs te optimaliseren.

Daarom werd in het volgende hoofdstuk het verband tussen de verdampingssnelheid van het solvent en de kinetische stabilisatie van oververzadigde AVDs besproken. De verdampingskinetiek van de zeven organische solventen op zich en van oplossingen van PVPVA en PVPVA met FNB of NAP werd onderzocht met behulp van TGA. Hieruit bleek dat 10 °C onder het respectievelijke kookpunt van het solvent MeOH het traagste verdampte en DCM het snelste. PVPVA vertraagde het verdampingsproces voor alle solventen, maar dit effect was het meest uitgesproken voor de relatief sneller verdampende solventen, namelijk DCM, EtAc en Ac. De AFIs hadden tegengestelde effecten: FNB verhoogde de verdampingssnelheid opnieuw, terwijl in aanwezigheid van NAP het verdampingsproces nog trager was dan wanneer er enkel PVPVA in de oplossing aanwezig was. Aangezien dit laatste een aanwijzing kon zijn van interacties tussen NAP en PVPVA en/of NAP en het solvent, werd de aanwezigheid van interacties in oplossing verder onderzocht met FT-IR. Hieruit bleek dat waterstofbindingen werden gevormd tussen NAP en MeOH, EtOH, PrOH en ACN, en tussen NAP en PVPVA, waarbij dit laatste het meest uitgesproken was in solventen die niet interageerden met PVPVA, namelijk in DCM en ACN. Op basis van deze resultaten, werden de ‘spray drying’ procesparameters zodanig aangepast dat de verdampingssnelheid van MeOH verhoogd werd of in geval van DCM, ofwel verhoogd of verlaagd

werd. Voor AVDs van FNB resulteerde een hogere verdampingssnelheid van zowel MeOH als DCM in een hogere mate van vaste toestand oververzadiging die bereikt kon worden. De omgekeerde trend werd echter waargenomen in geval van AVDs van NAP, wat verklaard werd door de relatieve positie van de T_{out} ten opzichte van de AVD product T_g. Hoewel het in sommige gevallen mogelijk was om door middel van een aanpassing van de 'spray drying' procesparameters de hoogst mogelijke geneesmiddelbelading te verhogen, was deze toename echter beperkt. Daarom werd er besloten dat het fasegedrag van deze AVDs van NAP en FNB voornamelijk bepaald werd door de AFI-polymeer-solvent combinatie en niet zozeer door de gebruikte procesparameters.

Tijdens het uitvoeren van dit project was de analyse van de vaste toestand met behulp van mDSC en XRPD niet altijd eenvoudig. Daarom werd in hoofdstuk zeven benadrukt dat het belangrijk was om meer dan één analytische techniek te gebruiken voor de karakterisering van de vaste toestand van AVDs, waarbij dat er gefocust werd op de complementariteit van mDSC en XRPD.

In het laatste hoofdstuk werd de voorkeur voor oververzadigde AVDs in plaats van AVDs met een lagere geneesmiddelbelading gekaderd. Vervolgens werden de verschillende factoren die de kinetische stabilisatie van de oververzadigde toestand kunnen beïnvloeden een voor een besproken: de fysicochemische eigenschappen van de AFI, de carrier en het solvent, de productiemethode, de procesparameters en omgevingsfactoren. Tenslotte werden de mogelijke uitdagingen tijdens de productie van oververzadigde vaste dispersies behandeld, waarvan een zeer belangrijk aspect het uitbalanceren van een hoge geneesmiddelbelading, een goede fysische stabiliteit en het gewenste dissolutieprofiel was.

References

1. Williams RO, Watts AB, Miller DA. *Formulating Poorly Water Soluble Drugs*. Springer; 2012.

2. Stewart KD, Johnston JA, Matza LS, et al. Preference for pharmaceutical formulation and treatment process attributes. *Patient Prefer Adherence*. 2016;10:1385-1399. doi:10.2147/PPA.S101821

3. Jermain S V., Brough C, Williams RO. Amorphous solid dispersions and nanocrystal technologies for poorly water-soluble drug delivery – An update. *Int J Pharm*. 2018;535(1-2):379-392. doi:10.1016/j.ijpharm.2017.10.051

4. Chiou WL. The rate and extent of oral bioavailability versus the rate and extent of oral absorption: Clarification and recommendation of terminology. *J Pharmacokinet Pharmacodyn*. 2001;28(1):3-6. doi:10.1023/A:1011544501243

5. Khojestah SC, Wong H, Hop CECA. Drug metabolism and pharmacokinetics quick guide. In: *Drug Metabolism and Pharmacokinetics Quick Guide*. Springer; 2011:47-56.

6. Rafii F. The role of colonic bacteria in the metabolism of the natural isoflavone daidzin to equol. *Metabolites*. 2015;5(1):56-73. doi:10.3390/metabo5010056

7. Braeckmans M, Brouwers J, Masuy I, Servais C, Tack J, Augustijns P. The influence of gastric motility on the intraluminal behavior of fosamprenavir. *Eur J Pharm Sci*. 2020;142(November 2019):105117. doi:10.1016/j.ejps.2019.105117

8. Van Den Abeele J, Brouwers J, Tack J, Augustijns P. Exploring the link between gastric motility and intragastric drug distribution in man. *Eur J Pharm Biopharm*. 2017;112:75-84. doi:10.1016/j.ejpb.2016.10.027

9. Koziolek M, Alcaro S, Augustijns P, et al. The mechanisms of pharmacokinetic food-drug interactions – A perspective from the UNGAP group. *Eur J Pharm Sci*. 2019;134(January):31-59. doi:10.1016/j.ejps.2019.04.003

10. Stillhart C, Vučićević K, Augustijns P, et al. Impact of gastrointestinal physiology on drug absorption in special populations—An UNGAP review. *Eur J Pharm Sci*. 2020;147(November 2019):105280. doi:10.1016/j.ejps.2020.105280

11. Palleria C, Di Paolo A, Giofrè C, et al. Pharmacokinetic drug-drug interaction and their implication in clinical management. *J Res Med Sci*. 2013;18(7):600-609.

12. Lipinski CA, Lombardo F, Dominy BW, Feeney PJ. Experimental and Computational Approaches to Estimate Solubility and Permeability in Drug Discovery and Develop ment Settings. *Adv Drug Deliv Rev*. 1997;23:3-25. doi:10.1016/S0169-409X(00)00129-0

13. Lipinski CA. Drug-like properties and the causes of poor solubility and poor permeability. *J Pharmacol Toxicol Methods*. 2000;44(1):235-249. doi:10.1016/S1056-8719(00)00107-6

14. Rampogu S, Lee G, Kulkarni AM, et al. Computational Approaches to Discover Novel Natural Compounds for SARS-CoV-2 Therapeutics. *ChemistryOpen*. 2021;10(5):593-599. doi:10.1002/open.202000332

15. Lipinski CA. Rule of five in 2015 and beyond: Target and ligand structural limitations, ligand chemistry structure and drug discovery project decisions. *Adv Drug Deliv Rev*. 2016;101:34-41. doi:10.1016/j.addr.2016.04.029

16. Krämer SD, Aschmann HE, Hatibovic M, et al. When barriers ignore the “rule-of-five.” *Adv Drug Deliv Rev*. 2016;101:62-74. doi:10.1016/j.addr.2016.02.001

17. Shultz MD. Two Decades under the Influence of the Rule of Five and the Changing Properties of Approved Oral Drugs. *J Med Chem*. 2019;62(4):1701-1714. doi:10.1021/acs.jmedchem.8b00686

18. Gleeson MP, Hersey A, Montanari D, Overington J. Probing the links between in vitro potency, ADMET and physicochemical parameters. *Nat Rev Drug Discov*. 2011;10(3):197-208. doi:10.1038/nrd3367

19. Dibó G. Combinatorial chemistry has matured in the last three decades: Dedicated to Professor Árpád Furka on the occasion of his 80th birthday. *Mol Divers*. 2012;16(1):1-3. doi:10.1007/s11030-011-9351-0

20. Pereira DA, Williams JA. Origin and evolution of high throughput screening. *Br J Pharmacol*. 2007;152(1):53-61. doi:10.1038/sj.bjp.0707373

21. Bull SC, Doig AJ. Properties of protein drug target classes. *PLoS One*. 2015;10(3):1-45. doi:10.1371/journal.pone.0117955

22. Johnson TW, Gallego RA, Edwards MP. Lipophilic Efficiency as an Important Metric in Drug Design. *J Med Chem*. 2018;61(15):6401-6420. doi:10.1021/acs.jmedchem.8b00077

23. Morphy R. The influence of target family and functional activity on the physicochemical properties of pre-clinical compounds. *J Med Chem*. 2006;49(10):2969-2978. doi:10.1021/jm0512185

24. Williams HD, Trevaskis NL, Charman SA, et al. Strategies to Address Low Drug Solubility in Discovery and Development. *Pharmacol Rev*. 2013;65(1):315-499. doi:10.1124/pr.112.005660

25. Ricarte RG, Van Zee NJ, Li Z, Johnson LM, Lodge TP, Hillmyer MA. Recent Advances in Understanding the Micro- and Nanoscale Phenomena of Amorphous Solid Dispersions. *Mol Pharm*. 2019;16(10):4089-4103. doi:10.1021/acs.molpharmaceut.9b00601

26. Amidon G, H L, Shah V, Crison J. A theoretical basis for a biopharmaceutic drug classification: the correlation of in vitro drug product dissolution and in vivo bioavailability. *Pharm Res*. 1995;12(3):413-420.

27. European Medicines Agency. ICH guideline M9 on biopharmaceutics classification system based biowaivers. *Ema*. 2018;44(August):1-17.

28. Services H. M9 Biopharmaceutics Classification System- Based Biowaivers Guidance for Industry M9 Biopharmaceutics Classification System- Based Biowaivers Guidance for Industry. 2021;(May).

29. Macheras P, Karalis V. A non-binary biopharmaceutical classification of drugs: The ABΓ system. *Int J Pharm*. 2014;464(1-2):85-90. doi:10.1016/j.ijpharm.2014.01.022

30. Butler JM, Dressman JB. The developability classification system: Application of biopharmaceutics concepts to formulation development. *J Pharm Sci*. 2010;99(12):4940-4954. doi:10.1002/jps

31. Wu CY, Benet LZ. Predicting drug disposition via application of BCS: Transport/absorption/ elimination interplay and development of a biopharmaceutics drug disposition classification system. *Pharm Res*. 2005;22(1):11-23. doi:10.1007/s11095-004-9004-4

32. Benet LZ, Broccatelli F, Oprea TI. BDDCS applied to over 900 drugs. *AAPS J*. 2011;13(4):519-547.

doi:10.1208/s12248-011-9290-9

33. Benet LZ, Hosey CM, Ursu O, Oprea TI. BDDCS, the Rule of 5 and drugability. *Adv Drug Deliv Rev*. 2016;101:89-98. doi:10.1016/j.addr.2016.05.007

34. Broccatelli F, Cruciani G, Benet LZ, Oprea TI. Bddcs class prediction for new molecular entities. *Mol Pharm*. 2012;9(3):570-580. doi:10.1021/mp2004302

35. Yu LX, Amidon GL, Polli JE, et al. Biopharmaceutics classification system: The scientific basis for biowaiver extensions. *Pharm Res*. 2002;19(7):921-925. doi:10.1023/A:1016473601633

36. Cheng CL, Yu LX, Lee HL, Yang CY, Lue CS, Chou CH. Biowaiver extension potential to BCS Class III high solubility-low permeability drugs: Bridging evidence for metformin immediate-release tablet. *Eur J Pharm Sci*. 2004;22(4):297-304. doi:10.1016/j.ejps.2004.03.016

37. Yazdanian M, Briggs K, Jankovsky C, Hawi A. The " High Solubility " Definition of the Current FDA Guidance on Biopharmaceutical Classification System May be Too Strict for Acidic Drugs. *Pharmaeutical Res*. 2004;21(2):293-299.

38. Singh A, Van den Mooter G. Spray drying formulation of amorphous solid dispersions. *Adv Drug Deliv Rev*. 2016;100:27-50. doi:10.1016/j.addr.2015.12.010

39. Janssens S, Van den Mooter G. Review: physical chemistry of solid dispersions. *J Pharm Pharmacol*. 2009;61(12):1571-1586. doi:10.1211/jpp/61.12.0001

40. Dokoumetzidis A, Macheras P. A century of dissolution research: From Noyes and Whitney to the Biopharmaceutics Classification System. *Int J Pharm*. 2006;321(1-2):1-11. doi:10.1016/j.ijpharm.2006.07.011

41. Van Den Mooter G. The use of amorphous solid dispersions: A formulation strategy to overcome poor solubility and dissolution rate. *Drug Discov Today Technol*. 2012;9(2):e79-e85. doi:10.1016/j.ddtec.2011.10.002

42. Bergström CAS, Charman WN, Porter CJH. Computational prediction of formulation strategies for beyond-rule-of-5 compounds. *Adv Drug Deliv Rev*. 2016;101:6-21. doi:10.1016/j.addr.2016.02.005

43. Stella VJ, Nti-Addae KW. Prodrug strategies to overcome poor water solubility. *Adv Drug Deliv Rev*. 2007;59(7):677-694. doi:10.1016/j.addr.2007.05.013

44. Bergström CAS, Wassvik CM, Johansson K, Hubatsch I. Poorly soluble marketed drugs display solvation limited solubility. *J Med Chem*. 2007;50(23):5858-5862. doi:10.1021/jm0706416

45. Wassvik CM, Holmén AG, Draheim R, Artursson P, Bergström CAS. Molecular characteristics for solid-state limited solubility. *J Med Chem*. 2008;51(10):3035-3039. doi:10.1021/jm701587d

46. Persson LC, Porter CJH, Charman WN, Bergström CAS. Computational prediction of drug solubility in lipid based formulation excipients. *Pharm Res*. 2013;30(12):3225-3237. doi:10.1007/s11095-013-1083-7

47. Ran Y, He Y, Yang G, Johnson JLH, Yalkowsky SH. Estimation of aqueous solubility of organic compounds by using the general solubility equation. *Chemosphere*. 2002;48(5):487-509. doi:10.1016/S0045-6535(02)00118-2

48. Ran Y, Jain N, Yalkowsky SH. Prediction of Aqueous Solubility of Organic Compounds by the General Solubility Equation (GSE). *J Chem Inf Comput Sci*. 2001;41(3-6):1208-1217. doi:10.1021/ci010287z

49. Emami S, Siahi-Shadbad M, Adibkia K, Barzegar-Jalali M. Recent advances in improving oral drug bioavailability by cocrystals. *BioImpacts*. 2018;8(4):305-320. doi:10.15171/bi.2018.33

50. Navnit S, Harpreet S, Duk Soon C, Hitesh C, A. Waseem M. *Amorphous Solid Dispersions*. (Navnit S, Harpreet S, Duk Soon C, Hitesh C, A. Waseem M, eds.). Springer; 2014. doi:10.1007/978-1-4939-1598-9

51. Van den Mooter G. De vaste toestand van farmaceutische producten. In: *Fysicochemie van Het Geneesmiddel*. Acco; 2015:43-76.

52. Lin X, Hu Y, Liu L, et al. Physical Stability of Amorphous Solid Dispersions: a Physicochemical Perspective with Thermodynamic, Kinetic and Environmental Aspects. *Pharm Res*. 2018;35(6). doi:10.1007/s11095-018-2408-3

53. Kissi EO, Grohganz H, Löbmann K, Ruggiero MT, Zeitler JA, Rades T. Glass-Transition Temperature of the β-Relaxation as the Major Predictive Parameter for Recrystallization of Neat Amorphous Drugs. *J Phys Chem B*. 2018;122(10):2803-2808. doi:10.1021/acs.jpcb.7b10105

54. Roudaut G, Simatos D, Champion D, Contreras-Lopez E, Le Meste M. Molecular mobility around the glass transition temperature: A mini review. *Innov Food Sci Emerg Technol*. 2004;5(2):127-134. doi:10.1016/j.ifset.2003.12.003

55. Aso Y, Yoshioka S, Kojima S. Molecular Mobility-Based Estimation of the Crystallization Rates of Amorphous Nifedipine and Phenobarbital in Poly(vinylpyrrolidone) Solid Dispersions. *J Pharm Sci*. 2004;93(2):384-391. doi:10.1002/jps.10526

56. Shamblin SL, Hancock BC, Pikal MJ. Coupling between chemical reactivity and structural relaxation in pharmaceutical glasses. *Pharm Res*. 2006;23(10):2254-2268. doi:10.1007/s11095-006-9080-8

57. Heljo VP, Nordberg A, Tenho M, et al. The effect of water plasticization on the molecular mobility and crystallization tendency of amorphous disaccharides. *Pharm Res*. 2012;29(10):2684-2697. doi:10.1007/s11095-011-0658-4

58. Mehta M, Kothari K, Ragoonanan V, Suryanarayanan R. Effect of Water on Molecular Mobility and Physical Stability of Amorphous Pharmaceuticals. *Mol Pharm*. 2016;13(4):1339-1346. doi:10.1021/acs.molpharmaceut.5b00950

59. Vasconcelos T, Marques S, das Neves J, Sarmento B. Amorphous solid dispersions: Rational selection of a manufacturing process. *Adv Drug Deliv Rev*. 2016;100:85-101. doi:10.1016/j.addr.2016.01.012

60. Huang S, Williams RO. Effects of the Preparation Process on the Properties of Amorphous Solid Dispersions. *AAPS PharmSciTech*. 2018;19(5):1971-1984. doi:10.1208/s12249-017-0861-7

61. Chiou WL, Riegelman S. Pharmaceutical Applications of Solid Dispersion Systems. *J Pharm Sci*. 1971;60(9):1281-1302. doi:10.1002/jps.2600600902

62. Van Duong T, Van den Mooter G. The role of the carrier in the formulation of pharmaceutical solid dispersions. Part II: amorphous carriers. *Expert Opin Drug Deliv*. 2016;13(12):1681-1694. doi:10.1080/17425247.2016.1198769

63. Saraf I, Roskar R, Modhave D, et al. Forced Solid-State Oxidation Studies of Nifedipine-PVP Amorphous Solid Dispersion. *Mol Pharm*. 2022;19(2):568-583. doi:10.1021/acs.molpharmaceut.1c00678

64. Van den Mooter G, Wuyts M, Blaton N, et al. Physical stabilisation of amorphous ketoconazole

in solid dispersions with polyvinylpyrrolidone K25. *Eur J Pharm Sci*. 2001;12(3):261-269. doi:10.1016/S0928-0987(00)00173-1

65. Baird JA, Taylor LS. Evaluation of amorphous solid dispersion properties using thermal analysis techniques ☆. *Adv Drug Deliv Rev*. 2012;64(5):396-421. doi:10.1016/j.addr.2011.07.009

66. Nair R, Nyamweya N, Gönen S, Martínez-Miranda LJ, Hoag SW. Influence of various drugs on the glass transition temperature of poly(vinylpyrrolidone): A thermodynamic and spectroscopic investigation. *Int J Pharm*. 2001;225(1-2):83-96. doi:10.1016/S0378-5173(01)00767-0

67. Gupta P, Bansal AK. Devitrification of amorphous celecoxib. *AAPS PharmSciTech*. 2005;6(2):223-230. doi:10.1208/pt060232

68. Liu X, Feng X, Williams RO, Feng III. Characterization of amorphous solid dispersions. *J Pharm Investig*. 2018;48(1):19-41. doi:10.1007/s40005-017-0361-5

69. Bhujbal S V., Mitra B, Jain U, et al. Pharmaceutical amorphous solid dispersion: A review of manufacturing strategies. *Acta Pharm Sin B*. 2021;11(8):2505-2536. doi:10.1016/j.apsb.2021.05.014

70. He Y, Ho C. Amorphous Solid Dispersions: Utilization and Challenges in Drug Discovery and Development. *J Pharm Sci*. 2015;104(10):3237-3258. doi:10.1002/jps.24541

71. Anane-Adjei AB, Jacobs E, Nash SC, et al. Amorphous Solid Dispersions: Utilization and Challenges in Preclinical Drug Development within AstraZeneca. *Int J Pharm*. Published online 2021:121387. doi:10.1016/j.ijpharm.2021.121387

72. Clinicaltrial.gov. Accessed November 15, 2021. https://clinicaltrials.gov/

73. Ghule P, Gilhotra R, Jithan A, Bairagi S, Aher A. Amorphous solid dispersion: A promising technique for improving oral bioavailability of poorly water-soluble drugs. *SA Pharm J*. 2018;85(1):50-56.

74. Pandi P, Bulusu R, Kommineni N, Khan W, Singh M. Amorphous solid dispersions: An update for preparation, characterization, mechanism on bioavailability, stability, regulatory considerations and marketed products. *Int J Pharm*. 2020;586(May):119560. doi:10.1016/j.ijpharm.2020.119560

75. Edueng K, Mahlin D, Bergström CAS. The Need for Restructuring the Disordered Science of Amorphous Drug Formulations. *Pharm Res*. 2017;34(9):1754-1772. doi:10.1007/s11095-017-2174-7

76. Schönfeld B, Westedt U, Wagner KG. Vacuum drum drying – A novel solvent-evaporation based technology to manufacture amorphous solid dispersions in comparison to spray drying and hot melt extrusion. *Int J Pharm*. 2021;596(January). doi:10.1016/j.ijpharm.2021.120233

77. Qiang W, Löbmann K, McCoy CP, Andrews GP, Zhao M. Microwave-induced in situ amorphization: A new strategy for tackling the stability issue of amorphous solid dispersions. *Pharmaceutics*. 2020;12(7):1-19. doi:10.3390/pharmaceutics12070655

78. Huang Y, Dai W-G. Fundamental aspects of solid dispersion technology for poorly soluble drugs. *Acta Pharm Sin B*. 2014;4(1):18-25. doi:10.1016/j.apsb.2013.11.001

79. Repka MA, Bandari S, Kallakunta VR, et al. Melt extrusion with poorly soluble drugs – An integrated review. *Int J Pharm*. 2018;535(1-2):68-85. doi:10.1016/j.ijpharm.2017.10.056

80. Patil H, Tiwari R V., Repka MA. Hot-Melt Extrusion: from Theory to Application in Pharmaceutical Formulation. *AAPS PharmSciTech*. 2016;17(1):20-42. doi:10.1208/s12249-015-

0360-7

81. Mendonsa N, Almutairy B, Kallakunta VR, et al. Manufacturing strategies to develop amorphous solid dispersions: An overview. *J Drug Deliv Sci Technol*. 2020;55(June 2019):101459. doi:10.1016/j.jddst.2019.101459

82. Crowley MM, Zhang F, Repka MA, et al. Pharmaceutical applications of hot-melt extrusion: Part I. *Drug Dev Ind Pharm*. 2007;33(9):909-926. doi:10.1080/03639040701498759

83. Bhairav BA, Kokane PA, Saudagar RB. Hot Melt Extrusion Technique-A Review. *Res J Sci Technol*. 2016;8(3):155. doi:10.5958/2349-2988.2016.00022.x

84. Lang B, McGinity JW, Williams RO. Hot-melt extrusion-basic principles and pharmaceutical applications. *Drug Dev Ind Pharm*. 2014;40(9):1133-1155. doi:10.3109/03639045.2013.838577

85. Thiry J, Krier F, Evrard B. A review of pharmaceutical extrusion: Critical process parameters and scaling-up. *Int J Pharm*. 2015;479(1):227-240. doi:10.1016/j.ijpharm.2014.12.036

86. Einfal T, Planinšek O, Hrovat K. Methods of amorphization and investigation of the amorphous state. *Acta Pharm*. 2013;63(3):305-334. doi:10.2478/acph-2013-0026

87. Willart JF, Caron V, Lefort R, Danède F, Prévost D, Descamps M. Athermal character of the solid state amorphization of lactose induced by ball milling. *Solid State Commun*. 2004;132(10):693-696. doi:10.1016/j.ssc.2004.09.007

88. Descamps M, Willart JF. Perspectives on the amorphisation/milling relationship in pharmaceutical materials. *Adv Drug Deliv Rev*. 2016;100:51-66. doi:10.1016/j.addr.2016.01.011

89. Fetch HJ. Defect-induced melting and solid-state amorphization. *Nature*. 1992;356:133-135.

90. Loh ZH, Samanta AK, Sia Heng PW. Overview of milling techniques for improving the solubility of poorly water-soluble drugs. *Asian J Pharm Sci*. 2014;10(4):255-274. doi:10.1016/j.ajps.2014.12.006

91. Pas T, Smeets B, Ramon H, et al. Mechanodegradation of Polymers: A Limiting Factor of Mechanochemical Activation in the Production of Amorphous Solid Dispersions by Cryomilling. *Mol Pharm*. 2020;17(8):2987-2999. doi:10.1021/acs.molpharmaceut.0c00376

92. Pas T, Bergonzi A, Michiels E, et al. Preparation of Amorphous Solid Dispersions by Cryomilling: Chemical and Physical Concerns Related to Active Pharmaceutical Ingredients and Carriers. *Mol Pharm*. 2020;17(3):1001-1013. doi:10.1021/acs.molpharmaceut.9b01265

93. Singh A, Van den Mooter G. Spray drying formulation of amorphous solid dispersions. *Adv Drug Deliv Rev*. 2016;100:27-50. doi:10.1016/j.addr.2015.12.010

94. Paudel A, Worku ZA, Meeus J, Guns S, Van Den Mooter G. Manufacturing of solid dispersions of poorly water soluble drugs by spray drying: Formulation and process considerations. *Int J Pharm*. 2013;453(1):253-284. doi:10.1016/j.ijpharm.2012.07.015

95. Vehring R. Pharmaceutical particle engineering via spray drying. *Pharm Res*. 2008;25(5):999-1022. doi:10.1007/s11095-007-9475-1

96. Farid M. A new approach to modelling of single droplet drying. 2003;58:2985-2993. doi:10.1016/S0009-2509(03)00161-1

97. Nešić S, Vodnik J. Kinetics of droplet evaporation. *Chem Eng Sci*. 1991;46(2):527-537. doi:10.1016/0009-2509(91)80013-O

98. Mezhericher M, Levy A, Borde I. Modelling the morphological evolution of nanosuspension droplet in constant-rate drying stage. *Chem Eng Sci*. 2011;66(5):884-896. doi:10.1016/j.ces.2010.11.028

99. Boel E, Koekoekx R, Dedroog S, et al. Unraveling particle formation: From single droplet drying to spray drying and electrospraying. *Pharmaceutics*. 2020;12(7):1-58. doi:10.3390/pharmaceutics12070625

100. de Souza Lima R, Ré MI, Arlabosse P. Drying droplet as a template for solid formation: A review. *Powder Technol*. 2020;359:161-171. doi:10.1016/j.powtec.2019.09.052

101. Mezhericher M, Levy A, Borde I. Modelling of particle breakage during drying. *Chem Eng Process Process Intensif*. 2008;47(8):1404-1411. doi:10.1016/j.cep.2007.06.018

102. Mezhericher M, Levy A, Borde I. Spray drying modelling based on advanced droplet drying kinetics. *Chem Eng Process Process Intensif*. 2010;49(11):1205-1213. doi:10.1016/j.cep.2010.09.002

103. Sadek C, Schuck P, Fallourd Y, Pradeau N, Le Floch-Fouéré C, Jeantet R. Drying of a single droplet to investigate process–structure–function relationships: a review. *Dairy Sci Technol*. 2015;95(6):771-794. doi:10.1007/s13594-014-0186-1

104. Nguyen DN, Clasen C, Van den Mooter G. Pharmaceutical Applications of Electrospraying. *J Pharm Sci*. 2016;105(9):2601-2620. doi:10.1016/j.xphs.2016.04.024

105. Wang S, Langrish T. A review of process simulations and the use of additives in spray drying. *Food Res Int*. 2009;42(1):13-25. doi:10.1016/j.foodres.2008.09.006

106. Vicente J, Pinto J, Menezes J, Gaspar F. Fundamental analysis of particle formation in spray drying. *Powder Technol*. 2013;247:1-7. doi:10.1016/j.powtec.2013.06.038

107. Walzel P. Influence of the Spray Method on Product Quality and Morphology in Spray Drying. *Chem Eng Technol*. 2011;34(7):1039-1048. doi:10.1002/ceat.201100051

108. Kemp IC, Hartwig T, Herdman R, Hamilton P, Bisten A, Bermingham S. Spray drying with a two-fluid nozzle to produce fine particles: Atomization, scale-up, and modeling. *Dry Technol*. 2016;34(10):1243-1252. doi:10.1080/07373937.2015.1103748

109. Langrish TAG. Assessing the rate of solid-phase crystallization for lactose: The effect of the difference between material and glass-transition temperatures. *Food Res Int*. 2008;41(6):630-636. doi:10.1016/j.foodres.2008.04.010

110. Charlesworth DH, Marshall WR. Evaporation from drops containing dissolved solids. *AIChE J*. 1960;6(1):9-23. doi:10.1002/aic.690060104

111. Grosshans H, Griesing M, Mönckedieck M, et al. Numerical and experimental study of the drying of bi-component droplets under various drying conditions. *Int J Heat Mass Transf*. 2016;96:97-109. doi:10.1016/j.ijheatmasstransfer.2015.12.062

112. Grosshans H, Griesing M, Hellwig T, Pauer W, Moritz HU, Gutheil E. A new model for the drying of mannitol-water droplets in hot air above the boiling temperature. *Powder Technol*. 2016;297:259-265. doi:10.1016/j.powtec.2016.04.023

113. Raula J, Eerikäinen H, Kauppinen EI. Influence of the solvent composition on the aerosol synthesis of pharmaceutical polymer nanoparticles. *Int J Pharm*. 2004;284(1-2):13-21. doi:10.1016/j.ijpharm.2004.07.003

114. Lin JC, Gentry JW. Spray drying drop morphology: Experimental study. *Aerosol Sci Technol*.

2003;37(1):15-32. doi:10.1080/02786820300888

115. Gregson FKA, Ordoubadi M, Miles REH, et al. Studies of competing evaporation rates of multiple volatile components from a single binary-component aerosol droplet. *Phys Chem Chem Phys*. 2019;21(19):9709-9719. doi:10.1039/c9cp01158g

116. Wulsten E, Kiekens F, van Dycke F, Voorspoels J, Lee G. Levitated single-droplet drying: Case study with itraconazole dried in binary organic solvent mixtures. *Int J Pharm*. 2009;378(1-2):116-121. doi:10.1016/j.ijpharm.2009.05.060

117. Vehring R, Foss WR, Lechuga-Ballesteros D. Particle formation in spray drying. *J Aerosol Sci*. 2007;38(7):728-746. doi:10.1016/j.jaerosci.2007.04.005

118. Tsotsas E, Mujumdar AS. Front Matter, Volume 3: Product Quality and Formulation. In: Tsotsas E, Mujumdar AS, eds. *Modern Drying Technology*. Wiley-VCH Verlag GmbH & Co. KGaA; 2014:I-XXXV. doi:10.1002/9783527631728.fmatter3

119. Poozesh S, Bilgili E. Scale-up of pharmaceutical spray drying using scale-up rules: A review. *Int J Pharm*. 2019;562(January):271-292. doi:10.1016/j.ijpharm.2019.03.047

120. Wan F, Bohr A, Jonas Maltesen M, et al. Critical Solvent Properties Affecting the Particle Formation Process and Characteristics of Celecoxib-Loaded PLGA Microparticles via Spray-Drying. *Pharm Res*. 2013;30:1065-1076. doi:10.1007/s11095-012-0943-x

121. Tian Y, Caron V, Jones DS, Healy AM, Andrews GP. Using Flory-Huggins phase diagrams as a pre-formulation tool for the production of amorphous solid dispersions: A comparison between hot-melt extrusion and spray drying. *J Pharm Pharmacol*. 2014;66(2):256-274. doi:10.1111/jphp.12141

122. Guns S, Dereymaker A, Kayaert P, Mathot V, Martens JA, Van Den Mooter G. Comparison between hot-melt extrusion and spray-drying for manufacturing solid dispersions of the graft copolymer of ethylene glycol and vinylalcohol. *Pharm Res*. 2011;28(3):673-682. doi:10.1007/s11095-010-0324-2

123. Haser A, Cao T, Lubach J, Listro T, Acquarulo L, Zhang F. Melt extrusion vs. spray drying: The effect of processing methods on crystalline content of naproxen-povidone formulations. *Eur J Pharm Sci*. 2017;102:115-125. doi:10.1016/j.ejps.2017.02.038

124. Li Y, Mann AKP, Zhang D, Yang Z. Processing impact on in vitro and in vivo performance of solid dispersions—a comparison between hot-melt extrusion and spray drying. *Pharmaceutics*. 2021;13(8). doi:10.3390/pharmaceutics13081307

125. Lehmkemper K, Kyerematen SO, Heinzerling O, Degenhardt M, Sadowski G. Long-Term Physical Stability of PVP- and PVPVA-Amorphous Solid Dispersions. *Mol Pharm*. 2017;14(1):157-171. doi:10.1021/acs.molpharmaceut.6b00763

126. S'Ari M, Blade H, Cosgrove S, et al. Characterization of Amorphous Solid Dispersions and Identification of Low Levels of Crystallinity by Transmission Electron Microscopy. *Mol Pharm*. 2021;18(5):1905-1919. doi:10.1021/acs.molpharmaceut.0c00918

127. Hancock BC, Shamblin SL, Zografi G. Molecular Mobility of Amorphous Pharmaceutical Solids Below Their Glass Transition Temperatures. *Pharm Res*. 1995;12(6):799-806. doi:10.1023/A:1016292416526

128. Guo Y, Shalaev E, Smith S. Physical stability of pharmaceutical formulations: Solid-state characterization of amorphous dispersions. *TrAC - Trends Anal Chem*. 2013;49:137-144. doi:10.1016/j.trac.2013.06.002

129. DeBoyace K, Wildfong PLD. The Application of Modeling and Prediction to the Formation and Stability of Amorphous Solid Dispersions. *J Pharm Sci*. 2018;107(1):57-74. doi:10.1016/j.xphs.2017.03.029

130. Medarević D, Djuriš J, Barmpalexis P, Kachrimanis K, Ibrić S. Analytical and computational methods for the estimation of drug-polymer solubility and miscibility in solid dispersions development. *Pharmaceutics*. 2019;11(8):1-33. doi:10.3390/pharmaceutics11080372

131. Mahieu A, Willart J-F, Dudognon E, Danède F, Descamps M. A New Protocol To Determine the Solubility of Drugs into Polymer Matrixes. *Mol Pharm*. 2013;10(2):560-566. doi:10.1021/mp3002254

132. Prudic A, Ji Y, Sadowski G. Thermodynamic phase behavior of API/polymer solid dispersions. *Mol Pharm*. 2014;11(7):2294-2304. doi:10.1021/mp400729x

133. Prudic A, Kleetz T, Korf M, Ji Y, Sadowski G. Influence of copolymer composition on the phase behavior of solid dispersions. *Mol Pharm*. 2014;11(11):4189-4198. doi:10.1021/mp500412d

134. Prudic A, Ji Y, Luebbert C, Sadowski G. Influence of humidity on the phase behavior of API/polymer formulations. *Eur J Pharm Biopharm*. 2015;94:352-362. doi:10.1016/j.ejpb.2015.06.009

135. Luebbert C, Huxoll F, Sadowski G. Amorphous-Amorphous Phase Separation in API/Polymer Formulations. *Molecules*. 2017;22(2):296. doi:10.3390/molecules22020296

136. Dohrn S, Luebbert C, Lehmkemper K, Kyerematen SO, Degenhardt M, Sadowski G. Solvent influence on the phase behavior and glass transition of Amorphous Solid Dispersions. *Eur J Pharm Biopharm*. 2021;158:132-142. doi:10.1016/j.ejpb.2020.11.002

137. Dohrn S, Reimer P, Luebbert C, et al. Thermodynamic Modeling of Solvent-Impact on Phase Separation in Amorphous Solid Dispersions during Drying. *Mol Pharm*. 2020;17(7):2721-2733. doi:10.1021/acs.molpharmaceut.0c00418

138. Luebbert C, Real D, Sadowski G. Choosing Appropriate Solvents for ASD Preparation. *Mol Pharm*. 2018;15(11):5397-5409. doi:10.1021/acs.molpharmaceut.8b00892

139. Dohrn S, Rawal P, Luebbert C, et al. Predicting process design spaces for spray drying amorphous solid dispersions. *Int J Pharm X*. 2021;3(February):100072. doi:10.1016/j.ijpx.2021.100072

140. Knopp MM, Tajber L, Tian Y, et al. Comparative Study of Different Methods for the Prediction of Drug-Polymer Solubility. *Mol Pharm*. 2015;12(9):3408-3419. doi:10.1021/acs.molpharmaceut.5b00423

141. Rask MB, Knopp MM, Olesen NE, Holm R, Rades T. Comparison of two DSC-based methods to predict drug-polymer solubility. *Int J Pharm*. 2018;540(1-2):98-105. doi:10.1016/j.ijpharm.2018.02.002

142. Mathers A, Hassouna F, Klajmon M, Fulem M. Comparative Study of DSC-Based Protocols for API-Polymer Solubility Determination. *Mol Pharm*. 2021;18(4):1742-1757. doi:10.1021/acs.molpharmaceut.0c01232

143. Kang N, Lee J, Choi JN, Mao C, Lee EH. Cryomilling-induced solid dispersion of poor glass forming/poorly water-soluble mefenamic acid with polyvinylpyrrolidone K12. *Drug Dev Ind Pharm*. 2015;41(6):978-988. doi:10.3109/03639045.2014.920024

144. Bangalore S, Kamalakkannan G, Parkar S, Messerli FH. Fixed-Dose Combinations Improve Medication Compliance: A Meta-Analysis. *Am J Med*. 2007;120(8):713-719.

doi:10.1016/j.amjmed.2006.08.033

145. Lehmkemper K, Kyerematen SO, Heinzerling O, Degenhardt M, Sadowski G. Impact of Polymer Type and Relative Humidity on the Long-Term Physical Stability of Amorphous Solid Dispersions. *Mol Pharm*. 2017;14(12):4374-4386. doi:10.1021/acs.molpharmaceut.7b00492

146. Sekiguchi K, Obi N, Ueda Y. Studies on Absorption of Eutectic Mixture. II. Absorption of fused Conglomerates of Chloramphenicol and Urea in Rabbits. *Chem Pharm Bull (Tokyo)*. 1964;12(2):134-144. doi:10.1248/cpb.12.134

147. Van Eerdenbrugh B, Raina S, Hsieh Y-L, Augustijns P, Taylor LS. Classification of the Crystallization Behavior of Amorphous Active Pharmaceutical Ingredients in Aqueous Environments. *Pharm Res*. 2014;31(4):969-982. doi:10.1007/s11095-013-1216-z

148. Velazquez MM, Valero M, Rodríguez LJ, Costa SMB, Santos MA. Hydrogen bonding in a non-steroidal anti-inflammatory drug-Naproxen. *J Photochem Photobiol B Biol*. 1995;29(1):23-31. doi:10.1016/1011-1344(95)90245-7

149. Jubert A, Legarto ML, Massa NE, Tévez LL, Okulik NB. Vibrational and theoretical studies of non-steroidal anti-inflammatory drugs Ibuprofen [2-(4-isobutylphenyl)propionic acid]; Naproxen [6-methoxy-α-methyl-2-naphthalene acetic acid] and Tolmetin acids [1-methyl-5-(4-methylbenzoyl)-1H-pyrrole-2-acetic acid]. *J Mol Struct*. 2006;783(1-3):34-51. doi:10.1016/j.molstruc.2005.08.018

150. Paudel A, Van Humbeeck J, Van Den Mooter G. articles Theoretical and Experimental Investigation on the Solid Solubility and Miscibility of Naproxen in. *Mol*. 2010;7(4):1133-1148. doi:10.1021/mp100013p

151. Van Eerdenbrugh B, Taylor LS. An ab initio polymer selection methodology to prevent crystallization in amorphous solid dispersions by application of crystal engineering principles. *CrystEngComm*. 2011;13(20):6171-6178. doi:10.1039/c1ce05183k

152. Friesen DT, Shanker R, Crew M, Smithey DT, Curatolo WJ, Nightingale JAS. Hydroxypropyl Methylcellulose Acetate Succinate-Based Spray Spray-Dried Dispersions: An Overview. 2008;5(6):1003-1019.

153. Shibata Y, Fujii M, Sugamura Y, et al. The preparation of a solid dispersion powder of indomethacin with crospovidone using a twin-screw extruder or kneader. *Int J Pharm*. 2009;365(1-2):53-60. doi:10.1016/j.ijpharm.2008.08.023

154. Rowe RC, Sheskey PJ, Quinn ME. *Handbook of Pharmaceutical Excipients*. Pharmaceutical Press; 2009.

155. Nakamichi K, Nakano T, Yasuura H, Izumi S, Kawashima Y. The role of the kneading paddle and the effects of screw revolution speed and water content on the preparation of solid dispersions using a twin-screw extruder. *Int J Pharm*. 2002;241(2):203-211. doi:10.1016/S0378-5173(02)00134-5

156. Saerens L, Dierickx L, Quinten T, et al. In-line NIR spectroscopy for the understanding of polymer-drug interaction during pharmaceutical hot-melt extrusion. *Eur J Pharm Biopharm*. 2012;81(1):230-237. doi:10.1016/j.ejpb.2012.01.001

157. Lang B, McGinity JW, Williams RO. Dissolution enhancement of itraconazole by hot-melt extrusion alone and the combination of hot-melt extrusion and rapid freezing-effect of formulation and processing variables. *Mol Pharm*. 2014;11(1):186-196. doi:10.1021/mp4003706

158. Bikiaris D, Papageorgiou GZ, Stergiou A, et al. Physicochemical studies on solid dispersions of poorly water-soluble drugs: Evaluation of capabilities and limitations of thermal analysis techniques. *Thermochim Acta*. 2005;439(1-2):58-67. doi:10.1016/j.tca.2005.09.011

159. Kyerematen SO, Pudlas M, Woehrle GH. A fast and reliable empirical approach for estimating solubility of crystalline drugs in polymers for hot melt extrusion formulations. *J Pharm Sci*. 2014;103(9):2847-2858. doi:10.1002/jps.23941

160. Di L, Fish P V., Mano T. Bridging solubility between drug discovery and development. *Drug Discov Today*. 2012;17(9-10):486-495. doi:10.1016/j.drudis.2011.11.007

161. Poozesh S, Mahdi Jafari S. Are traditional small-scale screening methods reliable to predict pharmaceutical spray drying? *Pharm Dev Technol*. 2019;24(7):915-925. doi:10.1080/10837450.2019.1616208

162. Wyttenbach N, Janas C, Siam M, et al. Miniaturized screening of polymers for amorphous drug stabilization (SPADS): Rapid assessment of solid dispersion systems. *Eur J Pharm Biopharm*. 2013;84(3):583-598. doi:10.1016/j.ejpb.2013.01.009

163. Parikh T, Gupta SS, Meena AK, Vitez I, Mahajan N, Serajuddin ATM. Application of Film-Casting Technique to Investigate Drug-Polymer Miscibility in Solid Dispersion and Hot-Melt Extrudate. *J Pharm Sci*. 2015;104(7):2142-2152. doi:10.1002/jps.24446

164. Janssens S, De Zeure A, Paudel A, Van Humbeeck J, Rombaut P, Van Den Mooter G. Influence of preparation methods on solid state supersaturation of amorphous solid dispersions: A case study with itraconazole and eudragit E100. *Pharm Res*. 2010;27(5):775-785. doi:10.1007/s11095-010-0069-y

165. Defrese MK, Farmer MA, Long Y, Timmerman LR, Bae Y, Marsac PJ. Approaches to Understanding the Solution-State Organization of Spray-Dried Dispersion Feed Solutions and Its Translation to the Solid State. *Mol Pharm*. 2020;17(12):4548-4563. doi:10.1021/acs.molpharmaceut.0c00729

166. Hugo M, Kunath K, Dressman J. Selection of excipient, solvent and packaging to optimize the performance of spray-dried formulations: Case example fenofibrate. *Drug Dev Ind Pharm*. 2013;39(2):402-412. doi:10.3109/03639045.2012.685176

167. Paudel A, Van Den Mooter G. Influence of solvent composition on the miscibility and physical stability of naproxen/PVP K 25 solid dispersions prepared by cosolvent spray-drying. *Pharm Res*. 2012;29(1):251-270. doi:10.1007/s11095-011-0539-x

168. Thakore SD, Prasad R, Dalvi S V., Bansal AK. Role of solvent in differential phase behavior of celecoxib during spray drying. *Int J Pharm*. 2020;585(May):119489. doi:10.1016/j.ijpharm.2020.119489

169. Wan F, Maltesen MJ, Bjerregaard S, Foged C, Rantanen J, Yang M. Particle engineering technologies for improving the delivery of peptide and protein drugs. *J Drug Deliv Sci Technol*. 2013;23(4):355-363. doi:10.1016/S1773-2247(13)50052-9

170. Yani Y, Kanaujia P, Chow PS, Tan RBH. Effect of API-Polymer Miscibility and Interaction on the Stabilization of Amorphous Solid Dispersion: A Molecular Simulation Study. *Ind Eng Chem Res*. 2017;56(44):12698-12707. doi:10.1021/acs.iecr.7b03187

171. Yuan X, Xiang TX, Anderson BD, Munson EJ. Hydrogen Bonding Interactions in Amorphous Indomethacin and Its Amorphous Solid Dispersions with Poly(vinylpyrrolidone) and Poly(vinylpyrrolidone-co-vinyl acetate) Studied Using 13C Solid-State NMR. *Mol Pharm*. 2015;12(12):4518-4528. doi:10.1021/acs.molpharmaceut.5b00705

172. Smallwood I. *Handbook of Organic Solvent Properties*. 1st ed.; 1996.

173. Kestur US, Van Eerdenbrugh B, Taylor LS. Influence of polymer chemistry on crystal growth inhibition of two chemically diverse organic molecules. *CrystEngComm*. 2011;13(22):6712-6718. doi:10.1039/c1ce05822c

174. Van Eerdenbrugh B, Baird JA, Taylor LS. Crystallization tendency of active pharmaceutical ingredients following rapid solvent evaporation - classification and comparison with crystallization tendency from undercooled melts. *J Pharm Sci*. 2010;99(9):3826-3838. doi:10.1002/jps

175. Surwase SA, Boetker JP, Saville D, et al. Indomethacin: New polymorphs of an old drug. *Mol Pharm*. 2013;10:4472-4480. doi:10.1021/mp400299a

176. Watterson S, Hudson S, Svärd M, Rasmuson ÅC. Thermodynamics of fenofibrate and solubility in pure organic solvents. *Fluid Phase Equilib*. 2014;367:143-150. doi:10.1016/j.fluid.2014.01.029

177. Ma Q, Georgiev G, Cebe P. Constraints in semicrystalline polymers: Using quasi-isothermal analysis to investigate the mechanisms of formation and loss of the rigid amorphous fraction. *Polymer (Guildf)*. 2011;52(20):4562-4570. doi:10.1016/j.polymer.2011.08.006

178. Righetti MC, Gazzano M, Delpouve N, Saiter A. Contribution of the rigid amorphous fraction to physical ageing of semi-crystalline PLLA. *Polymer (Guildf)*. 2017;125:241-253. doi:10.1016/j.polymer.2017.07.089

179. Magoń A, Pyda M. Study of crystalline and amorphous phases of biodegradable poly(lactic acid) by advanced thermal analysis. *Polymer (Guildf)*. 2009;50(16):3967-3973. doi:10.1016/j.polymer.2009.06.052

180. Schneider H, Saalwächter K, Roos M. Complex Morphology of the Intermediate Phase in Block Copolymers and Semicrystalline Polymers As Revealed by 1H NMR Spin Diffusion Experiments. *Macromolecules*. 2017;50(21):8598-8610. doi:10.1021/acs.macromol.7b00703

181. Vyazovkin S. “Nothing Can Hide Itself from Thy Heat”: Understanding Polymers via Unconventional Applications of Thermal Analysis. *Macromol Rapid Commun*. 2019;40(1):1-15. doi:10.1002/marc.201800334

182. Leng J, Kang N, Wang DY, Wurm A, Schick C, Schönhals A. Crystallization behavior of nanocomposites based on poly(L-lactide) and MgAl layered double hydroxides – Unbiased determination of the rigid amorphous phases due to the crystals and the nanofiller. *Polymer (Guildf)*. 2017;108:257-264. doi:10.1016/j.polymer.2016.11.065

183. Monteyne T, Heeze L, Mortier STFC, et al. The use of Rheology Combined with Differential Scanning Calorimetry to Elucidate the Granulation Mechanism of an Immiscible Formulation During Continuous Twin-Screw Melt Granulation. *Pharm Res*. 2016;33(10):2481-2494. doi:10.1007/s11095-016-1973-6

184. Litvinov VM, Guns S, Adriaensens P, et al. Solid state solubility of miconazole in poly[(ethylene glycol)-g-vinyl alcohol] using hot-melt extrusion. *Mol Pharm*. 2012;9(10):2924-2932. doi:10.1021/mp300280k

185. Dedroog S, Pas T, Vergauwen B, Huygens C, Van den Mooter G. Solid-state analysis of amorphous solid dispersions: Why DSC and XRPD may not be regarded as stand-alone techniques. *J Pharm Biomed Anal*. 2020;178. doi:10.1016/j.jpba.2019.112937

186. Vasconcelos T, Sarmento B, Costa P. Solid dispersions as strategy to improve oral bioavailability

of poor water soluble drugs. *Drug Discov Today*. 2007;12(23-24):1068-1075. doi:10.1016/j.drudis.2007.09.005

187. Christina B, Taylor LS, Mauer LJ. Physical stability of L-ascorbic acid amorphous solid dispersions in different polymers: A study of polymer crystallization inhibitor properties. *Food Res Int*. 2015;76:867-877. doi:10.1016/j.foodres.2015.08.009

188. Qi S, Moffat JG, Yang Z. Early stage phase separation in pharmaceutical solid dispersion thin films under high humidity: Improved spatial understanding using probe-based thermal and spectroscopic nanocharacterization methods. *Mol Pharm*. 2013;10(3):918-930. doi:10.1021/mp300557q

189. Ayenew Z, Paudel A, Van Den Mooter G. Can compression induce demixing in amorphous solid dispersions? A case study of naproxen-PVP K25. *Eur J Pharm Biopharm*. 2012;81(1):207-213. doi:10.1016/j.ejpb.2012.01.007

190. Huang J, Wigent RJ, Schwartz JB. Drug–Polymer Interaction and Its Significance on the Physical Stability of Nifedipine Amorphous Dispersion in Microparticles of an Ammonio Methacrylate Copolymer and Ethylcellulose Binary Blend. *J Pharm Sci*. 2008;97:251-262. doi:10.1002/jps

191. Zhang X, Rao Q, Qiu Z, et al. Using Acetone/Water Binary Solvent to Enhance the Stability and Bioavailability of Spray Dried Enzalutamide/HPMC-AS Solid Dispersions. *J Pharm Sci*. 2021;110(3):1160-1171. doi:10.1016/j.xphs.2020.10.010

192. Chen Y, Huang W, Chen J, Wang H, Zhang S, Xiong S. The Synergetic Effects of Nonpolar and Polar Protic Solvents on the Properties of Felodipine and Soluplus in Solutions, Casting Films, and Spray-Dried Solid Dispersions. *J Pharm Sci*. 2018;107(6):1615-1623. doi:10.1016/j.xphs.2018.02.006

193. Theil F, Milsmann J, Kyerematen SO, Anantharaman S, Rosenberg J, Van Lishaut H. Extraordinary Long-Term-Stability in Kinetically Stabilized Amorphous Solid Dispersions of Fenofibrate. *Mol Pharm*. 2017;14(12):4636-4647. doi:10.1021/acs.molpharmaceut.7b00735

194. Alsulays BB, Park JB, Alshehri SM, et al. Influence of molecular weight of carriers and processing parameters on the extrudability, drug release, and stability of fenofibrate formulations processed by hot-melt extrusion. *J Drug Deliv Sci Technol*. 2015;29:189-198. doi:10.1016/j.jddst.2015.07.011

195. Zhang M, Li H, Lang B, et al. Formulation and delivery of improved amorphous fenofibrate solid dispersions prepared by thin film freezing. *Eur J Pharm Biopharm*. 2012;82(3):534-544. doi:10.1016/j.ejpb.2012.06.016

196. Wu JX, Yang M, Berg F Van Den, Pajander J, Rades T, Rantanen J. Influence of solvent evaporation rate and formulation factors on solid dispersion physical stability. *Eur J Pharm Sci*. 2011;44(5):610-620. doi:10.1016/j.ejps.2011.10.008

197. Dedroog S, Boel E, Kindts C, Appeltans B, Van den Mooter G. The underestimated contribution of the solvent to the phase behavior of highly drug loaded amorphous solid dispersions. *Int J Pharm*. Published online 2021:121201. doi:10.1016/j.ijpharm.2021.121201

198. Al-Obaidi H, Brocchini S, Buckton G. Anomalous properties of spray dried solid dispersions. *J Pharm Sci*. 2009;98:4757-4737. doi:10.1002/jps

199. Mugheirbi NA, Mosquera-Giraldo LI, Borca CH, Slipchenko L V., Taylor LS. Phase Behavior of Drug-Hydroxypropyl Methylcellulose Amorphous Solid Dispersions Produced from Various Solvent Systems: Mechanistic Understanding of the Role of Polymer using Experimental and Theoretical Methods. *Mol Pharm*. 2018;15(8):3236-3251.

doi:10.1021/acs.molpharmaceut.8b00324

200. Taylor LS, Li N, Cape JL, et al. Water-induced phase separation of spray-dried amorphous solid dispersions. *Mol Pharm*. 2020;17(10):4004-4017. doi:10.1021/acs.molpharmaceut.0c00798

201. Ziaee A, Albadarin AB, Padrela L, Faucher A, O'Reilly E, Walker G. Spray drying ternary amorphous solid dispersions of ibuprofen – An investigation into critical formulation and processing parameters. *Eur J Pharm Biopharm*. 2017;120(May):43-51. doi:10.1016/j.ejpb.2017.08.005

202. Paudel A, Loyson Y, Guy V den M. An Investigation into the Effect of Spray Drying Temperature and Atomizing Conditions on Miscibility, Physical Stability, and Performance of Naproxen–PVP K 25 Solid Dispersions. *J Pharm Sci*. 2013;102:1249-1267. doi:10.1002/jps

203. Patel AD, Agrawal A, Dave RH. Investigation of the effects of process variables on derived properties of spray dried solid-dispersions using polymer based response surface model and ensemble artificial neural network models. *Eur J Pharm Biopharm*. 2014;86(3):404-417. doi:10.1016/j.ejpb.2013.10.014

204. Boel E, Giacomini F, Van den Mooter G. Solvent influence on manufacturability, phase behavior and morphology of amorphous solid dispersions prepared via bead coating. *Eur J Pharm Biopharm*. 2021;167(May):175-188. doi:10.1016/j.ejpb.2021.07.013

205. Chiu CY, Yen YJ, Kuo SW, Chen HW, Chang FC. Complicated phase behavior and ionic conductivities of PVP-co-PMMA-based polymer electrolytes. *Polymer (Guildf)*. 2007;48(5):1329-1342. doi:10.1016/j.polymer.2006.12.059

206. Worku ZA, Aarts J, Singh A, Van Den Mooter G. Drug-polymer miscibility across a spray dryer: A case study of naproxen and miconazole solid dispersions. *Mol Pharm*. 2014;11(4):1094-1101. doi:10.1021/mp4003943

207. Joo SH, Kim JH, Kang SW, Jang J, Kang YS. Propylene sorption and coordinative interactions for poly(N-vinyl pyrrolidone-co-vinyl acetate)/silver salt complex membranes. *J Polym Sci Part B Polym Phys*. 2007;45(16):2263-2269. doi:10.1002/polb.21244

208. Tomasko DL, Timko MT. Tailoring of specific interactions to modify the morphology of naproxen. *J Cryst Growth*. 1999;205(1):233-243. doi:10.1016/S0022-0248(99)00237-7

209. Paudel A, Nies E, Van Den Mooter G. Relating hydrogen-bonding interactions with the phase behavior of naproxen/PVP K 25 solid dispersions: Evaluation of solution-cast and quench-cooled films. *Mol Pharm*. 2012;9(11):3301-3317. doi:10.1021/mp3003495

210. Sailaja U, Thayyil MS, Kumar NSK, Govindaraj G. Molecular dynamics of amorphous pharmaceutical fenofibrate studied by broadband dielectric spectroscopy. *J Pharm Anal*. 2016;6(3):165-170. doi:10.1016/j.jpha.2014.09.003

211. Taylor LS, Langkilde FW, Zografi G. Fourier transform Raman spectroscopic study of the interaction of water vapor with amorphous polymers. *J Pharm Sci*. 2001;90(7):888-901. doi:10.1002/jps.1041

212. Islam MIU, Langrish TAG. An investigation into lactose crystallization under high temperature conditions during spray drying. *Food Res Int*. 2010;43(1):46-56. doi:10.1016/j.foodres.2009.08.010

213. Thayer AM, Houston C. Finding solutions. Custom manufacturers take on drug solubility issues to help pharmaceutical firms move products through development. *Chem Eng News*. 2010;88(22):13-18. doi:10.1016/j.jenvp.2009.05.001

214. Lin X, Hu Y, Liu L, et al. Physical stability of amorphous solid dispersions. Published online 2018. doi:10.1007/s11095-018-2408-3

215. Bhugra C, Pikal MJ. Role of Thermodynamic , Molecular , and Kinetic Factors in Crystallization From the Amorphous State. 2008;97(4):1329-1349. doi:10.1002/jps

216. Zhou D, Zhang GGZ, Law D, Grant DJW, Schmitt EA. Physical stability of amorphous pharmaceuticals: Importance of configurational thermodynamic quantities and molecular mobility. *J Pharm Sci*. 2002;91(8):1863-1872. doi:10.1002/jps.10169

217. Graeser KA, Patterson JE, Zeitler JA, Gordon KC, Rades T. Correlating thermodynamic and kinetic parameters with amorphous stability. *Eur J Pharm Sci*. 2009;37(3-4):492-498. doi:10.1016/j.ejps.2009.04.005

218. Sun Y, Zhu L, Wu T, Cai T, Gunn EM, Yu L. Stability of Amorphous Pharmaceutical Solids: Crystal Growth Mechanisms and Effect of Polymer Additives. *AAPS J*. 2012;14(3):380-388. doi:10.1208/s12248-012-9345-6

219. Ivanisevic I. Physical Stability Studies of Miscible Amorphous Solid Dispersions. *J Pharm Sci*. 2010;99(9):4008-4012.

220. Guo Y, Shalaev E, Smith S. Trends in Analytical chemistry Physical stability of pharmaceutical formulations : solid-state characterization of amorphous dispersions. *Trends Anal Chem*. 2013;49:137-144. doi:10.1016/j.trac.2013.06.002

221. Takeuchi I, Shimakura K, Kuroda H, Nakajima T, Goto S, Makino K. Estimation of Crystallinity of Nifedipine-Polyvinylpyrrolidone Solid Dispersion by Usage of Terahertz Time-Domain Spectroscopy and of X-Ray Powder Diffractometer. *J Pharm Sci*. 2015;104(12):4307-4313. doi:10.1002/jps.24671

222. Meng F, Dave V, Chauhan H. Qualitative and quantitative methods to determine miscibility in amorphous drug-polymer systems. *Eur J Pharm Sci*. 2015;77:106-111. doi:10.1016/j.ejps.2015.05.018

223. Laggner P, Paudel A. Density fluctuations in amorphous pharmaceutical solids. Can SAXS help to predict stability? *Colloids Surfaces B Biointerfaces*. 2018;168:76-82. doi:10.1016/j.colsurfb.2018.05.003

224. Paudel A, Geppi M, Van den Mooter G. Structural and Dynamic Properties of Amorphous Solid Dispersions : The Role of Solid-State Nuclear Magnetic Resonance Spectroscopy and Relaxometry. *J Pharm Sci*. 2014;103(9):2635-2662. doi:10.1002/jps.23966

225. Hancock BC, Shamblin SL. Molecular mobility of amorphous pharmaceuticals determined using differential scanning calorimetry. *Thermochim Acta*. 2001;380(2):95-107. doi:10.1016/S0040-6031(01)00663-3

226. Thakral NK, Zanon RL, Kelly RC, Thakral S. Applications of Powder X-Ray Diffraction in Small Molecule Pharmaceuticals: Achievements and Aspirations. *J Pharm Sci*. Published online 2018:1-14. doi:10.1016/j.xphs.2018.08.010

227. Randall CS, Rocco WL, Ricou P. XRD in pharmaceutical analysis: A versatile tool for problem-solving. *Am Pharm Rev*. Published online 2010.

228. Wanapun D, Kestur US, Kissick DJ, Simpson GJ, Taylor LS. Selective detection and quantitation of organic molecule crystallization by second harmonic generation microscopy. *Anal Chem*. 2010;82(13):5425-5432. doi:10.1021/ac100564f

229. Bates S, Zografi G, Engers D, Morris K, Crowley K, Newman A. Analysis of amorphous and

nanocrystalline solids from their X-ray diffraction patterns. *Pharm Res*. 2006;23(10):2333-2349. doi:10.1007/s11095-006-9086-2

230. Pecharsky VK, Zavalij PY. *Fundamentals of Powder Diffraction and Structural Characterization of Materials - Second Edition*.; 2009.

231. DeBoyace K, Zdaniewski C, Wildfong PLD. Differential scanning calorimetry isothermal hold times can impact interpretations of drug-polymer dispersability in amorphous solid dispersions. *J Pharm Biomed Anal*. Published online 2018. doi:10.1016/j.jpba.2017.12.001

232. Q.M. Craig D, Reading M. *Thermal Analysis of Pharmaceuticals*.; 2007.

233. Zhang S, Lee TWY, Chow AHL. Thermodynamic and kinetic evaluation of the impact of polymer excipients on storage stability of amorphous itraconazole. *Int J Pharm*. 2019;555(December 2018):394-403. doi:10.1016/j.ijpharm.2018.11.063

234. Lehmkemper K, Kyerematen SO, Bartels M, Degenhardt M, Sadowski G. Physical stability of API/polymer-blend amorphous solid dispersions. *Eur J Pharm Biopharm*. 2018;124(October 2017):147-157. doi:10.1016/j.ejpb.2017.12.002

235. Panini P, Rampazzo M, Singh A, Vanhoutte F, Van den Mooter G. Myth or truth: The glass forming ability class III drugs will always form single-phase homogenous amorphous solid dispersion formulations. *Pharmaceutics*. 2019;11(10). doi:10.3390/pharmaceutics11100529

236. Blaabjerg LI, Bulduk B, Lindenberg E, Löbmann K, Rades T, Grohganz H. Influence of Glass Forming Ability on the Physical Stability of Supersaturated Amorphous Solid Dispersions. *J Pharm Sci*. 2019;108(8):2561-2569. doi:10.1016/j.xphs.2019.02.028

237. Kapourani A, Vardaka E, Katopodis K, Kachrimanis K, Barmpalexis P. Crystallization tendency of APIs possessing different thermal and glass related properties in amorphous solid dispersions. *Int J Pharm*. 2020;579(December 2019):119149. doi:10.1016/j.ijpharm.2020.119149

238. Li N, Taylor LS. Tailoring supersaturation from amorphous solid dispersions. *J Control Release*. 2018;279(April):114-125. doi:10.1016/j.jconrel.2018.04.014

239. Qian F, Wang J, Hartley R, et al. Solution behavior of PVP-VA and HPMC-AS-Based amorphous solid dispersions and their bioavailability implications. *Pharm Res*. 2012;29(10):2766-2776. doi:10.1007/s11095-012-0695-7

240. Knopp MM, Chourak N, Khan F, et al. Effect of polymer type and drug dose on the in vitro and in vivo behavior of amorphous solid dispersions. *Eur J Pharm Biopharm*. 2016;105:106-114. doi:10.1016/j.ejpb.2016.05.017

241. Jackson MJ, Kestur US, Hussain MA, Taylor LS. Dissolution of Danazol Amorphous Solid Dispersions: Supersaturation and Phase Behavior as a Function of Drug Loading and Polymer Type. *Mol Pharm*. 2016;13(1):223-231. doi:10.1021/acs.molpharmaceut.5b00652

242. Dohrn S, Luebbert C, Lehmkemper K, Kyerematen SO, Degenhardt M, Sadowski G. Phase behavior of pharmaceutically relevant polymer/solvent mixtures. *Int J Pharm*. 2020;577(November 2019):119065. doi:10.1016/j.ijpharm.2020.119065

243. Fu N, Woo MW, Chen XD. Single Droplet Drying Technique to Study Drying Kinetics Measurement and Particle Functionality: A Review. *Dry Technol*. 2012;30(15):1771-1785. doi:10.1080/07373937.2012.708002

244. Adhikari B, Howes T, Bhandari BR, Truong V. Experimental studies and kinetics of single drop drying and their relevance in drying of sugar-rich foods: A review. *Int J Food Prop*. 2000;3(3):323-351. doi:10.1080/10942910009524639

245. Boel E, Smeets A, Vergaelen M, De la Rosa VR, Hoogenboom R, Van den Mooter G. Comparative study of the potential of poly(2-ethyl-2-oxazoline) as carrier in the formulation of amorphous solid dispersions of poorly soluble drugs. *Eur J Pharm Biopharm*. 2019;144(June):79-90. doi:10.1016/j.ejpb.2019.09.005

246. Mahmah O, Tabbakh R, Kelly A, Paradkar A. A comparative study of the effect of spray drying and hot-melt extrusion on the properties of amorphous solid dispersions containing felodipine. *J Pharm Pharmacol*. 2014;66(2):275-284. doi:10.1111/jphp.12099

247. Moinuddin SM, Ruan S, Huang Y, et al. Facile formation of co-amorphous atenolol and hydrochlorothiazide mixtures via cryogenic-milling: Enhanced physical stability, dissolution and pharmacokinetic profile. *Int J Pharm*. 2017;532(1):393-400. doi:10.1016/j.ijpharm.2017.09.020

248. Li W, Song J, Li J, et al. Co-amorphization of atorvastatin by lisinopril as a co-former for solubility improvement. *Int J Pharm*. 2021;607(103). doi:10.1016/j.ijpharm.2021.120971

249. Ziaee A, O'Dea S, Howard-Hildige A, et al. Amorphous solid dispersion of ibuprofen: A comparative study on the effect of solution based techniques. *Int J Pharm*. 2019;572(August). doi:10.1016/j.ijpharm.2019.118816

250. Butreddy A, Bandari S, Repka MA. Quality-by-design in hot melt extrusion based amorphous solid dispersions: An industrial perspective on product development. *Eur J Pharm Sci*. 2021;158(September 2020):105655. doi:10.1016/j.ejps.2020.105655

251. Pawar J, Tayade A, Gangurde A, Moravkar K, Amin P. Solubility and dissolution enhancement of efavirenz hot melt extruded amorphous solid dispersions using combination of polymeric blends: A QbD approach. *Eur J Pharm Sci*. 2016;88:37-49. doi:10.1016/j.ejps.2016.04.001

252. Thiry J, Lebrun P, Vinassa C, et al. Continuous production of itraconazole-based solid dispersions by hot melt extrusion: Preformulation, optimization and design space determination. *Int J Pharm*. 2016;515(1-2):114-124. doi:10.1016/j.ijpharm.2016.10.003

253. Gu B, Linehan B, Tseng YC. Optimization of the Büchi B-90 spray drying process using central composite design for preparation of solid dispersions. *Int J Pharm*. 2015;491(1-2):208-217. doi:10.1016/j.ijpharm.2015.06.006

254. Ziaee A, Albadarin AB, Padrela L, Femmer T, O'Reilly E, Walker G. Spray drying of pharmaceuticals and biopharmaceuticals: Critical parameters and experimental process optimization approaches. *Eur J Pharm Sci*. 2019;127(November 2018):300-318. doi:10.1016/j.ejps.2018.10.026

255. Smeets A, Koekoekx R, Clasen C, Van den Mooter G. Amorphous solid dispersions of darunavir: Comparison between spray drying and electrospraying. *Eur J Pharm Biopharm*. 2018;130(June):96-107. doi:10.1016/j.ejpb.2018.06.021

256. Hengsawas Surasarang S, Keen JM, Huang S, Zhang F, McGinity JW, Williams RO. Hot melt extrusion versus spray drying: hot melt extrusion degrades albendazole. *Drug Dev Ind Pharm*. 2017;43(5):797-811. doi:10.1080/03639045.2016.1220577

257. Duret C, Wauthoz N, Sebti T, Vanderbist F, Amighi K. Solid dispersions of itraconazole for inhalation with enhanced dissolution, solubility and dispersion properties. *Int J Pharm*. 2012;428(1-2):103-113. doi:10.1016/j.ijpharm.2012.03.002

258. Kawakami K, Hasegawa Y, Deguchi K, et al. Competition of Thermodynamic and Dynamic Factors During Formation of Multicomponent Particles via Spray Drying. *J Pharm Sci*. 2013;102(2):518-529. doi:10.1002/jps

259. Gaiani C, Morand M, Sanchez C, et al. How surface composition of high milk proteins powders is influenced by spray-drying temperature. *Colloids Surfaces B Biointerfaces*. 2010;75(1):377-384. doi:10.1016/j.colsurfb.2009.09.016

260. Maas SG, Schaldach G, Littringer EM, et al. The impact of spray drying outlet temperature on the particle morphology of mannitol. *Powder Technol*. 2011;213(1):27-35. doi:10.1016/j.powtec.2011.06.024

261. Tan SP, Kha TC, Parks SE, Stathopoulos CE, Roach PD. Effects of the spray-drying temperatures on the physiochemical properties of an encapsulated bitter melon aqueous extract powder. *Powder Technol*. 2015;281:65-75. doi:10.1016/j.powtec.2015.04.074

262. Jermain S V., Miller D, Spangenberg A, et al. Homogeneity of amorphous solid dispersions–an example with KinetiSol®. *Drug Dev Ind Pharm*. 2019;45(5):724-735. doi:10.1080/03639045.2019.1569037

263. Luebbert C, Klanke C, Sadowski G. Investigating phase separation in amorphous solid dispersions via Raman mapping. *Int J Pharm*. 2018;535(1-2):245-252. doi:10.1016/j.ijpharm.2017.11.014

264. Lu J, Cuellar K, Hammer NI, et al. Solid-state characterization of Felodipine-Soluplus amorphous solid dispersions. *Drug Dev Ind Pharm*. 2016;42(3):485-496. doi:10.3109/03639045.2015.1104347

265. Widjaja E, Kanaujia P, Lau G, et al. Detection of trace crystallinity in an amorphous system using Raman microscopy and chemometric analysis. *Eur J Pharm Sci*. 2011;42(1-2):45-54. doi:10.1016/j.ejps.2010.10.004

266. Qian F, Huang J, Zhu Q, et al. Is a distinctive single Tg a reliable indicator for the homogeneity of amorphous solid dispersion? *Int J Pharm*. 2010;395(1-2):232-235. doi:10.1016/j.ijpharm.2010.05.033

267. Everaerts M, Tigrine A, De La Rosa VR, et al. Unravelling the miscibility of poly(2-oxazoline)s: A novel polymer class for the formulation of amorphous solid dispersions. *Molecules*. 2020;25(16). doi:10.3390/molecules25163587

268. Dukić A, Mens R, Adriaensens P, et al. Development of starch-based pellets via extrusion/spheronisation. *Eur J Pharm Biopharm*. 2007;66(1):83-94. doi:10.1016/j.ejpb.2006.08.015

269. Lequieu W, Van De Velde P, Du Prez FE, Adriaensens P, Storme L, Gelan J. Solid state NMR study of segmented polymer networks: Fine-tuning of phase morphology via their molecular design. *Polymer (Guildf)*. 2004;45(23):7943-7951. doi:10.1016/j.polymer.2004.09.024

270. Dobry DE, Settell DM, Baumann JM, Ray RJ, Graham LJ, Beyerinck RA. A model-based methodology for spray-drying process development. *J Pharm Innov*. 2009;4(3):133-142. doi:10.1007/s12247-009-9064-4

271. Saboo S, Mugheirbi NA, Zemlyanov DY, Kestur US, Taylor LS. Congruent release of drug and polymer: A “sweet spot” in the dissolution of amorphous solid dispersions. *J Control Release*. 2019;298(February):68-82. doi:10.1016/j.jconrel.2019.01.039

272. Craig DQM. The mechanisms of drug release from solid dispersions in water-soluble polymers. *Int J Pharm*. 2002;231(2):131-144. doi:10.1016/S0378-5173(01)00891-2

273. Tres F, Posada MM, Hall SD, Mohutsky MA, Taylor LS. Mechanistic understanding of the phase behavior of supersaturated solutions of poorly water-soluble drugs. *Int J Pharm*. 2018;543(1-

2):29-37. doi:10.1016/j.ijpharm.2018.03.038

274. Saboo S, Moseson DE, Kestur US, Taylor LS. Patterns of drug release as a function of drug loading from amorphous solid dispersions: A comparison of five different polymers. *Eur J Pharm Sci*. 2020;155(July):105514. doi:10.1016/j.ejps.2020.105514

275. Browne E. Factors affecting the stability and performance of amorphous solid dispersions of poorly soluble active pharmaceutical ingredients.

Annex

Annex 1. Boiling point and dielectric constants of organic solvents

Organic solvent	Boiling point (°C)	Dielectric constant at 20 °C
Methanol	64.7	32.6
Ethanol	78.2	22.4
Isopropanol	82.3	18.3
Acetonitrile	81.6	37.5
Acetone	56.3	20.6
Dichloromethane	39.7	9.1
Ethyl acetate	77.1	6.0

Annex 2. Overview of HPLC-UV methods

A flow rate of 1 mL/min and an injection volume of 10 µL was employed in all cases. MeOH stands for methanol and ACN for acetonitrile

API	Mobile phase	λ (nm)	t_R (min)	LOD (µg/mL)	LOQ (µg/mL)
Naproxen	25 mM acetate buffer pH 3.50/ MeOH 30/70 V/V	270	4	0.026	0.088
Indomethacin	20 mM phosphate buffer pH 6.80/ ACN 65/35 V/V	252	4	0.016	0.052
fenofibrate	25 mM acetate buffer pH 3.50/ ACN 15/85 V/V	290	5	0.015	0.049
Diazepam	20 mM phosphate buffer pH 6.80/ MeOH 20/80 V/V	250	5	0.003	0.012

Annex 3. Position of the Tg and Tg width of spray dried ASDs

A.3.1. Position of the Tg and Tg width (Tg_w) of ASDs of indomethacin and PVPVA prepared by spray drying with different organic solvents. The drug loadings ranged from 70 wt% to 90 wt%.

Solvent	70 wt%		75 wt%		80 wt%		85 wt%		90 wt%	
	Tg (°C)	Tg_w (°C)	Tg (°C)	Tg_w (°C)	Tg (°C)	Tg_w (°C)	Tg (°C)	Tg_w (°C)	Tg (°C)	Tg_w (°C)
MeOH	62.10	31.11	63.56	35.73	59.02	31.74	54.75	32.78	53.05	30.14
EtOH	63.01	31.52	59.19	31.53	57.36	32.36	53.46	28.16	53.12	27.06
PrOH	62.62	37.42	58.83	36.35	53.65	34.88	-	-	-	-
ACN	63.93	30.42	60.18	33.12	55.38	30.85	53.77	31.1	51.45	28.58
Ac	-	-	-	-	55.25	33.32	52.81	31.56	52.72	28.13
DCM	-	-	-	-	57.67	34.03	51.56	29.54	53.01	27.71
EtAc	-	-	-	-	56.33	35.17	52.20	31.9	-	-

A.3.2. Position of the Tg and Tg width (Tg_w) of ASDs of fenofibrate and PVPVA prepared by spray drying with different organic solvents. The drug loadings ranged from 5 wt% to 35 wt%.

Solvent	20 wt%		25 wt%		30 wt%		35 wt%	
	Tg (°C)	Tg_w (°C)	Tg (°C)	Tg_w (°C)	Tg (°C)	Tg_w (°C)	Tg (°C)	Tg_w (°C)
EtOH	72.39	50.57	65.51	52.05	55.78	62.28	-	-
PrOH	70.39	48.15	62.24	54.07	56.19	58.91	-	-
ACN	73.08	48.29	62.46	49.09	53.52	58.77	-	-
Ac	74.91	51.51	59.64	74.61	47.96	69.56	29.98	80.49
DCM	74.89	69.54	56.14	75.45	49.40	74.27	-	-
EtAc	71.47	54.14	65.47	48.42	56.55	58.1	-	-
	5 WT%		**10 WT%**		**15 WT%**		**20 WT%**	
	Tg (°C)	Tg_w (°C)	Tg (°C)	Tg_w (°C)	Tg (°C)	Tg_w (°C)	Tg (°C)	Tg_w (°C)
MeOH	100.00	43.98	93.29	45.92	83.60	42.44	75.50	50.3

A.3.3. Position of the Tg and Tg width (Tg_w) of ASDs of diazepam and PVPVA prepared by spray drying with different organic solvents. The drug loadings ranged from 25 wt% to 70 wt%.

Solvent	25 wt%		30 wt%		35 wt%		40 wt%		45 wt%	
	Tg (°C)	Tg_w (°C)	Tg (°C)	Tg_w (°C)	Tg (°C)	Tg_w (°C)	Tg (°C)	Tg_w (°C)	Tg (°C)	Tg_w (°C)
MeOH	88.71	41.01	87.09	44.04	86.93	42.18	50.36 85.29	62.85	50.31 83.36	60.86
EtOH	88.25	40.85	83.62	42.06	83.65	48.87	77.99	47.36	71.37	48.96
PrOH	87.99	46.15	81.55	47.67	76.89	63.32	62.34	71.26	63.61	58.41
ACN	88.43	40.1	85.39	42.86	80.83	46.76	77.08	43.52	75.02	47.73
Ac	83.36	49.39	81.20	52.2	80.30	51.44	79.80	54.93	71.54	67.09
DCM	94.79	81.4	40.66 91.48	85.79	47.62 93.55	79.74	47.33 96.69	86.24	48.27 92.76	86.35
EtAc	-	-	-	-	65.56	59.46	64.27	53.72	62.39	70.66
	50 WT%		**55 WT%**		**60 WT%**		**65 WT%**		**70 WT%**	
	Tg (°C)	Tg_w (°C)	Tg (°C)	Tg_w (°C)	Tg (°C)	Tg_w (°C)	Tg (°C)	Tg_w (°C)	Tg (°C)	Tg_w (°C)
EtOH	69.25	40.55	65.06	42.37	56.88	35.11	55.30	34.50	54.84	36.91
PrOH	50.55	52.35	50.93	47.96	51.99	55.07	51.57	45.39	48.60	41.61
ACN	66.89	40.49	55.11	40.28	56.57	36.92	55.73	34.05	52.75	37.38
DCM	45.15 94.53	79.89	46.45 89.22	81.7	47.11 88.50	72.93	-	-	-	-
EtAc	50.67	63.58	50.77	53.02	50.74	47.5	52.69	49.63	40.45	43.28

Annex 4. Observations during/after spray drying of PVPVA samples with different organic solvents

A.4.1. Average amount of residual solvent present in spray dried PVPVA batches per solvent ± standard deviation

Solvent	Residual solvent (wt%)
MeOH	3.89 ± 0.08
EtOH	3.75 ± 0.17
PrOH	3.66 ± 0.09
ACN	2.72 ± 0.03
Ac	3.32 ± 0.45
DCM	3.34 ± 0.04
EtAc	2.63 ± 0.05

A.4.2. Range of outlet temperatures observed during spray drying of 10% w/V PVPVA solutions per solvent. The inlet temperature was always installed at the boiling point of the respective solvent.

Solvent	T_{out} (°C)
MeOH	49 – 42
EtOH	57 – 53
PrOH	59 – 55
ACN	61 – 57
Ac	43 – 41
DCM	31 – 27
EtAc	56 – 54

Annex 5. Solid-state characterization of film casted ASDs of IMC, FNB or DZP with PVPVA and different organic solvents

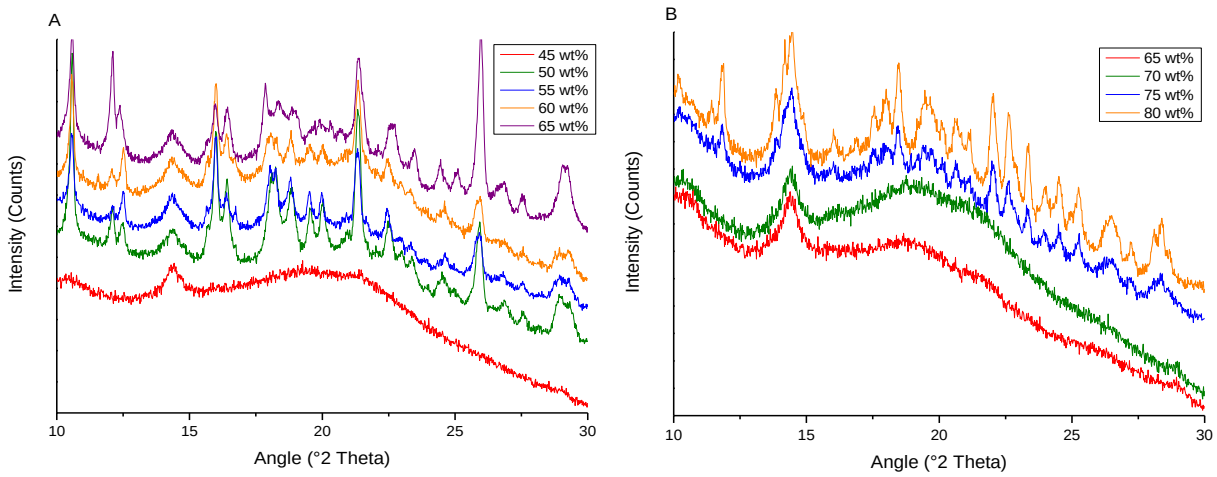

A.5.1. XRPD diffractograms of film casting of IMC and PVPVA using Ac (A) and PrOH (B). For Ac, the color code from bottom to top was: 45 wt% (red), 50 wt% (green), 55 wt% (blue), 60 wt% (orange) and 65 wt% (purple). In case of PrOH, higher drug loadings of 65 wt% (red), 70 wt% (green), 75 wt% (blue) and 80 wt% (orange) are depicted. The diffraction peak at 15 °2θ originated from the Kapton film.

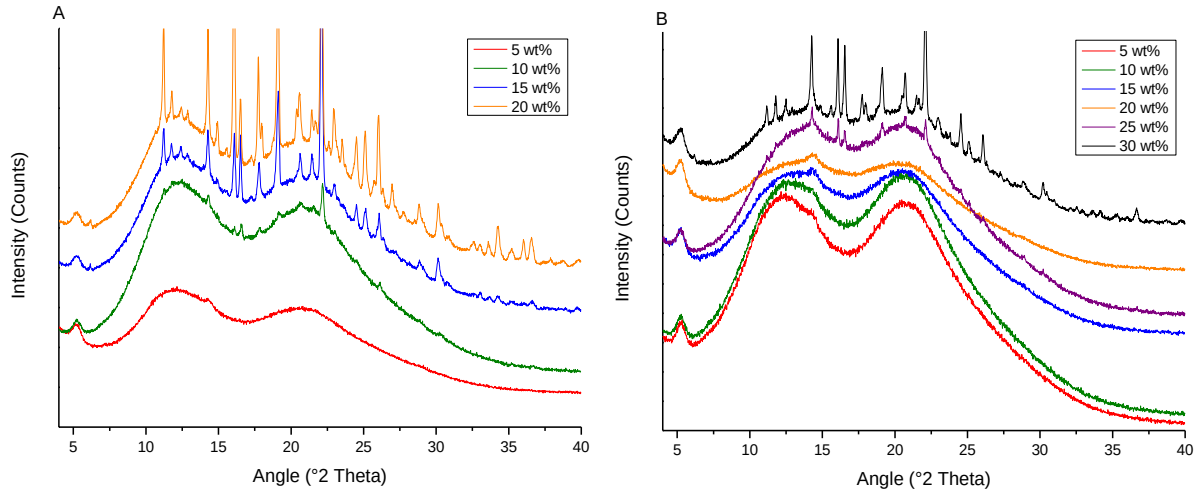

A.5.2. XRPD diffractograms of film casting of FNB and PVPVA with MeOH (A) and Ac (B). In both cases, the color code was as follows: 5 wt% (red), 10 wt% (green), 15 wt% (blue), 20 wt% (orange), 25 wt% (purple) and 30 wt% (black). The diffraction peaks at 5 and 15 °2θ originated from the Kapton film.

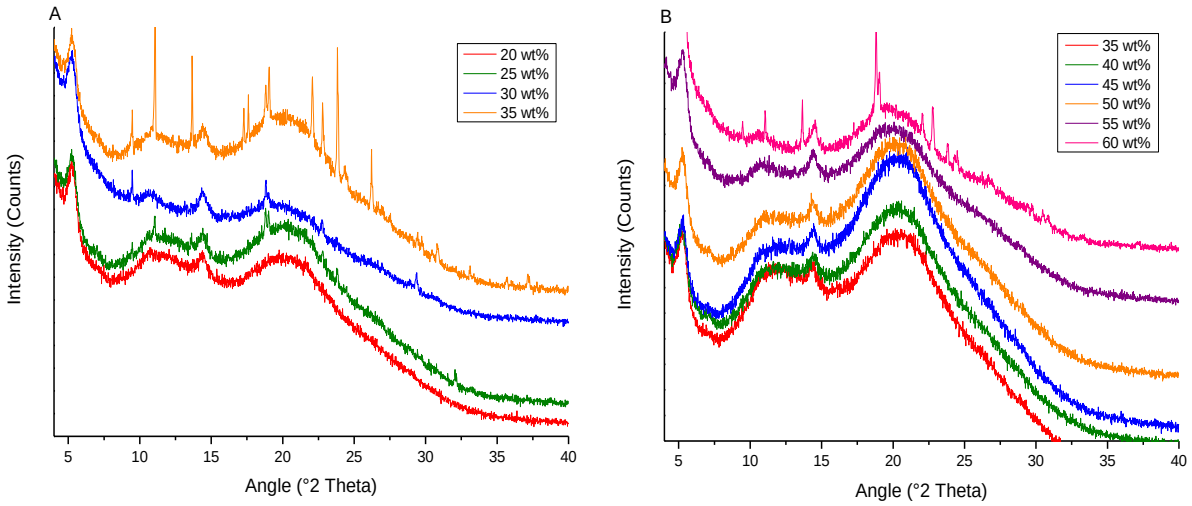

A.5.3. XRPD diffractograms of film casting of DZP and PVPVA with Ac (A) and DCM (B). For Ac, the drug loadings ranged from 20 wt% (red) to 35 wt% (orange), while for DCM, a broader range from 35 wt% (red) to 70 wt% (black) is shown. The diffraction peaks at 5 and 15 °2θ originated from the Kapton film.

Annex 6. Solid-state characterization of spray dried ASDs of IMC, FNB or DZP with PVPVA and different organic solvents

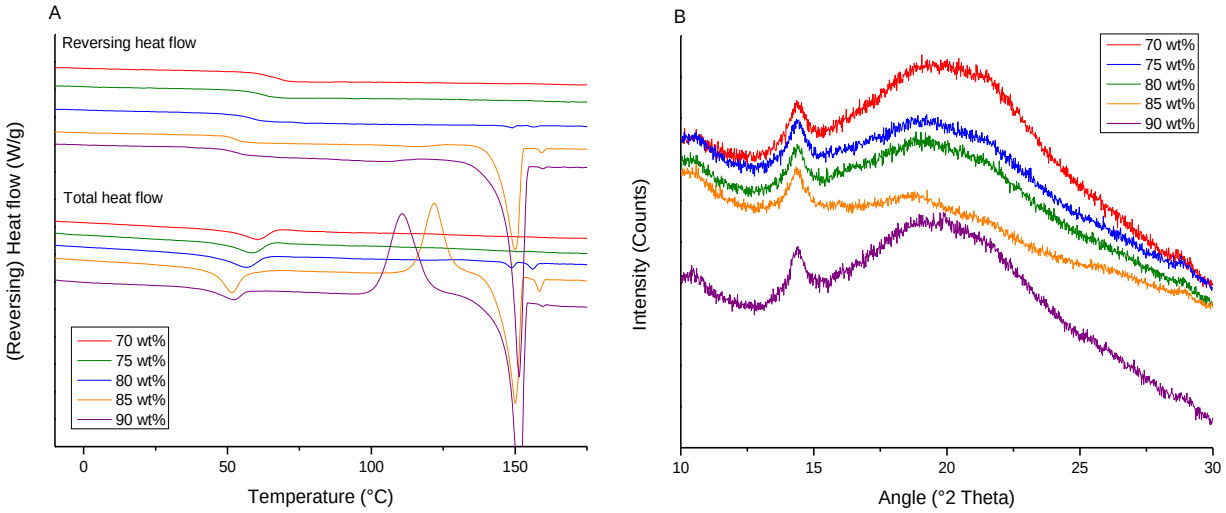

A.6.1. mDSC thermograms (A) and corresponding XRPD diffractograms (B) from spray drying of IMC and PVPVA with MeOH. In Fig A, both the reversing and the total heat flow are shown. Exothermic signals are depicted upwards. Both in Fig A and B, the drug loadings were increased from 70 wt% (red), 75 wt% (green), 80 wt% (blue), 85 wt% (orange) to 90 wt% (purple). The diffraction peak at 15 °2θ originated from the Kapton film.

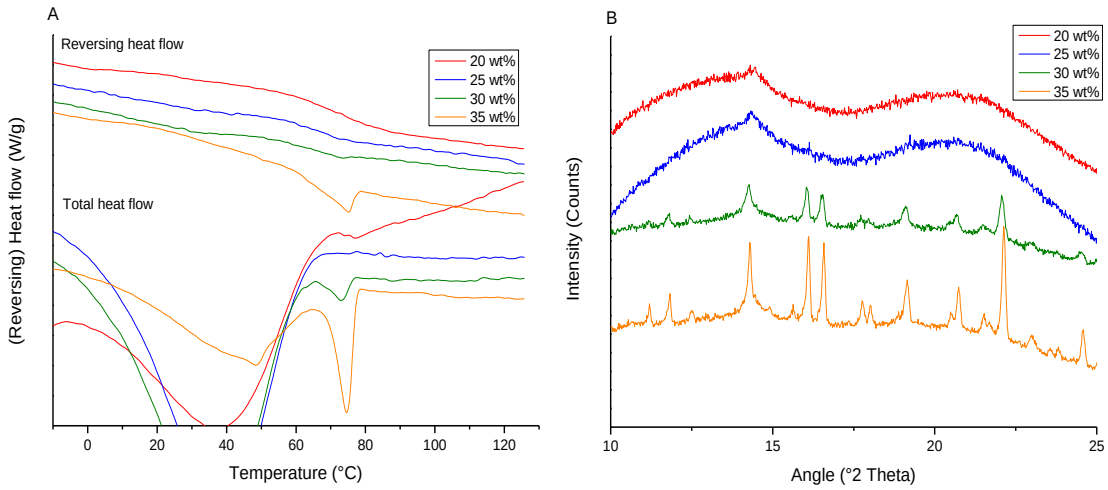

A.6.2. mDSC thermograms (A) and XRPD diffractograms (B) from spray dried FNB and PVPVA with Ac. The mDSC thermograms shown both the reversing and the total heat flow and exothermic events are depicted upwards. In both figures, the following color code was applied: 20 wt% (red), 25 wt% (blue), 30 wt% (green) and 35 wt% (orange). The diffraction peak at 15 °2θ originated from the Kapton film.

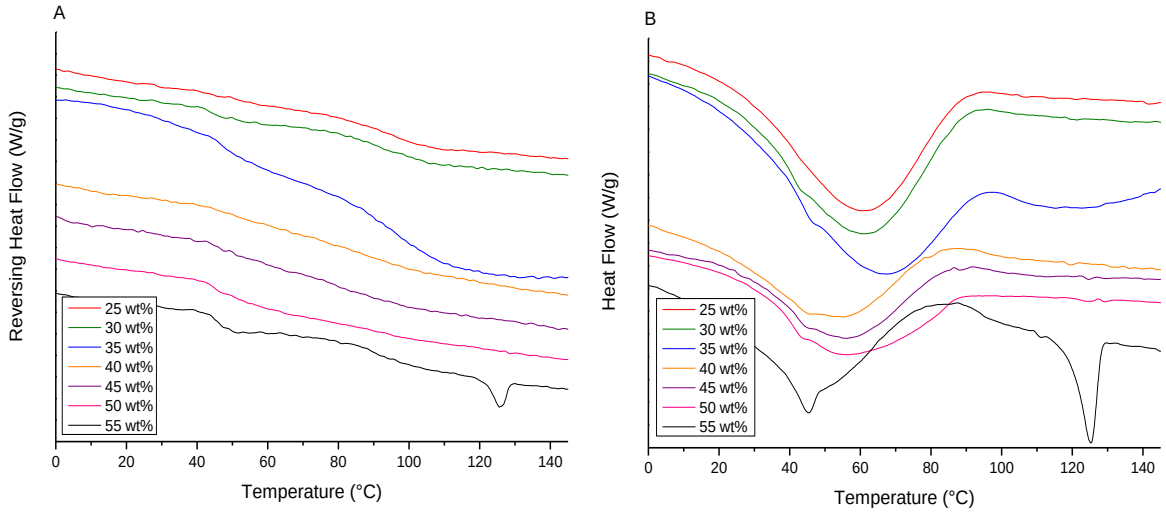

A.6.3. mDSC thermograms showing the reversing heat flow (A) and total heat flow (B) of spray dried DZP and PVPVA with DCM. In both figures, the following color code was applied: 25 wt% (red), 30 wt% (green), 35 wt% (blue), 40 wt% (orange), 45 wt% (purple), 50 wt% (pink), 55 wt% (black). Exothermic signals are depicted upwards.

Annex 7. Comparison of highest drug loadings acquired by spray drying with different solvents and thermodynamic solubilities of the APIs in the solvents

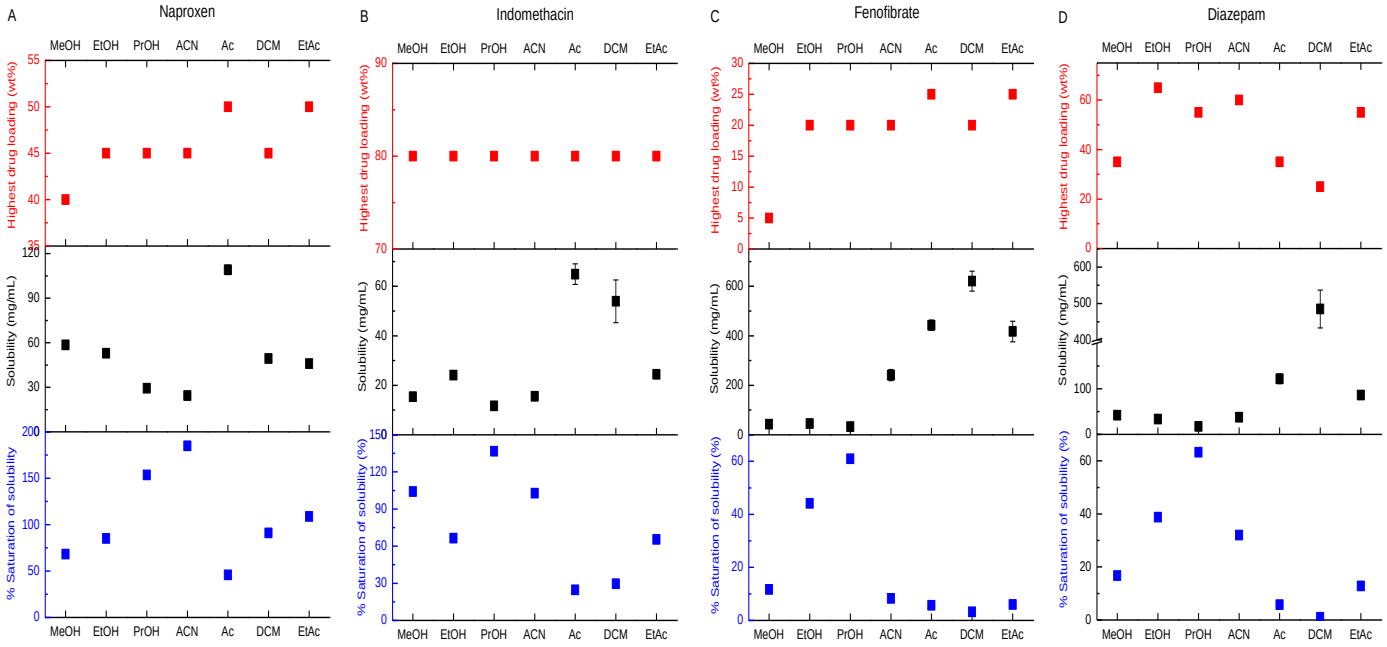

A.7.1. Correlation between the highest drug loadings acquired by spray drying, the thermodynamic solubilities and the % saturation of solubility for the respective highest drug loading of NAP (A), IMC (B), FNB (C) and DZP (D) per solvent. The highest drug loadings are shown in red, the thermodynamic solubility of the pure drug compound in black and the % saturation of solubility in blue. The error bars indicate the standard deviation on the thermodynamic solubility. When not visible, the standard deviation was smaller than the square shown in the scatter plot.

Annex 8. FT-IR peak positions

A.8.1. Peak positions (cm^{-1}) for PVPVA and NAP in the spectral region from 1800 to 1600 cm^{-1} per solvent.

Solvent	PVPVA			NAP				10:90 w:w NAP:PVPVA				
MeOH	1740	1719	1664	1738	1708	1636	1608	1740	1719	1664	1636	1608
EtOH	1741	1720	1666	1738	1708	1636	1608	1741	1720	1666	1636	1608
PrOH	1742	1722	1668	1738	1708	1636	1608	1742	1722	1668	1636	1608
ACN	1735	-	1681	1740	-	1636	1608	1735	-	1681	1636	1608
DCM	1735	-	1681	1748	1710	1636	1607	1735	-	1681	1636	1607

A.8.2. Peak positions (cm^{-1}) for PVPVA and FNB in the spectral region from 1800 to 1600 cm^{-1} per solvent.

Solvent	PVPVA			FNB			10:90 w:w FNB:PVPVA			
MeOH	1740	1719	1664	1733	1654	1600	1740	1719	1664	1600
EtOH	1741	1720	1666	1734	1655	1600	1741	1720	1666	1600
PrOH	1742	1722	1668	1735	1655	1600	1742	1722	1668	1600
ACN	1735	-	1681	1732	1656	1600	1735	-	1681	1600
DCM	1735	-	1681	1732	1654	1600	1735	-	1681	1600

A.8.3. Comparison of peak positions (cm^{-1}) for PVPVA, NAP and 30 wt% NAP and PVPVA samples in the spectral region from 1800 to 1600 cm^{-1} in solution and in the dried state.

Solvent	Condition	PVPVA			NAP				30:70 w:w NAP:PVPVA				
MeOH	Dissolved	1740	1719	1664	1738	1708	1636	1608	1740	1719	1664	1636	1608
	Dried	1733	-	1664	1732	1687	1632	1605	1733	-	1670	1634	1607
DCM	Dissolved	1735	-	1681	1748	1710	1636	1607	1735	-	1681	1636	1607
	Dried	1735		1670	1732	1687	1632	1605	1733	-	1671	1633	1605

A.8.4. Comparison of peak positions (cm^{-1}) for PVPVA, FNB and 30 wt% FNB and PVPVA samples in the spectral region from 1800 to 1600 cm^{-1} in solution and in the dried state.

Solvent	Condition	PVPVA			FNB			30:70 w:w FNB:PVPVA			
MeOH	Dissolved	1740	1719	1664	1733	1654	1600	1740	1719	1664	1600
	Dried	1733	-	1664	1731	1657	1600	1733	-	1657	1600
DCM	Dissolved	1735	-	1681	1733	1654	1600	1735	-	1681	1600
	Dried	1735		1670	1731	1657	1600	1733	-	1658	1600

Annex 9. Further investigations of peak shift in FT-IR spectra of FNB and PVPVA

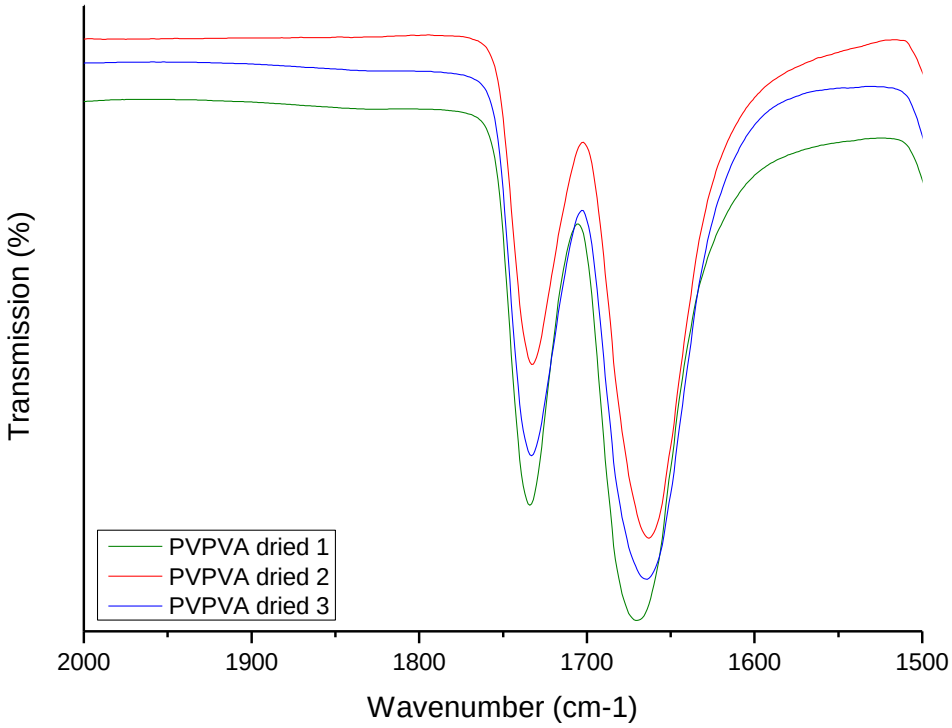

A.9.1. FT-IR spectra of PVPVA after drying for 1 min at RT from a solution of 10% w/V PVPVA in DCM. Three aliquots from the same solution were analyzed. The transmittance is shown in arbitrary units.

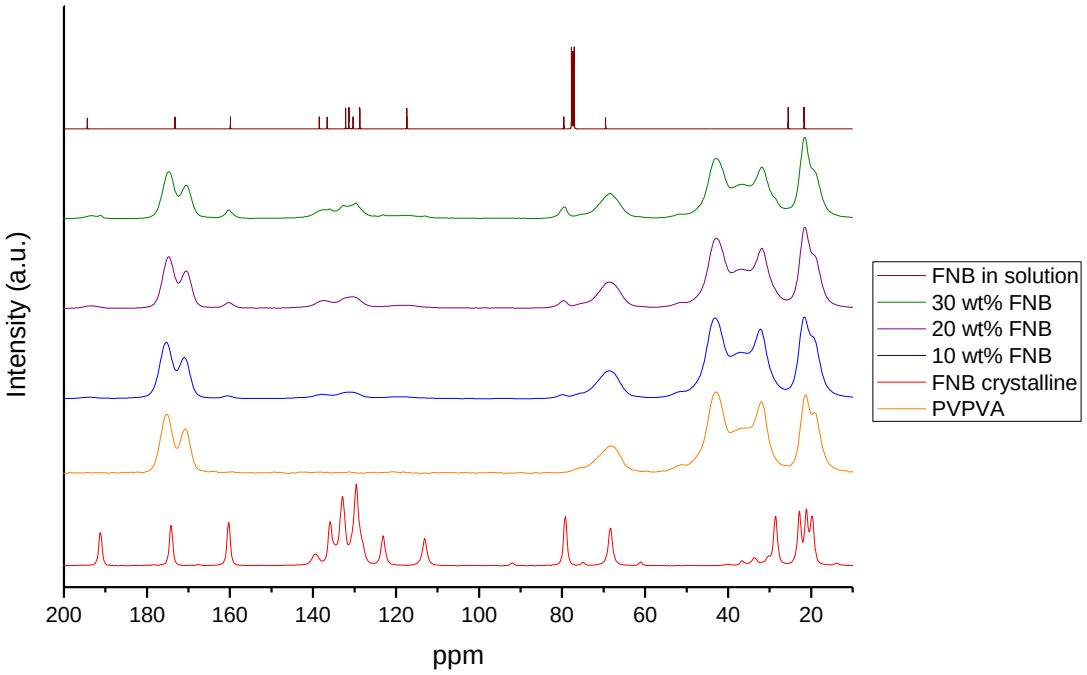

A.9.2. ^{13}C NMR spectra of crystalline FNB (red), PVPVA (orange), spray dried ASD of 10 wt% FNB and PVPVA (blue), one with 20 wt% FNB (purple), one with 30 wt% FNB (green) and the spectrum of FNB in chloroform-d (brown). The intensity is shown in arbitrary units.

Annex 10. Observations during/after spray drying of samples of NAP and PVPVA or FNB and PVPVA with different organic solvents

A.10.1. Average amount of residual solvent (wt%) in ASDs of 40 wt% NAP and PVPVA spray dried using MeOH and ASDs of 45 wt% NAP and PVPVA spray dried using DCM ± standard deviation.

Solvent	Condition	Residual solvent after secondary drying (wt%)
MeOH	Standard evaporation rate	1.40 ± 0.08
	Higher evaporation rate	0.93 ± 0.08
DCM	Standard evaporation rate	1.12 ± 0.09
	Higher evaporation rate	0.85 ± 0.11
	Lower evaporation rate	0.73 ± 0.06

A.10.2. Average amount of residual solvent (wt%) in ASDs of 5 wt% FNB and PVPVA spray dried using MeOH and ASDs of 20 wt% FNB and PVPVA spray dried using DCM ± standard deviation.

Solvent	Condition	Residual solvent after secondary drying (wt%)
MeOH	Standard evaporation rate	4.05 ± 0.25
	Higher evaporation rate	2.73 ± 0.18
DCM	Standard evaporation rate	2.77 ± 0.04
	Higher evaporation rate	1.92 ± 0.12
	Lower evaporation rate	1.83 ± 0.08

A.10.3. Outlet temperatures (T_{out}) observed during spray drying of ASDs of 5 wt% FNB and PVPVA using MeOH and ASDs of 20 wt% FNB and PVPVA using DCM.

Solvent	Condition	$T_{out, begin}$ (°C)	$T_{out, end}$ (°C)	ΔT (°C)
MeOH	Standard evaporation rate	51	44	7
	Higher evaporation rate	61	59	2
DCM	Standard evaporation rate	32	29	3
	Higher evaporation rate	44	42	2
	Lower evaporation rate	28	22	6

Annex 11. Solid-state characterization of ASDs of FNB or NAP with PVPVA spray dried using DCM

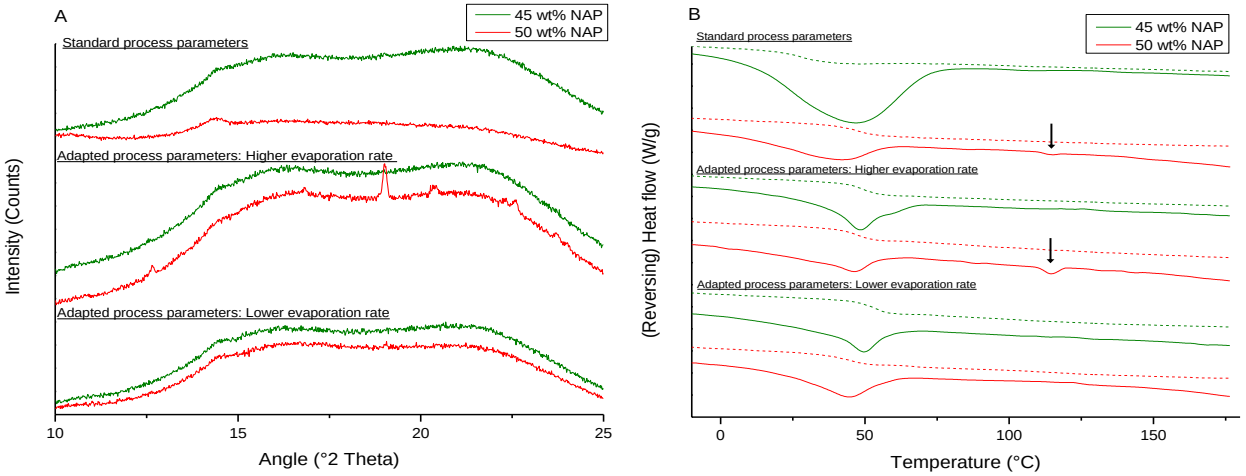

A.11.1. XRPD diffractograms (A) and mDSC thermograms (B) of 45 wt% (green) and 50 wt% (red) NAP and PVPVA spray dried using DCM with standard process parameters and parameters that gave rise to an increased evaporation rate. For the mDSC analysis, both the total heat flow (full line) and reversing heat flow (dotted line) are depicted. Exothermic signals are directed upwards. The arrows indicate the position of an endothermic melting event of NAP.

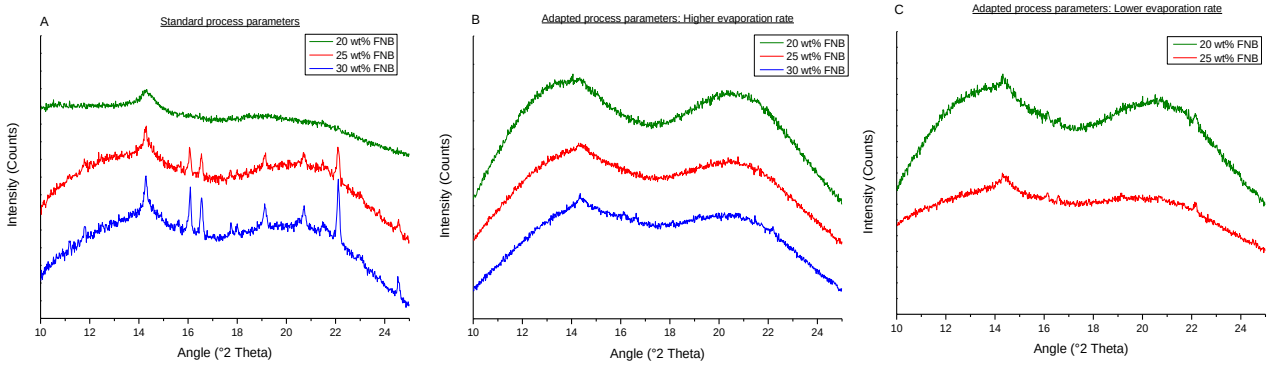

A.11.2. XRPD diffractograms of 20 wt% (green), 25 wt% (red) and 30 wt% (blue) FNB and PVPVA spray dried using DCM with standard process parameters (A), parameters that resulted in a lower evaporation rate (B) and ones that resulted in an increased evaporation rate (C). The intensity is shown in arbitrary units.

Contributions

Scientific acknowledgements

The Department of Materials Engineering (KU Leuven), the Department of Mechanical Engineering (KU Leuven), Polymer Chemistry and Materials (KU Leuven), the Division of Soft Matter, Rheology and Technology (SMaRT, KU Leuven), the Institute for Materials Research (UHasselt) and the Division of Pharmaceutical Analysis (KU Leuven) are acknowledged for the use of their facilities. Bernard Appeltans, Nico Coenen, Anja Vananroye, Danny Winant, Gunter Reekmans and Jasper Beyens are acknowledged for technical support. The scientific expertise of Christophe Huygens (Laboratoires SMB) and Prof. Adriaensens (UHasselt) was highly appreciated.

Personal contributions

Sien Dedroog planned and performed all the experiments, analyzed the data and wrote the text, with the following exceptions:

For Chapter 1, a part of section 1.3.3. regarding spray drying has been published as a review paper with a joint first authorship: Boel E., Koekoekx R., Dedroog S., Babkin I., Vetrano M.R., Clasen C., Van den Mooter G. Unraveling Particle Formation: From Single Droplet Drying to Spray Drying and Electrospraying. Pharmaceutics, 12(7), 625 (2020).

For Chapter 3, 4, 5 and 6 Danny Winant performed the TGA experiments to determine the polymer degradation temperature or the amount of residual solvent content in the ASDs. The TGA experiments to study the evaporation kinetics were carried out by Sien Dedroog.

For Chapter 4, the GFA study and the preparation of ASDs of indomethacin by film casting were caried out by Eline Boel (KU Leuven). She also wrote the text concerning these results. Célestine Kindts (KU Leuven) prepared and analyzed ASDs of indomethacin and diazepam by spray drying as part of her master thesis. Bernard Appeltans (KU Leuven) performed the SEM experiments and helped by the executing of the solubility experiments.

For Chapter 6, ssNMR and liquid state NMR experiments were performed by Gunter Reekmans and Prof. Adriaensens at UHasselt. SEM images were acquired by Bernard Appeltans (KU Leuven).

Chapter 7 is a joint first authorship paper with Timothy Pas. All figures were made by Timothy Pas, while Table 7.1. was made by Sien Dedroog. Section 7.4.1.3. regarding difficulties of XRPD in detecting nanocrystallinity, the part of section 7.4.2.2. discussing the overlap of residual solvent evaporation with crystallization during thermal analysis and section 7.4.2.3. about the possible issues of enthalpy recovery coinciding with melting events, were based on results acquired by Timothy Pas.

Conceptualization and writing of this chapter were done fifty-fifty by Timothy Pas and Sien Dedroog. SEM images were acquired by Bernard Appeltans (KU Leuven).

Prof. Guy Van den Mooter was the supervisor of this project. He helped to conceptualize and develop the research strategy, to design the experimental methodology and to correctly interpret the data. He also reviewed the full text of this work.

Conflict of interest statement

Laboratoires SMB (26-28 Rue de la Pastorale, 1080 Brussels) and Het Fonds voor Wetenschappelijk Onderzoek Vlaanderen (FWO) are acknowledged for their financial support.

The authors declare no conflict of interest.

Curriculum Vitae

Education

- 2017-2022: Doctoral training in Pharmaceutical Sciences, KU Leuven
- 2015-2017: Master in Drug Development, specialization pharmacy, Pharmaceutical Sciences, KU Leuven
- 2012-2015: Bachelor in Pharmaceutical Sciences, KU Leuven

Scientific publications

- Dedroog, S., Huygens, C., Van den Mooter, G., 2019. Chemically identical but physically different: a comparison of spray drying, hot melt extrusion and cryo-milling for the formulation of high drug loaded amorphous solid dispersions of naproxen. Eur. J. Pharm. Biopharm. 135, 1–12.
- Dedroog, S., Pas, T., Vergauwen, B., Huygens, C., Van den Mooter, G., 2020. Solid-state analysis of amorphous solid dispersions: Why DSC and XRPD may not be regarded as stand-alone techniques. J. Pharm. Biomed. Anal. 178, 112937.
- Dedroog, S., Boel, E., Kindts, C., Appeltans, B., Van den Mooter, G., 2021. The underestimated contribution of the solvent to the phase behavior of highly drug loaded amorphous solid dispersions. Int. J. Pharm. 609, 121201
- Boel, E., Koekoekx, R., Dedroog, S., Babkin, I., Vetrano, M.R., Clasen, C., Van den Mooter, G., 2020. Unraveling particle formation: From single droplet drying to spray drying and electrospraying. Pharmaceutics 12, 1–58.

Oral presentations at international meetings

- Chemically identical, but physically different: A comparison of spray drying, hot melt extrusion and cryo-milling for the formulation of high drug loaded amorphous solid dispersions of naproxen. PSSRC annual symposium edition 12. Leuven, Belgium. 12-14 September 2018.
- Chemically identical, but physically different: A comparison of spray drying, hot melt extrusion and cryo-milling for the formulation of high drug loaded amorphous solid dispersions of naproxen. Evonik Seminar. Darmstadt, Germany. 5 June 2019.
- Solvent selection as a decisive factor for formulating high drug loaded amorphous solid dispersions. PSSRC annual symposium edition 13. Düsseldorf, Germany. 12-14 September 2019.

- Unraveling the importance of solvent selection for the formulation of high drug loaded amorphous solid dispersions. PSSRC annual symposium edition 14. Online. 23 June 2020.

Oral presentations at national meetings

- The power of orthogonal analytical techniques: Application of mDSC and XRPD for the solid-state analysis of amorphous solid dispersions. BSPS. Brussels, Belgium. 20 May 2019.

Poster presentations at international meetings

- The power of orthogonal analytical techniques: Application of mDSC and XRPD for the solid-state analysis of amorphous solid dispersions. ULLA summer school. Helsinki, Finland. 26 June-6 July 2019.